

Dissertation
submitted to the
Combined Faculties for the Natural Sciences and for Mathematics
of the Ruperto-Carola University of Heidelberg, Germany
for the degree of
Doctor of Natural Sciences

put forward by
Dipl.-Phys. Daniel Kiefhaber
born in Kaiserslautern

Date of oral examination: 06.02.2014

Optical measurement of short wind waves — from the laboratory to the field

Referees:

Prof. Dr. Bernd Jähne

Prof. Dr. Ulrich Platt

Abstract

With the Reflective Stereo Slope Gauge and the Medium Angle Slope Gauge, two new imaging instruments for the measurement of short wind waves on the ocean have been developed, validated, and deployed to a four week field experiment. Using active illumination with near-infrared LED light sources they are independent of natural light. Unlike other reflection-based techniques, they can be operated day and night under a wide range of environmental conditions. The instruments' performance was carefully validated in the laboratory and in the field. Their unique capabilities of simultaneously measuring the two-dimensional slope probability distribution and the mean square slope (mss) of the waves, as well as wave height and a parameter linked to local surface curvature are demonstrated. Extensive measurements of short wave statistics from an air-sea interaction experiment off the coast of Peru are reported. A large variability of surface conditions due to the changing presence of surfactants on spatial scales smaller than one hundred meters was encountered. In a laboratory experiment, the dependence of gas transfer velocities on the suppression of waves by the soluble artificial surfactant Triton X-100 was investigated. It is shown that mss describes gas transfer velocities better than wind speed or the friction velocity. The new instruments can provide robust routine ship-borne measurements of mss, a key component in the effort of replacing wind speed with mean square slope as the standard parameter for gas transfer velocities.

Zusammenfassung

Zwei neue Instrumente zur Vermessung von kleinskaligen Windwellen auf dem Ozean, die Reflective Stereo Slope Gauge und die Medium Angle Slope Gauge, wurden entwickelt, validiert und in einem vierwöchigen Feldexperiment eingesetzt. Durch die Benutzung von LED-Lichtquellen zur Beleuchtung sind sie unabhängig von natürlichem Licht. Im Gegensatz zu anderen reflexionsbasierten Messtechniken können sie dadurch bei Tag und Nacht unter sehr unterschiedlichen Umweltbedingungen eingesetzt werden. Die Leistung der Instrumente wurde in Labor- und Feldexperimenten sorgfältig validiert. Ihre einzigartigen Fähigkeiten zur gleichzeitigen Messung der zweidimensionalen Wahrscheinlichkeitsverteilung der Wellenneigung und der mittleren quadratischen Neigung (mss), sowie von Wellenhöhen und einem Parameter, der die lokale Krümmung der Wasseroberfläche beschreibt, werden demonstriert. Umfangreiche Messungen der Statistik kleinskaliger Wellen aus einem Feldexperiment vor der Küste von Peru werden vorgestellt. Aufgrund der wechselhaften Bedeckung der Ozeanoberfläche mit Oberflächenfilmen wurden sehr variable Bedingungen vorgefunden, die sich auf Skalen von weniger als hundert Metern stark änderten. In einem Laborexperiment wurde der Einfluss der Unterdrückung von Wellen durch den künstlichen, löslichen Oberflächenfilm Triton X-100 auf Gastransfergeschwindigkeiten untersucht. Es wird gezeigt, dass die mss den Transfer besser beschreibt als die Wind- oder Schubspannungsgeschwindigkeit. Die neuen Instrumente sind in der Lage, routinemäßig robuste Messungen der mss auf Schiffen durchzuführen. Dies ist eine Schlüsselkomponente in den Bemühungen, in Gasaustauschparametrisierungen Windgeschwindigkeit durch mss zu ersetzen.

Contents

1	Introduction	1
2	Theory	7
2.1	Waves on the water surface	7
2.1.1	Conservation of mass and momentum	7
2.1.2	Linear waves in viscous fluids	11
2.1.3	The Marangoni effect	15
2.1.4	The wave action balance	17
2.1.5	Non-linear waves	19
2.1.6	Wave nomenclature	20
2.2	Description of wave fields	21
2.2.1	Spectral description of the wave field	22
2.2.2	Probability distributions	25
2.2.3	Statistical parameters	27
2.2.4	Mean square slope	29
2.3	Air-sea gas exchange and waves	30
2.3.1	Mass transport in fluids	30
2.3.2	Modeling gas exchange	31
2.3.3	The facet model	32
2.3.4	Parameterizations of air-sea gas exchange	33
3	Methods	35
3.1	Optical measurement of ocean waves	35
3.1.1	Imaging Slope Gauge	36
3.1.2	Polarimetric Slope Sensing	38
3.1.3	Stereopsis	42
3.1.4	Helmholtz stereopsis	45
3.2	Height measurement	48
3.2.1	Stereo triangulation	48
3.2.2	Disparity estimation	49

3.3	Slope measurement	50
3.3.1	Statistical measurement of surface slope	50
3.3.2	Measurement of mean square slope	51
3.4	Curvature measurement	53
3.4.1	Reflections off the curved water surface	53
3.4.2	Speckle statistics	54
4	Setup and calibration	57
4.1	Instruments	57
4.1.1	The RSSG	57
4.1.2	The MASG	59
4.2	Calibration	60
4.2.1	RSSG calibration	60
4.2.2	MASG	64
5	Experiments	67
5.1	Laboratory experiments	67
5.1.1	The Marseille wind-wave facility	67
5.1.2	The Marseille 2011 experiment	68
5.1.3	The Marseille 2012 experiment	69
5.1.4	The Aeolotron 2011 experiment	69
5.2	Field experiments	70
5.2.1	OSSPRE 2011	70
5.2.2	Peru 2012	71
6	Data processing	73
6.1	Ship motion estimation	73
6.1.1	Instrument synchronization	74
6.1.2	Complementary filtering	74
6.2	Wave height	77
6.2.1	Disparity estimation	77
6.2.2	Motion correction	80
6.2.3	Implementation	80
6.3	Wave slope	82
6.3.1	Averaging speckle images	82
6.3.2	Probability of slope zero	86
6.3.3	Mean square slope	86
6.4	Curvature	87
6.5	Imaging Slope Gauge	90
6.5.1	Chromatic aberration	91
6.5.2	RGB image interpolation	92

6.5.3	Log-polar spectra	93
6.5.4	Mean square slope	94
6.5.5	Full Workflow	94
7	Results	97
7.1	Instrument validation	97
7.1.1	Height measurement	98
7.1.2	Slope measurement	103
7.2	Statistical wave measurements	111
7.2.1	Slope probability distribution measurements	111
7.2.2	Surface curvature measurements	119
7.3	Waves and gas exchange	123
7.3.1	Wave suppression by surfactants	124
7.3.2	Effect on gas transfer velocity	128
7.3.3	The facet model	132
8	Discussion	137
8.1	Routine measurements of wave slope statistics	137
8.2	Gas exchange and waves	138
8.3	Future measurement of waves in the field	141
8.3.1	Long wave measurements	141
8.3.2	Curvature measurements	142
8.3.3	Drones	143
9	Conclusion and Outlook	145
9.1	Conclusion	145
9.2	Outlook	147
	Bibliography	149
A	Appendix	163
A.1	Height from disparity	163
A.2	Marseille 2011	165
A.3	Marseille 2012	165
A.4	OSSPRE 2011	168
A.5	Meteor M91	168
A.6	Aeolotron 2011	168
A.7	Reflectance measurements	168

1

Introduction

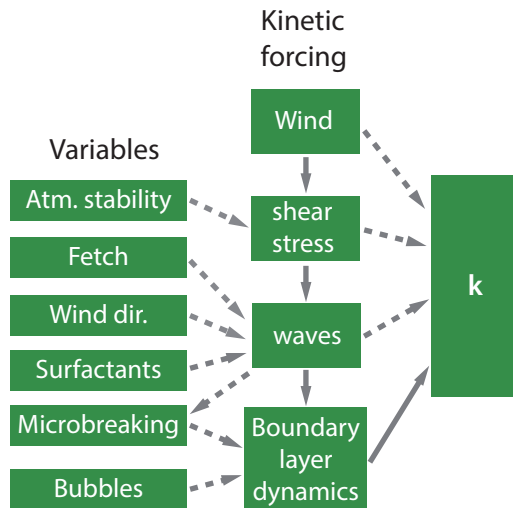
The ocean in the global carbon cycle

The ocean is a net sink for anthropogenic carbon dioxide (CO₂) emissions. About 25 % – 30 % of fossil fuel CO₂ emissions are taken up by the world ocean (Le Quéré et al. 2010, Sabine et al. 2004). Since pre-industrial times, a total of 155 PgC¹ of anthropogenic carbon has been sequestered by the ocean (Khatiwala et al. 2013). Compared to the estimated total reservoir size of approximately 38000 PgC (IPCC 2007) this may seem a small amount. Still, a decrease in oceanic pH value due to the uptake of anthropogenic CO₂ is recorded, the ocean acidifies (Doney et al. 2009). This causes an imbalance in the ocean's carbonate equilibrium leading to reduced growth of reef-building coral (Hoegh-Guldberg et al. 2007) and other key marine organisms depending on carbonate shells (Orr et al. 2005).

From an atmospheric point of view, the oceanic uptake reduces the rate at which the concentration of CO₂ increases. To predict this mitigation and its consequences for future climate evolution, coupled climate models are required which account for changes in the oceanic sink (Cox et al. 2000). Changes in the wind speed distribution already lead to a weakening of net CO₂ uptake by the Southern Ocean (Le Quéré et al. 2007). On regional scales, the strength of the oceanic sink is known to vary significantly on interannual time scales (Dore et al. 2003). Good parameterizations of air-sea gas transfer are a key component in modeling the development of the strength of the oceanic sink in the future.

The average yearly flux of CO₂ from atmosphere to ocean is estimated to be 2.3 ± 0.6 Pg/yr (for the years 2000-2010, Khatiwala et al. 2013). Uncertainties in the parameterizations of air-sea gas exchange are a major contributor to the overall error

¹PgC = Peta gram carbon; 1 Pg = 10¹⁵ g

**Figure 1.1**

Simplified scheme of the factors influencing the transfer velocity k . Wind transfers momentum into the water, creating a shear current and waves. Both the shear current and breaking waves affect the dynamics in the boundary layer. The near-surface turbulence ultimately controls the transfer velocity. A number of environmental variables can affect the different elements of the chain. Modified after Wanninkhof et al. (2009).

margins (Takahashi et al. 2009).

Processes controlling air-sea transfer velocities

The transfer velocity² of sparingly soluble gases like CO_2 is controlled by the hydrodynamics very close to the water surface in the aqueous mass boundary layer, in which turbulent motion is inhibited (Soloviev et al. 2007). A simplified overview of the main factors influencing the transfer velocity is shown in Fig. 1.1. By far the majority of kinetic forcing at the water surface is due to the wind. However, wind does not directly affect the boundary layer dynamics, but indirectly through inducing a shear current and waves. Still, since the quantity that is ultimately of interest, near-surface turbulence, is very difficult to measure, semi-empirical parameterizations for k using wind speed U as a parameter are widely used.

Two small-scale processes have been credited with being responsible for the enhancement of transfer velocities over the levels expected from shear-generated turbulence at low to moderate wind speeds: Microscale wave breaking and (micro) Langmuir circulation (Frew et al. 2004).

Microscale wave breaking (Banner and Phillips 1974) denotes the instability of short gravity waves with wavelengths of the order of decimeters. Because of the short wavelengths and small amplitudes of the waves involved, turbulent kinetic energy (TKE) from the breaking process is created close to the surface (Jessup et al. 1997), leading to a large enhancement of gas exchange (Siddiqui et al. 2004, Zappa et al. 2001). Longer waves which break producing more spectacular “whitecaps” inject most of their TKE deep into the well-mixed bulk of the water body. Therefore, they do not contribute as much to gas exchange³. Zappa et al. (2004) show that microscale breaking is responsible for up to 75 % of the total transfer at moderate wind speeds.

²flux = transfer velocity \times concentration difference.

³Bubble plumes created in whitecapping contribute, especially at high wind speeds.

Small-scale Langmuir circulations are created by the interaction of the shear current with waves. They are near-surface helices with their axis almost aligned with the wind (Caulliez 1998). These vortices have been observed both in the laboratory (Melville et al. 1998) and in the field (Veron et al. 2009). Their appearance has been shown to coincide with the enhancement of gas exchange during initial wave growth (Veron and Melville 2001).

Estimating air-sea fluxes

One approach to get to an estimate of global air-sea CO₂ fluxes is combining large numbers of worldwide $\Delta p\text{CO}_2$ measurements⁴ with a parameterization linking the transfer velocity k to wind speed U (Takahashi et al. 2002). Existing parameterizations have very different functional forms, e.g. piecewise linear (Liss and Merlivat 1986), quadratic (Wanninkhof 1992), cubic (Wanninkhof and McGillis 1999), or polynomial (Nightingale et al. 2000). To obtain global CO₂ fluxes, Takahashi et al. (2009) use a quadratic relation of transfer velocity with wind speed found by Ho et al. (2006). The scaling factor in the relation is taken from “bomb” ¹⁴C measurements (Naegler et al. 2006, Sweeney et al. 2007). The errors associated with uncertainties in the k-U-parameterization are estimated to be $\pm 30\%$.

Parameterizations with wind speed are neat, because it is a very accessible parameter. Available satellite data products or meteorological models allow global estimates. Locally, wind speed is routinely recorded on research vessels. Using a k-U-parameterization it is thus possible to obtain fluxes for any trace gas from the measurement of concentration differences between the atmosphere and the ocean (e.g. Quack et al. 2004).

Ho et al. (2011) argue that wind speed is a sufficient correlate for gas exchange time scales of the order of days to weeks. While this may be correct, experiments have also shown that wind speed is not generally a good parameter describing local transfer velocities: In the presence of surface active substances (surfactants⁵), which may form a mono-molecular surface layer, gas exchange rates are significantly lower than for clean water surfaces (e.g. Asher and Pankow 1986, Broecker et al. 1978, Jähne et al. 1987). This is due to the damping effect that these mono-molecular layers have on waves (Alpers 1989, Bock and Mann 1989), which then in turn do not produce as much near-surface turbulence. Especially in coastal areas, where biological activity can be strong and very variable, surfactants can have an immense impact on transfer velocities (Frew et al. 2004).

This was also noted by Kock et al. (2012) who were only able to close their budget of N₂O in the upper ocean in coastal upwelling regions by using a parameterization that explicitly accounts for a reduction of transfer velocities due to surfactants.

⁴ $\Delta p\text{CO}_2$ is the difference in partial pressure of CO₂ in the air and the water.

⁵surfactant = surface active agent

Alternative parameterizations for transfer velocities

A number of alternative parameters have been proposed to describe air-sea gas transfer. A parameter that is closely related to near-surface turbulence is the turbulent kinetic energy (TKE) dissipation ϵ . An expression linking it to transfer velocities can be derived from different assumptions on the near-surface turbulence structure (Kitaigorodskii 1984, Lamont and Scott 1970). Experimentally, ϵ has been found capable of explaining transfer velocities under very different turbulence generation conditions, e.g. in rivers, estuaries, a model oceans (Zappa et al. 2007). To determine ϵ , measurements of the flow field are required. This requires underwater instrumentation, making ϵ a very inaccessible parameter.

Another alternative that has been successfully used to describe transfer velocities is the divergence of the flow field at the surface (Banerjee and McIntyre 2004, McKenna and McGillis 2004). It is related to surface renewal, i.e. the replacement of fluid particles at the surface with water from the bulk. It is possible to measure surface divergence using thermal imagery (Asher et al. 2012), so that underwater equipment is not required. However, because of the small scale of the divergence structures, measurements cannot easily be upscaled to large footprints.

Jähne et al. (1984) proposed to use the mean square slope of the wave field, σ_s^2 . It is a measure for the roughness of the water surface. While there is no direct theoretical justification for its use as a correlate for transfer velocities, evidence was collected in numerous laboratory and field studies that σ_s^2 can account for the effects of surfactants on gas transfer (e.g. Bock et al. 1999, Degreif 2006, Frew et al. 2004, Hara et al. 1995, Krall 2013). Zappa et al. (2004) show that σ_s^2 is a good correlate for the spatial coverage of microscale breaking. This and the fact that Langmuir circulations also require the presence of small-scale waves may explain why σ_s^2 is a good correlate for the transfer velocity. While from a theoretical point of view, TKE dissipation ϵ or surface divergence are preferred due to their more direct link to near-surface turbulence, mean square slope has a decisive advantage: It can in principle be measured by remote sensing and on all scales. Field measurements have been conducted for example from small research catamarans (Bock and Hara 1995), platforms (e.g. Zappa et al. 2012), airplanes (Cox and Munk 1954a), satellite imagery (Bréon and Henriot 2006, Ebuchi and Kizu 2002) or satellite radar backscatter (Glover et al. 2007).

It was already noted that the accessibility of a parameter is crucial for its chances of success in replacing wind speed as a correlate for gas exchange. In the first step, a robust measurement technique is needed, capable of measuring local mean square slope (mss) with minimal effort. Such a technique has not been available thus far for the open ocean. Only if it is possible to measure the mss routinely on research vessels, there is a chance that the k-U-relationships will be replaced one day. The feasibility of upscaling a local k-mss-parameterization to global scales has already been demonstrated (Frew et al. 2007).

The goal of this study is to explore optical techniques for the measurement of

waves in the field and find a robust way to measure mean square slope (and other parameters of short wind waves). The novel instruments are then deployed to a field campaign to measure short wave characteristics as part of an air-sea interaction experiment. Furthermore, the suitability of wave parameters for the description of transfer velocities is investigated from laboratory data.

2

Theory

In this chapter, an introduction into the theoretical description of free waves at the water surface is given. Starting from fundamental conservation principles and the governing equation of fluid mechanics, the Navier-Stokes equation, the path to its solution for small-amplitude, irrotational waves is presented. The effect of a viscoelastic mono-molecular layer of surface active material is accounted for and an overview of the theory of Marangoni wave damping is given. Important statistical concepts for the description of wave fields are introduced – the wave spectrum and probability distribution functions. The chapter concludes with a very brief introduction of the mechanisms and description of air-sea gas exchange.

2.1 Waves on the water surface

2.1.1 Conservation of mass and momentum

The continuity equation

The continuity equation for fluids is simply an expression of mass conservation. In integral form, it states that

$$\frac{d}{dt} \left(\int_V \rho \, dv \right) = - \int_S \rho \mathbf{u} \cdot \mathbf{n} \, ds, \quad (2.1)$$

namely that changes in the density ρ of a fluid in a volume V can only be due to a flow of mass through the surface S of the volume. Here, $\mathbf{u} \cdot \mathbf{n}$ is the velocity component normal to the surface. By applying Gauss' theorem to the right hand

Table 2.1.: Symbols used in sec. 2.1.

Symbol	Description	Unit
$\mathbf{x} = (x, y)$	(surface) position vector	m
t	time	s
$\eta(\mathbf{x}, t)$	vertical water surface displacement	m
$\xi(\mathbf{x}, t)$	horizontal water surface displacement	m
$\mathbf{u} = (u, v, w)$	velocity vector	m/s
$\mathbf{k} = (k_x, k_y)$	wavenumber vector (2D), $ \mathbf{k} = k$	rad/m
h	water depth	m
ω	wave angular frequency	rad/s
τ_{ij}	stress tensor	N/m ²
ρ	fluid density	kg/m ³
μ	dynamic viscosity	Pa s
ν	kinematic viscosity	m ² /s
p	pressure	Pa
σ	surface tension	N/m
ϵ	surface dilatational elasticity $d\sigma/d \ln A$	N/m
g	gravitational acceleration	m/s ²
$\phi(\mathbf{x}, t)$	velocity potential	m ² /s
$\psi(\mathbf{x}, t)$	vorticity field	m ² /s
\mathcal{N}	wave action	J s
$n(\mathbf{k})$	wave action density	J s/m ²

side and changing the order of differentiation and integration (e.g. Johnson 1997; p. 4), the continuity equation is obtained in the more familiar differential form

$$\frac{\partial \rho}{\partial t} + \nabla \cdot (\rho \mathbf{u}) = \frac{\partial \rho}{\partial t} + \rho(\nabla \cdot \mathbf{u}) + (\mathbf{u} \cdot \nabla)\rho = \frac{D\rho}{Dt} + \rho(\nabla \cdot \mathbf{u}) = 0. \quad (2.2)$$

The operator $D/Dt \equiv \partial/\partial t + (\mathbf{u} \cdot \nabla)$, the *material derivative*, expresses that the change of a fluid variable (here: density) for an observer at a fixed location is either due to local temporal changes $\partial/\partial t$ or due to advection by the mean flow \mathbf{u} . Such a reference frame that is fixed in space is referred to as *Eulerian* reference frame. In contrast to this, a *Lagrangian* reference frame is moving with a fluid particle along the streamlines of the mean current. For incompressible fluids, the derivative of the density $D\rho/Dt = 0$, so that the equation reduces to

$$\nabla \cdot \mathbf{u} = 0. \quad (2.3)$$

The Navier-Stokes equation

Newton's Second Law requires that the rate of change of momentum of a fluid in a volume V is the result of the forces acting on the fluid in V and the rate of flow of momentum across the surface S of V :

$$\int_V \left(\rho \frac{Du_i}{Dt} - \frac{\partial \tau_{ij}}{\partial x_j} - \rho F_i \right) dv = 0, \quad (2.4)$$

where the summation convention was used. $\mathbf{F} \equiv (F_1, F_2, F_3)$ represents the *body forces*, acting on the fluid as a whole, and τ_{ij} is the stress tensor. This tensor describes the *local forces* acting on the fluid volume; τ_{ij} represents the i -component of the stress (force per unit area) on a surface with a surface normal in the j -direction. The tensor is symmetric and can be represented by

$$\tau_{ij} = -p\delta_{ij} + 2\mu e_{ij}, \quad (2.5)$$

where p is the pressure, δ_{ij} is the Kronecker delta, μ is the dynamic viscosity, and

$$e_{ij} = \frac{1}{2} \left(\frac{\partial u_i}{\partial x_j} + \frac{\partial u_j}{\partial x_i} \right) \quad (2.6)$$

is the *rate of strain tensor* for an incompressible fluid (Johnson 1997).

Inserting eq. (2.6) and (2.5) into eq. (2.4), assuming constant viscosity, and using the continuity equation for an incompressible fluid (eq. (2.3)), this becomes the *Navier-Stokes equation*

$$\frac{Du_i}{Dt} = -\frac{1}{\rho} \frac{\partial p}{\partial x_i} + F_i + \frac{\mu}{\rho} \frac{\partial}{\partial x_j} \left(\frac{\partial u_i}{\partial x_j} + \frac{\partial u_j}{\partial x_i} \right), \quad (2.7)$$

or written in vector notation

$$\frac{\partial \mathbf{u}}{\partial t} + (\mathbf{u} \cdot \nabla) \mathbf{u} = \mathbf{F} - \frac{1}{\rho} \nabla p + \frac{\mu}{\rho} \nabla^2 \mathbf{u}. \quad (2.8)$$

The material derivative was expanded on the left hand side of eq. (2.8) to highlight the “problem” with the Navier-Stokes equation: The advection term $(\mathbf{u} \cdot \nabla) \mathbf{u}$ is quadratic in \mathbf{u} , the equation thus a non-linear differential equation. In certain situations, when only small velocities are involved, the non-linear term can be neglected to first order of accuracy, being quadratic in small quantities. One of these cases is the development of (surface) wave theory for small-amplitude waves, which is given in the following.

Linear dispersion relation

A derivation of the velocity field and the dispersion relation of linear (small-amplitude) waves in irrotational, inviscid flow is found in most textbooks on water waves or fluid mechanics (e.g. Dean 1991, Johnson 1997, Kinsman 1965, Kundu 2008). The *linear dispersion relation* is a good approximation for the behavior of longer waves (such as swells, see sec. 2.1.6) in clean water, when almost no energy is dissipated. Only the resulting dispersion and phase velocity relations are given here, omitting the derivation.

The solution to the problem of waves in viscous fluids with a viscoelastic surface layer consisting of surface active material is discussed in the next section. The solution for inviscid flow (in the deep water limit) is then obtained in the limit $\mu \rightarrow 0$ as a special case. The required assumptions on the boundary conditions and the Navier-Stokes equation for inviscid waves are also included in the case of viscous fluids.

The dispersion relation of wave frequency ω and wavenumber k for inviscid, irrotational flow in linear, small-amplitude approximation is given by

$$\omega = \sqrt{k \left(g + \frac{\sigma k^2}{\rho} \right) \tanh kh}, \quad (2.9)$$

where h is the water depth, g the acceleration of gravity and σ the surface tension. The dispersion relation can be simplified for waves propagating in deep water to

$$\omega = \sqrt{k \left(g + \frac{\sigma k^2}{\rho} \right)}, \quad c(k) = \frac{\omega}{k} = \sqrt{\frac{g}{k} + \frac{\sigma k}{\rho}} \quad (2.10)$$

because $\tanh kh \approx 1$ for large kh (see Fig. 2.1a). The phase velocity $c(k) = \omega/k$ has a minimum at $k = 370$ rad/m, equivalent to a wavelength $\lambda = 2\pi/k = 1.7$ cm (see Fig. 2.1b). In the vicinity of this wavenumber, there are always two solutions with different wavenumbers but the same phase velocity. By nonlinear interaction, these can then exchange energy resonantly (Longuet-Higgins 1963a). In shallow water (i.e. for small kh), $\tanh kh \approx kh$, so that for gravity waves the phase velocity becomes independent of the wavenumber and only depends on water height

$$\omega = k\sqrt{gh}, \quad c = \omega/k = \sqrt{gh}. \quad (2.11)$$

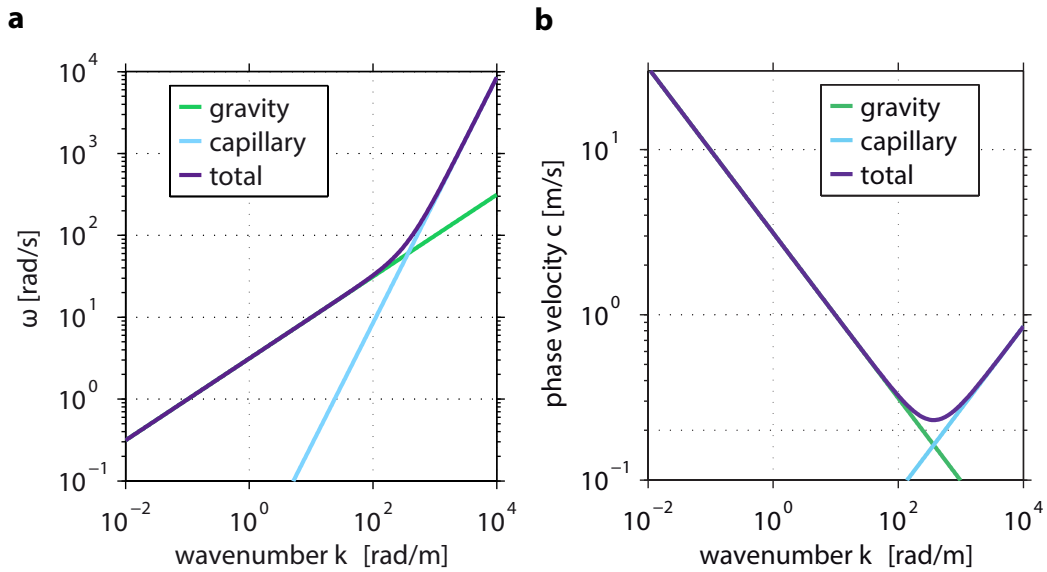


Figure 2.1: **a** Linear dispersion relation for deep water waves (purple) with the two asymptotic cases of pure gravity (green) and pure capillary (blue) waves. **b** The phase velocity $c = \omega/k$ has a minimum at $k = 370$ rad/m and then increases for both gravity towards lower wavenumbers and capillary waves towards higher wavenumbers.

2.1.2 Linear waves in viscous fluids

Linear wave theory is usually derived for inviscid flow. The results are applicable in a wide range of conditions for larger gravity waves. Whenever short waves are of interest, both non-linear and viscous effects may become relevant. While viscous damping of waves by the viscosity of water itself is usually negligible (except for very high wavenumbers, e.g. Apel 1994), viscoelastic films on top of the water surface can affect wave propagation, especially for small-scale waves, in a profound way (van den Tempel and van de Riet 1965).

Surfactants

Surface active agents (= surfactants) are substances with hydrophilic and hydrophobic parts. While they may be soluble or insoluble, their energetically preferred state is having the hydrophilic (polar) end submerged in water with the hydrophobic part sticking out of the surface. Therefore, these substances tend to form monomolecular layers on top of the water surface (Hühnerfuss 2006). These layers change the hydrodynamic boundary conditions, their dilatational elasticity and viscosity severely affect the propagation of waves. This will be outlined below. For a complete hydrodynamic derivation, the reader is referred to the cited references.

Equations of motion

The velocity field in an incompressible but viscous fluid can be described by the superposition of a gradient of a velocity potential ϕ and the rotation of a vorticity field¹ Ψ (Levich 1962):

$$\mathbf{u} = \mathbf{u}_1 + \mathbf{u}_2 = -\nabla\phi + \nabla \times \Psi. \quad (2.12)$$

For an inviscid fluid, the velocity field is irrotational and can be described as the gradient of a velocity potential alone.

The divergence of the velocity field in eq. (2.12) is given by

$$\nabla \cdot \mathbf{u} = -\nabla^2\phi + \nabla \cdot (\nabla \times \Psi) = -\Delta\phi \stackrel{!}{=} 0, \quad (2.13)$$

where the last equality is due to the continuity equation (2.3). This is the *Laplace equation* for the velocity potential.

Inserting eq. (2.12) into the linearized Navier-Stokes equation (2.8) yields

$$\frac{\partial}{\partial x} \left[-\rho \frac{\partial\phi}{\partial t} + p \right] + \frac{\partial}{\partial z} \left[-\rho \frac{\partial\psi}{\partial t} + \mu\Delta\psi \right] = 0 \quad (2.14)$$

$$\frac{\partial}{\partial z} \left[-\rho \frac{\partial\phi}{\partial t} + p + \rho gz \right] - \frac{\partial}{\partial x} \left[-\rho \frac{\partial\psi}{\partial t} + \mu\Delta\psi \right] = 0, \quad (2.15)$$

where eq. (2.13) has been used. A solution to eq. (2.14) and eq. (2.15) is given by

$$-\rho \frac{\partial\phi}{\partial t} + p + \rho gz = c_1 \rightarrow c_1 = p_0, \quad (2.16)$$

$$-\rho \frac{\partial\psi}{\partial t} + \mu\Delta\psi = c_2 \rightarrow c_2 = 0, \quad (2.17)$$

with constants c_1, c_2 , which are determined from the case of zero flow to be equal to the atmospheric pressure p_0 and 0 (Lucassen-Reynders and Lucassen 1969; from here on referred to as LRL69). Equations (2.16) and (2.17), together with eq. (2.13) are solved by damped harmonic functions of the form

$$\phi = Z_1(z)e^{i(kx-\omega t)}, \quad (2.18)$$

$$\psi = Z_2(z)e^{i(kx-\omega t)}. \quad (2.19)$$

Note that in contrast to its conventional use in the linear theory of waves for inviscid flow, here $k = \kappa + i\beta$ is a complex wavenumber to account for wave damping. The depth-dependences $Z_1(z)$ and $Z_2(z)$ are obtained by inserting eq. (2.18) and eq. (2.19) into the Laplace equation and eq. (2.17) and by solving the resulting ordinary

¹The field is a three component vector field with vanishing derivatives in the y -direction. The components of the rotation of Ψ in the x - and z -direction depend only on the y -component of ψ . In the following, ψ denotes this y -component of Ψ .

differential equations to give

$$\phi = Ae^{lz} e^{i(kx-\omega t)}, \quad (2.20)$$

$$\psi = Be^{mz} e^{i(kx-\omega t)}. \quad (2.21)$$

Some care has to be taken when defining the penetration depths l and m of the velocity potential ϕ and the stream function ψ as was pointed out by Bock and Mann (1989): For $z \rightarrow -\infty$, the velocity fields due to wave motion at the surface need to vanish. This can be guaranteed by defining

$$l := \sqrt[+]{k^2}, \quad (2.22)$$

$$m := \sqrt[+]{k^2 - i\omega\rho/\mu}, \quad (2.23)$$

where the $\sqrt[+]{}$ denotes the root with positive real part.

If the fluid above the interface (air, for surface waves) also has a non-neglectable viscosity, equivalent equations are required for the upper fluid and a no-slip boundary condition at the interface connects the two fluids. In the following, the viscosity of air is neglected. To derive the dispersion relation of ω and k , the constants A and B need to be determined by applying the boundary condition at the surface.

Boundary conditions

The kinematic boundary condition at the free surface states that the fluid particles move with the velocity of the flow. The condition for the change in vertical surface displacement η is identical with the case of inviscid irrotational waves:

$$w|_{z=\eta} = \frac{D\eta}{Dt} \Big|_{z=\eta} \approx \frac{\partial\eta}{\partial t} \Big|_{z=0} \quad (2.24)$$

The last equality is an approximation which is only valid for small-amplitude waves, where the maximum surface displacement is much smaller than the wavelength $a \ll \lambda$. Since then also the associated velocities are small, the advection component of the material derivative is a term of second-order in small quantities and can be neglected. Furthermore, the derivative can be evaluated at $z = 0$ instead of $z = \eta$ (Kundu 2008).

A second boundary condition exists if the surface is covered with a surface film. Then, horizontal displacement ξ is possible (with the film's elasticity as a restoring force):

$$u|_{x=\xi} = \frac{D\xi}{Dt} \Big|_{x=\xi} \approx \frac{\partial\xi}{\partial t} \Big|_{x=0} \quad (2.25)$$

Again, small-amplitude approximation simplifies the boundary condition. A bottom boundary condition was already implicitly used above. It was required that the

velocity fields decay to zero for $z \rightarrow -\infty$. Therefore, the properties of deep water waves are derived.

The dynamic boundary conditions for a viscoelastic fluid are

$$\frac{\partial \sigma}{\partial x} + (\tau'_{zx} - \tau_{zx}) = 0 \quad (2.26)$$

for the x-direction, tangential to the undisturbed water surface, and

$$\sigma \frac{\partial^2 \eta}{\partial x^2} + (\tau'_{zz} - \tau_{zz}) = 0 \quad (2.27)$$

for the z-direction, normal to the undisturbed interface. Here primed quantities are on the air side of the interface, unprimed quantities on the water side. The approximation of small wave amplitude was implicitly made here, as in the Young-Laplace equation, relating pressure and surface tension, the inverse radius $1/r$ was replaced by the curvature $\partial^2 \eta / \partial z^2$. This requires the wave slope $\partial \eta / \partial x \sim a / \lambda$ to be a small quantity (Kundu 2008). A detailed derivation of these boundary conditions is given by LRL69.

The gradient of surface tension in the tangential boundary condition eq. (2.26) is converted with the definition of the (possibly complex) *surface dilatational elasticity*²

$$\epsilon = \frac{d\sigma}{d \ln A}. \quad (2.28)$$

This elasticity describes the change in surface tension due to a change in area A of a surface element (Lucassen 1982). With this, the gradient of surface tension in the x-direction becomes

$$\frac{\partial \sigma}{\partial x} = \epsilon \frac{\partial \ln A}{\partial x} = \epsilon \frac{\partial^2 \xi}{\partial x^2}, \quad (2.29)$$

where ξ denotes *horizontal* displacement. In the last equality it was used that the relative change in area $\Delta A / A$ is equal to the gradient in horizontal displacement $\partial \xi / \partial x$ (LRL69).

Combining the kinematic boundary conditions eq. (2.24) and eq. (2.25) and the dynamic boundary conditions eq. (2.27) and eq. (2.26) with the solutions obtained for the velocity potential eq. (2.20) and the stream function eq. (2.21), the following set of equations is obtained (e.g. Bock and Mann 1989):

$$[\rho \omega^2 - \rho g l + 2i\omega \mu l^2 - \sigma k^2 l] A + [-i\rho g k - 2\omega \mu m k - \sigma i k^3] B = 0, \quad (2.30)$$

for the normal boundary condition, and

$$[2\omega \mu k l + i\epsilon k^3] A + [i\omega \mu (k^2 + m^2) - \epsilon k^2 m] B = 0, \quad (2.31)$$

²Davies and Rideal (1963; p. 265) use an alternative description, defining a compressibility of the surface film, $C_S = \epsilon^{-1}$.

for the tangential condition. The two equations form a homogeneous linear system of equations in terms of A and B; for a nontrivial solution, its determinant

$$\begin{vmatrix} (\rho\omega^2 - \rho gl + 2i\omega\mu l^2 - \sigma k^2 l) & (-i\rho gk - 2\omega\mu mk - \sigma ik^3) \\ (2\omega\mu kl + i\epsilon k^3) & (i\omega\mu(k^2 + m^2) - \epsilon k^2 m) \end{vmatrix} \stackrel{!}{=} 0 \quad (2.32)$$

must vanish. For $\mu = 0$ and $\epsilon = 0$, the well-known dispersion relation for inviscid flow (in the deep water limit) is obtained (see eq. (2.10)):

$$\omega^2 = gk + \frac{\sigma k^3}{\rho}. \quad (2.33)$$

The major difference between the solution for flow without an elastic surface layer and the solution presented here is the additional term in the dynamic boundary condition. In the case of a clean water surface, the viscous tangential stress vanishes for free waves. For coverage with a mono-molecular slick, it is balanced by the tangential stress exerted on the water due to surface tension gradients.

2.1.3 The Marangoni effect

Marangoni waves

Figure 2.2a shows the determinant in eq. (2.32) for a fixed frequency of $\omega = 157.1$ rad/s (= 25 Hz) and an elasticity $\epsilon = 20$ mN/m. Plotted are the real and imaginary part of the complex wavenumber $k = \kappa + i\beta$. The imaginary part β determines the damping rate of the waves.

The determinant has four solutions: two correspond to transversal gravity-capillary waves, propagating in the positive and negative x-direction ($\kappa = \pm 640$ rad/m). They are almost undamped, $\beta = \pm 12$ rad/m $\ll \kappa$. Two additional solutions exist that only appear for non-zero elastic modulus ϵ : These are the *Marangoni waves*. Since they are predominantly associated with horizontal motion, they are also called “longitudinal waves”. Their damping coefficients are of the same order as the real part of the wave number ($k = (294 + 117i)$ rad/m), so that their amplitude decreases to less than 10 % over only one wavelength Alpers (1989). Because of their longitudinal motion, Marangoni waves create strong velocity gradients in the boundary layer. This is probably the reason for the enhanced viscous energy dissipation.

Marangoni wave were first detected experimentally by Lucassen (1968a;b). He found waves with a dispersion relation consistent with that predicted by Marangoni theory. More important than the characteristics of the Marangoni waves themselves are their interactions with the transversal gravity-capillary waves.

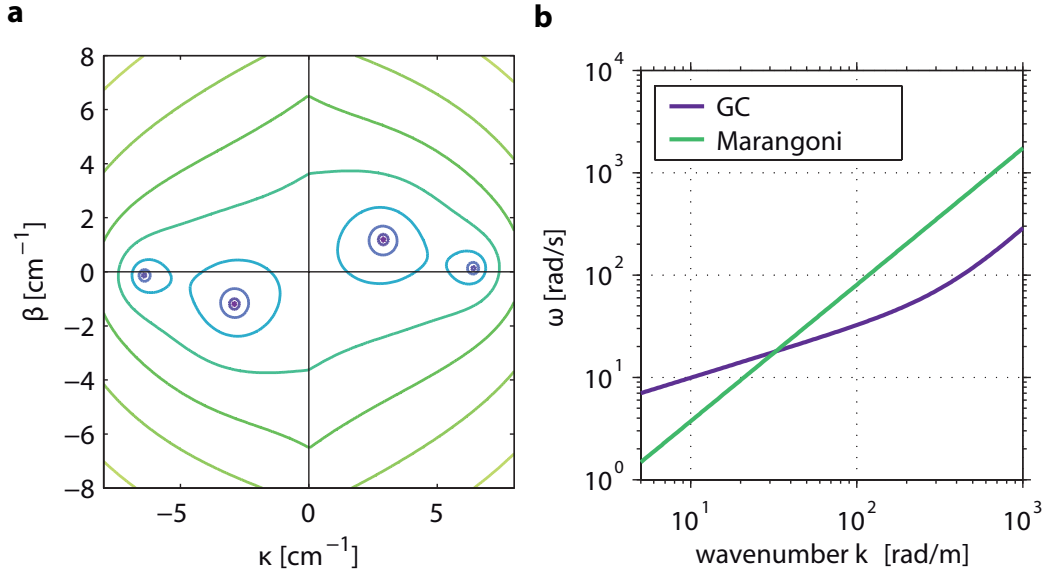


Figure 2.2.: **a** The determinant in eq. (2.32) for $\omega = 157.1$ rad/s, $\rho = 1000$ kg/m³, $\sigma = 72.6$ mN/m, $\mu = 1$ mPa s. There are four poles, two corresponding to gravity-capillary waves (close to the $\beta = 0$ line), two corresponding to Marangoni waves. **b** Dispersion relation of gravity-capillary and Marangoni waves for a monomolecular film of CEM3AB ($\epsilon = 25.5$ mN/m). The curves intersect at approx. $k = 32$ rad/m.

Marangoni wave damping

Marangoni waves themselves are damped rapidly. The energy they dissipate must come from the transversal gravity-capillary waves. Thus, these waves also lose energy, an effect that is referred to as *Marangoni wave damping* or simply the *Marangoni effect*. The transfer of energy from transversal to Marangoni waves is not unlike a forced damped harmonic oscillator: Transversal wave propagation dilates and compresses the slick on the surface. If the frequency of the wave at a certain wave number is near the frequency of the Marangoni wave at this wave number, the energy transfer is greatly enhanced.

An approximate dispersion relation for Marangoni waves is given by Alpers (1989); a similar relation was already derived by Lucassen (1968a):

$$\omega_M^3 = [(-i)\epsilon^2/(\rho\mu)] k_M^4 \quad (2.34)$$

From the exact hydrodynamic equations, this relation is obtained when both the gravity and surface tension terms are eliminated and only the terms with *gradients* in surface tension are kept.

Figure 2.2b shows the intersection of the dispersion relations of Marangoni and gravity-capillary modes on a slick covered water surface. The intersection point is dependent on the type of surfactant used, here the value for the dilatational elasticity ϵ is that of CEM3AB (Alpers 1989). The existence of a frequency, at which maximum

damping of the waves occurs, was verified in numerous experimental studies (e.g. Cini and Lombardini 1981, Hühnerfuss et al. 1987). On the other hand, slicks are known to affect the wave field over a wide range of wavenumbers and frequencies, as will also be demonstrated in sec. 7.3. To understand the underlying mechanisms of this broadband wave dampening, the total energy balance of waves needs to be considered. This will be discussed in the following section.

Slicks and spills

The derivation given above is valid for mono-molecular layers of surfactants only. These are substances which have both hydrophobic and hydrophilic parts, so they preferably accumulate on the surface with the hydrophobic part sticking out of the water.

A different situation arises in oil *spills*: Crude oil is not surface active, it does not have a hydrophilic part. Its components are long paraffin chains or benzene-type structures; they are fully unpolar and hydrophobic. Therefore, crude oil does not create mono-molecular surface films, but rather thick layers on top of the water Hühnerfuss (2006). Because of its high viscosity, it can also efficiently dampen the waves, but Marangoni waves can only be excited in slicks. A dispersion relation for the case of a layer with a viscous fluid on top of another fluid is given by Jenkins and Jacobs (1997).

2.1.4 The wave action balance

For waves which interact with currents or propagate in a basin with varying depth, and in the absence of forcing, *wave energy* E is not conserved, but *wave action* $\mathcal{N} = E/\omega$ is (Janssen 2004). The wave action balance in the presence of forcing then takes the form

$$\frac{\partial}{\partial t} \mathcal{N} + \nabla \cdot (\mathbf{c}_g \mathcal{N}) = S = S_{\text{in}} + S_{\text{nl}} + S_{\text{ds}}. \quad (2.35)$$

The wave action is balanced by three source terms for atmospheric input S_{in} , non-linear wave-wave interactions S_{nl} and dissipation (mostly by wave breaking) S_{ds} . Note that in contrast to the material derivative (see eq. (2.2)), wave action is not advected with the current velocity, but with the group velocity of the wave group, $c_g = \partial\omega/\partial k = c_{\text{ph}}/2$, which is half the phase velocity in the absence of currents.

The source terms, especially for wind input and dissipation, are subject to ongoing research (Holthuijsen 2007) and a comprehensive discussion cannot be given here. In the context of wave damping by surfactants, it is the term for non-linear interactions which plays a prominent role.

Non-linear wave-wave interactions

The non-linear interactions between wave quadruplets were first described by Hasselmann (1962; 1963). From perturbation theory for weakly non-linear waves, he found that sets of four waves could exchange energy when the conditions

$$\mathbf{k}_1 + \mathbf{k}_2 = \mathbf{k}_3 + \mathbf{k}_4, \quad (2.36)$$

$$\omega_1 + \omega_2 = \omega_3 + \omega_4 \quad (2.37)$$

are fulfilled. The spectral energy transfer can then be described in terms of the action density $n(\mathbf{k}) = \Psi(\mathbf{k})/\omega$, where $\Psi(\mathbf{k})$ is the wavenumber power spectrum, which will be defined in eq. (2.49). The rate of change of the action density by non-linear interactions is given by (see Young 1999; sec. 4.4)

$$\frac{\partial n(\mathbf{k})}{\partial t} = \iiint G(\mathbf{k}_1, \mathbf{k}_2, \mathbf{k}_3, \mathbf{k}_4) \times \delta(\mathbf{k}_1 + \mathbf{k}_2 - \mathbf{k}_3 - \mathbf{k}_4) \times \delta(\omega_1 + \omega_2 - \omega_3 - \omega_4) \\ [n_1 n_3 (n_4 - n_2) + n_2 n_4 (n_3 - n_1)] d\mathbf{k}_1 d\mathbf{k}_2 d\mathbf{k}_3, \quad (2.38)$$

where δ is the Kronecker delta and G is a coupling constant. Both energy and momentum of the wave field are conserved by eq. (2.38), the energy is merely redistributed within the wave power spectrum (Young 1999).

Shape stabilization

Non-linear interactions play an important role in determining the shape of the spectrum. Wind-wave spectra typically have a characteristic shape with a single peak and a decay of spectral density towards higher frequencies (or wavenumbers). Young and Vledder (1993) could show that this universal shape is largely due to the S_{nl} term in the wave action balance. They used numerical models to show that a perturbation in the form of a reduction of spectral energy at a given frequency was responded with increased non-linear transfer of energy to this frequency, until the original shape of the spectrum was restored. They named this effect *shape stabilization*.

Shape stabilization is also a main reason for the overall damping effect of surfactants on wave spectral energy. Experimentally it is found that energy is reduced not only in those frequency regions where resonant transfer to Marangoni modes is possible. This was explained by Alpers (1989), who noted that the non-linear transfer of energy *away* from a certain frequency depends on the spectral energy at this frequency, while the transfer of energy *to* this frequency does not. A dip in the wind-wave spectrum, as observed under the influence of surface films, will thus be balanced by non-linear transfer from other frequencies. Therefore, spectral energy will be reduced even far from the resonance region.

In the first studies on the Marangoni effect, monochromatic, mechanically generated waves were used. Obviously, the four-wave resonance conditions eq. (2.36) were

not fulfilled in that case. This has to be accounted for when comparing damping factors for wind-generated wave fields with those from monochromatic measurements.

2.1.5 Non-linear waves

The dispersive nature of linear deep water waves usually limits non-linear interactions. Two waves with different wavenumbers propagate at different phase velocities which limits the time they can interact to exchange energy (or wave action). However, linear theory assumes infinitesimal amplitude of waves and reality is more complex, especially in the short wave range.

Stokes waves

Stokes (1849) found an approximate solution for the surface displacement of pure gravity waves. He showed that the solution to the Laplace equation for the velocity potential for inviscid and irrotational flow with the appropriate boundary conditions at the surface and bottom could be expanded into a series of terms of increasing order. By truncating the series after the third order, the (instantaneous) wave profile is given as

$$\eta = -a \cos kx + \frac{1}{2}ka^2 \cos 2kx - \frac{3}{8}k^2a^2 \cos 3kx, \quad (2.39)$$

which results in waves that have a sharper crest and a flat trough (Kinsman 1965). The phase speed of Stokes waves is slightly higher than that of linear waves and increases with amplitude a :

$$c = \sqrt{\frac{g}{k}(1 + a^2k^2)} \quad (2.40)$$

The factor a^2k^2 describes the steepness of the wave, since $ak = \pi H/\lambda$, where H is the wave height and λ the wavelength. Steeper waves propagate faster than smoother waves, a fact well-known to surfers: When a new swell from a distant storm comes to shore, the steepest waves will arrive first (Butt and Russell 2004).

From Stokes' solution, in the limit of infinitesimal amplitudes, the linear profile and phase velocity are obtained. An interesting consequence of this solution is that the orbitals of individual fluid particles are not circular anymore. The propagation of Stokes waves thus induces a current at the surface, the *Stokes drift*.

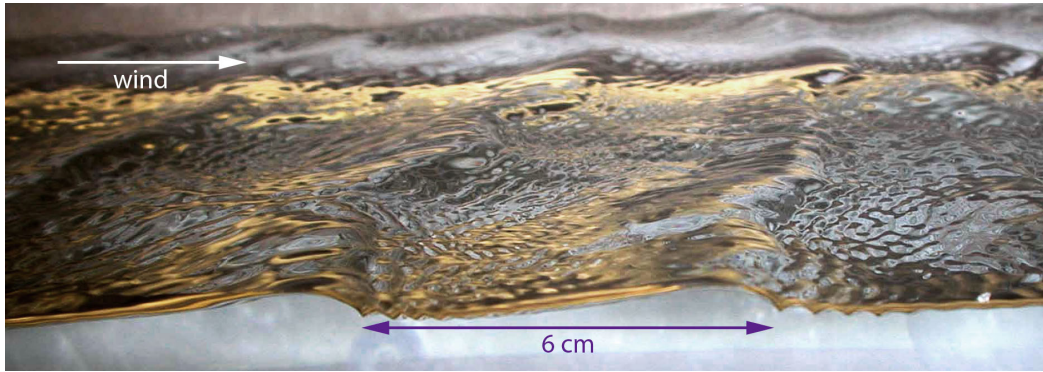


Figure 2.3.: Parasitic capillary waves riding in front of short gravity waves with $\lambda = 6$ cm wavelength. The capillaries have a shape very close to that described by Crapper (1957). Wave development is limited by the interaction length of wind and waves, the *fetch*, of only 2.4 m. Wind speed is 6 m/s. Modified after Huhn (2008).

Crapper waves

For pure capillary waves, whose restoring force is surface tension alone, an exact solution was found by Crapper (1957). The profile of these waves is similar to an inverted Stokes wave, they have round crests and narrower troughs. They also have an opposite behaviour in phase velocity. The effect of increased amplitude (or *steepness* ak) is to slow them down:

$$c = \sqrt{\frac{k\sigma}{\rho} \left(1 + \frac{a^2 k^2}{16}\right)^{-1/4}}, \quad (2.41)$$

where the first factor $k\sigma/\rho$ with fluid density ρ and surface tension σ is the result for the phase velocity of capillary waves for infinitesimal amplitudes. Crapper waves are omnipresent as *parasitic capillaries* (see Fig. 2.3), which propagate on the leeward side of short gravity waves and are fed energy from the instability of their carrier wave.

2.1.6 Wave nomenclature

In wave literature (and this work), a number of terms describing waves are commonly used. Here, a short definition of some commonly used expressions is attempted.

Swell describes very long waves, with wavelengths on the order of multiple hundreds of meters. These waves are not generated by or in equilibrium with local wind, but come from distant storms. If their origin is sufficiently far away, due to interference of waves with slightly different wavenumbers (or steepness), they usually arrive in groups (Kinsman 1965).

Wind-sea is the term used to generally describe the waves that were created locally

by the wind. They need not be in equilibrium (i.e. *fully developed*). Unless the local wind has storm force, dominant wavelengths are typically on the order of meters to tens of meters. The spectrum and the angular spreading of locally generated waves is usually broader than that of swells.

Gravity waves are surface displacements which are restored by gravity. This implies that their wavelengths are sufficiently larger than that of the phase velocity minimum at 1.7 cm. In deep water, longer waves have larger phase velocities. Because the term gravity wave applies to waves with wavelengths of centimeters to hundreds of meters, additional specifications are often given, e.g. short gravity waves. However, there is no clear definition of when a wave is short, it is depending on the context. Short usually means shorter than the wavelength of the *dominant wave*, the wavenumber of the peak in the power spectrum. This, of course, is depending on wind speed.

Capillary waves are those waves, whose restoring force is surface tension, not gravity. Thus, they are limited to very short wavelengths, corresponding to very high curvature (low curvature radius). Waves in the transition region between gravity and capillary waves around the minimum in phase velocity at $\lambda = 1.7$ cm are also named *gravity-capillary waves*. Pure capillaries have shorter wavelengths and have higher phase velocities at shorter wavelengths.

2.2 Description of wave fields

At any given time and place, the ocean surface wave field is a superposition of many waves with different wavenumbers. A full description of the temporal evolution of the two-dimensional surface elevation on a large area on scales of millimeters to kilometers would create massive amounts of data. Apart from the fact that no measurement technique exists to capture such a data set, the useful information contained in it is limited. In the study of many physical interactions phase-resolved measurements are not required (Janssen 2004). Therefore, a spectral description of the wave field is generally preferred.

An alternative way of describing certain average properties of the wave field is using various statistical measures, e.g. variances and higher order moments of the probability distribution functions of wave height and slope. In the description of processes that depend on the wave field, e.g. air-sea gas exchange (sec. 2.3), the challenge then is to identify the statistical parameters which characterize the dependency without loss of information.

Table 2.2.: Symbols used in sec. 2.2 and sec. 2.3.

Symbol	Description	Unit
$\mathbf{x} = (x, y)$	horizontal two-dimensional position vector	m
$\mathbf{k} = (k_x, k_y)$	wavenumber vector (2D)	rad/m
t	time	s
ω	angular frequency	rad/s
$\eta(\mathbf{x}, t)$	water surface elevation	m
$\hat{\eta}(\mathbf{k}, \omega)$	Fourier complex amplitude function for η	$\text{m}^3 \text{s}$
$\mathbf{s}(\mathbf{x}, t)$	two component slope vector $(s_x, s_y) = \nabla \eta$	-
$\hat{\mathbf{s}}(\mathbf{k}, \omega)$	Fourier complex amplitude function for \mathbf{s}	-
$R(\mathbf{r}, \tau)$	auto-correlation of $\eta(\mathbf{x}, t)$	m^2
$X(\mathbf{k}, \omega)$	(height/displacement) power density spectrum	$\text{m}^4 \text{s}$
$\Psi(\mathbf{k})$	wavenumber power density spectrum	m^4
$\Phi(\omega)$	frequency power density spectrum	$\text{m}^2 \text{s}$
$S(\mathbf{k}, \omega)$	slope power density spectrum	$\text{m}^2 \text{s}$
$B(\mathbf{k})$	saturation (curvature) spectrum	-
u_*	(water-side) friction velocity $u_* = \sqrt{\tau/\rho}$	m/s
H_s	significant wave height, $H_s = 4\sigma_\eta$	m
j_c	concentration flux	$\text{mol}/(\text{s m}^2)$
D	(molecular) diffusivity	m^2/s
$K(z)$	turbulent diffusivity	m^2/s
c	concentration	mol/m^3
Sc	Schmidt number $Sc = \nu/D$	-
n	Schmidt number exponent	-
k	transfer velocity	m/s
σ_s^2	mean square slope (mss)	-
\mathcal{F}	Fourier transform	-

2.2.1 Spectral description of the wave field

The statistical and spectral description used in this thesis mostly follows the ideas and concepts given by Phillips (1977) and Longuet-Higgins (1957).

Power density spectrum

The surface displacement $\eta(\mathbf{x}, t)$ is defined as the displacement from the mean water level, so that $\bar{\eta} = 0$. Then, the *power density spectrum* $X(\mathbf{k}, \omega)$ of the waves is defined as the Fourier transform of the autocorrelation of $\eta(\mathbf{x}, t)$:

$$X(\mathbf{k}, \omega) := \mathcal{F}[R(\mathbf{r}, \tau)] = \iiint R(\mathbf{r}, \tau) e^{-i(\mathbf{k}\mathbf{r} - \omega\tau)} \mathbf{d}\mathbf{r} \mathbf{d}\tau, \quad (2.42)$$

with the autocorrelation function itself being

$$R(\mathbf{r}, \tau) = \lim_{T, X, Y \rightarrow \infty} \frac{1}{TXY} \int_{0,0,0}^{T,X,Y} \eta^*(\mathbf{x}, t) \eta(\mathbf{x} + \mathbf{r}, t + \tau) d\mathbf{x} dt. \quad (2.43)$$

The autocorrelation is here taken to be independent of position \mathbf{x} and time t . The formal requirement for this is that the surface displacement η is a wide-sense stationary process (Oppenheim and Schaffer 2010). This is fulfilled if a mean and a covariance exists. The mathematical treatment of wave spectra requires some care, because the surface displacement η does not generally need to be square integrable (which is a prerequisite for its Fourier transform to exist). However, since physical wave fields in finite oceans will be studied here, it is safe to assume that the total energy of the wave field is finite and the spectra are band-limited. Because all records of surface displacement are also finite and have limited resolution, the discrete Fourier transform (DFT) of the data always exists. For more general cases, wave spectra can be defined in terms of Fourier-Stieltjes integrals (e.g. Phillips 1977) or using generalized formulations of the Fourier transform (e.g. Kinsman 1965).

If the Fourier transform of the squared surface displacement $\eta(\mathbf{x}, t)$ exists, the displacement power density spectrum can be directly expressed through the Fourier components of η , because the autocorrelation is³

$$R(\mathbf{r}, \tau) = \iiint d\mathbf{x} dt \eta^*(\mathbf{x}, t) \eta(\mathbf{x} + \mathbf{r}, t + \tau) \quad (2.44)$$

$$= \frac{1}{(2\pi)^6} \iiint d\mathbf{x} dt d\mathbf{k} d\omega d\mathbf{k}' d\omega' \hat{\eta}^*(\mathbf{k}, \omega) \hat{\eta}(\mathbf{k}', \omega') e^{-i(\mathbf{k}\cdot\mathbf{x}-\omega t)} e^{i(\mathbf{k}'(\mathbf{x}+\mathbf{r})-\omega'(t+\tau))} \quad (2.45)$$

$$= \frac{1}{(2\pi)^3} \iiint d\mathbf{k} d\omega d\mathbf{k}' d\omega' \hat{\eta}^*(\mathbf{k}, \omega) \hat{\eta}(\mathbf{k}', \omega') e^{i(\mathbf{k}'\mathbf{r}-\omega'\tau)} \frac{1}{(2\pi)^3} \iiint d\mathbf{x} dt e^{-i((\mathbf{k}-\mathbf{k}')\cdot\mathbf{x}-(\omega-\omega')t)} \quad (2.46)$$

$$= \frac{1}{(2\pi)^3} \iiint d\mathbf{k} d\omega |\eta(\mathbf{k}, \omega)|^2 e^{i(\mathbf{k}'\mathbf{r}-\omega'\tau)} \quad (2.47)$$

$$= \mathcal{F}^{-1} [|\eta(\mathbf{k}, \omega)|^2]. \quad (2.48)$$

In eq. (2.46), the Fourier transform of the Dirac delta distribution was used, the last integral was replaced by $\delta(\mathbf{k} - \mathbf{k}', \omega - \omega')$. Thus, the power density spectrum, being $X(\mathbf{k}, \omega) = \mathcal{F}[R(\mathbf{r}, \tau)]$ is given by the squared magnitude of the Fourier components of surface displacement $|\eta(\mathbf{k}, \omega)|^2$.

Reduced spectra are obtained by integration of the power density spectrum, yield-

³For the sake of legibility, the maximum number of integrals is limited to 3 and the normalization factors from eq. (2.43) are suppressed.

ing the *wavenumber (power density) spectrum*

$$\Psi(\mathbf{k}) = \int_{-\infty}^{\infty} X(\mathbf{k}, \omega) d\omega, \quad (2.49)$$

and the *frequency (power density) spectrum*

$$\Phi(\omega) = \iint_{-\infty}^{\infty} X(\mathbf{k}, \omega) d\mathbf{k}. \quad (2.50)$$

Slope spectra

For small-scale (short wavelength) waves, it is easier to measure surface slope $\mathbf{s}(\mathbf{x}, t) = \nabla\eta(\mathbf{x}, t)$ instead of displacement. With the Fourier representation of displacement

$$\eta(\mathbf{x}, t) = \frac{1}{(2\pi)^3} \iiint_{-\infty}^{\infty} \hat{\eta}(\mathbf{k}, \omega) e^{-i(\mathbf{kx}-\omega t)} d\mathbf{k} d\omega, \quad (2.51)$$

the derivative can be computed in Fourier space so that the slope component in the x-direction

$$s_x(\mathbf{x}, t) = \frac{\partial\eta(\mathbf{x}, t)}{\partial x} = \frac{1}{(2\pi)^3} \iiint_{-\infty}^{\infty} (-ik_x) \hat{\eta}(\mathbf{k}, \omega) e^{-i(\mathbf{kx}-\omega t)} d\mathbf{k} d\omega. \quad (2.52)$$

Fourier transform of the left hand side and comparison of the coefficients shows that

$$\hat{s}_x(\mathbf{k}, \omega) = -ik_x \hat{\eta}(\mathbf{k}, \omega), \quad (2.53)$$

so that the derivative of the displacement reduces to a multiplication in Fourier space. With the equivalent expression for the second slope component, the sum of the squared magnitude of the Fourier coefficients of slope is

$$|\hat{\mathbf{s}}(\mathbf{k}, \omega)|^2 = |\hat{s}_x(\mathbf{k}, \omega)|^2 + |\hat{s}_y(\mathbf{k}, \omega)|^2 = (k_x^2 + k_y^2) |\hat{\eta}(\mathbf{k}, \omega)|^2 = k^2 |\hat{\eta}(\mathbf{k}, \omega)|^2, \quad (2.54)$$

where $k^2 = k_x^2 + k_y^2$. Comparison with eq. (2.48) shows that the *slope power density spectrum* is related to the power density spectrum of displacement by

$$S(\mathbf{k}, \omega) = |\hat{\mathbf{s}}(\mathbf{k}, \omega)|^2 = k^2 |\hat{\eta}(\mathbf{k}, \omega)|^2 = k^2 X(\mathbf{k}, \omega). \quad (2.55)$$

And completely analogous to the definitions in eq. (2.49) and eq. (2.50), upon integration the *slope wavenumber (power density) spectrum* $S_k(\mathbf{k})$ and the *slope frequency (power density) spectrum* $S_\omega(\omega)$ are obtained.

Saturation spectrum

For historical reasons, the wavenumber spectrum of curvature

$$B(\mathbf{k}) = k^4 \Psi(\mathbf{k}) = k^2 S_k(\mathbf{k}) \quad (2.56)$$

is usually named *saturation spectrum* (or *degree of saturation*). This goes back to the pioneering work of Phillips (1958), who argued that there must be an *equilibrium range* in the displacement wavenumber spectrum $\Psi(\mathbf{k}, \omega)$. In this range, waves are fully developed and the energy input from the wind is in equilibrium with wave breaking. Then, from dimensional analysis he concluded that the spectrum in this region (at wavenumbers much larger than the spectral peak, but well below the gravity-capillary range) is proportional to k^{-4} . In the limiting case of a fully developed wave spectrum, the saturation spectrum B is not depending on k anymore. Although his assumptions on wave breaking turned out to be incorrect (Phillips 1985) and the saturation spectrum generally does depend on k , the dependence is much weaker than that of $\Psi(\mathbf{k})$ or $S_k(\mathbf{k})$, so that a representation of wave spectra in terms of the saturation spectrum has lower dynamical range. For the saturation range, Phillips (1985) gives

$$B(\mathbf{k}) = \frac{\beta}{\sqrt{g}} f(\theta) u_* k^{1/2}, \quad (2.57)$$

with an empirical scaling factor β . The friction velocity $u_* = \sqrt{\tau/\rho}$ is a measure for the shear stress τ at the water surface. The angular spreading of the wave propagation with respect to the wind is described by $f(\theta)$. For even higher wavenumbers, Jähne and Riemer (1990) proposed a spectral cutoff, from which the spectral energy in the saturation spectrum decreases with k^{-2} . Rocholz (2008) did not observe such a cutoff in his data, after he had corrected his optical system for the reduction of contrast at high spatial frequencies by measuring and correcting the modulation transfer function.

2.2.2 Probability distributions

Random amplitude/phase model

Instead of using a spectral description, it is also possible to describe the water surface in terms of probability distributions. In linear theory, the sea surface elevation is

described as a superposition of harmonic waves

$$\eta(\mathbf{x}, t) = \sum_{n=1}^N a_n \cos(\mathbf{k}_n \cdot \mathbf{x} - \omega_n t) + b_n \sin(\mathbf{k}_n \cdot \mathbf{x} - \omega_n t) \quad (2.58)$$

$$= \sum_{n=1}^N A_n \cos(\mathbf{k}_n \cdot \mathbf{x} - \omega_n t - \phi_n). \quad (2.59)$$

Here, amplitudes a_n and b_n are random amplitudes which, by the law of large numbers, are Gaussian distributed for large N (with the same mean and standard distribution). The surface elevation $\eta(\mathbf{x}, t)$ is then also described by a Gaussian distribution. The amplitude $A_n = \sqrt{a_n^2 + b_n^2}$ is Rayleigh distributed, the phases ϕ_n follow a uniform distribution (see Holthuijsen 2007).

Slope probability distribution

Because of non-linearities, the distribution of $\eta(\mathbf{x}, t)$ has higher order moments that distort the Gaussian distribution. For weakly non-linear waves, these can be obtained from perturbation analysis. The probability density function (pdf) of surface elevation can then be expressed in terms of the normalized elevation $f = (\eta - \bar{\eta})/\sigma_\eta$, with the mean value $\bar{\eta}$ and its root-mean square (rms) value σ_η . The pdf is then given by

$$p(\eta) = \frac{1}{\sqrt{2\pi}\sigma_\eta} \exp(-f^2/2) \left[1 + \frac{1}{6}\lambda_3 H_3 + \frac{1}{24}\lambda_4 H_4 + \frac{1}{72}\lambda_3^2 H_6 + \dots \right], \quad (2.60)$$

where λ_3 and λ_4 are coefficients of skewness and kurtosis and can be defined in terms of the cumulants of the distribution $p(\eta)$ (Longuet-Higgins 1963b). The H_n are Hermite polynomials of degree n . A similar expression was used by Cox and Munk (1954a) who found that their measured distributions of surface *slope* were approximately Gaussian but contained higher order terms. They proposed a truncated Gram-Charlier series of the form

$$p(s_x, s_y) = \frac{1}{2\pi\sigma_c\sigma_a} e^{-\frac{1}{2}(\xi^2 + \zeta^2)} \left[1 - \frac{1}{2}c_{21}(\xi^2 - 1) - \frac{1}{6}c_{03}(\zeta^3 - 3\zeta) + \frac{1}{24}c_{40}(\xi^4 - 6\xi^2 + 3) + \frac{1}{4}c_{22}(\xi^2 - 1)(\zeta^2 - 1) + \frac{1}{24}c_{04}(\eta^4 - 6\eta^2 + 3) \right], \quad (2.61)$$

where normalized slope components $\xi = s_x/\sigma_c$ and $\zeta = s_y/\sigma_a$ have been used. The cross-wind and along-wind rms slopes are denoted by σ_c and σ_a . The two correction terms on the first line, with coefficients c_{21} and c_{03} lead to a skewness of the distribution in the along-wind direction. In the cross-wind direction, a symmetrical distribution is expected, skewness terms disappear. The second line contains three peakedness terms. The resulting ‘‘peaked’’ pdf has higher probabilities for small and large slopes.

The use of a truncated Gram-Charlier series has been criticized (Tatarskii 2003, Wentz 1976) because it is not positive for all slopes and thus cannot represent a true pdf. A physical justification for the use of a truncated Gram-Charlier series was not given by Cox and Munk. Longuet-Higgins (1963b; 1982) demonstrates how the skewness and higher order terms are consequences of the non-linearity of waves and notes that the skewness should be correlated with wind stress τ at the surface. Liu et al. (1997) found that peakedness of the distribution is due to non-linear interaction of gravity waves and that the skewness is associated with the modulation of short waves by longer gravity waves. A similar result was also presented by Longuet-Higgins (1982), who finds that the modulation of ripples that are riding on longer waves and thus propagate on a tilted, slowly changing water surface, can lead to the right magnitude of distribution skewness.

A number of alternate descriptions of the slope pdf using either multiple Gaussians (e.g. Plant 2003, Tatarskii 2003) or non-Gaussian descriptions (Chapron et al. 2000, Joelson and Néel 2008, Liu et al. 1997) have been published. In the absence of a high resolution data set that also incorporates large slopes, it is nearly impossible to quantitatively determine the best description of the surface slope distribution.

2.2.3 Statistical parameters

Several statistical parameters are typically used to characterize wave fields of long gravity waves. These parameters are also given by the operational wave models, which predict the sea state for shipping and coastal protection.

Significant wave height

Significant wave height is defined as four times the root-mean-square wave height $H_s = 4\sigma_\eta$. Historically, it was defined as the average height of the highest third of all waves ($H_{1/3}$). Since obviously this definition depends on the used measurement resolution and/or frequency cutoff used to eliminate small-scale waves from the dataset, the more formal definition with the surface displacement has become the accepted way to compute this quantity (Holthuijsen 2007). It is equivalent to the old definition if the statistical distribution of wave height is a Rayleigh distribution (corresponding to a Gaussian distribution of surface displacement η), if the wave spectrum is narrow. Longuet-Higgins (1980) discusses the consequences of a broad spectrum with non-linearities and concludes that H_s overestimates $H_{1/3}$ by 7.5%.

Wave period / peak frequency

It is not trivial to define a mean wave period for a general wave field, which may have a very broad spectrum and consists of locally generated wind waves and swell. A “wave” can then be defined as the profile of the surface elevation between two successive downward zero-crossings (Holthuijsen 2007). For a broad wave spectrum and especially in the presence of small ripples, this definition may lead to problems with high resolution measurements.

The mean frequency between two zero crossings of surface displacement η is given by

$$\bar{f} = \sqrt{\frac{m_2}{m_0}}, \quad (2.62)$$

where m_0 and m_2 are the zeroth- and second-order moment of the frequency power spectrum $\Phi(\omega)$ (Holthuijsen 2007). This relation was derived for a surface with a Gaussian probability distribution for the elevation. Furthermore, the precise measurement of the second-order moment is not trivial. Noise in high frequencies is amplified, which requires the use of an upper cut-off frequency. Holthuijsen (2007) gives alternate definitions of mean period or height which have been defined to avoid the measurement of the second-order moment.

In many cases it is sufficient to characterize the peak frequency of the spectrum. If the spectrum consists of significant contributions of swell and wind-sea, separate peak frequencies are given.

Wave age

Wave age is used to differentiate “young” seas which have been generated by local wind and may not be in equilibrium and “mature” seas, which may be dominated by swell or in equilibrium with local wind. Wave age is commonly defined as c_{peak}/u_* , the ratio between the phase velocity of waves c_{peak} at the spectral peak and the friction velocity $u_* = \sqrt{\tau/\rho}$. Since for gravity waves the phase velocity increases with increasing wavelength, wave age is higher for swell than for locally generated waves. Wave age is often used for parameterizations of the drag coefficient $C_D = u_*^2/U_{10}^2$ with sea state (Drennan et al. 2003, Toba et al. 1990).

2.2.4 Mean square slope

Mean square slope (mss) σ_s^2 has been used often as a parameter describing the roughness of the sea surface. Unlike wave height parameters, it is also sensitive to the smaller scale waves. It is well defined in principle as the variance of surface slope. In practice, measurements are usually limited in one way or the other and mss can be determined in multiple ways. Each method has its advantages and limitations and may be more or less applicable for a certain purpose.

Brute-force From a record of surface slope, either a time-series at a single point, or a two-dimensional snapshot of the surface, or a combination of both, one can simply compute the variance. However, most measurement techniques can only record slopes up to a certain maximum value. In addition, they may lack the spatial (or temporal) resolution to resolve the smallest capillary waves, which typically have the largest slopes. Together, these effects lead to an underestimation of the mean square slope determined by computing the variance of the record. Because higher slopes occur increasingly often at higher wind speeds, the disparity between the “real” σ_s^2 and the measured mss likely increases with wind speed.

Probability distribution Any instrument with a limited slope measurement range (i.e. where the maximum resolvable slope is smaller than the maximum occurring slope) can measure *partial* probability distributions of slope. If the shape of the distribution is assumed to be known, the variance of the distribution can be estimated by fitting a model to the measured data. This then also accounts for the missing measurements of higher slope. However, since the determined mss then depends on an extrapolation of the measured partial distribution to higher values, such a procedure requires good knowledge of the actual pdf. In general, such a procedure can only be expected to give reliable estimates of mss when the measurement range is at least on the order of the rms slope. This will also be discussed in sec. 7.1.2.

Spectral integration Instead of determining mss in the space-time domain, it is also possible to compute it from slope spectra in the wavenumber-frequency domain. The integral of the slope spectrum over all wavenumbers/frequencies is mss. This is simply due to *Parseval's theorem*, which states that the total energy is conserved by Fourier transformation. Of course, the result is then identical to that of the brute-force method, with all the limitations discussed there. On the other hand, it is possible to study contributions of different wavenumber ranges to the overall mss. This way, one can determine the importance of waves on different scales for the overall roughness of the surface. In processes, where certain ranges of wavelengths are known to be more important than other (i.e. air-sea gas exchange, radar backscatter), it is possible to limit the description of roughness to the relevant scale.

2.3 Air-sea gas exchange and waves

It has long been recognized that waves play a crucial role in the exchange of heat, momentum and trace gases between the atmosphere and the ocean (e.g. Jähne et al. 1979). Still, it has so far not been possible to derive a physically based model of gas transfer that correctly accounts for wave effects. In this section, a very brief overview of gas exchange and its dependence on the wave field is given. For more details, the reviews of Jähne (2009), Jähne and Haußecker (1998) and Wanninkhof et al. (2009) are recommended.

2.3.1 Mass transport in fluids

Trace gases are transported in fluids (air or water) by turbulent and molecular motion. For large scale transport, turbulence is the more efficient mechanism. In the boundary layers close to the air-sea interface however, diffusion becomes important. The turbulent eddies cannot penetrate the surface; eddy size thus sinks approaching the interface. Turbulence becomes less efficient, molecular diffusion becomes relevant. Both transport mechanisms are typically described in analogy to Fick's law for diffusion by Reynolds decomposition:

$$j_c = -(D + K(z)) \frac{\partial c}{\partial z}, \quad (2.63)$$

in other words, the flux of a trace gas j_c is proportional to the gradient in its concentration (horizontal homogeneity is assumed, so that $\nabla c \equiv \partial c / \partial z$). The molecular diffusion constant D from Fick's law was complemented with a *turbulent* diffusion coefficient $K(z)$. Unlike D , the turbulent diffusivity has a depth dependence to account for the reduction of turbulence approaching the interface.

The transfer velocity

The boundary layers near the surface, with typical thicknesses of less than a millimeter constitute the overall bottleneck for the exchange of gases and heat between the atmosphere and the ocean, because of the significant reduction of $K(z)$ approaching the surface ($K(z) \rightarrow 0$).

This allows the definition of an integrated quantity, which macroscopically describes the rate of air-sea gas transfer. Such a macroscopic formulation is obtained from eq. (2.63) by integration:

$$c(z_2) - c(z_1) = -j_c \int_{z_1}^{z_2} (D + K(z))^{-1} dz = j_c R = j_c / k \quad (2.64)$$

Here, it was used that the flux density j_c is constant (due to mass conservation and in the absence of sources or sinks). The newly defined *transfer velocity* k (the inverse

transfer resistance R) now contains the structure of turbulence in the boundary layer. It generally depends on the integration boundaries z_1, z_2 . However, because $(D + K(z))$ is much smaller in the boundary layers than outside, most of the resistance is concentrated in the boundary layers. Therefore, the dependence of k on the integration boundaries is not strong, provided that the boundary layers are included in the integral.

2.3.2 Modeling gas exchange

Even though significant progress in measurement techniques has been made in the past years, exact knowledge of the turbulent motion under a wavy water surface – and thus knowledge of $K(z)$ – remains elusive. Measuring processes in the boundary layer is complicated, because of a) the thinness of the layers (typically 20 – 200 μm in the water); and b) the large amplitude of motion of the wavy water surface. Therefore both very high resolution (on the order of few μm) and a large measurement range (at least on the order of centimeters) are required to study realistic wind-driven surface conditions. So far, direct measurements of profiles of gas concentrations in the boundary layer have been limited to cases of either mechanically generated turbulence or wind waves with very low amplitude (Asher and Litchendorf 2009, Friedl 2013, Herlina and Jirka 2008, Münsterer and Jähne 1998).

A number of different models have been developed that describe the turbulence structure and allow to derive integrated expressions for the transfer velocity k (e.g. Coantic 1986, Deacon 1977, Lamont and Scott 1970). Jähne et al. (1987) proposed to use the generalized relation⁴

$$k = \frac{1}{\beta} u_* \text{Sc}^{-n}, \quad (2.65)$$

where the transfer velocity k depends on the friction velocity u_* , a dimensionless scaling parameter β which describes the strength of near-surface turbulence and the Schmidt number ($\text{Sc} = \nu/D$, with the kinematic viscosity ν) with exponent n . The Schmidt number exponent n is assumed to be $2/3$ for a smooth water surface (Deacon 1977) and $1/2$ at a rough, wavy water surface (Jähne et al. 1979). Experimental evidence suggests that the transition between those limiting cases is gradual (Krall 2013, Nielsen 2004, Richter and Jähne 2011). The variation of β with the sea state has still to be investigated. Both dimensionless parameters β and n depend on the wave field, the exact relations are unknown. Jähne et al. (1987) propose the mean square slope of the waves σ_s^2 as a parameter to describe the influence of the waves on gas exchange.

⁴Unless specified otherwise, u_* denotes the *water-side* friction velocity: $u_* = \sqrt{\rho_a/\rho_w} u_{*,a}$, with the air-side friction velocity $u_{*,a}$ and the densities of air and water.

2.3.3 The facet model

The facet model tries to account for the intermittency of gas exchange (Jähne et al. 2007): At a smooth water surface, the transfer velocity is assumed to be described by the Deacon (1977) model,

$$k_s = \frac{1}{\beta_s} u_* \text{Sc}^{-2/3}. \quad (2.66)$$

With the development of waves, and the onset of (microscale) wave breaking, some patches (or *facets*) start behaving like a rough surface, described by a “wavy” transfer velocity

$$k_w = \frac{1}{\beta_w} u_* \text{Sc}^{-1/2}, \quad (2.67)$$

with Schmidt number exponent $n = 1/2$. The fraction of the surface that is subject to the rough boundary conditions is denoted by a_w , and the total transfer velocity is then given by

$$k = (1 - a_w) \frac{u_*}{\beta_s} \text{Sc}^{-2/3} + a_w \frac{u_*}{\beta_w} \text{Sc}^{-1/2}. \quad (2.68)$$

A parameterization of the fraction of rough surface facets a_w in terms of the mean square slope σ_s^2 of the waves is given by Richter and Jähne (2011):

$$a_w(\sigma_s^2) = \frac{(\sigma_s^2)^\gamma}{\delta^\gamma + (\sigma_s^2)^\gamma}. \quad (2.69)$$

The gradual transition from smooth to rough surface conditions is depending on the mss and two model parameters δ and γ . These can be interpreted as the midpoint (δ) and the steepness (γ) of the transition of the Schmidt number exponent n from $2/3$ to $1/2$ (Krall 2013).

The model has been applied to transfer velocities measured at different laboratory facilities by Degreif (2006), Nielsen (2004) and Krall (2013) and different values for these parameters have been obtained. The observed deviations have been linked to experimental difficulties and influences by the geometry of the facilities.

Zappa et al. (2001) and Zappa et al. (2004) derive a similar model, where the surface is parted into facets that exhibit surface renewal due to microscale wave breaking and facets that do not. The fraction of the surface that is influenced by microscale breaking is shown to depend on the mean square slope of the surface.

2.3.4 Parameterizations of air-sea gas exchange

Despite irrefutable evidence that wind speed alone cannot fully describe the complex interactions controlling near-surface turbulence under all circumstances (Waninkhof et al. 2009), parameterizations using wind speed to quantify transfer velocities are still state-of-the-art (Ho et al. 2011).

This is not caused by the ignorance of the users, but for a practical reason: Wind speed is readily available both from local measurements and from global satellite products, while measuring other parameters requires extensive experimental effort. Thus, not only is it necessary to understand the basic physical processes driving gas exchange. For a parameterization to be successful, it is also required that instrumentation is available on all relevant scales to measure the required quantities without disproportional effort.

Frew et al. (2007) have shown that it is possible to use satellite measurements to determine parameters – other than wind speed – which describe the water surface roughness. They derived the mean square slope σ_s^2 in the wavenumber range of 40 – 100 rad/m from dual-frequency radar backscatter. Then, they used an empirical relation of the transfer velocity k and mss to derive an estimate for the global mean transfer velocity.

Mean square slope is not the most desirable parameter. There is no fundamental link between mss and gas exchange. Parameters such as turbulent kinetic energy dissipation or the surface divergence (see sec. 1) have a stronger theoretical foundation. However, these parameters are hard to measure even in the laboratory and it is certainly not possible to estimate them on larger scales. Currently, the only parameters that have the potential to replace wind speed are those connected to the waves, such as mean square slope. Measurements are possible on all scales (see sec. 1). So far, robust methods for local measurements have been lacking. In this work, new instruments capable of measuring mean square slope under a wide range of conditions are presented.

3

Methods

In this work, different instruments were developed and used to measure waves in the laboratory and in the field. All measurements are non-invasive and optical; they use cameras and natural or artificial light sources. Before the measurement principles of the *Reflective Stereo Slope Gauge* (RSSG) and of its successor the *Medium Angle Slope Gauge* (MASG) are presented in sec. 3.2, 3.3, and 3.4, an overview of the state of the art in optical wave measurement and imaging is given in sec. 3.1.

3.1 Optical measurement of ocean waves

Waves have been studied with optical techniques for more than 100 years, dating back to the pioneers Laas (1905; 1906; 1921) and Kohlschütter (1906) who used stereo photography to measure wave heights. A historical review of some of the techniques that were developed over the past decades is given in Kiefhaber (2010). Here, the focus is set on the state of the art and an overview of the most promising measurement principles is given. While in the laboratory, methods based on the refraction of light at the water surface are superior (Jähne et al. 1994), reflection-based methods have the advantage of not requiring parts to be submerged in the water. In field experiments, this significantly reduces the complexity of the setup. Most techniques rely on the reflection of natural light at the water surface. In contrast, the new Reflective Stereo Slope Gauge employs artificial light sources and is thus able to measure independent of natural lighting, also at night.

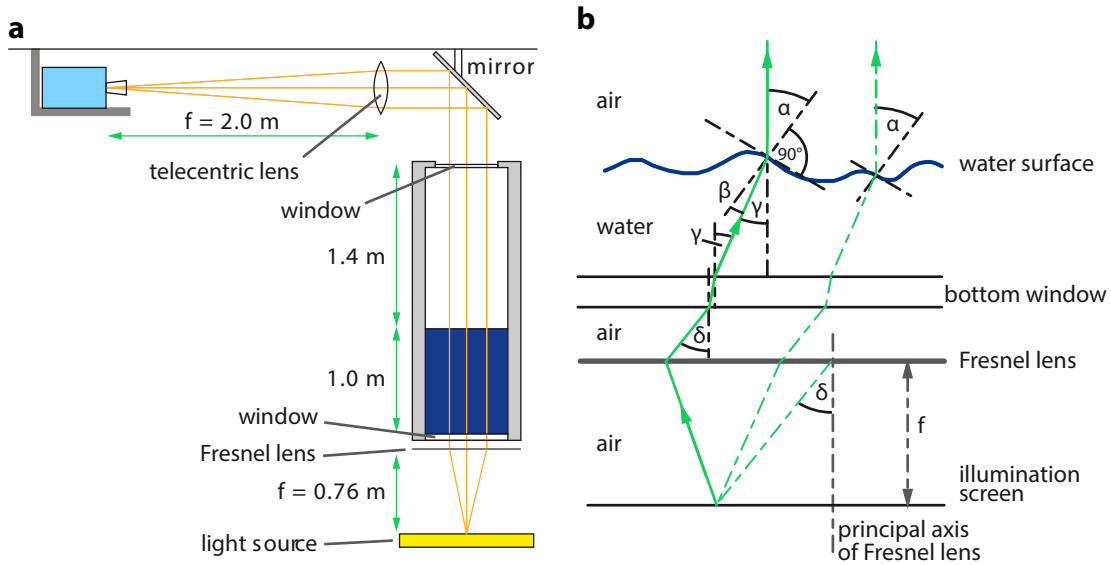


Figure 3.1: **a** The ISG setup at the Aeolotron: The camera is observing the refraction of light from an underwater position-coded light source. Modified after Kiefhaber et al. (2013). **b** The ray geometry of the ISG. The light source is placed in the focal plane of a Fresnel lens. This guarantees that all rays that are refracted by waves of the same slope are focused on one position, independent of wave height.

3.1.1 Imaging Slope Gauge

The arguably best method for measuring small-scale waves in the laboratory is the *imaging slope gauge* (e.g. Jähne and Riemer 1990, Zhang and Cox 1994). A *color imaging slope gauge* (CISG) was set up at the Aeolotron wind wave facility between 2009 and 2011 by Roland Rocholz and was used during several air-water gas exchange experiments (Krall 2013, Kräuter 2011). The measurement principle of the CISG is described in detail by Rocholz (2008); a detailed description of the specific setup at the Aeolotron can be found in Kiefhaber et al. (2013), so that only a short summary is given here.

Principle

The setup of the ISG is shown in Fig. 3.1a: A camera is observing the water surface from above. The camera aperture is placed in the focal point of a large lens (diameter $d = 0.32$ m, focal length $f = 2$ m). Then, only light rays that are parallel to the optical axis of the large lens (on the side away from the camera) are refracted into the camera (the focal point). Thus, all light rays are vertical at the water surface. The camera lens together with the large lens form an object-space telecentric lens. This guarantees a constant magnification factor independent of object distance. The mean water surface is in the second focal plane of the lens.

The light is coming from a light source that is installed underneath the wind wave facility. The light source is placed in the focal plane of a large Fresnel lens (diameter

$d = 0.89$ m, focal length $f = 0.76$ m). To understand the trace of a ray on its way from the light source to the camera, it is instructive to start at the water surface. Due to the telecentric lens, only light rays that are vertical at the water surface enter the camera. If the water surface normal is not vertical, the ray is refracted at the surface (see Fig. 3.1b). If it encloses the angle α with the surface normal above water, the refracted angle β to the surface normal in the water is given by Snell's law: $\sin \alpha = n_w \sin \beta$, where $n_w \approx 1.33$ is the refractive index of water. The ray is also refracted entering and leaving the bottom window, so that it leaves the Fresnel lens at an angle δ . Because the light source is placed in the focal plane of the Fresnel lens, all rays that have the same angle δ to the vertical at the Fresnel lens are refracted onto the same location on the light source (the extension of the well-known "parallel rays become focal point rays" of geometric optics). This effectively translates the surface slope α into a position on the light source, independent of wave height and position on the water surface. The dependence of the position on the light source on surface slope is almost linear (Jähne et al. 1994).

To measure the slope of the surface, the origin of the light rays on the light source need to be measured. In the new high speed imaging slope gauge, this is done by fast switching of four different intensity gradients on the LED light source (Kiefhaber et al. 2013). From ratios of these gradients, each position on the light source can be identified uniquely.

In the gas exchange experiment of 2011 which is analyzed in this thesis, a different coding-scheme was used. In the *color imaging slope gauge* (CISG) set up by Roland Rocholz, the light source position is color-coded with three linear wedges in red, green and blue, oriented at 45° , 0° , and -45° to the x-axis (Balschbach 2000). Since only two independent channels are needed to determine the 2D position, the third channel can be used for normalization, making measurements independent of surface curvature effects and dirt or bubbles in the water.

The advantage of the CISG, that both slope components can be measured from a single image, comes at a cost: The large custom planoconvex lens that is used to satisfy the telecentricity condition for measurements that are independent of wave height is not achromatic. Using light from broad wavelength band leads to significant chromatic aberration, as will be discussed in sec. 6.5.1. Also, the light output of the old color light source (fluorescent tubes with a colored transparency) was hardly sufficient even at relatively high integration times.

With the availability of a high speed camera, there is no more need for a multi-chromatic light source, the different slope components can be measured in sequence. A raw image rate of 6000 Hz still gives 2D slope images at a rate of 1250Hz (Fahle 2013). The integration time is then limited by the frame rate of the camera; only with the high power LEDs that have very recently become available such a scheme is possible.

Requirements and limitations

Because surface slope is measured from the refraction of light, it is necessary that either the light source or the camera are submerged in the water. While it is generally possible – and has been attempted, see Klinke and Jähne (1995) – to deploy an ISG on a buoy, such a complicated system is not well suited for routine field measurements. Also, it can hardly be considered non-invasive, since the buoy and the underwater light source will certainly affect water and wave motion.

The slope range that can be measured with the ISG is depending on the size of the light source, while the footprint on the water surface cannot be larger than the diameter of the large telecentric lens. For studies of the dynamics and interactions of small-scale waves in the laboratory, the ISG is the ideal instrument. For including effects of larger scale waves that are not much smaller than the image footprint additional instruments are required, e.g. a wave height measurement at a single point. An optical system for wave height measurements that can be fused with the ISG to measure the full range of waves in the Aeolotron facility has been set up by Horn (2013).

3.1.2 Polarimetric Slope Sensing

Polarimetric slope sensing has been introduced recently by Zappa et al. (2008) as a way to determine the surface slope of small-scale waves from the measurement of the polarization of reflected light. A new polarimeter with a very simple optical setup was designed and built for deployment to the SOLAS-Peru cruise (see sec. 5.2.2). The system is described in detail by Bauer (2013).

Principle

The polarization of light (coming from the sky or an artificial light source) that is reflected at the water surface – or any other dielectric surface – is partially polarized. The degree and orientation of polarization is dependent on the angle of incidence. This can be used to compute the two dimensional surface slope from images of the sea surface acquired with a special imaging *polarimeter*. A polarimeter does not only measure the brightness of light reflected at the water surface, but also its polarization, using an array of cameras and polarization optics.

The polarization of light that is reflected at the water surface is described by the Fresnel reflection coefficients (see, e.g. Jackson 1998). The coefficients R_p and R_s for light polarized in the directions parallel and orthogonal to the plane of reflection are shown in Fig. 3.2a. At low incidence angles, only about 2 % of the light is reflected. Only around 50° the reflection coefficients increase steeply to reach 1 at 90°. The component polarized in the direction orthogonal to the plane of reflection (see Fig. 3.3) increases monotonically. The component polarized in parallel with the plane of reflection first decreases slowly and is zero at Brewster's angle 53°. Then

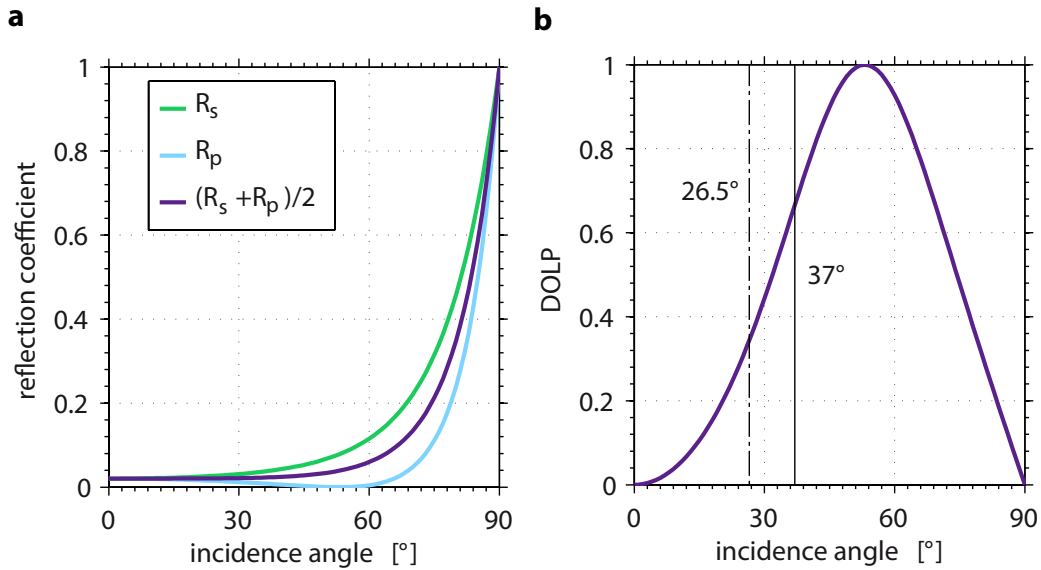


Figure 3.2.: **a** The Fresnel coefficients for reflection at the water surface: The component of light polarized in the direction parallel to the plane of reflection R_p (see Fig. 3.3) is not reflected at Brewster's angle 53° . The total reflection coefficient (the sum of the parallel R_p and orthogonal R_s components) is about 0.02 for normal incidence and constant up to almost 50° . It then increases steeply to reach 1 at 90° incidence. Reflected light is unpolarized at incidence angles 0° and 90° , and fully polarized at Brewster's angle.
b The degree of linear polarization (DOLP) as a function of incidence angle. The maximum is at Brewster's angle (53 degrees). The black lines denote camera viewing angles for maximum measurement range (dashed) and maximum sensitivity and linearity for low slopes (solid).

it also increases to reach full reflection at orthogonal incidence. This difference in the behavior of the two polarization components is utilized in polarimetric slope sensing.

Figure 3.3 shows the basic geometry for polarization measurements: A light ray falling onto a facet on the water surface under an incidence angle θ is (partly) reflected, the angle of reflection being identical to the angle of incidence. The light is partly polarized orthogonal to the plane of reflection, by measuring the orientation of polarization φ the slope of the surface normal in the direction orthogonal to the plane of reflection can be measured. The *degree of linear polarization*

$$\text{DOLP} = (R_s - R_p)/(R_s + R_p) \quad (3.1)$$

with the reflection coefficients R_s and R_p for light polarized orthogonal and parallel to the plane of reflection. From the DOLP, the incidence angle θ can be measured (Zappa et al. 2008). The DOLP is a non-linear function of incidence angle (see Fig. 3.2b). As was already described, reflected light is unpolarized at normal incidence and fully polarized at Brewster's angle 53° . Therefore the function can only be inverted

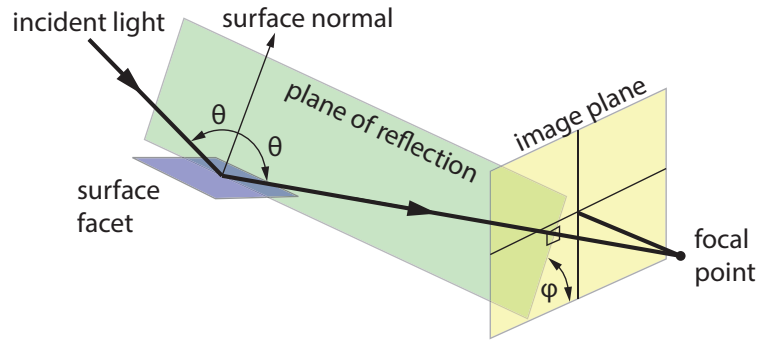


Figure 3.3.: Light is reflected from a surface facet into the camera. The incidence angle θ can be computed from the degree of linear polarization (DOLP), the angle between the plane of reflection and the x-axis of the image plane φ is given by the polarization orientation (modified after Zappa et al. 2008).

on one of the intervals $[0^\circ, 53^\circ]$ or $[53^\circ, 90^\circ]$. While the latter is advantageous in terms of the total reflection intensity (see Fig. 3.2a), only the lower interval is suited for wave measurements under field conditions. In the higher interval, the side of the wave tilted away from the instrument would likely be occluded by the wave itself. If the camera observes the water surface at an angle of 26.5° (see Fig. 3.2b), the range of slopes that can be measured is $\pm 26.5^\circ$. Near zero incidence angle, the slope of the DOLP is very low (and very non-linear). If only smaller slopes are expected, the ideal viewing angle is 37° , where the DOLP has the largest slope and is more linear.

To measure the polarization of light, a multi-camera system is needed. If only linear polarization occurs (an assumption that is valid for unpolarized light being reflected at the water surface), three cameras are sufficient to determine the polarization state (more precisely: the first three components of the Stokes vector of the light, see Bass 2010). A very simple setup has been used by Bauer (2013): Three cameras with parallel optical axes and located as close as possible to each other are each equipped with a linear polarization filter in different orientations (0° , 60° and 120° to horizontal). Pezzaniti et al. (2008) describe a more elegant solution: Four cameras share a custom lens, the light is split up by a block made of polarizing and non-polarizing beam splitters as well a half-wave and a quarter wave plate. In their configuration, all light that is entering the lens is used, no polarization filters are required that block light. However, a custom made lens is required, because the flange focal distance (or more precisely the distance from the back side of the lens to the camera sensor) of commercial lens mounts is not sufficient to accommodate the beam splitter block. This significantly increases the cost of such an instrument.

Requirements and limitations

The measurement scheme using DOLP and polarization orientation to retrieve the two slope angles makes a number of assumptions: 1. The polarization of the light source (in field measurements: the sky) is known. 2. All light that is captured by the polarimeter was reflected at the surface, there is no *upwelling light* that was scattered at particles in the water. 3. Wave slope does not exceed the interval in which the DOLP dependence on angle of incidence is unique.

The simplest way of guaranteeing requirement 1 is to measure only with overcast sky, when it is safe to assume that the light is unpolarized. While the blue sky is partly polarized by Rayleigh scattering, multiple scattering in clouds removes polarization. Barsic and Chinn (2012) present first results from polarization slope measurements that account for the polarization of the sky. They used a second polarimeter for the measurement of sky polarization, modelled the distribution with a Rayleigh sky and used an inverse model with a variational method to determine surface slope given the sky polarization.

Requirement 2 is not a problem in clean and deep water in the open ocean, but certainly is a problem in areas of high biological activity. Barsic and Chinn (2012), who measured at Duck Pier in the coastal waters of North Carolina, attribute most of the inaccuracies in their measurements to upwelling light.

The third requirement, the limited range of incidence angles, is the hardest, especially since it can be very hard to judge whether the slope was within the allowed interval. The actual measurement range of the instrument depends on the angle at which the polarimeter is tilted against the vertical. An angle of 26.5° ensures a symmetric interval of $\pm 26.5^\circ$ (dashed line in Fig. 3.2b). An angle of 37° (solid line in Fig. 3.2b) was used by Zappa et al. (2012). It is advantageous especially if measured surface slopes are mostly small, since it is in the steepest and most linear part of the DOLP, but leads to an asymmetric measurement interval of $[-37^\circ, +16^\circ]$. Note however that the given measurement ranges are only valid for the optical axis of the camera, i.e. in the image center. Away from the center, towards the top (bottom) of the image, the still water surface is observed at a higher (lower) angle. Thus the measurement range is in general depending on position in the image. This effectively limits the field of view of the lens. The polarimeter used by Zappa et al. (2012), for example, has a field of view of $4.8^\circ \times 3.6^\circ$. Also, especially under higher wind speed conditions when lots of capillary waves are present, it is hard to believe that slope does not regularly exceed 25° , requiring additional post processing effort to remove effects of the ambiguity of DOLP with incidence angle.

Nevertheless, polarimetric imaging is an intriguing new technique that allows the measurement of small-scale waves in the field with unprecedented resolution. Under the right environmental conditions, it can provide high quality wave slope data.

3.1.3 Stereopsis

As was already mentioned, stereo photography is the oldest quantitative optical wave measurement technique. It has been used in dozens of studies with differing success; this review is restricted to very recent examples. For a more complete list of studies employing stereo photography, the reader is referred to Kiefhaber (2010).

Principle

In stereo photography, two cameras acquire images of the same footprint on the water surface (or of any other object) simultaneously, but from two locations and under different angles. The distance of the water surface can be measured if it is possible to determine the stereo *disparity*, i.e. the distance between the two positions of an object in the two stereo images. The challenge of determining this disparity, which requires finding the same object (or structure on the water surface) in both images, is known as the *correspondence problem* of stereo photography. Corresponding points are typically found either by *block matching*, i.e. by comparing the gray values in a portion of one image with those in portions of the other image. Statistical measures are used to determine which area of the second image corresponds best to the selected window in the first image.

Kosnik and Dulov (2011) and Mironov et al. (2012) use block matching schemes (correlation analysis) combined with a high-pass filter to reduce large-scale image brightness gradients caused by inhomogeneities of the sky. This way, they extract the small-scale roughness features without brightness trends, increasing the chances of finding corresponding points. To decrease the number of false correspondences, they also simply restrict the analysis to areas with sufficient texture using a priori estimates.

In a series of papers, a group of authors reports their success with processing data from the *Wave Acquisition Stereo System* (WASS). This system is a two camera stereo setup, designed towards measuring gravity waves on a large footprint of 1000 m². Benetazzo (2006) and Benetazzo et al. (2012) describe the development of a local cross-correlation based block matching approach, using an a posteriori measure of confidence (a threshold in the normalized cross-correlation). In addition, they use a multi-resolution scheme, first computing the mean disparity over a larger image area, then requiring that at high resolution, the disparity will not deviate significantly from the mean. Gallego et al. (2011) report the use of a variational method for processing the WASS stereo images. Fedele et al. (2013) use another variational method which enforces smooth disparity maps in both spatial and temporal direction. For a water surface without too many breakers this is certainly a good assumption.

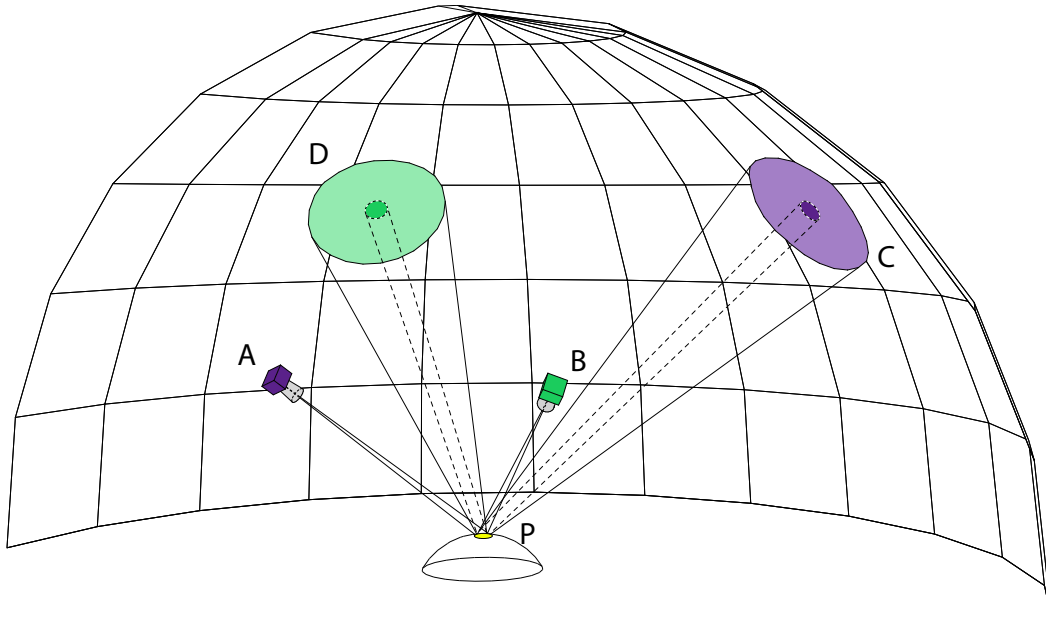


Figure 3.4.: If only specular reflections occur at the surface facet **P**, then cameras **A** and **B** see light coming from different parts of the sky **C** and **D**. If the surface were flat, light would be coming only from the inner circles. Curvature of the surface increases the area of the sky that is seen.

Requirements and limitations

Some of the main challenges of conventional stereo vision are depth discontinuities and the occlusion of background by foreground objects. The water surface is well behaved, it is generally continuous and for sufficiently high grazing angles without occlusions (except maybe in the case of spilling breakers). There is, however, one big problem: Due to the surface tension of water, the surface is always smooth at the scale of optical wavelengths. As a consequence, light is not scattered in all directions (as with a *Lambertian* reflector). Only directed – or *specular* – reflections occur. Conventional stereo vision algorithms on the other hand assume all surfaces to be fully Lambertian, without any specular reflections.

Figure 3.4 illustrates the consequences of this: If the surface that the camera is looking on (at **P**) is specularly reflecting, the light that ends up in camera **A** is coming from area **C** of the sky, while the light that ends up in camera **B** is coming from area **D**. If the luminance of the sky is different in areas **C** and **D**, e.g. due to different cloud cover, the two cameras will record different gray values for point **P**. The cameras do not see the (water) surface directly, but a virtual image of the sky that is reflected. If the surface is not flat but curved, as in Fig. 3.4, the bundle of rays (virtually) going from **A** (and **B**) to **P** is widened at the point of reflection. This leads to an increase of the area of the sky that is seen. In Fig. 3.4, the small dashed circles refer to the area that would be visible with a flat surface, the large circles with the depicted curved surface.

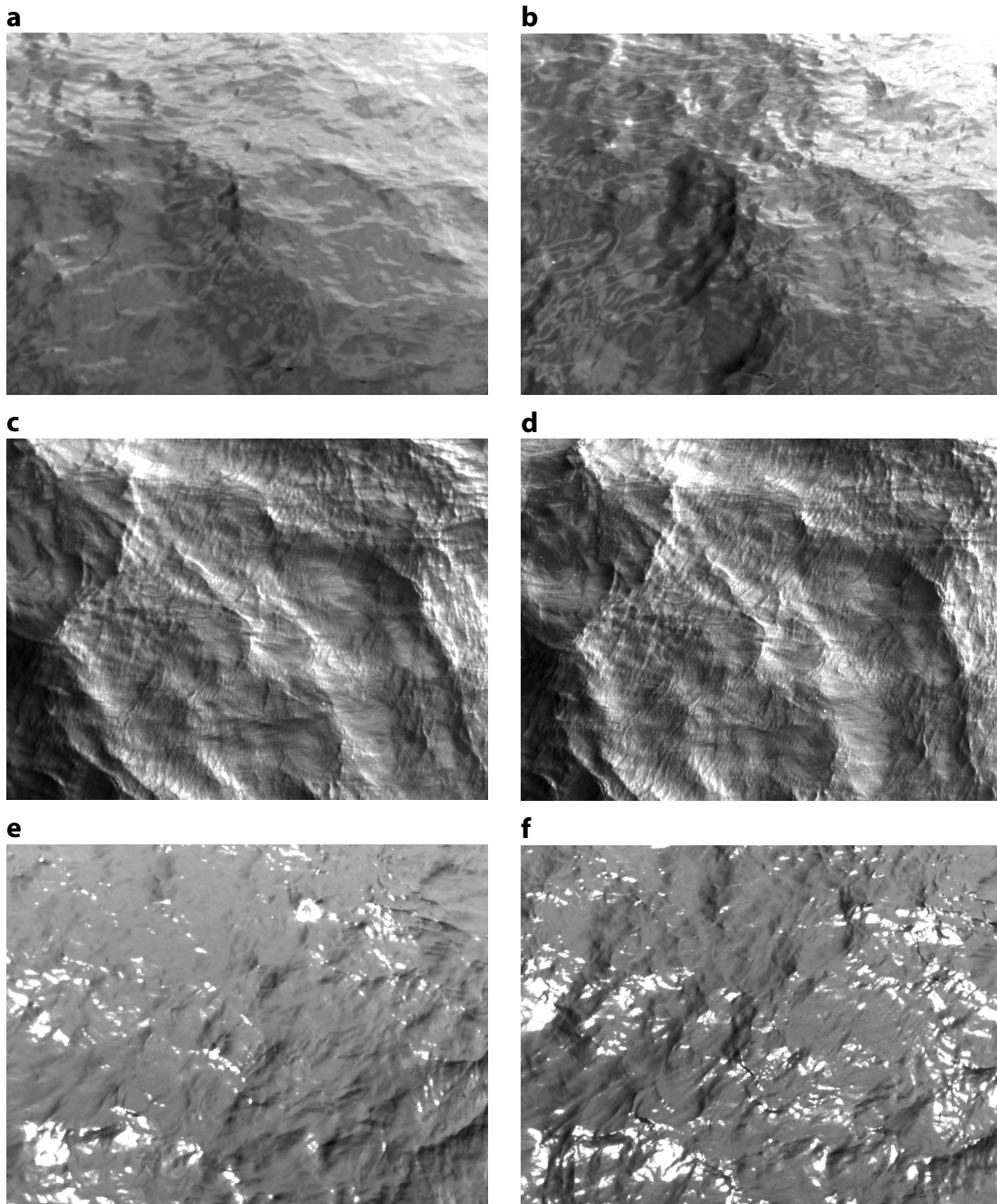


Figure 3.5.: Three stereo image pairs of the water surface: Under low wind speed conditions (**a** and **b**) it is obvious that gray value based block matching will fail. At higher wind speeds (**c** and **d**) when the surface is much rougher and a lot of small ripples are visible, the effects of the specularity of the water surface are not as pronounced. If the sun is not covered by clouds, the images are additionally contaminated by *sun glitter*, as in **e** and **f**. The images were acquired off the coast of Peru during the M91 cruise. The stereo cameras had a stereo base of 3 m and were looking to the water surface under an angle of 37° to the vertical.

Figure 3.5 shows the practical consequences in examples of stereo images of the water surface. These images were acquired with a stereo camera setup during the SOLAS-Peru experiment (see sec. 5.2.2): In panels 3.5a and 3.5b the water surface is relatively calm and the sky is inhomogeneous due to partial cloud cover. This leads to very different appearances of the water surface in the images, making it nearly impossible for gray value based matching techniques to find corresponding points. In Fig. 3.5c and 3.5d the water surface is roughened by higher wind speeds and a lot of very small scale ripples are visible. Due to their high curvature, they reflect light from a larger area of the sky. For high curvatures, the areas **C** and **D** in Fig. 3.4 overlap and the relative importance of the different viewing angles is reduced. In addition to this, cloud cover was also more homogeneous during the image acquisition. Panels 3.5e and 3.5f illustrate an additional problem: Whenever the sun is not covered by clouds, images are contaminated with *sun glitter*, direct reflections of the sun. These areas are usually overexposed and have different shape, further reducing the similarities between the images.

It should be noted that the effect of the different viewing angles in Fig. 3.5 is particularly large due to the specific arrangement of the cameras: a relatively large stereo base combined with slanted optical axes and a small footprint on the water surface. Parallel optical axes and a wider field of view at greater distance will help remedy the problem. Homogeneous cloud cover or blue sky will also contribute to higher quality stereo images. Still, it is doubtful that a stereo system can be used as a reliable source for wave data under a wide variety of conditions.

3.1.4 Helmholtz stereopsis

The shortcomings of the application of traditional stereo photography to the imaging of water waves can be overcome with an extension of the measurement method. Not only are the cameras placed in specific positions, the illumination is also considered and optimized.

Principle

Helmholtz stereopsis is a modification of the general stereopsis principle, geared towards working with specular surfaces. If artificial light sources are placed in areas **C** and **D** in Fig. 3.4 and natural light coming from other areas of the sky is filtered, it is possible to ensure the same lighting conditions for both cameras. Ideally, the light source for camera **A** would be placed at the position of camera **B** and vice versa. Then, the principle of *Helmholtz reciprocity* holds, that two light rays travelling along the same path but in opposite directions ($\mathbf{A} \rightarrow \mathbf{B}$, $\mathbf{B} \rightarrow \mathbf{A}$) will encounter identical reflections, refractions, and absorptions (Helmholtz 1867; p. 169). Based on this, Zickler et al. (2002; 2003) coined the term *Helmholtz stereopsis* for such a measurement system and showed how the problem of stereo vision with partially specular surfaces can be solved this way.

Well before this, Waas and Jähne (1992) and Dieter (1998) used such a system for stereo measurements at the fully specular water surface. The instrument used in this study - the *Reflective Stereo Slope Gauge* - is an improved version based on their original design. It is described in detail by Kiefhaber (2010). Figure 3.6a shows the core of the instrument, the two cameras have a stereo base of 300 mm and can be slanted towards each other at variable angles to guarantee maximum overlap at a target distance. Technical aspects of the instrument will be described in more detail in sec. 4.1.1.

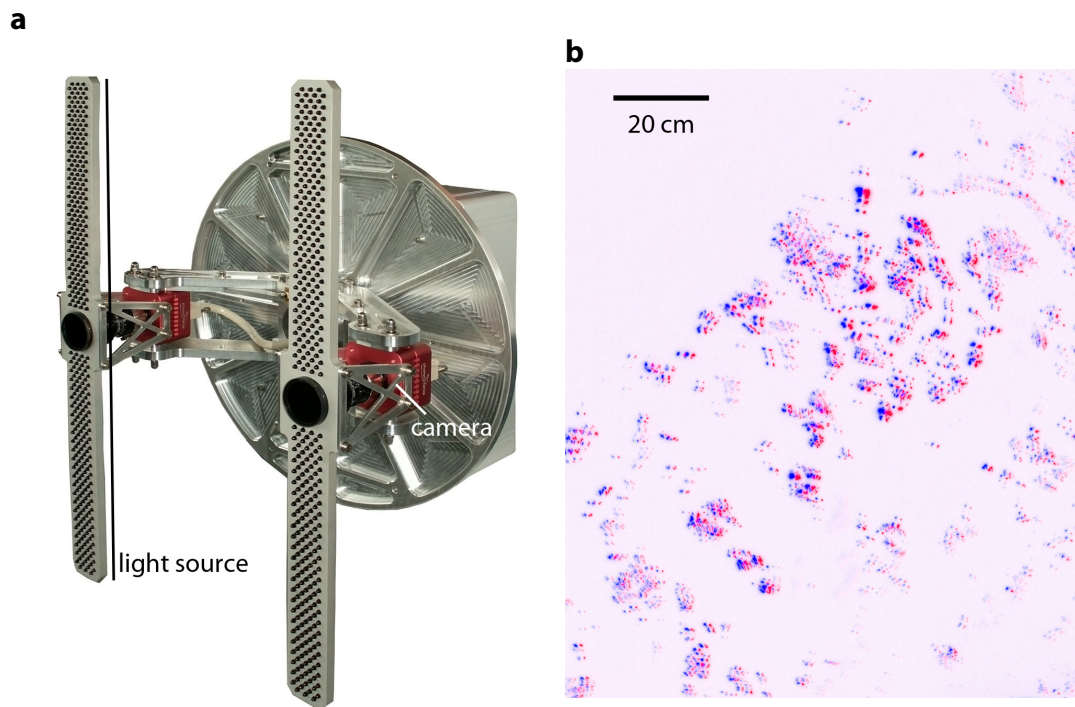


Figure 3.6.: **a** The Reflective Stereo Slope Gauge (picture taken from Kiefhaber (2010)). The stereo base is 300 mm, the two light sources are built from 350 near-infrared LEDs each. **b** False-color inverted stereo example image. The left camera is shown in red, the right camera in blue. White areas are dark in the original images and contain no reflections. The size of the footprint on the water surface is 1.3×1.1 m. Disparity can be estimated wherever there are reflections visible.

Requirements and limitations

The *Reflective Stereo Slope Gauge* (RSSG) was designed to be mostly independent of environmental conditions. It does not have requirements on the radiance distributions of the sky, due to its active light sources it can also measure at night. This is a major advantage over the other presented methods for field measurements. The use of light source with an emission spectrum in the near infrared (around 950 nm) additionally allows to remove most natural light from the images in daytime measurements. A major water absorption peak at 970 nm and the water content of the atmosphere is responsible for this.

Figure 3.6b is an example stereo image taken with the RSSG. It is displayed in false color, the left image is colored red, the right image blue. The original gray values were inverted, so that the dark background is now white, and the originally bright reflections are now dark. This was done to increase visibility of the reflections.

Comparing the RSSG image in Fig. 3.6 with the images from the passive stereo system in Fig. 3.5, two differences become clear immediately: Firstly, unlike with the passive system, the structures visible in the RSSG images have the same shape and brightness in both camera images. Therefore, a block matching scheme using cross-correlation will provide accurate results for reflection disparity. Secondly, there is a drawback to the enhanced quality of the visible structures. The reflections do not cover the whole image equally, there are areas where they are rather sparse. This prevents the estimation of dense disparity maps, which are required to measure the full shape of the surface. Especially on the open ocean in the presence of swell, some images show no reflections at all because the water surface is tilted in the wrong way.

While polarimetric slope sensing and (passive) stereopsis have the potential to measure the full two-dimensional slope (or elevation) distribution – the shape of the surface – the RSSG can only measure wave heights at the points, where reflections are visible (corresponding to points with zero slope). Because these reflections are moving about the images, a flexible interpolation scheme for non-gridded data is required to recover the two-dimensional surface structure. This was investigated by Schaper (2011).

In addition to the height measurements, the RSSG also provides insight in the small-scale structure of the water surface (related to the maximum local curvature and described in sec. 3.4) and a statistical way to measure the surface roughness parameter *mean square slope* σ_s^2 . This parameter is the variance of the slope probability distribution and commonly used to describe the influence of waves on air-sea gas exchange.

The set of parameters that can be measured with the RSSG is limited, other instruments promise more information about the wave field. On the other hand, the RSSG can deliver this information in a robust way and mostly independent of environmental conditions, day and night. This prerequisite of an instrument for measuring wave parameters during air-sea gas exchange experiments is not fulfilled by any of the other presented methods. In the following sections, the specific

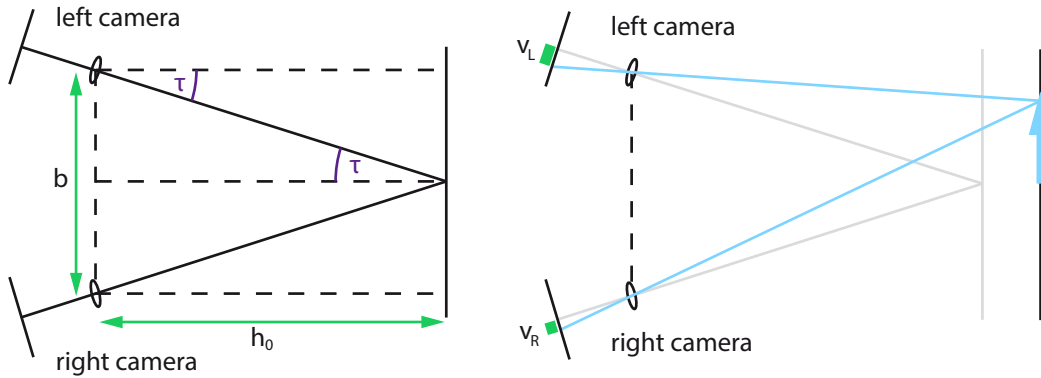


Figure 3.7.: Left: The stereo camera setup with slanted optical axes. Right: A structure at an arbitrary distance will be projected to two different positions in the left and right camera images.

measurement methods of the RSSG are described in detail.

3.2 Height measurement

3.2.1 Stereo triangulation

In Fig. 3.7, the basic geometry of the used stereo setup is shown. The optical axes of the two cameras are slanted towards each other to ensure maximum image overlap at the target distance h_0 . The tilt angle

$$\tau = \arctan[b/(2h_0)] \quad (3.2)$$

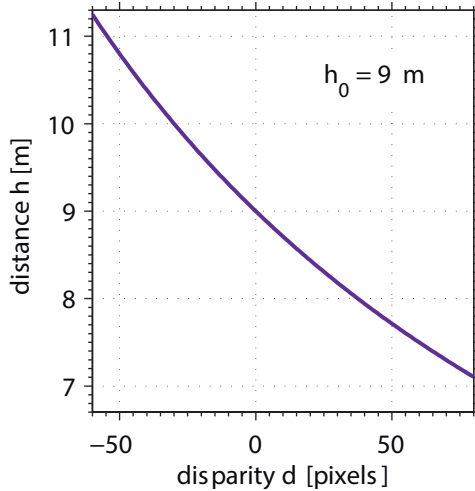
is determined by the stereo base b and the target distance h_0 .

The right side of Fig. 3.7 shows an example of how stereo triangulation works: Due to the different viewing angles of the two cameras, a structure at a distance h is projected to two different locations in the image, with (pixel) coordinates (u_L, v_L) and (u_R, v_R) in the left and right images, respectively. The *stereo disparity* \mathbf{d} is the difference between the two image positions:

$$\mathbf{d} = (u_L - u_R, v_L - v_R). \quad (3.3)$$

For a camera arrangement with slanted optical axes, the disparity is a function not only of the object distance, but also of the lateral position within the image footprint. In computer vision, stereo images are typically rectified to remove the dependence on the lateral position and simplify the search for corresponding points. For this specific application however, this turns out to be unfeasible and unnecessary.

The full expression for the dependence of the distance h on the disparity d is derived in appendix A.1. Here, only the result is presented (cf. Kiefhaber 2010; eq.


Figure 3.8

Distance as a function of stereo disparity for typical field experiment settings ($b = 300$ mm, $h_0 = 9$ m, $f = 72$ mm). Distance was computed for disparity measured in the image center ($v = 0$). The curve is slightly shifted for other image locations, due to the dependence on v in eq. (3.4).

(3.18)):

$$h = -\frac{b(4f^2h_0^2 - 2dbfh_0 + dvb^2 - v^2b^2)}{-4dfh_0^2 - (4bv^2 - 4dbv + 4bf^2)h_0 + dfb^2}. \quad (3.4)$$

The height h can be computed from the disparity d (only the component in the direction of the stereo baseline is of importance). The chosen stereo baseline b and focal length f , as well as the target distance h_0 determine the resolution of the system. The relation of h and d also depends on the position in the image, v is the pixel position¹ in the direction of the stereo base.

Figure 3.8a is a plot of eq. (3.4) for a typical situation in field measurements. The sensitivity at the target distance ($h_0 = 9$ m in the plotted scenario) is 30 mm/pixel. Wave heights of 4 m cause a change in disparity of about 140 pixels. Since the disparity can be determined with sub-pixel precision, this is absolutely sufficient to capture even shorter wind waves. In a laboratory scenario, with a shorter target distance of $h_0 = 3.5$ m, the sensitivity greatly increases to 4.5 mm/pixel.

3.2.2 Disparity estimation

The target distance of the RSSG can be adjusted so that the disparity at the mean water level is zero. Then, disparities are generally relatively small and a simplified and fast scheme can be used for their determination.

If the content of one image – or an *area of interest* (AOI) in one image – is merely a shifted version of the other image/AOI, so that the assumption of constant disparity is fulfilled and $g_2(\mathbf{x}') = g_2(\mathbf{x} + \Delta\mathbf{x}) = g_1(\mathbf{x})$, the disparity is equal to the maximum

¹ $v = 0$ for the image center.

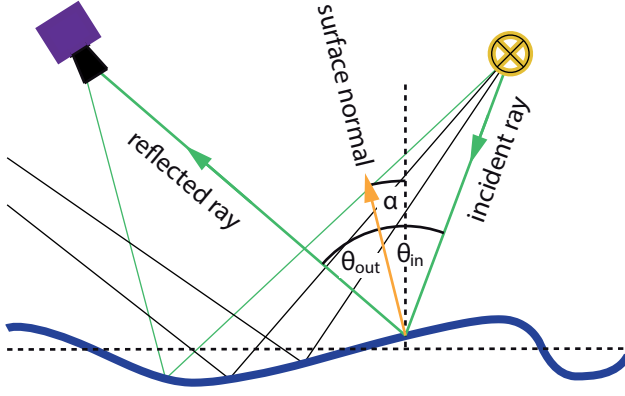


Figure 3.9
The slope measurement principle (modified after Kieffer 2010). For every pixel of the camera, a unique slope of the surface is required for light to be reflected from the light source to the camera.

of the cross-correlation

$$c(\mathbf{x}') = \iint_{-\infty}^{\infty} d\mathbf{x} g_1^*(\mathbf{x})g_2(\mathbf{x} + \mathbf{x}') \quad (3.5)$$

$$\leq \iint_{-\infty}^{\infty} d\mathbf{x} g_1^*(\mathbf{x})g_2(\mathbf{x} + \Delta\mathbf{x}) = \iint_{-\infty}^{\infty} d\mathbf{x} |g_1(\mathbf{x})|^2. \quad (3.6)$$

The cross-correlation can efficiently be computed in wavenumber space by Fourier transform:

$$c(\mathbf{x}') = \iint_{-\infty}^{\infty} d\mathbf{x} g_1^*(\mathbf{x})g_2(\mathbf{x}' + \mathbf{x}) = \mathcal{F}^{-1} [\hat{g}_1^*(\mathbf{k})\hat{g}_2(\mathbf{k})] \quad (3.7)$$

To prove the last equality is straightforward, it is directly analogous to the derivation in eq. (2.48) for the auto-correlation. Thus, the Fourier transform of the cross-correlation is simply the complex-conjugated product of the Fourier transforms of the two stereo images. The practical implementation of this disparity estimation scheme is detailed in sec. 6.2.

3.3 Slope measurement

3.3.1 Statistical measurement of surface slope

The slope measurement principle has already been described in detail in Kieffer (2010) and Kieffer et al. (2011). Only a brief summary is given here, a detailed description of the data processing routines will follow in sec. 6.3.

Light coming from the light source is only reflected into the camera for a unique surface slope (see Fig. 3.9). This slope varies from pixel to pixel. On average, in each pixel of the camera, the probability for the occurrence of a certain slope can be measured, giving part of the probability density function (pdf) of slope.

The principle is related to the *sun glitter* technique first used by Cox and Munk

(1954a;b). However, a different kind of averaging is used: Cox & Munk took images of reflections of the sun from an airplane flying at an altitude of 600 m. A single image of the water surface can then be sufficient to measure the pdf because of good spatial averaging – many surface elements contribute to each bin of the pdf.

In a typical RSSG experiment, the instrument is looking down to the water surface from an altitude of 9 m, the footprint on the surface is 1.3 m by 1.1 m and individual speckles are easily resolved. Therefore, temporal averaging is required to measure the pdf. A similar method was already used by Schooley (1954), who took flash photography images with a downward looking camera from a bridge on the Anacostia river.

While the slope measurement is simple in principle, calibration of the system is tedious, all characteristics of the cameras and light sources need to be accounted for. In shipborne experiments, additional difficulties arise from the motion of the ship, especially pitch and roll, which needs to be accounted for.

3.3.2 Measurement of mean square slope

Two methods are used to estimate mean square slope from partial probability distributions. Their applicability depends on the range of slopes for which the pdf is known, the first one was used with the RSSG, the second one with its successor, the medium angle slope gauge (MASG).

Probability of slope zero

Kieffer et al. (2011) derive a relation of mean square slope and the mean gray value in the image. The approximations that are necessary for this are not necessarily valid at all times. Therefore, a simplified approach is chosen here to motivate the measurement principle, it will then be validated experimentally by comparison with reference measurements.

To a first order of approximation, the probability distribution of slope components s_x, s_y is Gaussian and the probability

$$p(s_x, s_y) = \frac{1}{2\pi\sigma_x\sigma_y} e^{-x^2/2\sigma_x^2} e^{-y^2/2\sigma_y^2}. \quad (3.8)$$

The probability for slope zero then becomes

$$p(0, 0) = \frac{1}{2\pi\sigma_x\sigma_y} = \frac{1}{2\pi\sigma_x^2/\epsilon} = \frac{1}{2\pi\sigma_y^2\epsilon}, \quad (3.9)$$

when $\epsilon \equiv \sigma_x/\sigma_y$. With this, the mean square slope is

$$\sigma^2 = \sigma_x^2 + \sigma_y^2 = \epsilon \frac{1}{2\pi p(0, 0)} + \frac{1}{\epsilon} \frac{1}{2\pi p(0, 0)} = \left(\epsilon + \frac{1}{\epsilon}\right) \frac{1}{2\pi p(0, 0)}. \quad (3.10)$$

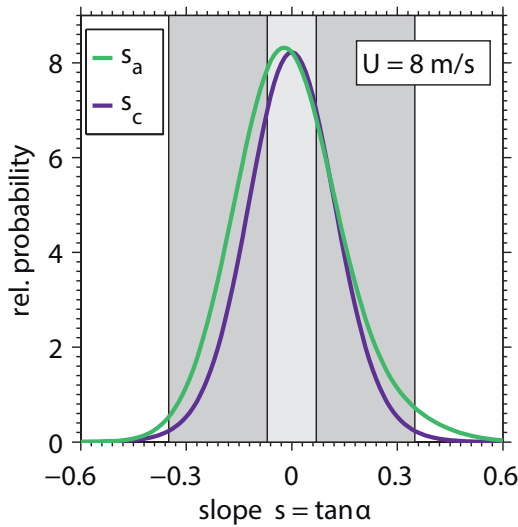


Figure 3.10
The slope pdf for a moderate wind speed of 8 m/s using the parameterization of Cox and Munk (1954a). The crosswind component (s_c) is symmetric around zero, while the alongwind component s_a is slightly skewed. The RSSG can measure slopes in the interval marked by the light gray area, the new MASG can measure slopes in the darker gray area.

The factor $\epsilon + 1/\epsilon$ is experimentally found to be almost constant over a large range of wind speeds in both the laboratory and the field (Kiefhaber 2010). Using the parameterization of Cox and Munk (1954a), a value of slightly larger than 2 is obtained.

Thus, to this approximation, the probability for slope zero is inversely related to mean square slope. On the other hand, the probability for slope zero is also proportional to the mean gray value of the center² of the RSSG image, because of the way the camera and the light source are tilted towards each other (Kiefhaber 2010). This provides a simple way of measuring mean square slope.

Direct measurement of the pdf

The images of the RSSG contain more information than just the probability of slope zero that was used in the previous section. The slope probability distribution is measured in the range given by the opening angle of the camera lens. The lenses used in the RSSG have a focal length of 70 mm. In combination with the camera sensor size of 10.5×8.7 mm this allows the measurement of slopes when the surface is tilted in the range $\alpha = \pm 4^\circ$ (equivalent to slope $s = \tan \alpha = \pm 0.07$). In this small range, only the very peak of the slope distribution is measured. This is demonstrated in Fig. 3.10: The pdf for the alongwind and crosswind slope are shown, using the parameterization given by Cox and Munk (1954a) for a medium wind speed of 8 m/s. From the small range of slopes seen by the RSSG, the standard deviation of the distribution cannot be determined in a robust way.

This is why a third camera with a third light source, named *medium angle slope gauge* (MASG), was added to the setup in 2012 (see sec. 4.1.2). The MASG camera has an 8 mm lens and a sensor size of 5.7×4.3 mm, so it can measure slopes up to $s = \pm 0.35$ ($\pm 20^\circ$). This corresponds to the darker gray area in Fig. 3.10. With

²at target distance, for other distances the position is shifted.

this system, at least at lower wind speeds, a direct estimate of the variance of the distribution can be obtained by fitting a model to the partial pdf.

This is certainly an improvement, although an even larger range would be desirable. Because the distance to the water surface at which the instrument can be mounted is usually not a free parameter in field experiments, the area which needs to be illuminated by the light source increases with the square of the maximum visible slope³. Therefore, for an increased measurement range, very bright light sources are required. At the time of construction of the RSSG in 2009, available high power LEDs were not capable of generating enough brightness for a wide measurement range. Due to the rapid development in this field, today the brightness of LEDs is not a constraint anymore.

3.4 Curvature measurement

The measurement of mean square slope and wave height was the main purpose of the RSSG when it was constructed. In this work, also the opportunities for measuring statistics of curvature are explored. Each reflection gives information on the local surface curvature, through its shape, size, and brightness. Because of the very long light sources (see Fig. 3.6a), the RSSG is not ideally suited for these measurements. Still, as will be shown in sec. 7.2.2, valuable information can be gained from the mean reflection brightness. Here, an overview of different curvature-related characteristics of the reflections in the images is given: The size of reflections (sec. 3.4.2), the brightness of reflections (sec. 3.4.2) and the number of reflections (sec. 3.4.2). The design requirements for an instrument dedicated to the measurement of curvature statistics will be discussed in sec. 8.3.2. With the RSSG, the mean brightness of reflections will be estimated (see sec. 6.4).

3.4.1 Reflections off the curved water surface

The reflections that are visible in Fig. 3.6b, the *speckles*, are generally images of the whole RSSG light source. This is a direct consequence of two features of the water surface: firstly, it is mostly differentiable in a mathematical sense, meaning that the slope is a continuous function without jumps. Secondly, local curvature radii are typically much smaller than the distance from the water surface to the RSSG. The effect of surface curvature can be understood with the help of the sketch in Fig. 3.11a: At every position on the water surface, a reflection is visible if the slope is in the interval $[\theta_0 - \Delta\theta, \theta_0 + \Delta\theta]$ (in Fig. 3.11a, $\theta_0 = 0$). The slope tolerance $\Delta\theta$ is half the solid angle under which the light source is seen when viewed from the water surface. The width of the interval $\Delta\theta$ is dependent on the position on the water surface, but changes much slower than the center slope θ_0 (the slope under which light from the center of the light source is reflected into the camera).

³In small angle approximation. The increase is even bigger for larger angles.

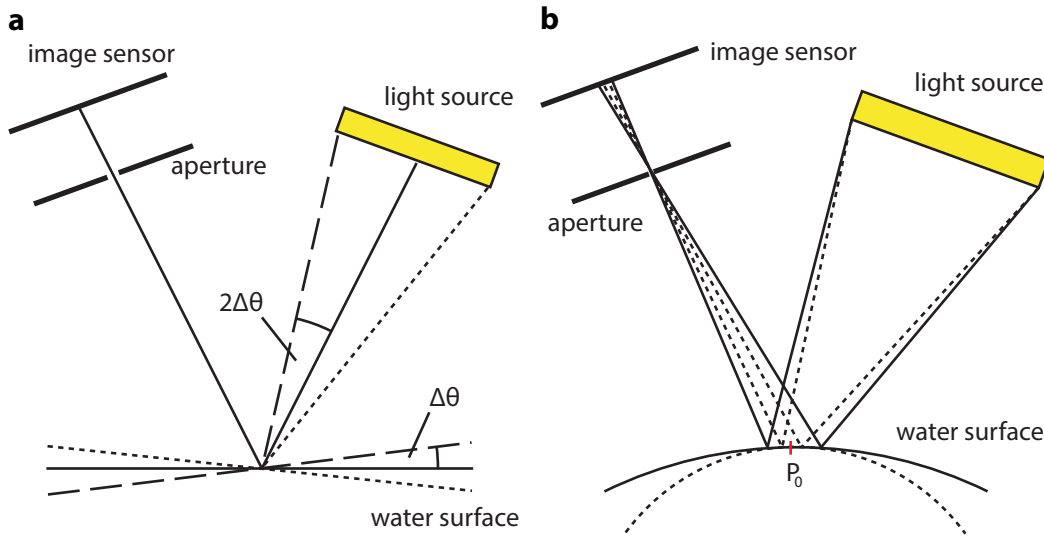


Figure 3.11.: **a** The influence of a finite light source: At each pixel, a reflection is visible for a range of slopes $\pm\Delta\theta$, the width of the interval is half the opening angle of the light source. **b** The influence of curvature: The size of the reflections decreases with R^2 , if R is the radius of surface curvature.

At a curved water surface, neighboring points have different slopes (see Fig. 3.11b). If the curvature radius is finite locally, the surface differentiable, and point P_0 has slope θ_0 , there must be a finite environment around P_0 in which slopes θ are in the interval $[\theta_0 - \Delta\theta, \theta_0 + \Delta\theta]$. Two cases are possible: 1) If the surface is monotonous there will be a closed line (on the 2D surface) on which light is coming from the edge of the light source, this will be the border of the reflection. 2) If an inflection point of surface elevation (an extremum of slope) is reached before condition 1 is fulfilled, two reflections are overlapping and merge into one. For the following development of a measurement technique for curvature it is necessary that case 1 occurs most of the time. This can be guaranteed by using a small, almost point-like light source.

3.4.2 Speckle statistics

Certain average properties of the reflections in the RSSG images can be given to characterize the speckle distribution, which is related to small-scale surface roughness (or surface curvature). Three possible quantities that are presented here are the average size and brightness of reflections, as well as the average number of reflections per image.

The size of speckles

The size of a reflection in the image is proportional to the size of the reflecting patch on the water surface. As can be seen from the sketch in Fig. 3.11b, the size of the patch decreases with decreasing curvature radius. This is because due to the faster change in slope, the maximum slope $\theta_0 \pm \Delta\theta$ is reached faster. The *active area*, the area that reflects on the water is proportional to the curvature radius squared, since $dx dy = R d\theta R d\phi$ and thus

$$A = \int_{\phi_0 \pm \Delta\phi} \int_{\theta_0 \pm \Delta\theta} R d\theta R d\phi = 4R^2 \Delta\theta \Delta\phi, \quad (3.11)$$

where ϕ_0 is the tilt angle of the surface in the y-direction, θ_0 the tilt in the x-direction, and $\Delta\phi$, $\Delta\theta$ are half the angles under which the light source is seen from the water surface. These angles decrease with increasing distance of the light source to the water surface h ; the active area is inversely proportional to h^2 .

In Fig. 3.11 a pinhole camera is assumed. The relation of speckle size and curvature is only correct for an in-focus water surface. If speckles are blurred, it is difficult to estimate the actual size. Also, the properties of the RSSG imaging system distort this simple relationship: The absorption length in the CMOS image sensor of the near infrared light emitted by the LEDs is much longer than for visible light. In crystalline silicon for example, the absorption coefficient is 11100 cm^{-1} for 500 nm light, still 2790 cm^{-1} at 650 nm, but only 156 cm^{-1} at 950 nm (Green 2008). Therefore, the light can go deep into the image sensor and hit neighboring pixels before it is absorbed. This limits the maximum sharpness that can be achieved in the images. Therefore, speckle size is not used as the measure for local surface curvature in RSSG images.

The brightness of speckles

The brightness of speckles in the images is determined by the brightness of the light source and the size of the entrance pupil of the lens, as well as by the distance of the reflecting water surface.

Every pixel integrates over a finite area $p_x \cdot p_y$ on the water surface. If this area fully lies in the active area A as specified in eq. (3.11), the brightness will be independent of curvature if the area of the curved water surface is not significantly larger than its projection on a plane. If the active area is smaller than a single pixel, the brightness will decrease as the size decreases with R^2 . Reflections are smaller than one pixel for curvature radii lower than $R = p/2\Delta\theta = 10.3 \text{ mm}$.⁴ Curvature radii smaller than 10 mm are not at all uncommon on the water surface in the presence of capillary waves which have even smaller wavelengths. For areas with larger curvature radii (but still in the limit of being much smaller than the distance to the instrument), the

⁴With the RSSG camera pixel pitch of 0.008 mm, a focal length of 72 mm and the distance to the water surface of 8000 mm, $p = 0.008/72 \cdot 8000 = 0.9 \text{ mm}$.

speckles should have the same (center) brightness in the image.

The integrated brightness (over the active area) is not affected by the finite pixel size. It increases quadratically with the local curvature radius. Therefore, it provides information on the local surface curvature if individual reflections can be identified. In the RSSG images, due to the length of the light sources, reflections often overlap. A watershed algorithm is used to separate them.

The number of speckles

Longuet-Higgins (1960) studied the effect of surface curvature on the specular reflections visible to an observer. He assumed an isotropic water surface with a Gaussian distribution of elevation, slope, and curvature. The light source is assumed point-like, the observer can see the whole water surface, unlike a camera with a restricted field of view. Under these assumptions, the number of specular reflections N is

$$N \propto \sigma_c^2 \cdot h^2, \quad (3.12)$$

where σ_c^2 is the mean square curvature and h is the height of light source and observer above the water. Thus the number of reflections can be directly linked to the mean square curvature, the integral of the curvature spectrum over all wavenumbers. However, since the RSSG and MASG light sources are not point-like, not all reflections can be separated, especially at higher wind speeds when reflections generally become smaller and their spacing decreases. State-of-the-art high power LEDs with a sufficiently small radiation angle (or optics for focusing on a small area) might be suited for building a quasi-point-like light source.

Since the curvature power spectrum $B(k) = k^4\Psi(k)$, with the height power spectrum $\Psi(k)$, mean square curvature contains information on very short waves (high k). This helps to understand also the composition of mean square slope: If small-scale waves are damped (low mean square curvature), mss is dominated by longer waves, if mean square curvature is high, short waves will also be the major contributor to mss.

4

Setup and calibration

4.1 Instruments

4.1.1 The RSSG

The Reflective Stereo Slope Gauge (RSSG, Fig. 3.6a) was already described in detail by Kiefhaber (2010). Only a brief overview of the most important components is given here.

Cameras

Two *Photonfocus* MV1-1312I-CL-12 CMOS cameras with CameraLink interface are used in the RSSG. The maximum resolution of the cameras is 1312×1082 pixels at a maximum frame rate of 108 fps. After the Marseille 2011 experiment, a frame rate of 50 fps was found to be a good compromise between sampling statistics and data generation. For all the following experiments, the frame rate was fixed at 50 fps.

One of the most important features of the cameras is their enhanced sensitivity in the near infrared (up to 1100 nm) which exceeds that of standard CCD/CMOS cameras. This permits the use of 950 nm LEDs in the light source. Near-infrared light at this wavelength is quickly absorbed in the water, the penetration depth is only 3.4 cm at 950 nm (Kou et al. 1993), due to a water absorption peak at 970 nm. This guarantees that light is only reflected at the water surface and not from below, e.g. off floating particles. In the laboratory, it ensures that the bottom of the water basin is not visible in the images.

Lenses with a focal length of 70 mm are used. The lenses (*Schneider Kreuznach* Tele-Xenar 2.2/70-0902) are broadband optimized for wavelengths up to 1000 nm.

Light sources

The two line-shaped light sources are built from 350 near infrared (940 nm) LEDs each (OSRAM SFH 4545). The LEDs have a standard 5 mm form factor and are aligned in a custom aluminum frame. Light is emitted in a very narrow cone with a half-width of $\pm 5^\circ$ only. At the time the RSSG was built (2009), available LEDs with wider emission cones did not provide sufficient radiant intensity (per solid angle).

The brightness of reflections from the water surface can change dramatically with small-scale roughness, spanning multiple orders of magnitude. Even though the cameras have a nominal resolution of 12 bit, this alone cannot cover the whole dynamic range. Therefore, it is necessary to adapt the brightness of the LED light sources to the surface conditions.

The light source current (and thus brightness) can be set with custom electronics (originally built by Günther Balschbach and Roland Rocholz in summer 2010). The new light source driver became necessary after the commercially available LED driver for industrial applications that was used before (Kiefhaber 2010) failed after a few hours during the deployment of the RSSG to the Baltic Sea in July 2010.

The RSSG LEDs have a DC rating of 100 mA, but can be driven with up to 1 A in pulsed operation. Up to 8 strings of LEDs are connected in parallel to one channel of the LED driver, which has the demanding task of delivering a range of 40 mA to 8 A of current for 200 or 400 μ s.

Inclination sensor

An industrial inclination sensor (*Kübler* Neigungssensor IS40) had been included in the RSSG setup to measure inclination of the instrument during ship-borne experiments. The data sheet did not contain any information about the measurement principle or limitations of the sensor. During processing of the data from the first field experiment and comparing the output of the inclination sensor with that of a full inertial measurement unit, it became clear that the inclination sensor was unable to measure correct angles in dynamic situations. Further data analysis has shown that the sensor in fact measures two-dimensional accelerations and deduces inclination from the assumption that gravity is the only acceleration acting on the sensor. As a result, the sensor was not used for the measurement of inclination, but only as a means to ensure synchronization of the RSSG with the inertial measurement unit (see sec. 6.1.1).

4.1.2 The MASG

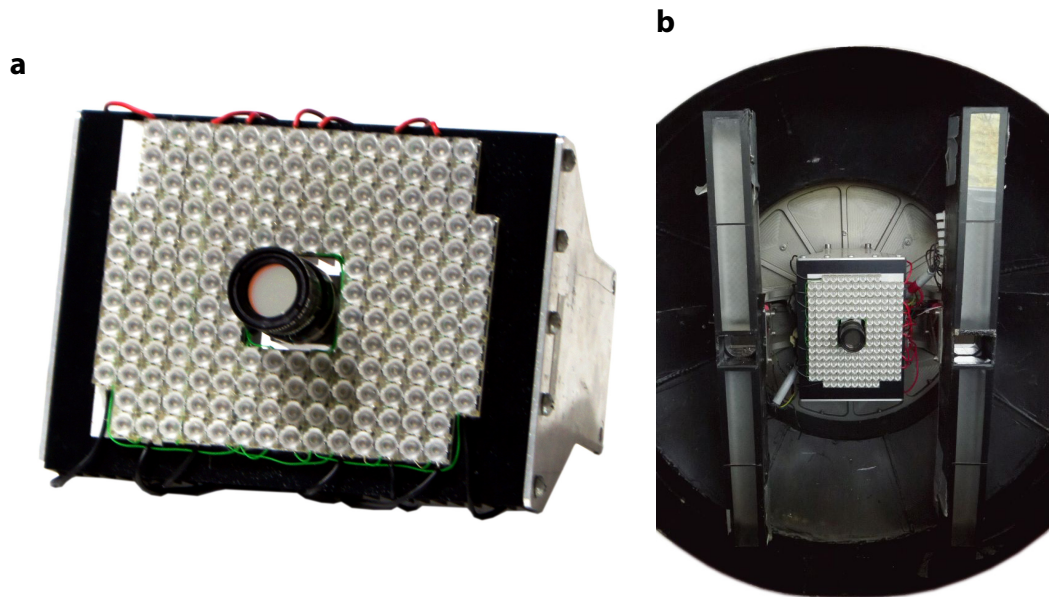


Figure 4.1.: **a** The Medium Angle Slope Gauge (MASG). The camera is mounted at the center of the light source, which is built from 182 high power 850 nm LEDs. The LEDs are glued to an aluminum cooling block (black). The size of the aluminum block is 20×20 cm. **b** The MASG can be mounted in between the two cameras and light sources of the RSSG.

The Medium Angle Slope Gauge is shown in Fig. 4.1a. Unlike the RSSG, it is a very compact and lightweight instrument. In the Marseille 2012 experiment, it was mounted inside the air space of the wind wave facility, separated from the RSSG. In the Meteor experiment, it was mounted in between the two RSSG cameras, as shown in Fig. 4.1b.

Light source

The light source consists of 182 OSRAM SFH 4715S high power near infrared LEDs. According to the manufacturer, the radiant intensity is 440 mW/sr in the forward direction. While this is lower than the value given for the RSSG LEDs (OSRAM SFH 4545: 550 mW/sr), the MASG LEDs have a half angle of $\pm 45^\circ$, while the half angle for the RSSG LEDs is only $\pm 5^\circ$. To increase the light source brightness in the footprint of the MASG camera, lenses (Carclo 10.0 mm Medium Spot Frosted TIR, #10413) were placed on each individual LED. With these lenses, the half angle decreased to about $\pm 25^\circ$ (see sec. 4.2.2).

The 182 LEDs are wired in 7 strings of 26 LEDs each. The light source is powered with a laboratory power supply set to constant current mode. In each of the strings, a high power resistor (5.6Ω , max. 10 W) is wired in series with the LEDs to balance the current distribution onto the parallel strings.

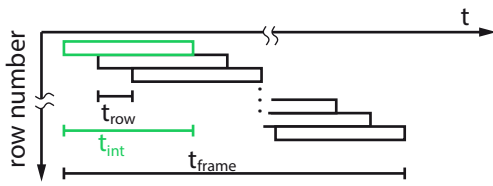


Figure 4.2 Rolling shutter mode of operation: The start of acquisition of each row is delayed by t_{row} relative to the row before. Each row is integrating light during t_{int} , the total duration of the acquisition of an image is t_{frame} .

Camera

A Basler acA2500-14gm gigabit ethernet camera is used in the MASG. Images have a resolution of 2592×1944 pixels and can be acquired at a maximum rate of 14 Hz. In the wavelength band of the LEDs (850 nm), every CCD/CMOS camera has a decent quantum efficiency, so that no specialized camera is required. The GigE link between camera and PC simplifies data acquisition, unlike for CameraLink, no dedicated frame grabber is needed.

The cameras are acquiring images in a *rolling shutter* mode of operation. This means that not all lines of the image are acquired at the same time. This is demonstrated in Fig. 4.2: The acquisition for each row is started individually, the time shift between two rows is $t_{\text{row}} = 35 \mu\text{s}$ (for full resolution of the Basler camera). The total time for image acquisition t_{frame} can be significantly larger than the integration time t_{int} , the time for which every line is collecting photons. For typical operation of the MASG, integration times are on the order of 5 ms, the resulting image acquisition time t_{frame} then is 73 ms.

The light source for the MASG thus needs to be active for 73 ms to illuminate every line of the image. At a frame rate of 10 Hz, this is equivalent to a duty cycle of 73%. Because of this high duty cycle, it was decided that pulsed operation of the light sources is not necessary. The small potential for saving thermal energy (27%) did not justify the additional expenses of buying or designing and building a dedicated LED driver, capable of pulsed operation.

4.2 Calibration

4.2.1 RSSG calibration

Camera calibration

For calibration of the cameras including removal of the very pronounced fixed pattern noise (Fig. 4.3a), a two-point radiometric calibration (flat field correction) was used. A mean dark image was acquired with covered lenses by averaging over many images. With the help of an integrating sphere, flat field images (image of a homogeneously illuminated surface) were acquired and geometric shading and vignetting could be corrected.

Because the lenses were used with fully opened aperture (f-number 2.2) in field experiments, shading played a role towards the image corners. However, the decrease

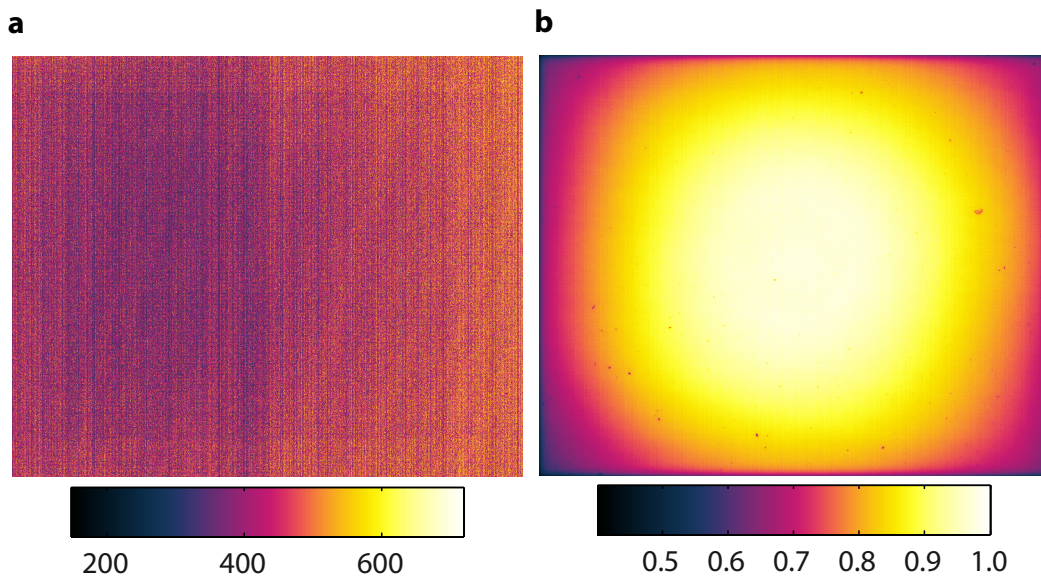


Figure 4.3.: **a** Dark image acquired with the left RSSG camera (displayed in false-color). A pronounced line pattern is visible.

b Flat field image (left camera), acquired with an integrating sphere.

due to shading was exceeded by far by the decrease due to the narrow angular distribution of the light sources.

In the flat field image (Fig. 4.3b), some dust can be seen on the imaging sensor. Before each experiment, the sensor was cleaned carefully with pressurized air. Dust still accumulated over time on the sensor. Most cameras have a near infrared stop filter placed on the sensor, which also separates the charged components from the dusty air. In the RSSG cameras with enhanced IR sensitivity, the sensor is exposed directly to the air and dust particles can easily accumulate on the sensor. This is not expected to have a big influence on the measurements, since most of the decrease of brightness due to dust is removed by the flat field correction.

Global brightness of light sources

Figure 4.4 shows the measured performance of the custom LED driver stage. The relative brightness of the light sources is given in terms of the “brightness setting”. For perfect operation of the LED driver, this setting should be equivalent to mA of current flowing through the LEDs. Clearly, this is not the case. In fact, the brightness does not even increase monotonically with the current settings but decreases slightly at 400 % (right light source) and 550 % (left light source). The reason for this behavior is unclear, but the effect was very reproducible and is not simply an artifact from the brightness measurement itself.

During development of the new imaging slope gauge drivers, which are based on the same principle, I noted that the proper selection of components for this type

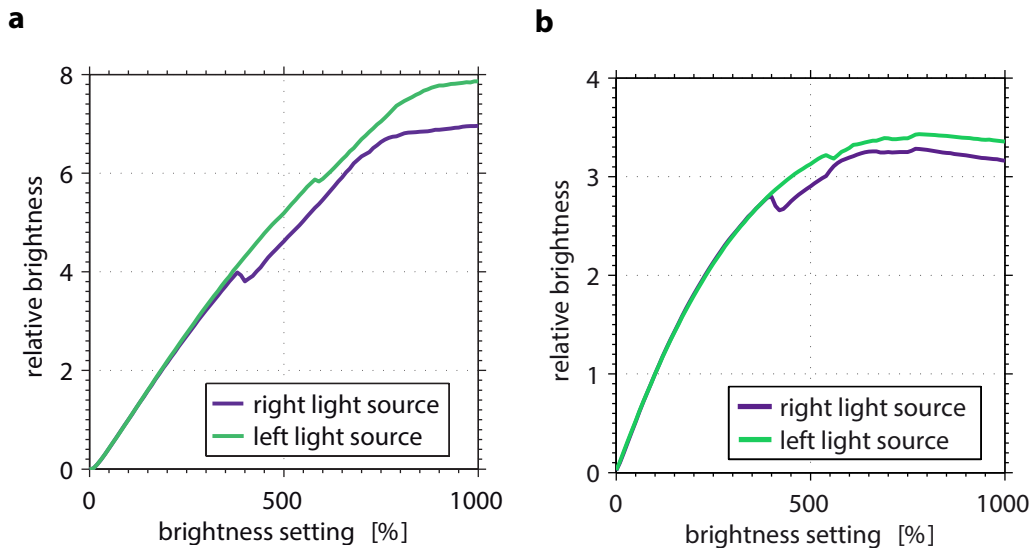


Figure 4.4.: Calibration of the RSSG light source brightness (**a** after the Marseille 2011 experiment, **b** after the Meteor M91 experiment).

of current source is crucial for correct operation. Delivery of a constant current over a wide dynamic range required careful optimization of the used combination of operational amplifiers, MOSFETs¹, and feedback resistors. Even minor changes of PCB² layout and IC package could significantly affect the performance.

While the requirements for the RSSG drivers are less demanding in terms of speed of operation, the fact that the selection of ideal components was not a concern during the development of the driver suggests that the peculiarities of Fig. 4.4 may well be due to a less than ideal circuit.

The significant change between the calibration in 2011 and the calibration in 2012 could be due to the following factors:

- Due to damages caused by a short circuit, several MOSFETs of the driver stage had to be replaced before the experiment in Marseille in September 2012.
- During the Marseille 2012 and Meteor 2012 experiments, a new camera driver was used which facilitated operation of the instrument. However, due to a bug in the code, the integration time of the cameras (and thus pulse length of the LEDs) was 400 μs instead of the earlier 200 μs (which was also used in the measurement of Fig. 4.4a).

The new calibration decreases for higher values. This is an artifact of the calibration procedure that was used: The current was increased from one setting to the next. The light source heated up during calibration and the LEDs got less efficient. Since LED settings were generally below 800 % during the Meteor M91 cruise, this does

¹metal-oxide semiconductor field effect transistor

²printed circuit board

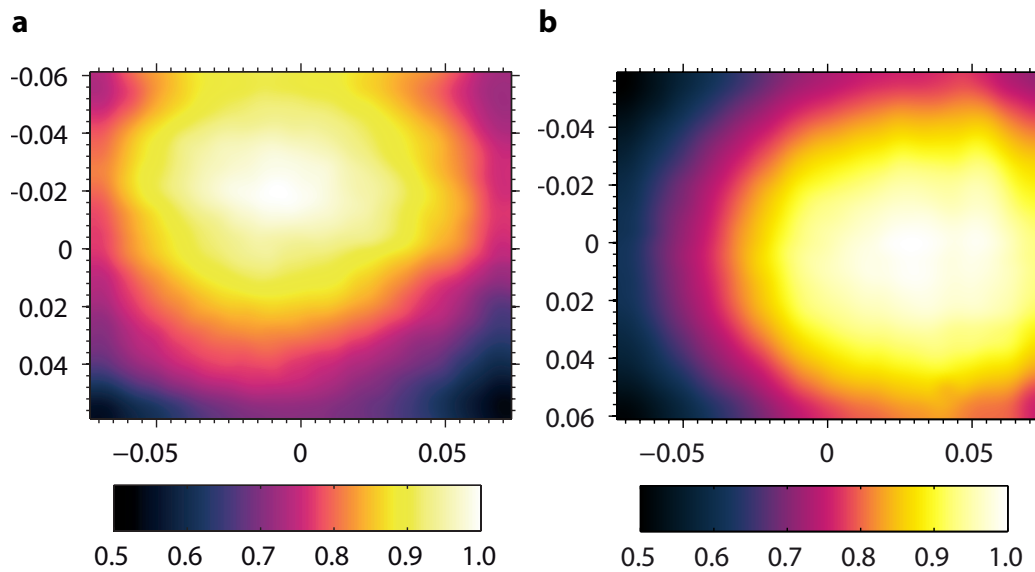


Figure 4.5.: The angular distribution of the emission of the **a** left and **b** right RSSG light sources. Axes are labeled in units of $\tan \alpha_x$ (to the right) and $\tan \alpha_y$ (to the bottom), with the angle to the principal axis α . Distributions are normalized to a maximum of 1 individually.

not effect data processing. Before the next deployment of the RSSG it is advisable to rebuild the LED drivers from scratch, with the knowledge gained in the design of imaging slope gauge drivers.

Angular distribution

The necessity of good knowledge of the angular distribution of the emitted intensity of the light sources is obvious from the general measurement principle: The probability of different slopes is measured from the brightness of reflections in the different parts of the image. Since the light that is reflected from different image parts is also emitted by the light sources under different angles, an error in the angular distribution is directly translated into an error in the measured probability distribution.

The angular distributions of the RSSG light sources in Fig. 4.5 were measured indirectly. A wall was covered in a special paper, the RSSG was placed such that the light sources illuminated the wall, the cameras recorded the reflected brightness. Since the reflected brightness itself depends on the angle, under which the surface is observed, it is necessary to correct for the angular dependence of the reflectance of the surface material.

Reflectances of several candidate materials were measured with a dedicated optical setup. The procedure and results for different materials are described in appendix A.7. The best suited material turned out to be a special kind of paper that is normally used for filtering.

The wall that was covered in this paper was at a distance of 8 m to the instrument

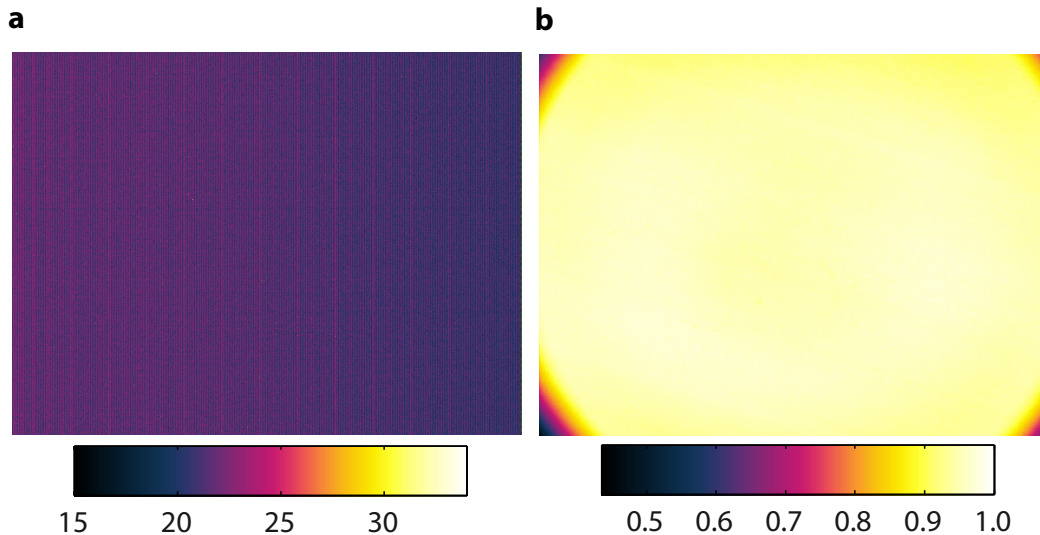


Figure 4.6.: **a** Dark image of the MASG camera. **b** Flat field image of the MASG camera.

to simulate the conditions of the field experiments. Brightness distributions of the reflected light were measured with the RSSG cameras and measurements were corrected for the angular dependence of the paper's reflectance (see Fig. A.5).

For the Marseille experiments, an alternate angular distribution was used. It was measured at a distance of 3.6 m to the reflector. This is equivalent to the distance of the instrument from the water surface at the Marseille wind-wave tank.

The “probability of slope zero” data processing scheme introduced in sec. 3.3.2 is not very sensitive to the exact angular distribution of the light sources, because of the small area in the center of the RSSG images over which intensities are averaged. On the other hand, the rapid decrease of the distributions in Fig. 4.5 towards the image corners is the reason for why the slope range of the instrument could not be extended with the existing light sources. For a wider field of view, a wider radiation angle of the LEDs is required.

4.2.2 MASG

Camera calibration

Compared to the RSSG cameras, fixed pattern noise is notably reduced. In the image corners, significant vignetting is visible in the integrating sphere flat field image (Fig. 4.6a). This is caused by the holder of the interference filter. Since only the very corners are affected, this does not have severe consequences for overall instrument performance. Like for the RSSG, a two-point calibration (flat field correction) is used to homogenize the image.

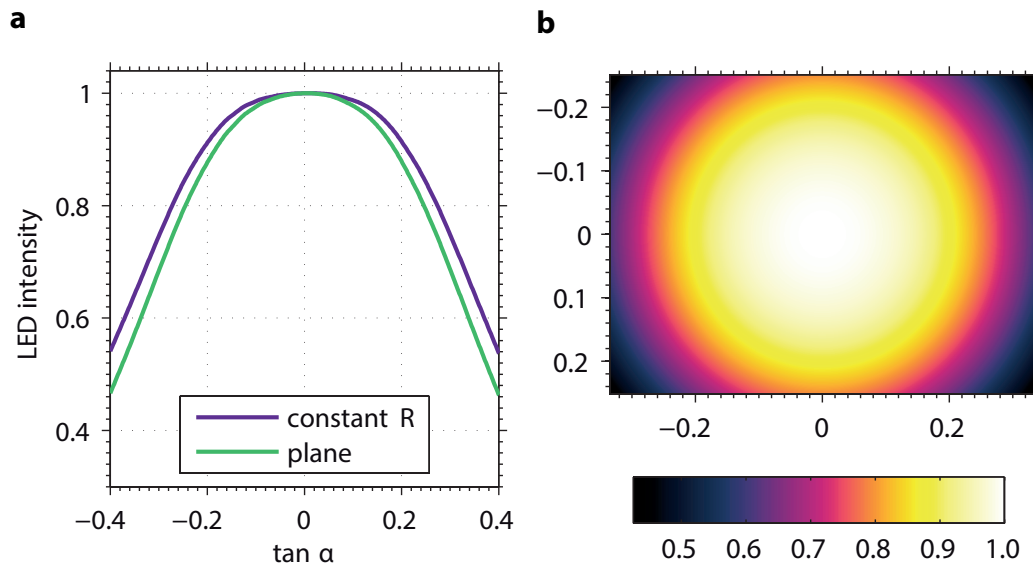


Figure 4.7: **a** The angular distribution of the emission of the MASG light source. The purple curve is for constant distance, the green curve for illumination of a plane ($\cos^2 \alpha$ dependency). **b** Correction matrix for MASG images, axes are given in pixels.

Global brightness

The efficiency of LED light generation is dependent on LED junction temperature. Especially with modern high power LEDs, good thermal management is critical for successful operation. The LEDs in the MASG light source are placed on a large aluminum cooling block. Before deployment to the experiments, the temperature increase of the light source was measured for different LED currents. At a light source current of 2.5 A (equivalent to an LED current of 312 mA), the light source warmed to about 40 °C. Considering the fact that the camera is directly connected to the light source (although with a 5 mm thermal barrier from PTFE), this was decided to be the maximum current during normal operation. During post-experiment calibration, it was noted that even at lower currents, there was a change in light source brightness with time after the light source had been switched on. During the experiments, the light source was switched on right before a measurement and turned off right after. Due to the slow time-constant of the heating of the light source, the brightness did not remain constant during the measurements. However, the angular distribution is not affected by this, so that the only effect is a relative over-representation of the first data records in the statistics of the whole measurement.

Angular distribution

The angular distribution of the MASG light source was measured directly with a setup similar to the one for the reflectance measurements (sec. A.7). The light source was placed on a motorized rotation stage. Images of the light source under different

angles were taken with the MASG camera, placed at a large distance (16 m). The result of this procedure is displayed in Fig. 4.7a as the purple line. An additional correction to the calibration curve is necessary: The images were acquired with a fixed distance from the camera to the light source. However, when the camera is looking at the water surface during measurements, the distance to the water surface is depending on the position in the image. Towards the corners of the image, the distance increases as the angle to the optical axis α increases. The required correction for the distance is $1/\cos \alpha$, for brightness it is $\cos^2 \alpha$, because of the $1/R^2$ dependence of brightness. The corrected calibration curve is shown in green in Fig. 4.7a.

In Fig. 4.7b, the actual correction matrix that is applied to the MASG images is shown. While the center of the image is almost homogeneous, towards the image corners the brightness decreases to 44% of the center value.

5

Experiments

In this thesis, results from five experiments are presented. Two laboratory experiments in Marseille-Luminy were conducted to validate the RSSG/MASG measurement principle with reference measurements in a well-known facility. During two field experiments, the RSSG was part of the instrumentation for air-sea interaction measurements. Most of the other data (all the air-sea flux data) is still being processed by collaborators. Together with the RSSG wave data, it will be possible to study correlations between air-sea exchange and wave field parameters. This correlation was also investigated in a laboratory experiment at the Aeolotron in Heidelberg.

5.1 Laboratory experiments

5.1.1 The Marseille wind-wave facility

The large *Pytheas* air-water interaction facility of the Mediterranean Institute of Oceanography (MIO)¹ in Marseille-Luminy is described in detail by Coantic and Bonmarin (1975). The water tank is 40 m long, 2.6 m wide and about 0.7 m deep. The wind tunnel above the water is 3.2 m wide and 1.5 m high. The facility is closed, the air is recirculated from the end to the beginning in a tube above the tunnel, in which wind is generated by an axial fan. Wind speeds can be set in the range of 0 – 13 m/s. The measurement section with optical access is at a fetch of 27 m, but fetch can be reduced by covering the water surface with bubble wrap. A wave maker controlled by an analogue voltage signal allows to generate plane gravity waves at prescribed frequencies.

¹Former affiliations of the facility are: IRPHE (Institut de Recherche sur les Phénomènes Hors Equilibre); and IMST (Institut de Mécanique Statistique de La Turbulence).

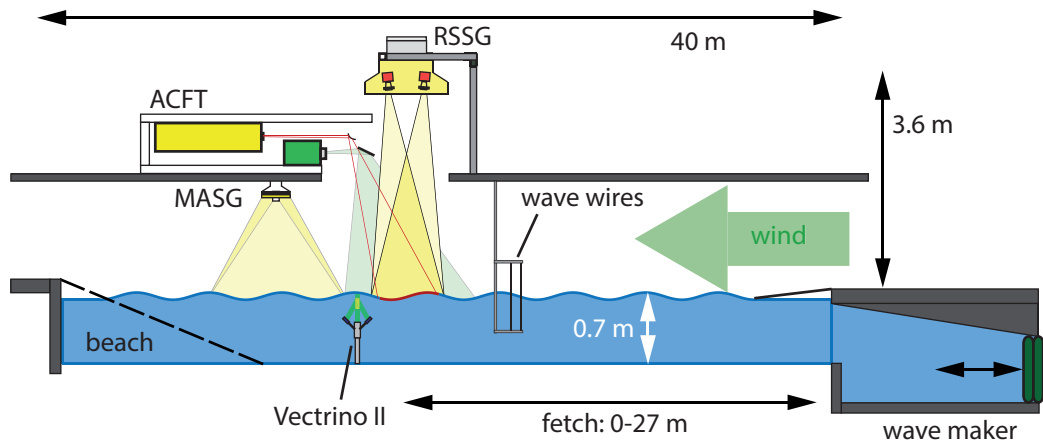


Figure 5.1.: Sketch of the setup at the Marseille wind-wave facility. In the 2011 experiment, only the RSSG and the wave wires were available, in the 2012 experiment, additional instrumentation included the MASG, a Nortek Vectrino II velocity profiler as well as the ACFT.

5.1.2 The Marseille 2011 experiment

Purpose of the one week experiment in March 2011 was to validate the RSSG measurement principle with reference measurements from other instruments. In addition to the RSSG, a set of capacitance type wave wires (operated by our local partner Guillemette Caulliez from MIO) was measuring wave height during the experiment. Also, data from slope measurements with a Laser Slope Gauge (LSG) was made available by Ms. Caulliez to be compared to the RSSG data.

These LSG measurements were not performed simultaneously, but under identical conditions in a prior experiment. Reproducibility of wave conditions was also checked in our experiment, as most measurements were repeated on multiple days.

A compilation of measurement conditions is given in app. A.3, detailed information on the experiment is also provided by Schaper (2011). Measurements were made on three consecutive days. Each day before the start of the experiment, the water surface was cleaned to remove surface active materials. A similar measurement schedule was used on the first two days, starting at 2 m/s wind speed and gradually increasing up to the maximum of the facility, 13 m/s. These measurements were performed mostly to validate the statistical slope measurement under a wide range of conditions. On the last day, the focus was set on validation of the height measurement, recording longer time series for statistical comparison with the wave wire (same wind speeds as before). Additional comparative measurements were performed in which the wave wire was placed into the RSSG image footprint. This allows a direct and synchronized comparison of wave height measurements.

5.1.3 The Marseille 2012 experiment

The two-week experiment in September 2012 was designed as a test for the upcoming field experiment on FS Meteor. Both the RSSG (including the all-new MASG light source and camera) and the Active Controlled Flux Technique (ACFT) instrument (operated by Leila Nagel) were deployed, to measure wave statistics and heat exchange. Figure 5.1 is a sketch of the facility and the deployed instruments, both the RSSG and the ACFT are looking at the same footprint at a fetch of 27 m. Water-sided turbulence was measured with a Nortek Vectrino II profiling velocimeter, in cooperation with Christopher Zappa and Sophia Brumer from Columbia University's Lamont-Doherty Earth Observatory (LDEO) and with an instrument provided free of charge by Nortek. Wind speed was monitored with a pitot tube; point statistics of wave height were also measured with a wave wire (provided by Guillemette Caulliez).

Local heat exchange was measured under different wind speed conditions and at different fetches. At the same time, wave statistics were measured at the same footprint. Therefore, this data set will allow to study the dependence of transfer velocities on fetch in the Marseille wind wave facility, and also the suitability of different parameters of the wave field as parameters in transfer velocity parameterizations. With the help of the Vectrino II profiler, the correlation of wave statistics with near-surface turbulence can be studied. However, the data from both the heat exchange and the turbulence measurements are still to be processed by my collaborators, results are not yet available.

5.1.4 The Aeolotron 2011 experiment

In the Aeolotron 2011 experiment, the transfer velocities of many species with a wide range of solubilities were measured. The experiment was conducted in cooperation with the group of Jonathan Williams of the MPI for Chemistry in Mainz. As additional parameters, the friction velocity and the wave field were measured.

Gas exchange was measured at eight different wind speeds, ranging from $U_{10} = 1.1 - 15$ m/s. The soluble surfactant *Triton X-100* was added to the water on three of the seven measurement days. On one day, 0.6 g were added to the 18.000 l of water, on two days the mass was 3 g.

On the Heidelberg side, gas exchange rates were measured by Krall (2013), friction velocity was measured by Bopp (2011), Kräuter (2011). The experiment is described in detail in the given references. Wave measurements with a Color Imaging Slope Gauge (CISG) (Rocholz 2008) were supervised by Roland Rocholz. Before this study, the wave data had never been properly processed and only preliminary and incomplete sets of mean square slope measurements had been available to Kräuter (2011) and Krall (2013). Thus, the effect of the surfactant on the wave field and the correlation of gas exchange with statistical parameters of the wave field are studied for the first time.

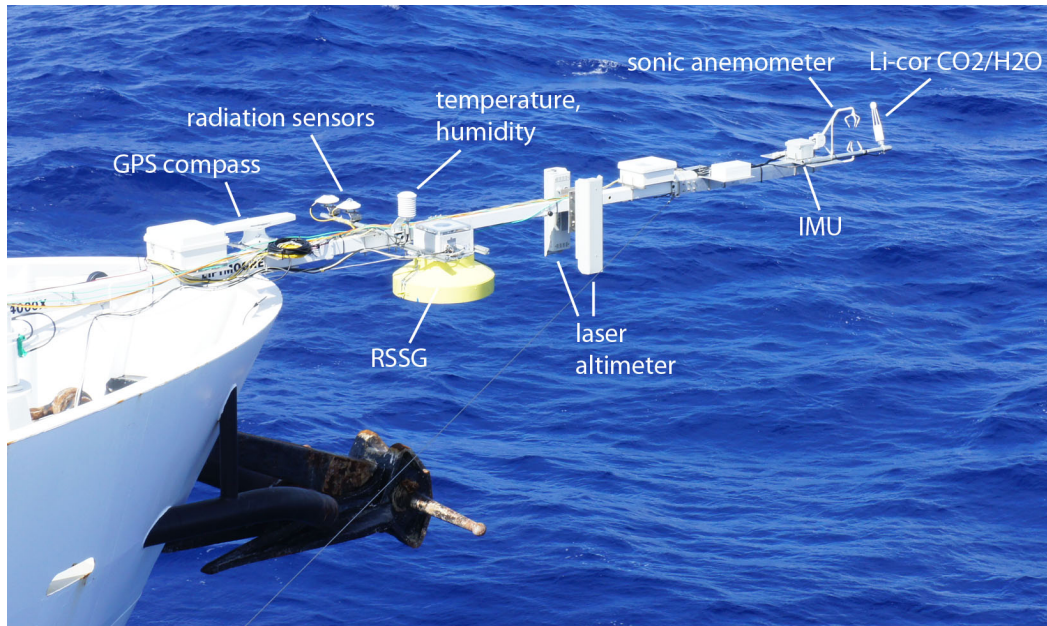


Figure 5.2.: Overview of instrumentation on the boom at the port bow of R/V Kilo Moana. The yellow "hat" is the RSSG, two Riegl laser altimeters are located right next to it, all other instruments are part of the eddy covariance turbulent flux system.

5.2 Field experiments

5.2.1 OSSPRE 2011

In December 2011, the RSSG was deployed to the tropical Pacific on board U.S. R/V Kilo Moana. The 10-day cruise (KM11-30) from Apia, Samoa to Honolulu, Hawaii, USA was part of the Ocean Surface Salinity Profiling Research (OSSPRE) project by William Asher and Andrew Jessup (both Applied Physics Laboratory, University of Washington, Seattle). The project aimed at measuring near-surface salinity and temperature profiles during tropical precipitation events.

The cruise was an add-on to the necessary transit of the Kilo Moana from Samoa to Hawaii and two days of measurement time were available in the course of the cruise. A plot of the cruise track can be found as Fig. A.2 in app. A.4. The main instrument was a surface salinity profiler, a modified wind surfing board with a 2 m keel that was equipped with temperature/salinity probes in depths of 0.2, 0.5, 1.0, and 2.0 m. This surfboard was towed behind the ship (tethered with a three point bridle, to make it fly out to the side, outside of the wake of the ship), towing speed was ca. 4 kn (2 m/s).

In addition, a boom was mounted near the port bow of the SWATH-type (small waterplane area twin hull) Kilo Moana. This boom was equipped with wave and air-sea flux measurement instruments. It was motorized and could be rotated inboard for cleaning and servicing the instrumentation. Instruments included a turbulent

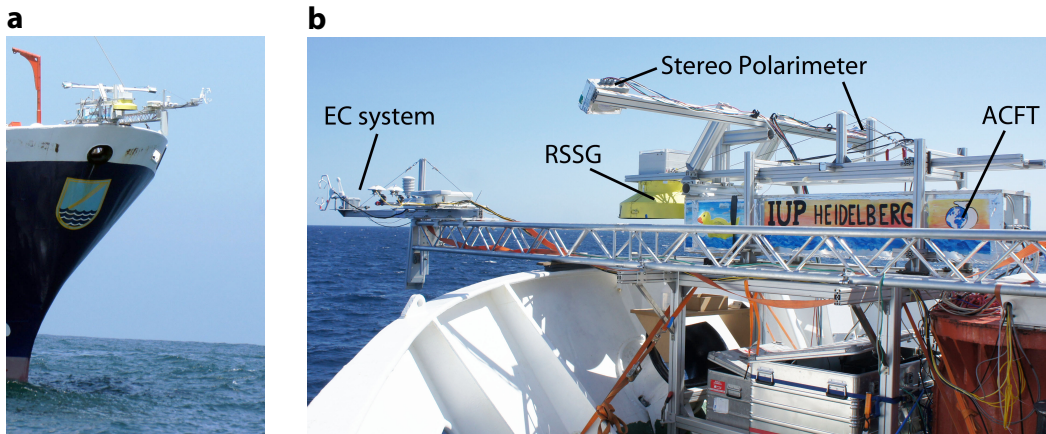


Figure 5.3: **a** The instrumentation at the bow of the Meteor, including the well-visible RSSG and the Stereo Polarimeter, as well as the eddy covariance system and the ACFT. **b** Close-up of the instruments, the eddy covariance system is mounted on a sled going back and forth on the boom in front, the RSSG is mounted on top of the ACFT and can also slide forward to look over the bow.

flux (eddy covariance) measurement system and two Riegl laser altimeters provided by Christopher Zappa from LDEO and the Reflective Stereo Slope Gauge. Figure 5.2 is an overview of the instrumentation of the boom. The RSSG is the yellow "hat", next to it are the two laser altimeters. The other instruments are part of the turbulent flux system. The dual GPS compass provides accurate measurements of position, speed, course, and heading. The pyranometer and pyrgeometer measure long- and shortwave radiation. At the tip of the boom, a Campbell CSAT-3 sonic anemometer measures 3D wind speed, a Li-cor open path CO₂ and H₂O analyzer is used for high speed concentration measurements. Ship motion is recorded by a Crossbow inertial measurement unit (IMU).

A list of measurement times and positions is given in app. A.4.

5.2.2 Peru 2012

A four-week cruise off the coast of Peru in December 2012 was the last major field experiment of the German BMBF SOPRAN (surface ocean in the anthropocene) project and a contribution to the international SOLAS initiative (surface ocean lower atmosphere studies). The cruise (M91) on the German research vessel FS Meteor went on a zig-zag course on and off the continental shelf and in and out of coastal upwelling regions (see also sec. A.5). The science party comprised biologists, chemists and physicists, studying different aspects of atmosphere-ocean interaction. Water samples were taken with a CTD/rosette at 98 stations. During deployment of the rosette, the vessel's position was kept automatically using its 360° bow thruster. This thruster created a lot of turbulence in the water in front of the bow of the ship, so that measurements of heat exchange or wave statistics were not possible.

Measurements were possible during deployment of the micro-structure probe, a free-falling device measuring small-scale turbulence and velocity profiles. In order to prevent the probe from drifting underneath the ship and risking that its tethering line gets caught by the screw, the Meteor was slowly steaming forward. The ship was controlled with the main screw and the rudder, the bow thruster was not used. Since the ship was steaming into the wind, the influence of the ship on the wave field was minimized.

Unfortunately, to being able to maneuver with the rudder, the vessel needed to maintain a minimum velocity of 1 – 2 kn (depending on wind speed) that was higher than desirable for the active controlled flux technique (ACFT), in which a patch of the water surface is heated with a laser. For this patch to come into equilibrium with the forced heat flux, it needs to stay in the footprint of the laser for a while, so high velocities of the ship relative to the water are a problem. This complicates data processing which is still ongoing, transfer velocities have not been obtained yet.

In addition to the RSSG, the newly developed Medium Angle Slope Gauge (MASG) was deployed to the field for the first time. As a third instrument, the experimental *Stereo Polarimeter* was deployed. It combines the measurement principles of polarimetric slope sensing (sec. 3.1.2) and traditional stereopsis (sec. 3.1.3). The processing of the stereo polarimeter data set is not part of this work.

6

Data processing

6.1 Ship motion estimation

Wave measurements from a moving platform (such as a ship, an aircraft, or a drone) are generally affected by the motion of the platform itself. For wave height measurements, the heave (motion along the direction of gravity) of the ship is most important, while for the statistical slope measurements also pitch and roll need to be accounted for. Figure 6.1 gives an overview of the principal rotations and axes of a ship. While the RSSG features an inclination sensor capable of measuring two-dimensional inclination angles, this sensor only works in static conditions. Its measurement is based on the assumption that gravity is the only acting acceleration. The additional accelerations due to ship motion contaminate the measurement. Therefore, this sensor was only used for synchronization with an inertial measurement unit (IMU) capable of tracking ship motion also in dynamic situations.

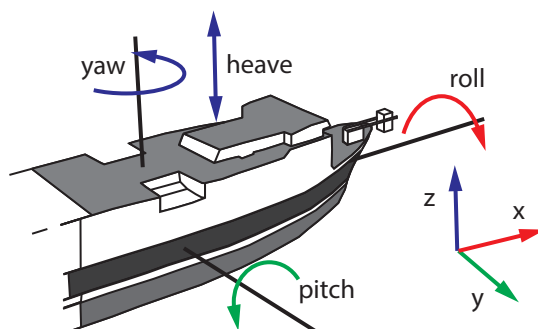


Figure 6.1

The principle axes and rotations of a ship: Roll is positive when the port (left) side is higher than the starboard (right) side, pitch is positive when the bow is up. Yaw is defined here to be consistent with a right-handed coordinate system, in contrast to the historical convention, where clockwise rotation is positive (N → E).

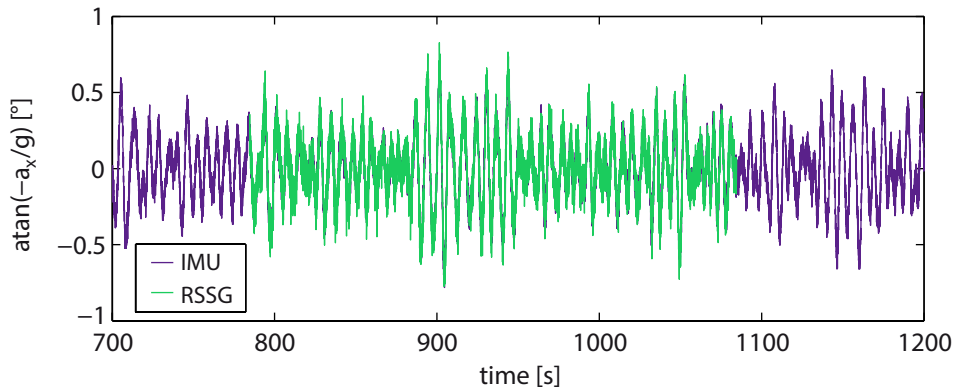


Figure 6.2.: Synchronization of the RSSG and the Crossbow IMU by cross-correlation of “pitch” measurements from the measurement of the direction of gravity (ignoring accelerations due to ship motion itself, which affect both measurements in the same way).

6.1.1 Instrument synchronization

Ship motion was measured with a *Crossbow* VG400 inertial measurement unit (IMU) that was part of Christopher Zappa’s eddy covariance flux system and the data was recorded separately from the RSSG data. The two data sets were synchronized by comparing the output of the IMU with that of a two-axis accelerometer (*Kübler* Neigungssensor IS40) that was included in the RSSG. By computing the cross-correlation of the two signals, a precise synchronization was possible. A typical example showing the excellent agreement of the two independent measurements is shown in Fig. 6.2. The purple line (Crossbow measurement) is fully hidden underneath the green line (RSSG measurement).

6.1.2 Complementary filtering

Different sensors are used for the measurement of platform motion. Their raw outputs need to be filtered and processed to obtain the target quantities roll, pitch, and heave. The Crossbow IMU measures three linear accelerations (accelerometer), as well as three angular rates (gyroscope). The Hemisphere dual GPS unit measures position, velocities and heading of the ship.

In the IMU data processing implementation, the process described by Edson et al. (1998) and Miller et al. (2008) is mostly followed. Motion data processing is described in detail in their publications.

The underlying idea for the fusion of the different measurements is that some sensors are well suited to measure fast changes, while others are long-term stable, thus providing good mean values and slow trends. This applies to the measurement of rotations as well as to velocities. The orientation of the IMU with respect to the direction of gravity can be measured with the accelerometer in static conditions. In

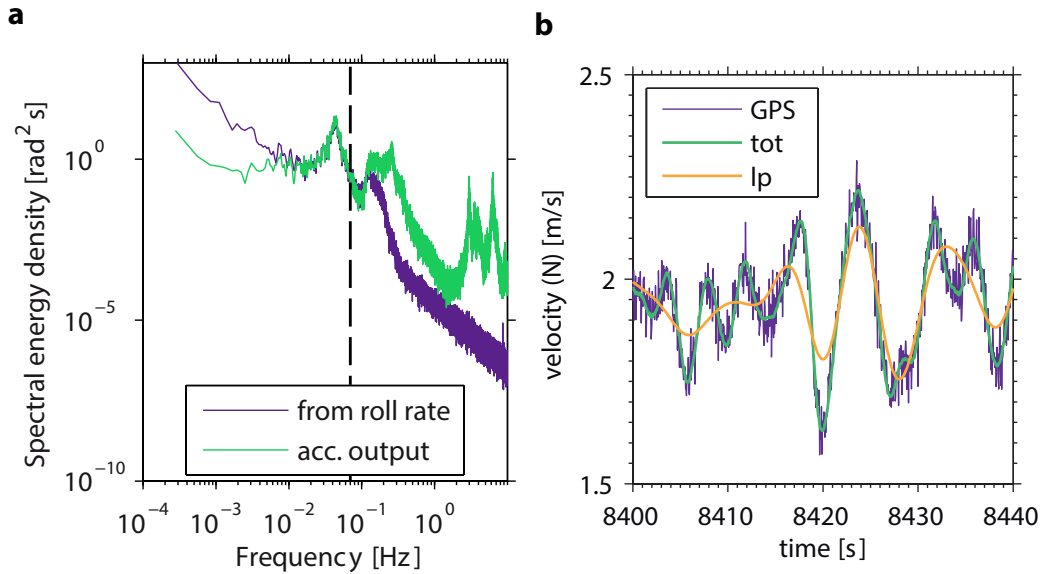


Figure 6.3.: **a** Comparison of roll angle power spectra determined from accelerometer output and roll rate. The chosen cutoff frequency for complementary filtering is set to 0.07 Hz, the black line.
b Raw GPS velocity (purple), low pass filtered GPS velocity (orange), fused velocity (green).

the absence of other accelerations, it detects the direction of gravity. Accelerations are forced onto the ship by waves. Their frequency depends on the wave spectrum. Therefore, with the accelerometer it is possible to measure low frequency changes of the ship's orientation. On the other hand, angles can be measured by integration of angular rates from the gyroscope. Since the MEMS¹ gyroscopes used in the Crossbow IMU and the integration itself are prone to zero-drifts, the integrated angular rates are not reliable on longer time scales. Thus, they are only used to measure high frequency changes in the ship's orientation. Low frequency and high frequency components are fused by complementary filtering: Both components are filtered with a fourth-order Butterworth filter² (Oppenheim et al. 1999; pp. 824). To avoid phase shifts, the filter is applied forward and backward³ (Miller et al. 2008).

The cutoff frequencies that are used for the low and high pass filters are given in Tab. 6.1.

The cutoff frequencies can be determined from power spectra of the components to be fused: Figure 6.3a shows the spectral energy density for the roll angle from both the accelerometer output and the integrated roll rate. The cutoff (black line) is set to 0.07 Hz, in the interval where both spectra coincide. At low and high frequencies, the $1/f^2$ slope from integration of the roll rate is clearly visible. The peaks measured

¹MEMS = microelectromechanical system

²Matlab® function butter.

³Matlab® function filtfilt.

Table 6.1.: Cutoff frequencies used in complimentary filtering.

quantity	frequency[Hz]	low frequency component	high frequency component
roll	0.07	accelerometer (IMU)	gyroscope (IMU)
pitch	0.07	accelerometer (IMU)	gyroscope (IMU)
yaw	0.15	heading (GPS)	gyroscope (IMU)
v_x	0.15	speed/course (GPS)	accelerometer (IMU)
v_y	0.15	speed/course (GPS)	accelerometer (IMU)
v_z	0.10	—	accelerometer (IMU)

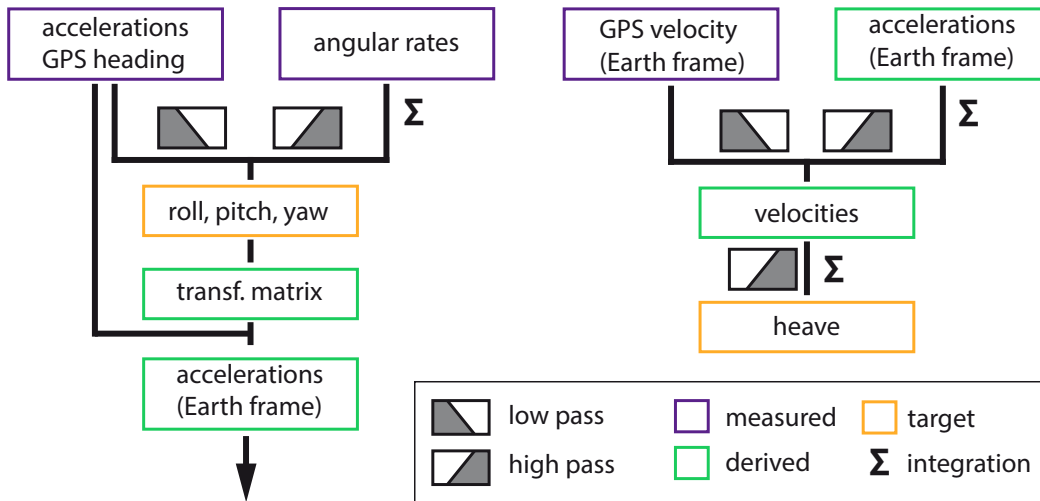


Figure 6.4.: Workflow for the processing of the ship motion data.

by the accelerometer at frequencies above 1 Hz are due to vibrations of the boom to which the instrument was mounted (see Fig. 5.2).

Figure 6.3b shows a short sequence of the velocity component in the y-direction (North). The raw GPS velocity is noisy (purple), the low pass filtered velocity (orange) removes the noise, but also part of the periodic structure. After adding the high pass filtered integrated accelerations, the curve (green) is close to the GPS velocity again. The fact that the periodic structure that was removed from the GPS signal by filtering reappears after adding the high pass filtered portion is a nice demonstration that the complementary filtering works.

The full workflow for the motion data processing is shown in Fig. 6.4. In the first step, measurements of the direction of gravity (accelerometer) and the GPS heading angle are fused with integrated angular rates by complementary filtering, yielding the roll, pitch, and yaw angles. The (time-dependent) coordinate transformation matrix from the strapdown IMU frame to the Earth frame is computed (Edson et al. 1998), and the accelerations are transformed into the Earth frame.

In the second filtering step, the GPS velocities are fused with the accelerations to obtain velocities. The z-component of velocity is then high pass filtered to remove trends and integrated to get the heave.

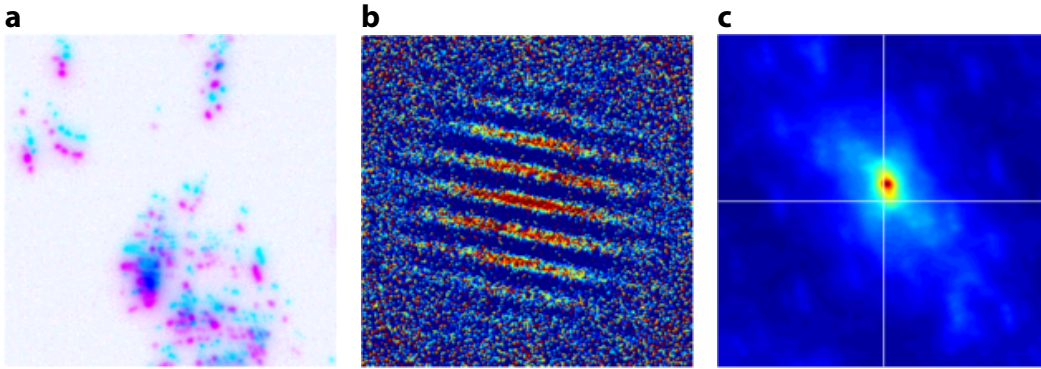


Figure 6.5.: **a** A typical portion from an RSSG stereo image, the left camera is displayed in red, the right camera in cyan and images are inverted so that white areas are dark background in the original monochrome images.
b The global phase factor in the Fourier domain.
c The resulting cross-correlation map after back-transformation.

6.2 Wave height

6.2.1 Disparity estimation

Disparity from cross-correlation

In sec. 3.2.1, eq. (3.4) related the disparity in the stereo image, i.e. the difference in object position in the two images, to the distance from the water surface. In sec. 3.1.4 it was shown how to obtain stereo images with nearly identical reflections from the specular water surface by using a Helmholtz stereopsis setup with two light sources.

Finding corresponding reflections can then effectively be done by computing the cross-correlation of two interrogation windows. The disparity can only be estimated when reflections are visible in the interrogation window. Thus, as was already noted in sec. 3.1.4, it is nearly impossible to recover the full 2D surface displacement. If the window size is sufficiently large (a size of 200×200 pixels turned out to be a reasonable value both in the lab and in the field) and the disparity is relatively small, it is effective to compute the cross-correlation in the frequency domain.

The basic idea behind this is that the Fourier transform of two images G_1 and G_2 , of which one is a shifted version of the other, is identical, except for a global phase factor (see e.g. Kiefhaber 2010),

$$\hat{C} = \hat{G}_2(\mathbf{k})\hat{G}_2^*(\mathbf{k}) = \exp(-2\pi i \mathbf{k} \cdot \Delta\mathbf{x}) |\hat{G}_1(\mathbf{k})|^2. \quad (6.1)$$

The cross-correlation is obtained by applying the inverse Fourier transform to this expression, which then has a peak at $\Delta\mathbf{x}$, the global disparity of the two images. In Fig. 6.5a, a typical 200×200 pixel portion of an RSSG stereo image is shown. The image is inverted so that parts that were originally dark background now appear white.

The left image is shown in blue, the right image in red. The product of the Fourier transforms of the two images as presented in eq. (6.1) is shown in Fig. 6.5b. Note that only the real part of the complex spectrum is displayed and that the left hand side of eq. (6.1) was normalized by the auto-covariance of g_1 for better visibility. The resulting cross-correlation map can be seen in Fig. 6.5c, the coordinate system is shifted, the white lines mark the location of the “DC” component at (spatial) frequency (0,0). Here, the LHS of eq. (6.1) was not normalized before back transformation. This is the reason for the relatively broad peak. Normalization leads to a very sharp peak, but was found to decrease the overall accuracy of the algorithm.

Matrix multiplication-based discrete Fourier transform

In a perfect setup, the reflections in the stereo images would only be shifted along the direction of the stereo baseline. While due to camera misalignments there is usually a small shift in the direction orthogonal to the baseline (the x-direction), the shift is constant throughout each experiment. Therefore, it is not necessary to compute the full 2D cross correlation shown in Fig. 6.5c. Knowledge of a narrow strip that is only a few columns wide is sufficient.

Since the number of columns that are required is much smaller than the width of the cross-correlation window, it is faster to compute the cross-correlation by matrix multiplication than using standard fast Fourier transform (FFT) algorithms that always reproduce the full 2D image in Fig. 6.5c. The inverse 2D discrete Fourier transform (DFT) is given by

$$C = \mathbf{W}_N \hat{C} \mathbf{W}_N, \quad (6.2)$$

where

$$\mathbf{W}_N = \left(w_N^{j \cdot k} \right)_{(j,k) \in \{0, N-1\}} = \begin{bmatrix} w_N^{0 \cdot 0} & \dots & w_N^{0 \cdot k} & \dots & w_N^{0 \cdot (N-1)} \\ \vdots & & \vdots & & \vdots \\ w_N^{j \cdot 0} & \dots & w_N^{j \cdot k} & \dots & w_N^{j \cdot (N-1)} \\ \vdots & & \vdots & & \vdots \\ w_N^{(N-1) \cdot 0} & \dots & w_N^{(N-1) \cdot k} & \dots & w_N^{(N-1) \cdot (N-1)} \end{bmatrix} \quad (6.3)$$

are $N \times N$ matrices with entries

$$w_N^{j \cdot k} = \frac{1}{\sqrt{N}} \exp(2\pi i(j \cdot k)/N). \quad (6.4)$$

Due to the rules of matrix multiplication, every column of the right hand \mathbf{W}_N in eq. (6.2) corresponds to the same column of the cross-correlation C . By cutting the right hand \mathbf{W}_N , the desired portion of C can be computed. To get the shifted cross-correlation displayed in Fig. 6.5c, it is necessary to swap the left and right half of the \mathbf{W}_N matrix that is multiplied from the right, as well as the upper and lower half of the \mathbf{W}_N matrix that is multiplied from the left.

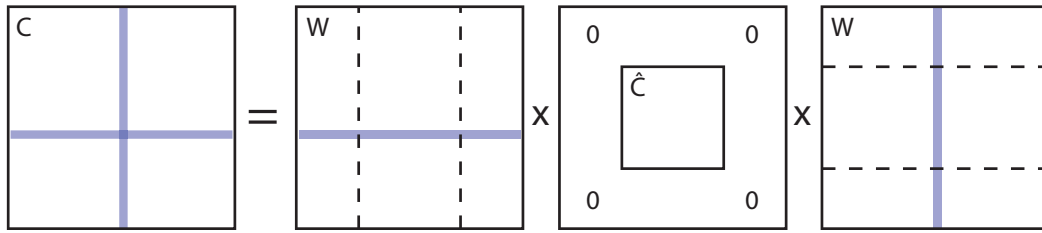


Figure 6.6.: Graphical representation of the principle of accelerated upscaling by discrete Fourier transform. The squares represent the matrices in eq. (6.2), for a detailed description see text.

Subpixel accuracy

The standard approach to find the maximum of the cross-correlation with subpixel precision is to zero-pad its Fourier transform before back transformation by FFT. This is sketched in Fig. 6.6: The Fourier transform of the cross-correlation (\hat{C}) is embedded in a larger array of zeros. The DFT matrices $\mathbf{W}_{N'}$ are computed for the larger array with dimension $N' \times N'$. The result is an interpolated cross-correlation matrix C with a higher resolution and size $N' \times N'$. If high accuracy for the disparity estimation is desired (e.g. 0.1 pixel or less) this quickly becomes a time and memory consuming process, as the size of the matrices scales with the square of the upsampling factor (e.g. 10×10 , if disparity accuracy of 0.1 pixel is desired).

As an alternative, the discrete Fourier transform using matrix multiplication can be used again: If the position of the maximum of the cross-correlation is already known with pixel precision, it is sufficient to compute an upsampled version of the cross-correlation in a small neighborhood around the peak. This approach is described by Guizar-Sicairos et al. (2008) for image registration.

The procedure is indicated by the purple shaded areas in Fig. 6.6. The right hand $\mathbf{W}_{N'}$ can be reduced to a few columns, the left hand $\mathbf{W}_{N'}$ to a few rows, each centered around the known approximate location of the maximum of cross-correlation. Only the square where the shaded areas intersect on the left hand side in C is computed then. Additional computational expenses can be saved by cutting the $\mathbf{W}_{N'}$ as shown by the dashed lines. After multiplying the right hand $\mathbf{W}_{N'}$ with \hat{C} , the areas above and below the dashed lines are zero, by the rules of matrix multiplication. Therefore, they do not need to be computed in the first place. A similar argument holds for the second multiplication.

In the original workflow described by Guizar-Sicairos et al. (2008), the cross-correlation is first upsampled by a factor of 2 using zero-padding and FFT. On this upsampled grid, the position of the maximum is located, the estimate is then refined to the desired accuracy using the matrix multiplication DFT.

For RSSG images, it turned out to be sufficient to determine the peak of the cross correlation in the original image resolution; an initial upsampling did not improve disparity estimation. The region around the peak was then upsampled by a factor of 10 using the matrix multiplication scheme.

6.2.2 Motion correction

The distance to the water surface d , obtained from the disparity and eq. (3.4), needs to be converted to wave height h by correcting for heave, pitch, and roll:

$$h = -(d \cos \theta \cos \phi - H), \quad (6.5)$$

where θ is the roll angle, ϕ the pitch angle, and H the heave. Heave has the largest effect on the measured wave height. Even at a roll of 10° , which rarely ever occurred in the field experiments, the correction is only 1.5%. At a mean distance of 8 m, this is equivalent to 12 cm, while heave can easily exceed 1 m.

An effect that cannot easily be corrected is the changing location of the measurement field on the water surface⁴. As the ship rolls from one side to the other, the footprint is scanned over different parts of the water surface. For the measurement of the targeted large scale waves, this should not have significant consequences.

6.2.3 Implementation

The full workflow of the height processing routines is shown in Fig. 6.7. An area of interest (AOI) is selected. The chosen size of the window is a compromise between the resolution of the measurement and the amount of dropout that can be tolerated. Smaller AOIs lead to a higher number of frames in which there are no reflections in the window in at least one of the images. On the other hand, for larger AOIs, the distance to the water surface is averaged over a larger area on the water surface; waves with wavelengths smaller than the AOI size cannot be resolved.

Two standard AOI window sizes are used: 200×200 pixels and 800×800 pixels. Reflections are detected with a simple gray value threshold. Images without reflections are not processed, the disparity is set to NaN. For the other images, the disparity is determined with pixel precision as described in sec. 6.2.1.

After all images have been processed, outliers are removed from the disparity vector for the 300 images and missing data points are interpolated. The process of disparity estimation is repeated, the result from the first pass is fed into the loop as an *a priori* shift applied to the right AOI (so that the expected disparity is 0).

In the second pass, the disparity is determined with subpixel precision (the maximum of the cross correlation is determined on a grid with 10 times the resolution of the image). After the second pass, data gaps are filled and the distance to the water surface is computed (see eq. (3.4)). The distance is needed for calibration of the slope and curvature measurements. To obtain the actual wave height, the motion correction as described in sec. 6.2.2 is applied.

⁴If the field of view of the camera is much larger than the amplitude of pitch and roll, the position of the interrogation window can be adapted to correct for ship motion.

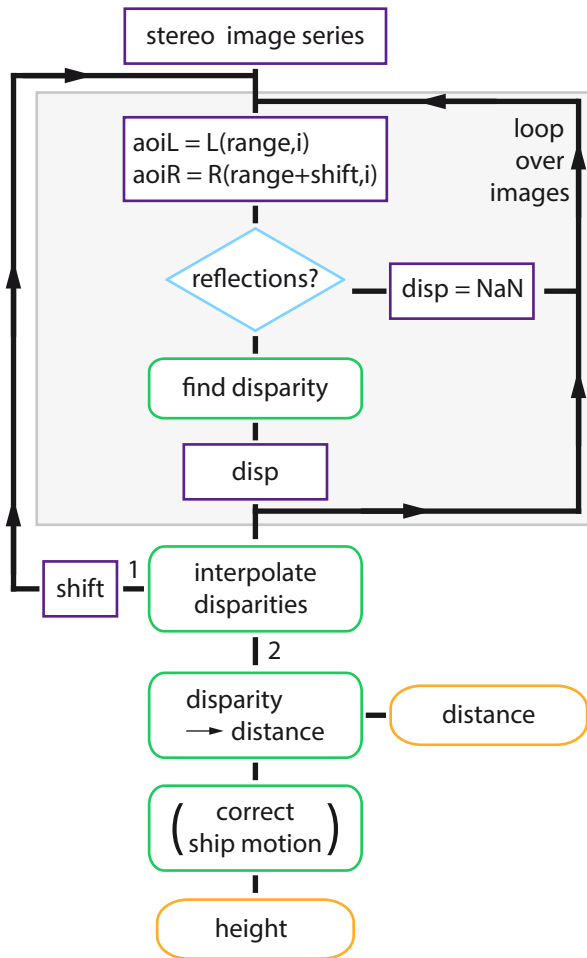


Figure 6.7
Workflow for height processing.

6.3 Wave slope

6.3.1 Averaging speckle images

For the Marseille laboratory experiments, averaging the speckle images is simple: The distance to the water surface is much larger than the maximum wave amplitude; and the footprint of the instrument remains in a fixed location. Because there are no time-dependent effects, all calibration procedures can be applied after the individual speckle images are averaged. Corrections are then only necessary because of the non-ideal characteristics of the cameras and the light sources.

The situation is more complex for the shipborne experiments: The ship is pitching and rolling, so that the assignment of slope to pixel position in the image (see sec. 3.3.1) becomes time-dependent. In addition, due to swell, large wind waves, and the ship's heave, the assumption of small relative changes in distance of the instrument to the water is no longer valid. These two factors require that the speckle images are corrected on an image-by-image basis *before* averaging.

MASG corrections

Due to the simpler geometry of the medium angle slope gauge (MASG) – an almost point-like light source virtually in the same position as the camera – calibration of the MASG images is less complex than that of the RSSG images.

Since the light source can be treated as a point source at the same position as the camera's (pinhole) aperture, it follows that light that is reflected into the camera under an angle α to the optical axis must have been emitted by the light source under the same angle α . The light is then projected onto the pixel at location $f \tan \alpha$. Because the assignment of LED emission angle to pixel position is independent of the distance of the reflecting surface – or of any motion of the ship – a universal light source calibration matrix can be computed. The decreasing LED emission to angles further away from the principle axis can then be corrected by dividing each MASG image by a calibration image, see sec. 4.2.2. This calibration could even be performed on-line, during the measurement.

The compensation for pitch and roll of the ship, as well as for the changing distance to the water surface is time-dependent. The change in distance affects the gray values of the reflections according to a $1/R^2$ law (cf. sec. 3.4.2); synchronized distance measurements from the RSSG can be used to correct for this.

The effect of pitch and roll can be understood with the help of Fig. 6.8: If the instrument is tilted by an angle ρ , the footprint on the water surface is shifted and distorted. The reflection condition is shifted; light is reflected into the center of the image when surface slope is $\tan \rho$. For an arbitrary pixel at position $f \tan \alpha$ on the sensor, the surface tilt now needs to be $\tan(\alpha + \rho)$ instead of $\tan \alpha$. Due to the non-linearity of the tangent, a non-linear transformation is generally needed to transform the camera pixel grid onto a surface slope grid. Because this is very costly

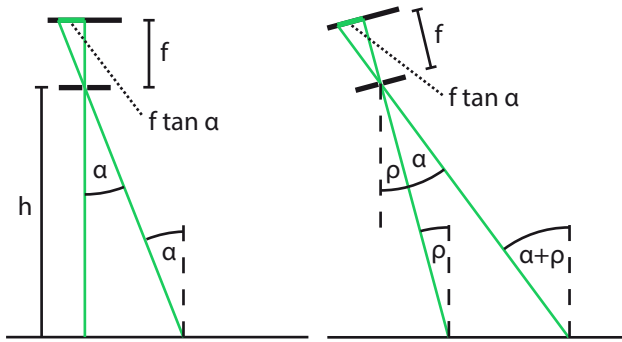


Figure 6.8
The effect of roll ρ on the slope distribution in the MASG images.

in terms of required processing time, a simplified solution is desired: If

$$\tan(\alpha + \rho) \approx \tan(\alpha) + \rho, \quad (6.6)$$

the transformation from the pixel grid to the slope grid is a mere translation, pitch and roll only add a constant offset to the measured slopes.

For a typical measurement⁵ at 8 m/s wind and the influence of swell, the RMS roll $\rho_{\text{rms}} = 0.021$ rad, and the maximum $\rho_{\text{max}} = 0.058$ rad. The maximum error of eq. (6.6) can then be estimated using $\alpha_{\text{max}} = 0.35$ rad (see sec. 3.3.2):

$$\tan(\alpha_{\text{max}} + \rho_{\text{max}}) = 0.4323, \quad \tan(\alpha_{\text{max}}) + \rho_{\text{max}} = 0.4230, \quad (6.7)$$

resulting in a maximum underestimation of the surface slope of 2.1%. For the RMS roll, the underestimation is only 0.8%. An error of this order of magnitude can certainly be tolerated. Therefore, the effect of pitch and roll on measured slope probability distributions can be approximated by a translation in gradient space. This procedure is shown in Fig. 6.9. An individual speckle image (shown on the left in false-color, background is shown as white) is added onto a larger slope grid (right). The offset of the position of the image in the grid is given by the measured pitch and roll angles.

RSSG corrections

The geometry of the RSSG is more complex than that of the MASG. Since the left camera does not observe light from the left, but from the right light source, the assumption of identical locations for camera and light source is not valid any more. Therefore, a distance-dependent calibration for the LED emission angle is necessary. Also the assignment of slope to pixel position is dependent on the distance to the water surface.

Figure 6.10a illustrates the dependence of the emission angle on the distance of the reflecting surface: At the stereo reference distance $h_0 = b/(2 \tan \alpha)$ (with the tilt of the camera α and the stereo baseline b), light that is reflected into the center

⁵Meteor M91; measurement 51, Run 736, 2012/12/23.

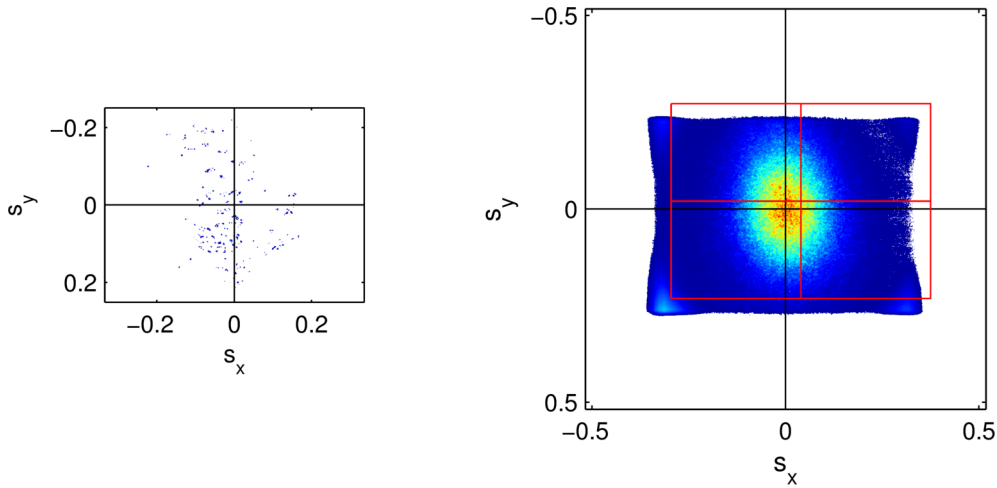


Figure 6.9.: A single speckle image (left, background removed) is added onto a larger slope grid (right). Pitch and roll of the ship are accounted for with a translation in the new grid (red frame).

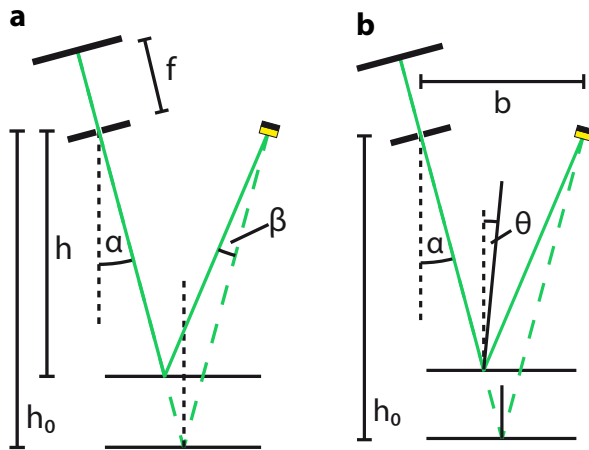


Figure 6.10
a At the stereo reference distance h_0 , light that is reflected into the camera along the optical axis is emitted in the direction of the principal axis of the light source. At a distance $h \neq h_0$, the light is emitted under the angle β to the principal axis.
b At distance $h_0 = b/2 \tan \alpha$, slope zero is assigned to the center of the image. At distances $h \neq h_0$, the assignment changes, reflections are visible if the water surface has slope θ .

of the image (along the optical axis of the lens) is emitted in the forward direction by the light source. The angle to the light source's principal axis is zero. When the reflecting surface is located at any other distance $h \neq h_0$, light is emitted under a non-zero angle β to the principal axis.

A similar effect occurs for the slope that is assigned to the center of the image: By definition, this slope is zero at the reference distance. At any distance $d \neq d_0$, reflections are visible if the reflecting surface has slope θ (see Fig. 6.10b).

The RSSG's cameras are equipped with 70 mm lenses, the field of view is only $8.4^\circ \times 6.9^\circ$ so that the maximum angle under which light enters the camera is 4.2° to the optical axis. This allows to apply small-angle approximation without significant errors.

The accumulation of the probability distribution from calibrated speckle images is then similar to the procedure described for the MASG. In addition to the offset

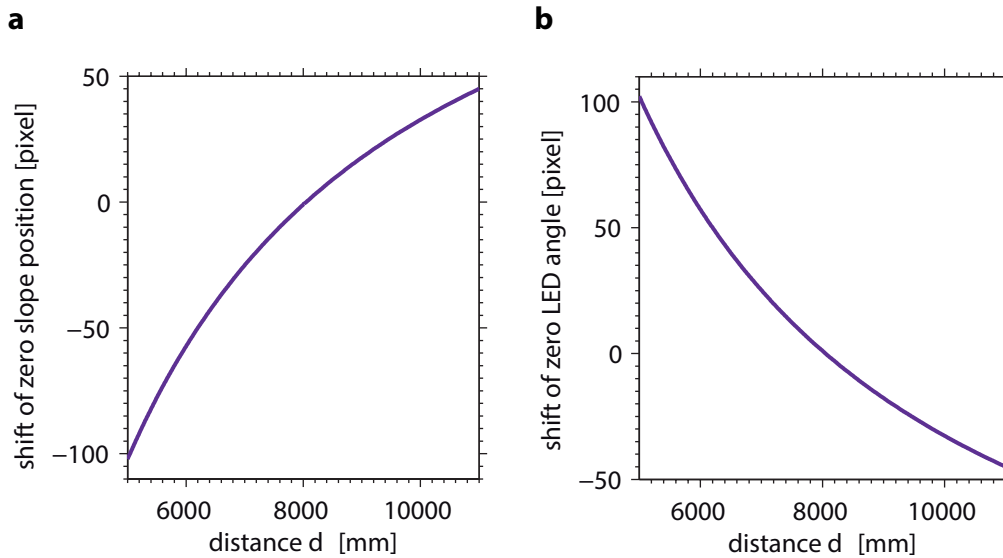


Figure 6.11: **a** A changing distance to the water surface shifts the position of slope zero in the image along the coordinate direction parallel to the baseline.
b The opposite shift needs to be applied in the LED calibration image.

due to the ship's pitch and roll, an additional offset is added to account for the distance-dependence of the slope-pixel position assignment.

Figure 6.11a shows the shift of the position of slope zero in the speckle images as a function of distance to the water surface. At the stereo reference distance $h_0 = 8.05$ m (value for the Meteor M91 experiment), the shift is zero, meaning that slope zero is in the center of the image. At a distance $h = 6.0$ m, the position is shifted by about 70 pixels. The same shift (opposite sign) applies to the LED correction image (see sec. 4.2.1), as shown in Fig. 6.11b.

Workflow

Figure 6.12 is a quick summary of the complete workflow for averaging RSSG/MASG images to obtain a slope pdf. First, a two-point radiometric calibration (Jähne 2005; sec. 10.3.3) is applied to the raw images. Next, the gray values are normalized to the mean distance ($1/h^2$ dependence of brightness, see sec. 3.4.2). The inhomogeneities of the light sources are corrected with a correction matrix (see sec. 4.2.1 and sec. 4.2.2). For the RSSG, this step is depending on distance to the water surface. The mean of these calibrated images is proportional to the slope pdf; 5 minutes of data are averaged for one estimate of the pdf. This is equivalent to 15000 RSSG images (acquired at 50 fps) and 3000 MASG images (acquired at 10 fps).

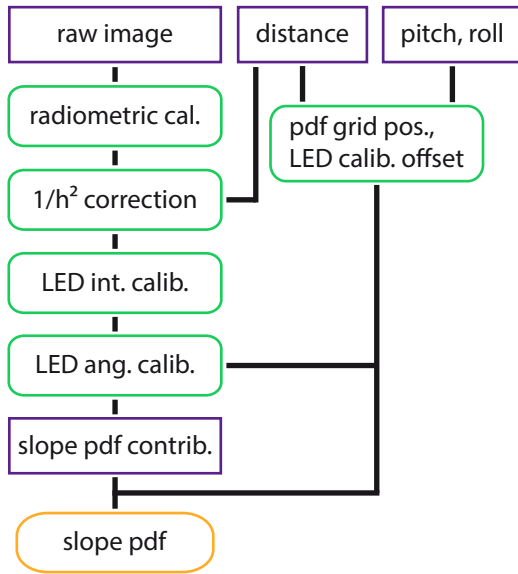


Figure 6.12 Workflow for averaging MASG/RSSG images: Raw images are calibrated for camera artifacts (radiometric calibration) and light source inhomogeneities (LED intensity and angular distribution calibration), calibrated images are added onto a total slope pdf. For the RSSG, the LED angular calibration is depending on distance to the water surface.

6.3.2 Probability of slope zero

Mean square slope $\sigma_s^2 = \langle s^2 \rangle$ cannot be estimated directly from the RSSG slope pdf because of the very narrow range of slope for which the probability is known and the uncertainties connected with ship motion and LED inhomogeneity correction.

However, in sec. 3.3.2 it was shown that, under certain conditions, the probability of slope zero is inversely proportional to mean square slope. The probability of slope zero can be estimated by averaging a small area in the center of the RSSG pdf.

The averaging window is 150×150 pixels, which corresponds to slopes in an interval $\pm 0.5^\circ$. The RSSG surface roughness parameter $\chi \propto \sigma_s^2$ is thus obtained from

$$\chi = \left(\frac{1}{N_x \cdot N_y} \sum_{-N_x/2}^{N_x/2} \sum_{-N_y/2}^{N_y/2} I(x, y) \right)^{-1}, \quad (6.8)$$

where $I(x, y)$ is the (unnormalized) slope pdf.

6.3.3 Mean square slope

The MASG slope pdf covers a larger range of slopes, making it possible to determine mean square slope σ_s^2 by fitting a model function to the measured distribution. Two different model functions were used, results are reported for both.

Gram-Charlier expansion Based on the results of their classic sun glitter experiments, Cox and Munk (1954b) and Bréon and Henriot (2006) propose the use of the truncated Gram-Charlier expansion given in eq. (2.61). An even more truncated expansion is used as one of the model functions, adding only two

skewness terms to a Gaussian distribution

$$p(\xi, \eta) = A \cdot \exp\left[-\frac{1}{2}(\xi^2 + \eta^2)\right] \left[1 - \frac{1}{2}c_{21}(\xi^2 - 1) - \frac{1}{6}c_{03}(\eta^3 - 3\eta)\right] + O, \quad (6.9)$$

with normalized coordinates $\xi = (x - x_0)/\sigma_x$ and $\eta = (y - y_0)/\sigma_y$. The model function has 8 free parameters, the amplitude A , two standard deviations σ_x , σ_y , two shifts of the coordinate origin x_0 , y_0 , two skewness terms c_{21} , c_{03} ⁶ and an additive offset O . Cox and Munk (1954a) added additional peakedness terms, but did not allow for a shift of the coordinate system or an offset. In the MASG data, the origin of the coordinate system cannot be determined with perfect accuracy and a certain level of additive noise cannot be ruled out.

Gaussian with offset The second model function is a pure two-dimensional Gaussian function

$$p(x, y) = A \cdot \exp\left[-\frac{1}{2}\left(\left(\frac{x - x_0}{\sigma_x}\right)^2 + \left(\frac{y - y_0}{\sigma_y}\right)^2\right)\right] + O \quad (6.10)$$

with 6 free parameters. The use of this function for the parameterization of slope probability distributions has been proposed by Ebuchi and Kizu (2002).

The model functions are fitted to the distribution using a trust-region algorithm⁷. The fits did not generally converge, but reached the user set tolerance level and aborted. From visual inspection, the fit result always seemed to reproduce the shape of the distribution adequately. An example for a Gram-Charlier fit is shown in Fig. 6.13. The pdf is shown in the raw MASG coordinate system, which is aligned with the ship. The wind was coming from 10.2° to port. In the large panel, the measured pdf is shown. In the small panels, profiles in the alongwind (right) and crosswind (upper) direction are shown. The 2D fit result is shown as a black line in the side panel.

6.4 Curvature

Two parameters of speckle images that are related to surface curvature are of interest: the mean integrated brightness of reflections (see sec. 3.4.2) and the number of reflections in an image (see sec. 3.4.2).

In the detail from a typical RSSG image (with inverted gray values) in Fig. 6.14a, the problem in estimating these quantities can be seen: the reflections are typically close together, blurred and out of focus. A segmentation with a simple gray value

⁶The original notation of Cox and Munk (1954b) is used here.

⁷Matlab® function fit from the curve fitting toolbox.

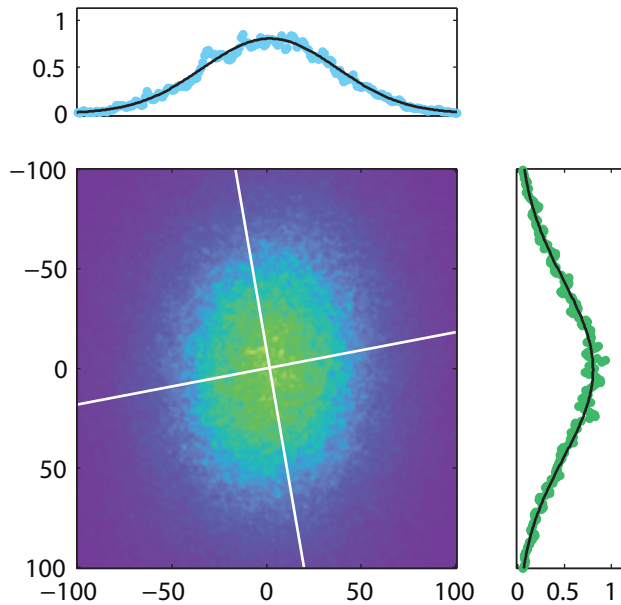


Figure 6.13
Example of a MASG pdf with a fitted Gram-Charlier model function. Two profiles along the white lines in the pdf are shown, these correspond to the alongwind (right panel) and crosswind (upper panel) direction.

threshold (Fig. 6.14b) detects large connected areas containing many speckles, a higher threshold misses small individual reflections.

A solution to the problem of overlapping or connected reflections is the use of a watershed algorithm. This algorithm treats the gray value image as a topographic relief. The gray value of each pixel is interpreted as an altitude. Then, by flooding the relief, it can be segmented in different catchment basins (around local minima or “valleys”) which are separated by watersheds (along the “mountain ridges”).

The result of the watershed segmentation⁸ is shown in Fig. 6.14c. The algorithm separates the reflections, but does not differentiate between foreground and background. However, this can be accomplished easily by multiplying the watershed result with the threshold segmentation in Fig. 6.14b. The final result is shown in Fig. 6.14d. An inherent problem of watershed algorithms is their tendency of over-segmentation. Especially at low wind speeds or in very slicky conditions this becomes a problem. The consequences will be discussed in sec. 7.2.2.

The full processing routine is shown in Fig. 6.15: After applying a two point radiometric calibration, the inhomogeneities of the LEDs are corrected and brightnesses are normalized to the mean distance. A global threshold is applied to select the foreground, and salt noise, individual pixels that are selected but not part of reflections, is removed⁹. For the second part of the segmentation, the corrected image is inverted and the watershed algorithm is applied. The raw label image is multiplied with the foreground mask to remove background areas from the labels, resulting in the final label image.

In the last step, the number of labels, as well as the average size and brightness of

⁸Matlab® function `watershed` which uses the algorithm of Meyer (1994).

⁹Opening operation followed by a dilation, each with a 3×3 matrix of ones as structuring element.

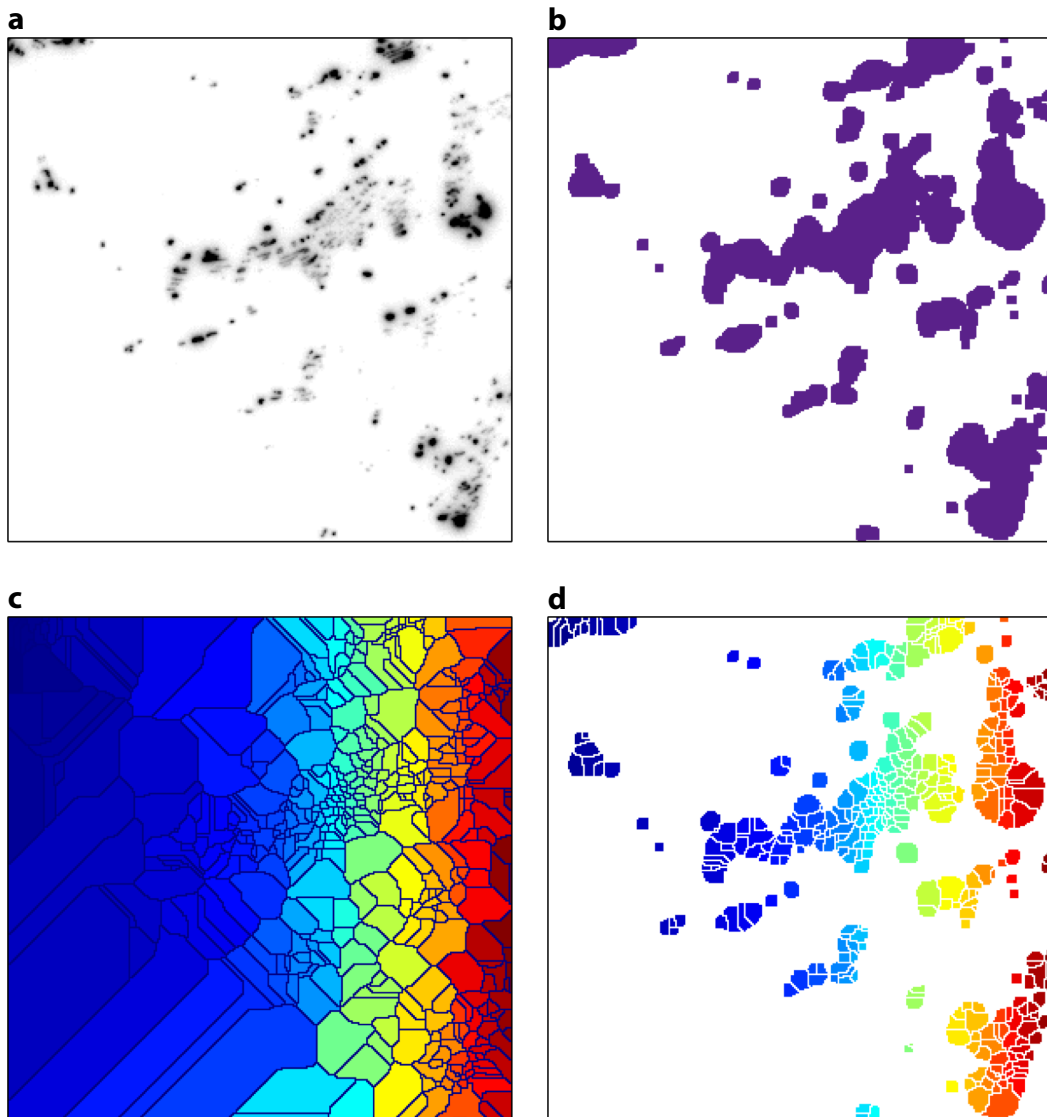


Figure 6.14.: **a** A 300×300 pixels portion of a typical RSSG image. The image is inverted, speckles are black, background is white. Contrast is enhanced for better visibility.
b A simple gray value threshold segmentation separates speckles from background.
c Result of the watershed segmentation.
d The product of the threshold and watershed segmentations, the final segmentation result.

the labeled areas is computed.

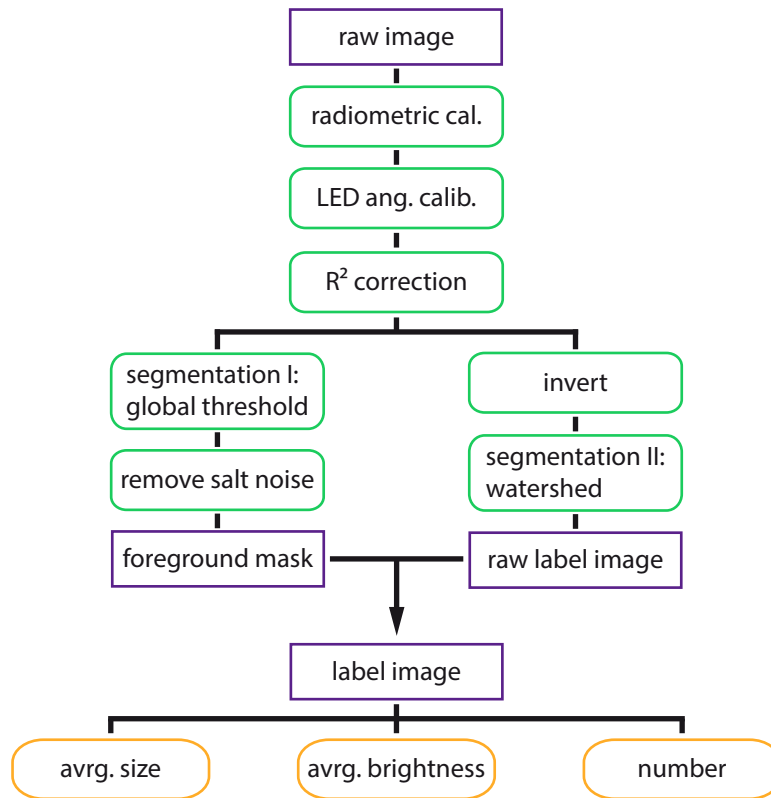


Figure 6.15.: Flowchart of the curvature data processing routine.

6.5 Imaging Slope Gauge

The data processing routines for the color imaging slope gauge were mostly developed by Roland Rocholz. In 2009-2011, when his imaging slope gauge was installed at the Aeolotron, the slope calibration was changed from using a third order model (Rocholz 2008) to using a look-up table (LUT), to better cope with non-linearities of the light source, especially near its borders.

A problem that was not solved by Rocholz was that of chromatic aberration of the telecentric lens (see Fig. 3.1a). This is the main reason for which the data set of the 2011 Aeolotron experiment has not been properly processed before.

Other processing steps (interpolation of RGB images, sec. 6.5.2 and conversion to log-polar spectra, sec. 6.5.3) that differ from the workflow given by Rocholz (2008) are described here for reference. Except for minor optimizations, the implementation was already done by Rocholz in 2009-2012.

6.5.1 Chromatic aberration

To first order, chromatic aberration is due to the dispersion of the glass of which the lens is made. This leads to slightly different focal lengths (and thus slightly different magnification factors) for different wavelengths. The effect can be seen in Fig. 6.16a, where an image of a calibration target is shown.

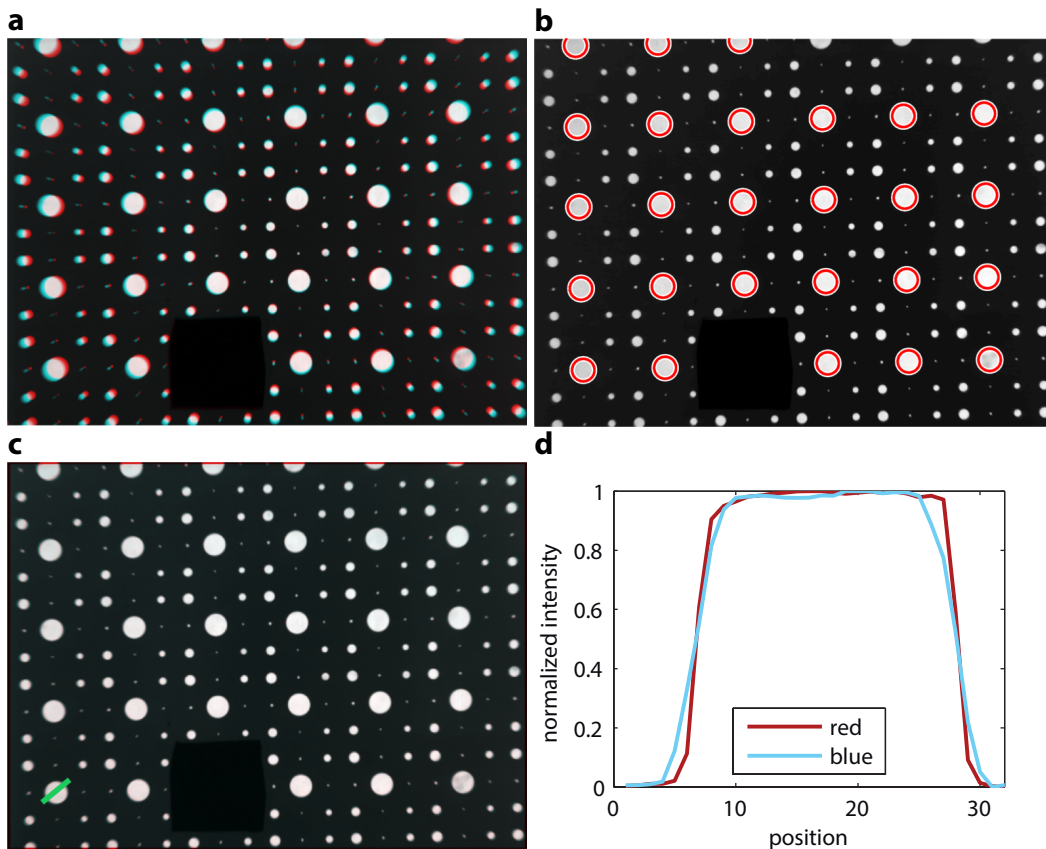


Figure 6.16.: **a** Chromatic aberration of the large lens. The red camera channel is shown in red, the blue channel in cyan.
b Example of the circle detection (the green channel is shown).
c After applying the correction for the change in focal length of the lens, the distortion disappears.
d Intensity profile along the green line in **c**, showing the good matching of the circle in the red and blue channel. However, the blue channel is more out of focus than the red channel.

To compensate the aberration, the positions of the circles are detected in all images¹⁰ (see Fig. 6.16b) and the scaling and translation parameters for a transformation are estimated with a least-squares regression¹¹. The transformation matrices are given in Tab. 6.2 in the form taken by `heurisko`[®].

¹⁰Matlab[®] function `imfindcircles`

¹¹Matlab[®] function `cp2tform`

Table 6.2.: Parameters for the affine transformation to compensate chromatic aberration.

channel	a_{11}	a_{12}	a_{21}	a_{22}	t_x	t_y
red	0.994146	0	0	0.994146	1.42	2.08
blue	1.009728	0	0	1.009728	-2.36	-3.54

The result of the correction is shown in Fig. 6.16c, a profile taken along one of the circles in the corner confirms the good matching (see Fig. 6.16d). A remaining problem is the different sharpness of the different color channels. The decrease in normalized intensity in the red channel is steeper than in the blue channel.

6.5.2 RGB image interpolation

Unlike the Hamburg wind-wave tank at which Rocholz (2008) conducted his experiments, the Aeolotron is a circular facility, capable of generating large breaking waves. These can entrain air into the water and create bubbles. Especially in the surface film experiments, the bubble lifetime at the water surface can be significant. Since bubbles at the surface can have infinite slope at their sides, they generally appear as dark rings in the unnormalized RGB images. A similar effect occurs when waves – mostly parasitic capillaries – have large slopes outside the measurement range of the light source. The lower water depth in the Hamburg facility allowed for a more compact setup, in which the distance from water surface to light source was small. This increased the CISG measurement range. To avoid excessive noise during the normalization step, it is necessary to interpolate these dark spots. This is done for each color channel individually by the following scheme:

$$C' = \left[\frac{(C \cdot I) * F}{I * F} \cdot M \right] + C \cdot (1 - M), \tag{6.11}$$

where “ \cdot ” denotes pointwise multiplication, “ $*$ ” two-dimensional convolution and F a binomial smoothing filter kernel¹². I is the RGB total intensity, M is a binary mask which is 1 if I is lower than a threshold.

The corrected brightness C' is identical to C for all areas of the image in which the intensity is above the threshold, only the dark spots are replaced (bracket term). The interpolation is done by isotropically “smearing in” the intensities from around the borders of the dark spot.

The result is shown in Fig. 6.17: In the normalization step, excessive noise is created (6.17b) in areas that were originally dark in the raw image (6.17a). If the interpolation is applied before normalization, noise is suppressed (6.17c).

¹²heurisko® function Bin16.

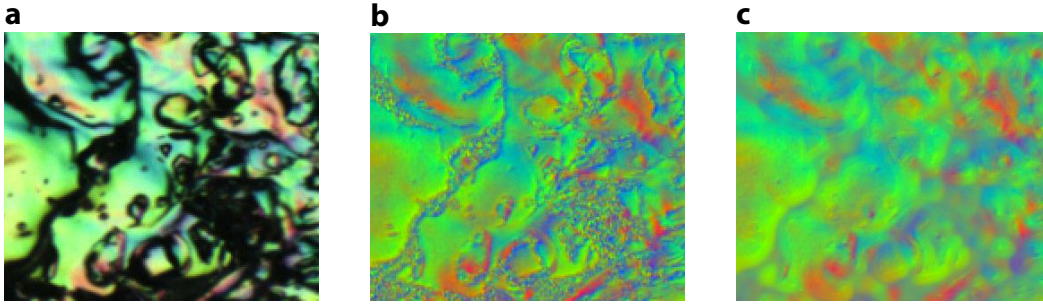


Figure 6.17: **a** Portion of an ISG raw image of a breaking wave. Due to double reflection or high slopes, there are many dark areas in the image for which slope cannot be determined. **b** If the raw image is normalized, the dark areas become very noisy which may affect the spectra. **c** If the raw image is processed according to eq. (6.11), the noise is suppressed.

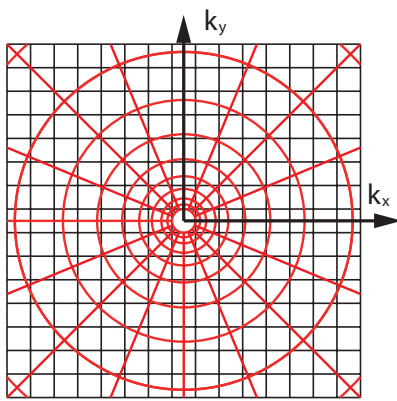


Figure 6.18 Conversion from a Cartesian (black) to a log-polar (red) grid: Near the origin, the log-polar grid has a much higher resolution than the Cartesian grid. The spectral energy contained in the lower frequencies needs to be carefully distributed into the new bins. Far away from the origin, each log-polar bin contains many Cartesian bins.

6.5.3 Log-polar spectra

While the computation of 3D power spectra from time series of 2D slope measurements is straightforward, some care has to be taken in transforming the coordinate system from (k_x, k_y, ω) to $(\log k, \theta, \omega)$, i.e. in going from a Cartesian to a polar coordinate system with a logarithmic axis for the magnitude of the wavenumber vector. A representation in these coordinates is desirable, since the spectra have a constant relative wavenumber resolution and the directionality of the wave field can immediately be extracted (Jähne and Riemer 1990).

An approach proposed by Rocholz (2012) is used for the computation of slope spectra on the new log polar grid: The (k_x, k_y) vectors of the original Cartesian spectrum are transformed to the new coordinates. In these new coordinates, they are treated as a scattered data set; this can be interpolated¹³ to obtain the values for the new $(\log k, \theta)$ grid coordinates.

In the high k range, the new coordinate system with the constant relative wavenumber resolution leads to a considerable amount of data compression. In the low k

¹³Matlab® function scatteredInterpolant

range however, the resolution of the new grid is generally higher than that of the old Cartesian grid (see Fig. 6.18). The consequence is that energy conservation is usually not guaranteed in the lower wavenumbers. The spectral shape in the higher wavenumbers however should be unaffected by these problems.

In the analysis of the CISG data from the Aeolotron, apart from the slope spectrum $S(\log k, \theta)$ itself, one more quantity is of interest: The omnidirectional saturation (or curvature) spectrum $B(\log k)$. It can be directly computed by integration of the slope spectrum $S(\log k, \theta)$ over all directions θ and multiplication with k^2 :

$$B(\log k) = \sum_{-\pi}^{\pi} k^2 S(\log k, \theta) \Delta\theta. \quad (6.12)$$

6.5.4 Mean square slope

From the log-polar slope power spectrum, it is easy to compute the contribution to mean square slope σ_s^2 for different wavenumber ranges. However, the changing size of the spectral bins needs to be accounted for, since $dk_x dk_y = k dk d\theta = k^2 d(\log k) d\theta$:

$$\sigma_s^2 \Big|_{k_{\min}}^{k_{\max}} = \int_{k_{\min}}^{k_{\max}} S(k, \theta) k dk d\theta \quad (6.13)$$

$$= \int_{k_{\min}}^{k_{\max}} S(\log k, \theta) k^2 d(\log k) d\theta \quad (6.14)$$

$$= \sum_{k_{\min}}^{k_{\max}} S(\log k, \theta) k^2 \Delta(\log k) \Delta\theta. \quad (6.15)$$

6.5.5 Full Workflow

In Fig. 6.19, the full processing routine for color imaging slope gauge data is shown. Except for the chromatic aberration correction (sec. 6.5.1), RGB interpolation of excessive slopes (sec. 6.5.2) and the coordinate transformation and integration steps (sec. 6.5.3 and sec. 6.5.4), all processing steps are described in detail by Rocholz (2008).

The raw image sequences consist of 1292×946 pixels 8 bit images with a Bayer pattern. In the demosaicing step, the R, G, B color subgrids (646×473 pixels) are registered using specialized isotropic filter kernels for interpolation (Schar 2000). After the chromatic aberration correction and interpolation of dark areas due to bubbles or high slopes, the measured intensities are normalized (cf. sec. 3.1.1) and offset corrected. The normalized intensities are then converted to slope by a table look-up. The look-up table was determined by Roland Rocholz with a spherical glass bowl of known radius that was partly submerged in the water.

From the slope image time series, the power spectrum is computed, the coordinate transform to log-polar coordinates is applied and the desired integrated spectra are derived.

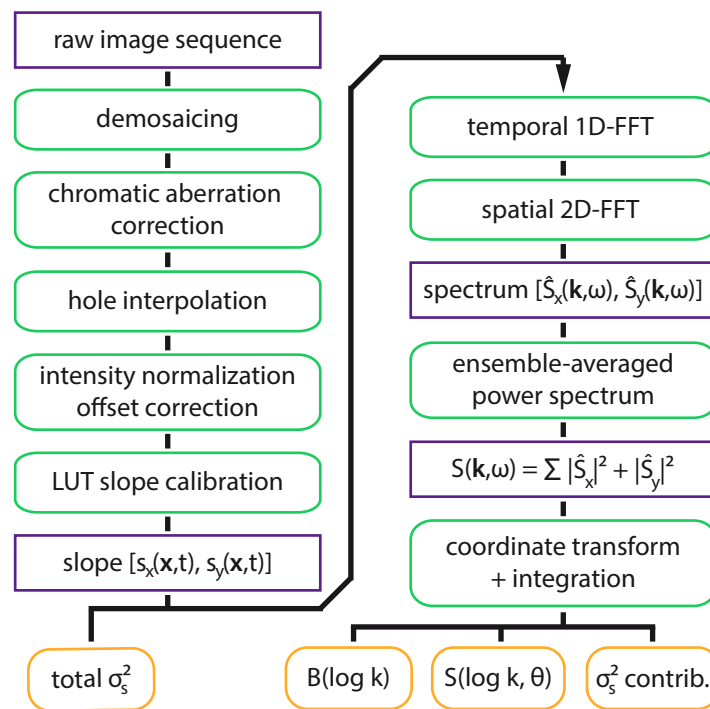


Figure 6.19.: Flowchart of the updated color imaging slope gauge data processing workflow (cf. Rocholz 2008; fig. 6.1).

7

Results

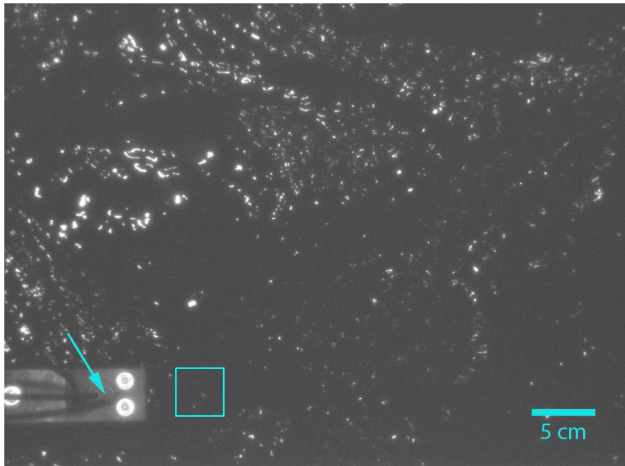
The newly developed instruments, the Reflective Stereo Slope Gauge (RSSG) and the Medium Angle Slope Gauge (MASG) were validated with reference measurements. The results will be presented in sec. 7.1. In sec. 7.2, measured wave slope distributions and statistical parameters from the Meteor M91 cruise are presented. The results of the analysis of the imaging slope gauge data from the laboratory and the possibilities of describing gas transfer velocities with statistical wave parameters are explored in sec. 7.3.

7.1 Instrument validation

Before the RSSG and WASG were deployed to field experiments, the measurement methods were validated in the laboratory. This validation was not attainable in Heidelberg: Because of the small width (60 cm) of the Heidelberg Aeolotron, the waves in the footprint of the RSSG are affected by the walls of the facility, if the RSSG is mounted at a reasonable distance¹. The Marseille *Pytheas* wind-wave facility (sec. 5.1.1) on the other hand is perfectly suited for this kind of validation experiment. The facility is 3 m wide, so the wave field in the center is not affected by the walls. Conditions are well characterized and reference data from other experiments is available, so simultaneous measurements with a reference system are not required. The RSSG was deployed to Marseille in March 2011 for a first evaluation, in September 2012 the RSSG and the new MASG were deployed.

Additional validation measurements were also made during the OSSPRE cruise in 2011, where an in-situ comparison with a Riegl laser altimeter was possible.

¹In field measurements at a distance of 8 m, the footprint is about 1.2×1.0 m.

**Figure 7.1**

Setup for the direct comparison of the RSSG with a wave wire. Shown is an RSSG raw image from the left camera. The RSSG image is evaluated in the cyan box (100×100 pixels, 4×4 cm). The wave wire holder is visible, it was positioned about 30 cm above the water surface, the wave wire extends vertically down from the tip of the arrow.

7.1.1 Height measurement

Laboratory verification

The RSSG height measurement principle (sec. 3.2) was verified by direct comparison of RSSG height data with wave heights measured with a capacitance-type wave wire (kindly provided and operated by Guillemette Caulliez). This is a thin insulated wire which is mounted vertically in the water. The capacitance between the wire and the water body is then proportional to the water height at the wire (Tucker and Charnock 1954).

The RSSG's performance was tested in simultaneous and nearly collocated measurements. Figure 7.1 displays an RSSG raw image acquired during this comparison. The wave wire holder is visible on the lower left side of the image. The holder is placed about 30 cm above the water surface, the wave wire extends down vertically from there. The disparity of the RSSG stereo images was only evaluated in a small interrogation window, the cyan box just about 10 cm upwind of the wave wire (wind is coming from the right side). The window size is 100×100 pixels, corresponding to about 4×4 cm on the water surface. Reconstructed wave heights from the RSSG were then shifted in time to account for the upwind location of the measurement and match the wave wire record.

The instruments were set up at a fetch of 27 m in the main measurement section of the facility. Two examples, measured at wind speeds of 11 m/s and 7 m/s, are shown in Fig. 7.2. The green line is the reference wave wire, the purple dots are individual RSSG height measurements. The deviations are of the order of a couple of millimeters. Compared to the laboratory wave height of less than 10 cm, this is relatively large, but since the RSSG has a measurement range of multiple meters, the accuracy is very good. It should also be kept in mind that the measurements were not fully collocated and the shape of the waves may have evolved between the RSSG footprint and the wave wire location.

To generate Fig. 7.2, the RSSG data was reprocessed using the final version of

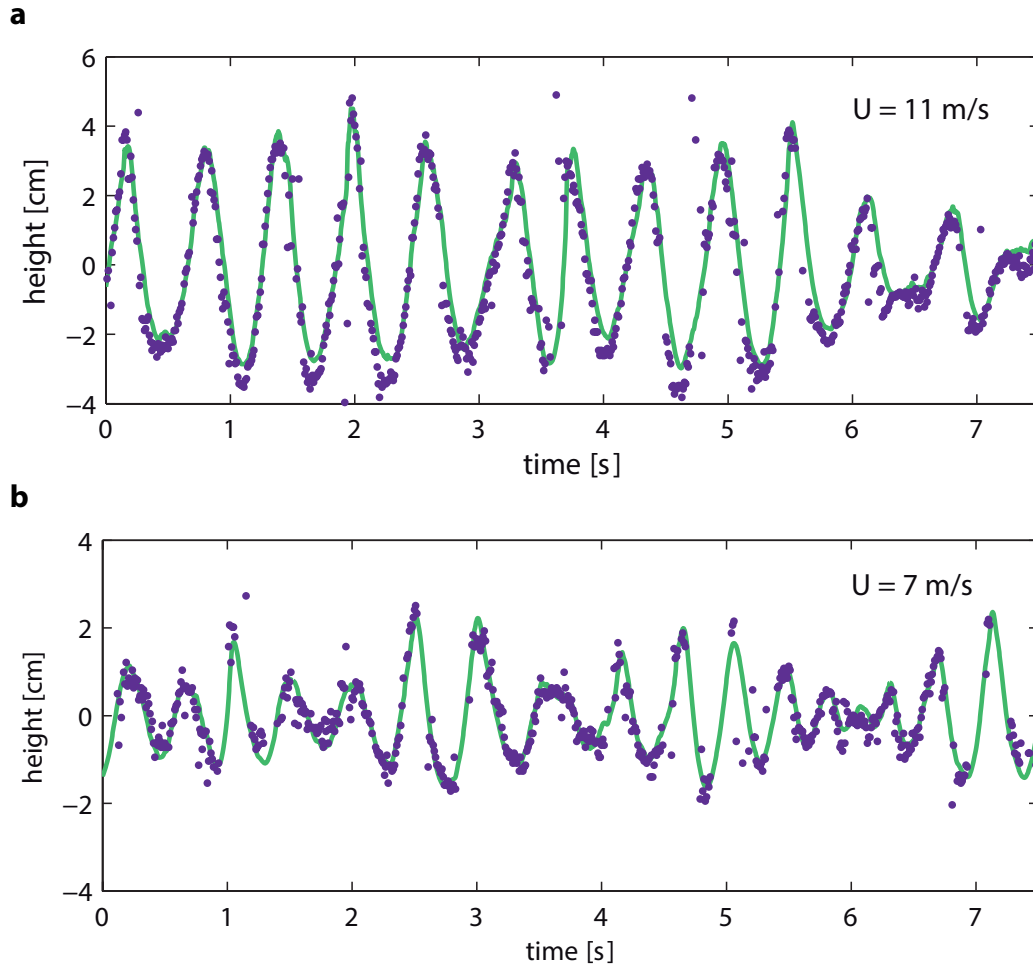


Figure 7.2.: Comparison of the RSSG height measurement (purple dots) and the reference wave wire (green line) that was installed just downwind of the RSSG interrogation window. Wind speed is **a** 11 m/s and **b** 7 m/s. The agreement is good, deviations are of the order of a couple of millimeters. At lower wind speeds, data dropout (missing data points) increases for the RSSG measurement. Dropout is caused by RSSG images, in which no reflections at all are visible in the interrogation window (here: 100×100 pixels) over which the disparity is estimated. The probability for this to occur decreases with increasing surface roughness at higher wind speeds.

the disparity estimation and height retrieval algorithms. The same code was also used to determine the wave heights in the field experiments, it was not tweaked to perform well under these laboratory conditions. The limiting factor for RSSG wave height measurements is not the absolute precision with which heights can principally be measured, but the level of data dropout. If there are no reflections in the interrogation window, the disparity cannot be estimated. Wave heights then need to be interpolated, if a continuous record is desired, e.g. for the computation of wave spectra or to calibrate the slope measurements. If high resolution measurements are not required, the interrogation window size can be increased so that the probability of not having any reflections in the window decreases.

For the comparison, a window size of 100×100 pixels was chosen. Measurements at this size are only possible at very rough surfaces (high wind speeds in the laboratory). In the first example (11 m/s), 92 % of the image pairs could be processed to give a valid height. In the second example, at 7 m/s, the dropout already increased significantly, only 76 % of the images could be processed. Fortunately, since reflections are coming from points with slopes near zero, the wave crests and wave troughs are usually measured. If wave heights are missing only on the sides of the waves, they are relatively easy to interpolate.

Frequency power spectra were computed from both RSSG and wave wire data to further analyze the capabilities of the RSSG. The result is shown in Fig. 7.3. The spectrum measured by the RSSG (purple) correctly reproduces the dominant wave peak measured by the wave wire (green). The RSSG spectrum is generally noisy, this is due to the short sampling time: The wave wire spectrum is from a 300 s time series, wave height was sampled at 250 Hz. Welch's method (Welch 1967) was used to get a good estimate of the power spectral density in the frequency band of interest: The full time series is cut into overlapping segments. A window² function is applied to each segment to reduce spectral leakage before the power spectral density is computed. For the RSSG on the other hand, only 4 short records of 18 s each are available. At the time of the experiment, this was the maximum continuous recording time. The spectra computed from the four measurement runs are averaged to produce the purple line in Fig. 7.3.

The RSSG wave spectrum deviates from the reference measurement at high and low frequencies. At low frequencies this is probably due to the short sampling time, leading to non-zero time averages for the low frequency components, as well as a broadening of the dominant wave peak. At high frequencies, the reason is clearer: An interrogation window size of 200×200 pixels was used here to reduce data dropout. This corresponds to a footprint size of roughly 80×80 mm. Waves on smaller scales cannot be resolved, because only the average disparity over the interrogation window is computed. The Nyquist wavenumber given by the finite size of the window is $k_{\text{Nyq}} = 41$ rad/m. Only longer waves (with lower wave numbers) can be resolved in this configuration. According to the linear dispersion relation, this corresponds to

²Hann window, $w(n) = 0.5(1 - \cos(2\pi n/(N - 1)))$.

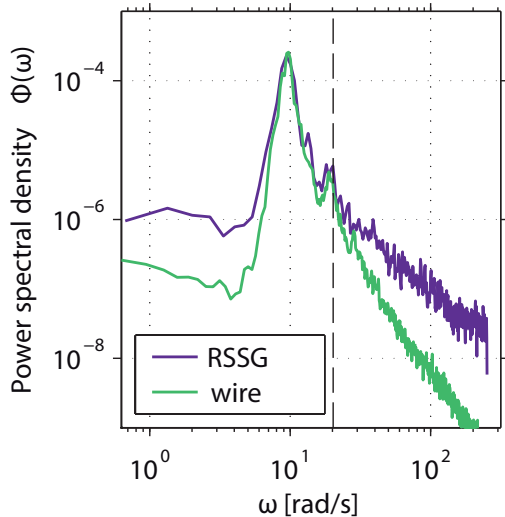


Figure 7.3 Wave spectra measured with the RSSG (purple) and a wave wire (green) at a fetch of 27 m and a wind speed of 13 m/s. While the agreement around the dominant wave peak is generally good, the RSSG overestimates energy in the high and low frequency regions. The reasons for this are discussed in the text.

a frequency of $\omega = 20$ rad/s. This is marked by the black dashed line in Fig. 7.3. It coincides well with the onset of overestimation of energy in the RSSG spectrum. Due to the wave and wind-induced current in the facility, the dispersion relation is shifted to higher frequencies by the Doppler effect. Therefore, the wavenumber cutoff is also shifted towards higher frequencies, so that the position of the line in Fig. 7.3 is slightly underestimated. Still, the increase in spectral energy at high frequencies is not physical and the spectrum cannot be trusted there.

Field verification

The RSSG performance was also evaluated in the field during the OSSPRE experiment in December 2011. A *Riegl* laser altimeter (model LD90-3100VHS, kindly provided by Christopher Zappa) was continuously monitoring wave heights at a position about 2 m upwind of the RSSG (see Fig. 5.2). The laser altimeter determines the water surface distance by measuring the travel time of laser pulses that are reflected at the water surface. Pulses are sent at a frequency of 2 kHz; 20 pulses are averaged so that the output rate is 100 Hz. The measurement accuracy specified by the manufacturer is ± 25 mm.

Similar to the RSSG, the *Riegl* altimeter measurement depends on the return of reflections to the instrument. At the specular water surface, most reflections are lost. Like the RSSG, the altimeter can only measure the height of patches with slope zero. Due to the high sampling rate, dropout is still very low, except for very smooth surfaces.

For a direct comparison, the disparity was evaluated from a 200×200 pixels window in the RSSG images, corresponding to approximately 20×20 cm on the water surface at a mean distance of 9.2 m. Missing data points in the RSSG time

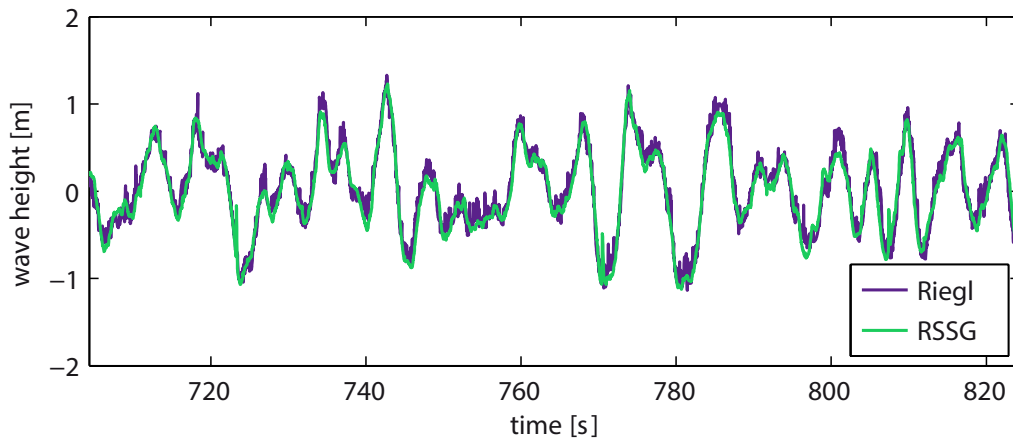


Figure 7.4.: Comparison of the RSSG height measurement with a Riegl laser altimeter in field conditions. Agreement is generally good. Data is from the OSSPRE cruise.

series were interpolated with piecewise cubic Hermite polynomials³ as proposed by Veron et al. (2009). Figure 7.4 shows the comparison of RSSG measurements with Riegl altimeter measurements. The measurements were shifted in time to account for the different locations of the instruments. The agreement is generally good (note the very different scale compared to the laboratory comparison), but deviations up to 20 cm occur (e.g. the spike in the trough at $t = 770$ s). To some extent, deviations are actual changes in the water surface shape during propagation from the altimeter measurement location to that of the RSSG. The spikes in the troughs that the RSSG occasionally measures on the other hand are certainly artifacts. However, such large differences are rare. It appears that the RSSG height measurement is generally more precise, provided that the surface is rough and there are sufficient reflections. The noise level on the altimeter measurement is significantly higher. On the other hand, data dropout rates are bigger for the RSSG, which lacks the ability to average many very high frequency measurements.

While in the laboratory study it was shown that the RSSG can measure wave heights with very high accuracy under favorable conditions, this field comparison demonstrates that these measurements are possible also for large wave amplitudes. The accuracy of the measurement is limited by the finite window size required for determining the disparity. The window size is a compromise between measurement resolution and data dropout, a window size of 200×200 pixels (footprint 20×20 cm) was found to be reasonable value.

³Matlab® function `interp1` with option `'pchip'`

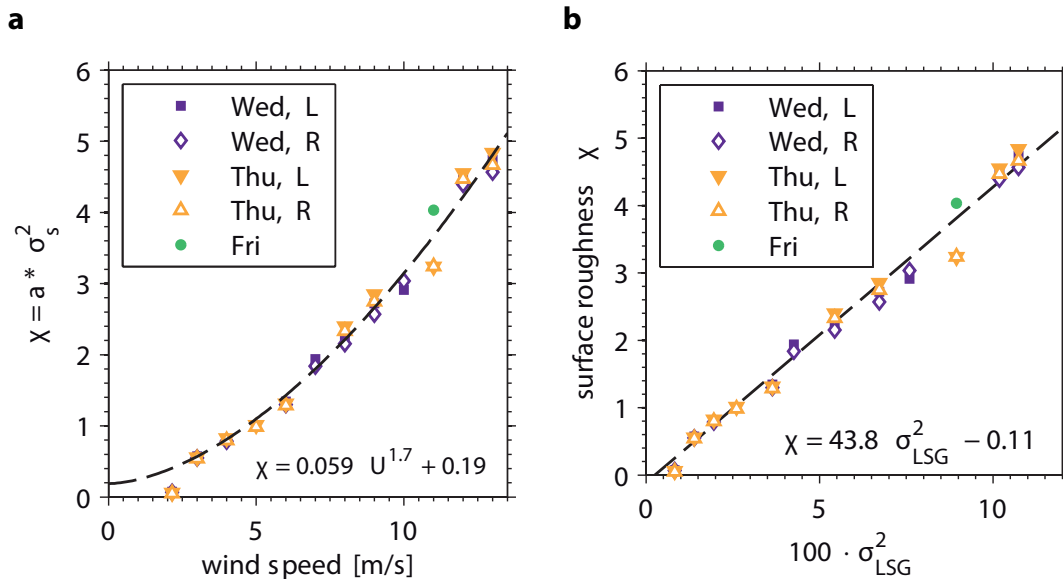


Figure 7.5.: Comparison of the RSSG surface roughness measurements and reference mss measurements from a Laser slope gauge. The wind speed range was $U_{\text{ref}} = 2\text{-}13$ m/s, fetch was 27 m. Data are shown from three different days (Wednesday, purple symbols, Thursday, orange symbols, Friday, green symbol) and from the evaluation of the left (filled symbols) and right (open symbols) camera images.

7.1.2 Slope measurement

RSSG verification

As was detailed in sec. 3.3.2, the RSSG cannot directly measure mean square slope σ_s^2 , the variance of the probability distribution of surface slope. From calibrated and averaged images of specular reflections, the (unnormalized) probabilities for slopes in the range $s = \pm 0.06$ can be measured. Because this range is significantly narrower than typical slope pdfs, the shape of the distribution – or its width – cannot be determined directly. Instead of measuring mss, the probability of zero slope $p(0,0)$ is measured. This probability is approximately proportional to $1/\sigma_s^2$ (see sec. 3.3.2). The RSSG surface roughness parameter χ is proportional to $1/p(0,0)$, thus it is expected that

$$\chi = a \cdot \sigma_s^2 \sim \sigma_s^2. \quad (7.1)$$

This validity of this approximation was tested in the Marseille 2011 experiment, when statistical slope measurements were conducted for 12 different wind speeds from 2 m/s to 13 m/s (the full range of the facility). In Fig. 7.5a, the surface roughness parameter χ is plotted against wind speeds for all measurements. Results are shown from measurements on three different days (Wednesday, purple symbols, Thursday, orange symbols, Friday, green symbol) to demonstrate the repeatability of conditions in the facility. It seems that the conditions are reproducible, no clear trends are visible between the Wednesday and Thursday measurements. The dashed line is the

fit result of a power law, the exponent is $n = 1.7$. Such a functional relationship is motivated by physics, it is merely meant to illustrate the non-linearity of the behavior of mss with wind speed in this facility. This is in contrast to the linear behavior of mss found from field measurements (Munk 2009).

The linearity of the dependence of χ on σ_s^2 was tested with reference σ_s^2 measurements which were kindly provided by Guillemette Caulliez. They were measured with a laser slope gauge at the same fetch as the RSSG measurements in an earlier experiment (Caulliez 2011). Figure 7.5b shows the result of the comparison. The RSSG surface roughness parameter χ is plotted against mss from the laser slope gauge measurements σ_{LSG}^2 . There are only minor deviations from the line fitted to the data.

Two points were excluded from the data set which was used to compute the fit: The lowest value (measured at a wind speed of 2 m/s) and the third highest measurement from Thursday (red symbols). At the lowest wind speed, the surface is undulated, but waves are barely visible. The slope probability distribution is very narrow here, violating the assumption that the RSSG only measures slope zero (see sec. 6.3.2), when a fraction of the image is averaged. The third highest measurement from Thursday is clearly below the fit line. It is not clear what exactly causes this deviation, the most likely explanation is a faulty record of which light source setting has been used for this measurement. Unfortunately, this wind speed was not measured on Wednesday. Data acquired on Friday suggests that the Thursday value is an outlier, the green data point coincides nicely with the fit. However, this data point was generated from very few RSSG images, since Friday was mostly reserved to the comparative measurements with the wave wire.

Overall, the correlation of the RSSG χ values with mean square slope σ_s^2 is very good over a wide range of wind speeds. Even though the conditions in the field generally differ from conditions in the lab (as will be discussed later), there is no reason to assume that the RSSG's χ should not correlate well with mean square slope under open ocean conditions. Still, no attempt is made to transfer the “calibration” given in Fig. 7.5b to field experiments. The absolute brightness of reflections in the images depends on distance to the water surface, integration time of the camera, changes in the LED drivers for the light sources, cutoff filters on the cameras, etc. It is generally possible to control all these factors in a fully developed instrument. However, especially during the 2011 Marseille experiment, the RSSG had prototype status, many minor changes were made before the 2012 Peru experiment. On the other hand, it was not necessary to transfer the calibration to the field, as it will be shown that the RSSG can be calibrated in-situ with the available MASG measurements (see Fig. 7.13).

Riegl altimeter slope measurement

The laser altimeter that was deployed to the Kilo Moana for the 2011 field experiment not only measures wave height. In addition to the distance to the water surface, two signal strength parameters are recorded. According to the user manual, the *amplitude* parameter gives the strength of the received signal. The *quality* parameter is the percentage of laser pulses that are returned at all.

The combination of both parameters allows to calculate the probability for zero slope. Unlike in the RSSG images, there is no averaging over a finite slope interval around zero, but only temporal averaging of a point measurement. On the other hand, the high sampling rate guarantees good statistics. The capabilities of the laser altimeter in this novel application were tested by comparing the measurements to simultaneous RSSG measurements. Because the laser altimeter measurements were not synchronized with the inertial measurement unit (sec. 6.1), motion correction is not possible.

Five minute averages were computed of both the mean gray value in the RSSG image center $m_{\text{RSSG}} = 1/\chi$ and

$$m_{\text{Riegl}} = \frac{a}{q} r^2, \quad (7.2)$$

where a denotes the amplitude and q the quality parameter and r is the measured distance to the water surface. In computing the mean value for the altimeter, missing data points were also accounted for. These occur, when during the 0.01 s sampling interval no reflections are returned at all.

Figure 7.6a shows the direct comparison of the RSSG and Riegl altimeter measurements. If the measurements during daytime are neglected, both instruments agree well, there is a strong correlation between the two signals. The reason for the discrepancy in the daytime measurements can be seen in Fig. 7.7. Two example false-color RSSG images are shown, Fig. 7.7a was acquired during daytime, Fig. 7.7b at night. The gray values have identical scaling, background is removed. While in the nighttime image, most of the area is background (white), during daytime, most pixels have gray values higher than the background, even far away from (bright) reflections.

This is caused by skylight that is reflected into the camera. This is also obvious from Fig. 7.6b: Shown are time series of the Riegl (purple) and the RSSG (green) mean signal amplitude (= mean gray value for the RSSG) for an example day. The orange line is the shortwave radiation measured with a pyranometer that was mounted on the instrument boom close to the RSSG. The RSSG signal follows the curve almost perfectly, proving that daytime measurements are in fact affected by daylight. The dashed black line separates daytime measurements (to the left) from nighttime measurements.

During the 2011 Kilo Moana cruise, 850 nm high pass filters (*Schneider Kreuznach B+W Infrarot 093*) were used to suppress natural light from the RSSG images. Before the 2012 Meteor cruise, the filters were upgraded because of the problems with

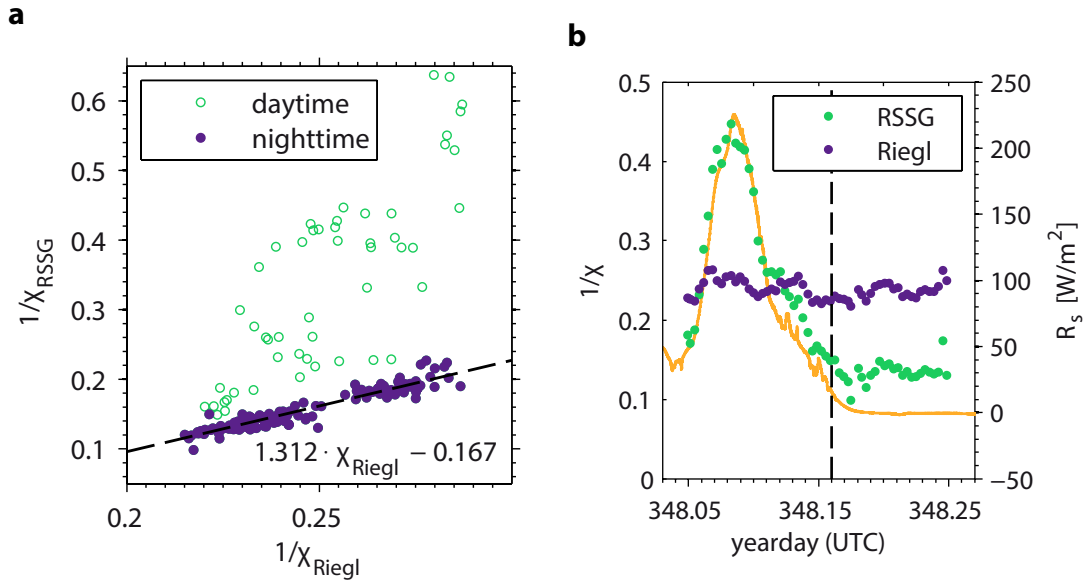


Figure 7.6.: **a** Correlation of the RSSG and Riegl laser altimeter estimates of the probability of slope zero. In nighttime measurements (filled circles) both agree well, during the day (open circles), the RSSG measurements are affected by skylight. **b** Time series of the RSSG and Riegl estimates under stable wind conditions. The Riegl value is stable, independent of daytime, while the RSSG value is sensible to ambient natural light. The solid line is the shortwave radiation measured close to the RSSG location. The dashed line (at yearday 348.16) separates the daytime from the nighttime points in (a).

daytime measurements. The new band pass filters ($950 \pm 50 \text{ nm}$, *Edmund Optics*) are significantly more efficient in suppressing daylight.

The good correlation of RSSG and Riegl altimeter measurements in Fig. 7.6a suggests that “mean square slope” – more precisely a “ χ ”, a surface parameter proportional to σ_s^2 – can be measured with the laser altimeter. Unfortunately, the range of this comparison is limited due to the very stable wind speed conditions along the tropical cruise track. These first results are very encouraging, the performance of the altimeters should be investigated under controlled conditions in the laboratory. From the time series in Fig. 7.6b, it does not appear that the altimeter measurement is affected by skylight. This is not surprising, as focused laser pulses are used and integration times are very short. Therefore, the intensity of skylight reflected into the detector of the altimeter is negligible compared to the intensity of the laser pulse.

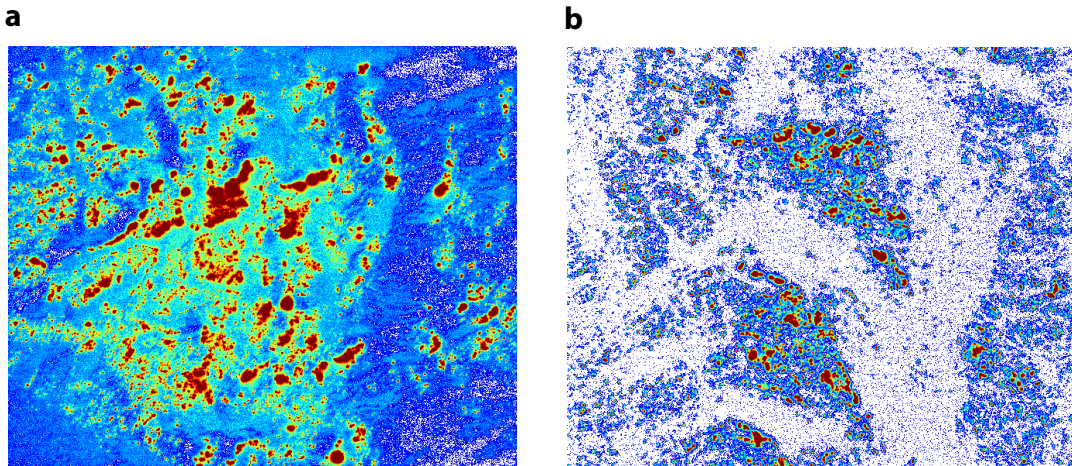


Figure 7.7.: Example RSSG images from the Kilo Moana cruise during **a** daytime and **b** nighttime. Both images are scaled to the same grey value range (contrast is enhanced) and background is removed. In the night image on the right, reflections are isolated and background is dark. In the day image, the background is not fully dark. This is due to skylight that is not fully filtered by the old infrared filters of the RSSG.

MASG verification

The medium angle slope gauge (MASG) was built in the summer of 2012 (sec. 4.1.2). Only then high power LEDs became available that allowed an extension of reflective slope measurements to a wider field of view. With the MASG it is now possible to easily and directly measure the slope probability distribution. The instrument was first tested during the Marseille experiment in September 2012. It was mounted inside the facility just downwind of the main measuring section. In a laboratory application where the distance to the water surface barely changes, data processing is very straightforward. The slope probability is proportional to the average brightness distribution in the image after corrections have been applied for the directional characteristic of the LED light source and the non-ideal behavior of the camera (see sec. 6.3).

The measured slope pdf is fitted with a model pdf (see also sec. 6.3.3). A number of different formulations have been proposed in the literature to describe the probability distribution of surface slopes, e.g. a truncated Gram-Charlier series (Bréon and Henriot 2006, Cox and Munk 1954b, Longuet-Higgins 1963a), a Gaussian distribution with an offset (Ebuchi and Kizu 2002), or non-Gaussian parameterizations (Joelson and Néel 2008, Liu et al. 1997). These formulations mostly differ for larger slopes, where the Gram-Charlier expansion used by Cox and Munk (1956) becomes negative and thus cannot represent the actual probability distribution (Wentz 1976).

The MASG is not able to differentiate between the different probability distributions, this task has to be left to a future *wide-angle* slope gauge with a larger measurement range. From the measurement range of the instrument, it is possible to extract mean square slope, solid estimates of higher moments require knowledge

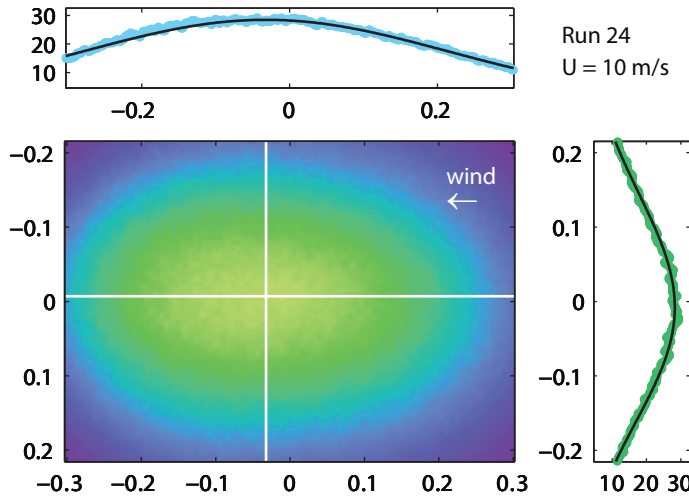


Figure 7.8
 Example of a two-dimensional slope probability distribution measured at the Pytheas facility in Marseille. Wind speed is 10 m/s, the wind is coming from the right. The skewness of the distribution and the anisotropy of the along- and cross-wind directions is clearly observed. The two profiles show the measured probabilities (blue and green dots) as well as the corresponding profiles of the fitted 2D model function (black solid line).

of the shape of the distribution at larger slopes (Tatarskii 2003).

Two different models were tested. The first one is a simple two-dimensional Gaussian distribution of the form

$$p(\xi, \eta) = a \exp\left[-\frac{1}{2}(\xi^2 + \eta^2)\right] + b, \quad (7.3)$$

with the normalized along-wind and cross-wind slope components $\eta = (s_a - s_{a0})/\sigma_a$ and $\xi = (s_c - s_{c0})/\sigma_c$. The offset b is required to correct for brightness contributions in the image that are not reflections from the MASG light source, the slope offsets s_{a0} and s_{c0} are important especially for the evaluation of ship-borne measurements, where perfect horizontal alignment of the system cannot be guaranteed. The second model, a truncated Gram-Charlier expansion similar to that used by Cox and Munk (1954b), has the form

$$p(\xi, \eta) = a \exp\left[-\frac{1}{2}(\xi^2 + \eta^2)\right] \left[1 - \frac{1}{2}c_{21}(\xi^2 - 1)\eta - \frac{1}{6}c_{03}(\eta^3 - 3\eta)\right] + b. \quad (7.4)$$

The two additional parameters c_{21} and c_{03} describe the *skewness* of the distribution in the along-wind direction. Cox and Munk (1956) also included three terms describing the *peakedness*. However, their slope measurement range is also considerably higher, so that it can be hoped to extract higher order moments of the distribution from the measurements. For the MASG pdfs, the fit was found to become increasingly unstable with the addition of even more free parameters. Cox & Munk did not need the slope offsets s_{a0} and s_{c0} in their fit. Because one of the effects of skewness is to shift the maximum of the distribution, these offsets are expected to diminish the skewness of the fitted distributions.

In Fig. 7.8, an example of a measured probability distribution is shown. The

wind is blowing from the right in the 2D distribution, along-wind slope is given on the x-axis, cross-wind on the y-axis, the x-axis is pointing upwind. The skewness of the distribution is clearly visible, the peak is shifted downwind. Profiles of the distribution are shown in the along-wind (upper panel) and crosswind (right panel) directions. The blue and green dots are the measured probabilities along the white lines in the 2D image, while the black lines are the corresponding profiles of the fitted model distribution (Gram-Charlier expansion, eq. (7.4)). Note that the model pdf was fitted to the two-dimensional distribution, not individually to the shown profiles. The agreement is generally good, only in the alongwind direction there are some deviations visible between slopes -0.1 and -0.2 .

In Fig. 7.9, profiles of the slope pdf measured at different wind speeds and the respective profiles of the Gram-Charlier fit are shown. In the cross-wind direction (right side, panels b, d, f, h), the fitted model pdf agrees well with the measurements at all wind speeds. In the along-wind direction, the agreement is good at the lower wind speeds; with increasing wind speed the skewness of the distribution as well as the deviation between model and measurement increases. This does not necessarily imply that the model does not describe the distribution accurately. Problems arise because with increasing wind speed the distribution becomes wider and the portion of the distribution that can be measured becomes smaller. While at the lowest wind speed, the probability drops to almost zero at the borders of the measured distribution, at the highest wind speed it barely drops to one half of the maximum.

The performance of the two different probability distribution models was tested by comparing the σ_s^2 that was extracted from the fits with the laser slope gauge reference measurements provided by Caulliez (2011). The result is shown in Fig. 7.10. The Gram-Charlier model (7.10b) correctly determines $\sigma_{s,c}^2$, the mss in the crosswind direction (green symbols). At low wind speeds, also the alongwind component (purple symbols) is recovered accurately. At higher wind speeds, the alongwind component is overestimated. The reasons for this were already discussed. Mean square slope obtained from fits with the Gaussian model (7.10a) agree better in the alongwind component at higher wind speeds, but are generally underestimated in the crosswind direction. Because wind forcing is expected to be lower in the field, the Gram-Charlier model, which performs better for lower forcing, was chosen to be used in processing the field data.

The MASG has been shown to being able to determine the mean square slope of the wave field. Unlike in RSSG measurements, there is no unknown scaling factor here, the fit of a model distribution gives direct access to absolute values of mean square slope.

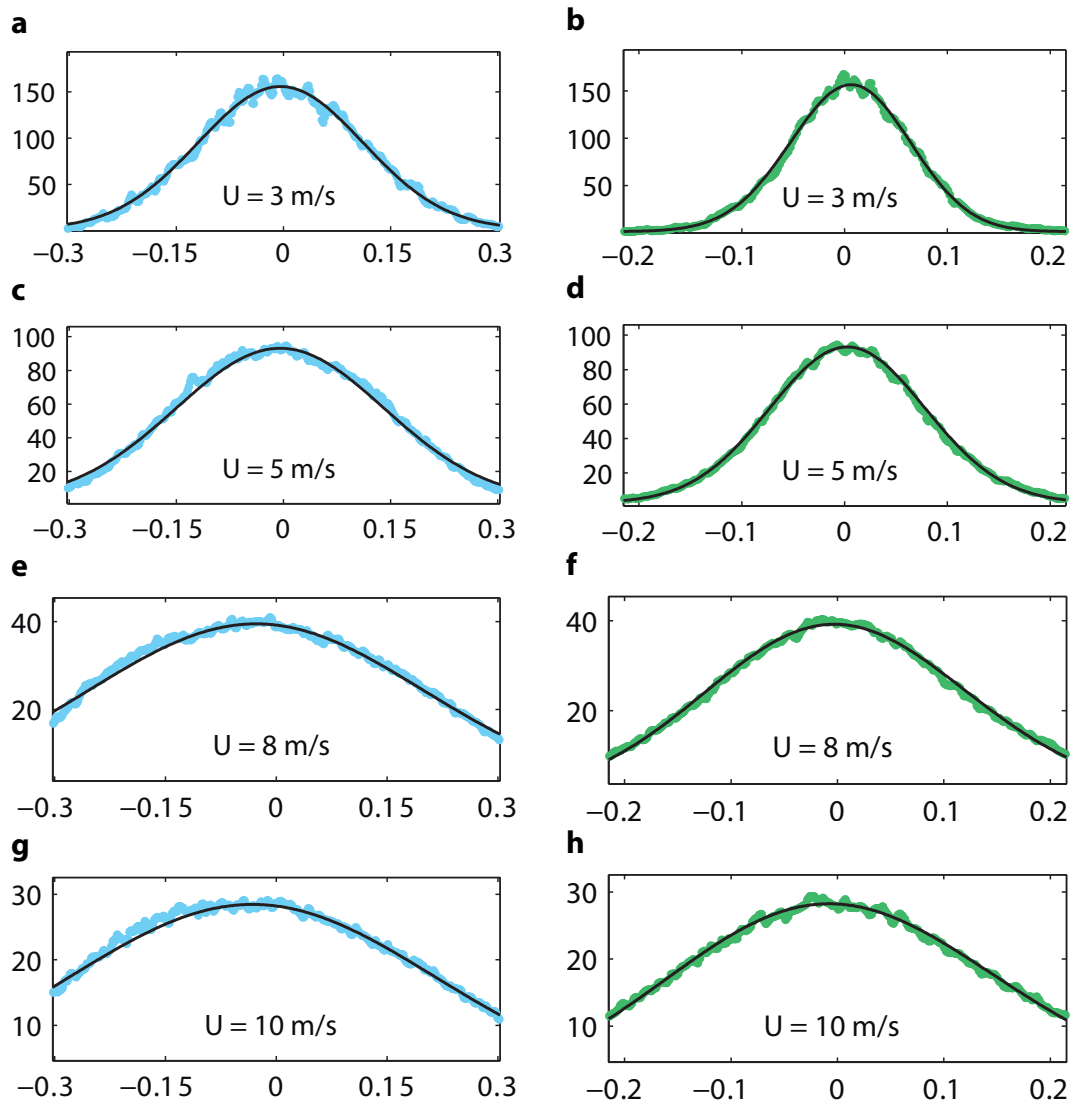


Figure 7.9.: Direct fit of the slope probability distribution from MASG images. The model function is a Gram-Charlier expansion including 2 skewness coefficients. The model describes the measured pdf accurately at low wind speeds (**a-d**), at higher wind speeds, there are some deviations, especially in the alongwind component (**e, g**).

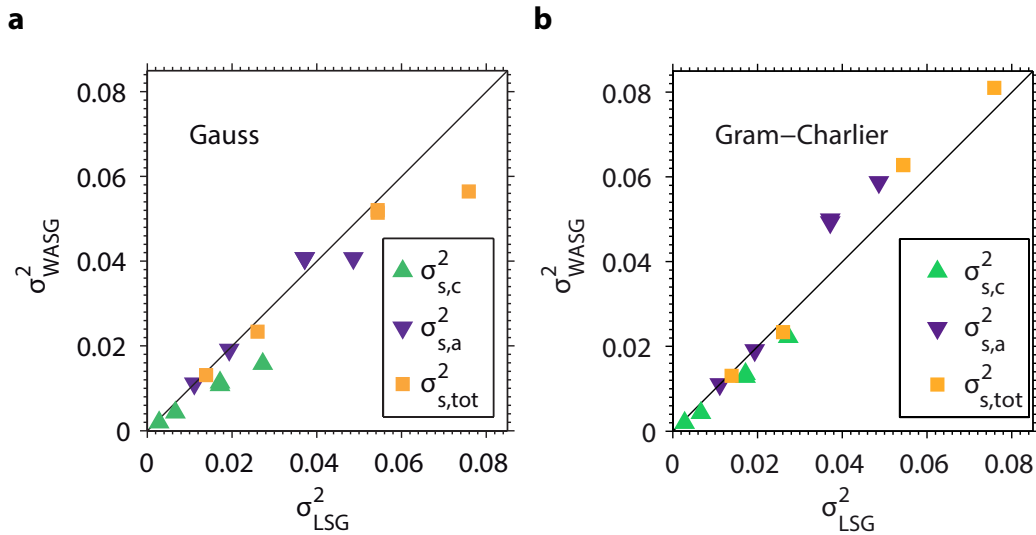


Figure 7.10.: Comparison of mean square slope extracted from fits using the two different model functions **a** eq. (7.3) and **b** eq. (7.4). Reference data measured with a laser slope gauge (LSG) was kindly provided by G. Caulliez. The Gram-Charlier expansion model better reproduces the reference σ_s^2 in the cross-wind direction (green symbols) and in the along-wind direction (purple symbols) at low wind speeds, at high wind speeds it overestimates mean square slope.

7.2 Statistical wave measurements

The measurement of wave slope statistics is the main task for which the RSSG (and MASG) were constructed for. Mean square slope has been shown to be a better parameter than wind speed to describe gas transfer rates (Frew et al. 2004, Jähne et al. 1987). However, because it is hard to measure in the field, this parameter is missing in many gas exchange studies. With the new instruments, mean square slope can be measured under a wide range of conditions in field experiments, day and night. From the Meteor cruise, a total of 181 measurements of mean square slope σ_s^2 from the MASG and 284 measurements of the surface roughness parameter χ from the RSSG are available.

7.2.1 Slope probability distribution measurements

The MASG measures the probability distribution of surface slope in the range of ± 0.35 (see sec. 3.3). A few typical examples are shown in Fig. 7.11. The wind is coming from the bottom of the 2D slope distributions and blowing upwards along the white lines. Cross-sections of the pdf including the fitted Gram-Charlier expansion are shown in the top (crosswind direction) and right (alongwind direction) panels.

In contrast to the laboratory measurements, the distributions are generally narrower, mostly owing to the fact that wind speeds were rather moderate. The pdf in Fig. 7.11a, b and d are almost isotropic and from the pdf alone it is not possible

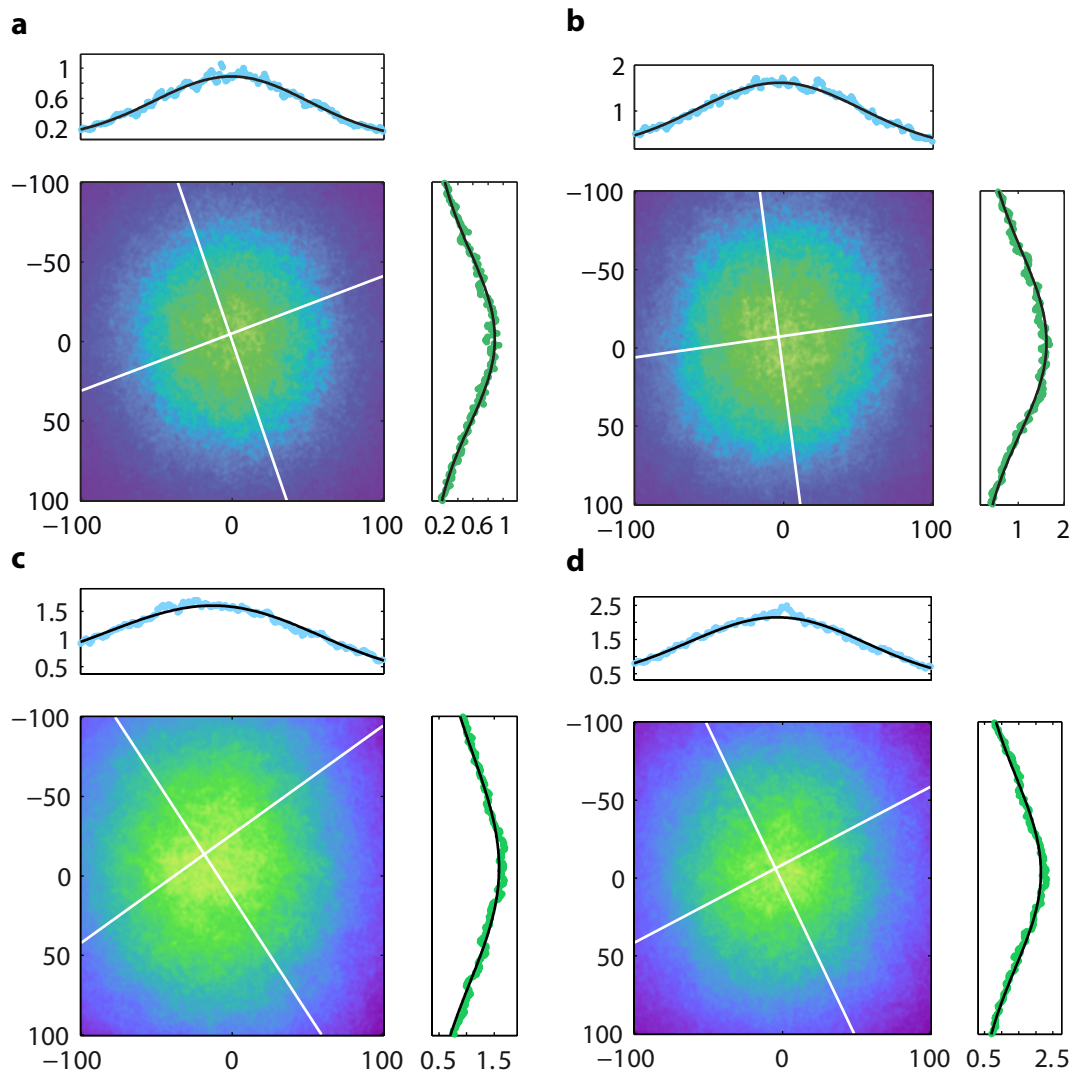
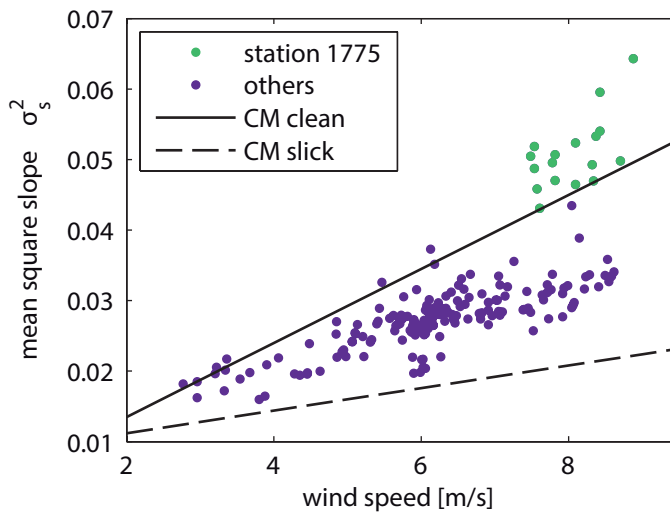


Figure 7.11.: Typical examples for slope probability distributions measured by the MASG during the Meteor cruise. The wind is coming from the bottom, and blows in the direction of the white line. Except for panel **c**, the pdfs have almost no anisotropy.


Figure 7.12

The dependence of mean square slope σ_s^2 measured by the MASG on wind speed U_{10} . Except for the measurements from one station, they lie in the range spanned by the two CM parameterizations.

to estimate wind direction. In the laboratory, the situation was clearly different (Fig. 7.8). While it is well known that the anisotropy is larger in the lab, the isotropy of the field measurements is still surprisingly pronounced.

Figure 7.11c was measured at a station with very complex conditions. Due to a mixture of swell, currents and higher wind speeds from different directions, it is likely that the measurements were seriously affected by the ship.

Mean square slope

The Gram-Charlier expansion described in sec. 7.1.2 was fitted to the measured pdf. From the fit, the mean square slope σ_s^2 was obtained. Figure 7.12 shows the distribution of the measured σ_s^2 plotted over wind speed. Additionally, the parameterizations given by Cox and Munk (1954a) (CM) for clean water (solid line) and water covered by an oil film (dashed line) are shown.

Wind speed data that was measured on the Meteor at a height of 35.3 m was scaled to the standard U_{10} , the wind speed at 10 m height. The empirical power law

$$\frac{U_1}{U_2} = \left(\frac{z_1}{z_2} \right)^p \quad (7.5)$$

was used for scaling, with $p = 0.11$ (Hsu et al. 1994). The power law is only an approximation for the logarithmic wind profile. However, in the absence of measurements of the friction velocity or the aerodynamic roughness length, the logarithmic profile cannot be applied. Also, the corrections on wind speed are not substantial, as U_{10} is only 12.5 % smaller than the measured wind speed. The CM relations were also scaled to U_{10} , since their wind speed was measured 41 ft (12.5 m) above the surface.

The scatter in the data in Fig. 7.12 is not surprising. It demonstrates that the roughness of the surface is not solely depending on wind speed. The measured

values agree with the range spanned by the two CM parameterizations, but are generally lower than the CM clean water case. An exception are the green points in the top right corner. All these data points were measured at a single station (station 1775). This is also the station that the pdf shown in Fig. 7.11c belongs to. As was already mentioned, conditions at this station were complex and contamination of these measurements by the interaction of the ship with currents and swell cannot be excluded.

The statistical error in determining the mss from a 5 minute average of MASG images is estimated to be 4 %. This estimate was obtained from the analysis of a very long measurement during the Marseille 2012 experiment under the assumption that conditions in the facility were stable. The error given here is the standard deviation of the 5 minute averages computed from this laboratory data set.

RSSG mean square slope calibration

The RSSG cannot measure mss directly, but derives a roughness parameter, χ , from the measurement of the probability for slope zero (sec. 6.3.2). This roughness parameter is expected to be proportional to the overall mean square slope, which was verified in the laboratory experiments (sec. 7.1.2). There, it was also possible to determine a calibration curve which relates χ to σ_s^2 . A straight forward way would be to apply this calibration also to the field data. However, since simultaneous measurements of mss are available from the MASG, a new in-situ calibration is determined. The resulting calibration differs from the laboratory measurements. This is due to the changes of the setup that occurred between March 2011 and December 2012. If only the laboratory calibration were available, these changes could be mostly corrected, but since the direct comparison with the MASG is possible, this is not necessary.

RSSG measurements were possible day and night, while the MASG data can only be analyzed for nighttime measurements. During daytime, MASG measurements are seriously affected by sky light (similar to the RSSG measurements during the OSSPRE cruise in 2011, see Fig. 7.6). RSSG measurements are not affected, because a different wavelength range is used in which natural light has been filtered by the water content of the atmosphere ($\lambda_{\text{peak}} = 940 \text{ nm}$ for the RSSG, $\lambda_{\text{peak}} = 850 \text{ nm}$ for the MASG). Therefore, a larger number of measurements were recorded with the RSSG.

The calibration curve is shown in Fig. 7.13, where the RSSG surface roughness parameter χ is plotted against the simultaneous and collocated measurements of σ_s^2 by the MASG. There is good overall correlation between the two measurement methods. The line shows a least squares regression for the whole data set. However, there is also a significant amount of scatter. The rms⁴ deviation is 5.9 %, but individual points can deviate by more than 20 %.

These deviations can partly be explained by the short averaging times: For each

⁴rms = root mean square

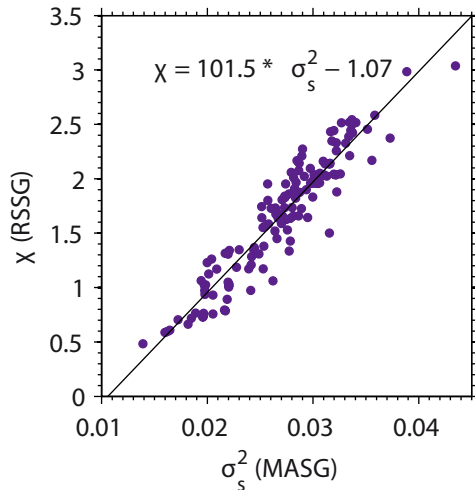


Figure 7.13

Calibration of the RSSG surface roughness parameter χ with $\text{mss } \sigma_s^2$ determined from the MASG data. Overall, the correlation is good, but scatter is also significant. For each measurement, only 5 min averages of speckle images were taken. Some of the scatter may be due to insufficient sampling.

measurement, only five minutes of data were averaged. A longer sampling time would be desirable, also to get a better average of the natural variability of the wave field. On the other hand, as will be shown in sec. 7.2.2, surface conditions were very variable due to the changing presence of surfactant coverage. Time scales during which slicks persisted could be as short as a couple of minutes. Therefore, short sampling intervals are required to resolve these fast changes in surface conditions.

The full set of RSSG measurements of mean square slope (calibrated surface roughness χ) is shown in Fig. 7.14. The data still lie in the range spanned by the two CM parameterizations. More data points coincide with the CM “slick” curve. This agrees with visual observations during the cruise. During multiple occasions, the water surface was obviously enriched with surface active material. The ocean color also changed notably from a dark blue in clear deep water to dark green in (coastal) areas with a lot of biological activity.

It should be noted that the CM parameterizations were not originally determined as upper or lower bounds on the measured mss distribution. They were fitted to the values of mss measured at an unmodified (and presumed clean) water surface and a water surface on which waves were damped by a deliberate oil film (Cox and Munk 1954a). Therefore, in clean water, mss values are expected to scatter around the CM “clean” parameterization. Mean square slope measured during the Meteor M91 cruise was thus systematically lower than that measured by CM. A reason why the measured mean square slope values were mostly higher than the CM “slick” parameterizations may be the different characteristics of natural surfactants (forming a mono-molecular layer) and oil spills (forming a thick viscous film, see sec. 2.1.3).

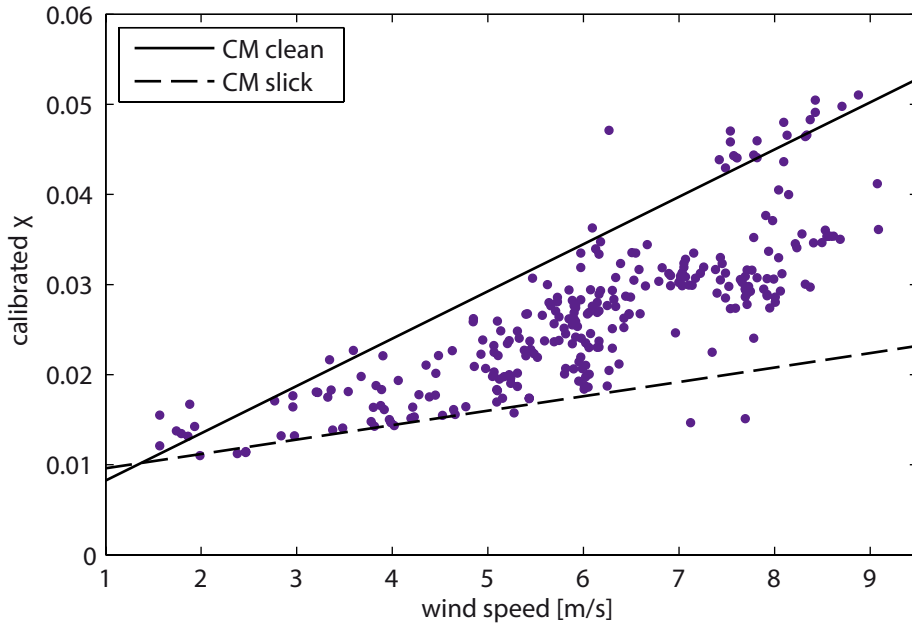


Figure 7.14.: The dependence of calibrated surface roughness χ (equivalent to mean square slope σ_s^2) on wind speed U_{10} .

Anisotropy of the wave field

The ratio between the mean square alongwind slope σ_a^2 and the mean square crosswind slope σ_c^2 was reported by CM to lie between 1.0 and 0.62. Bréon and Henriot (2006) (BH) give a functional dependence of the anisotropy parameter $\gamma = \sigma_a^2/\sigma_c^2$ on wind speed

$$\gamma = 0.585 + 0.76 U_{10}^{-1}. \quad (7.6)$$

This empirical relation was deduced from the analysis of 8 million globally distributed satellite images of sun glitter. In contrast to this, the CM dataset consists of 29 runs recorded during 9 days off the coast of Maui (Munk 2009). Because of the sheer number of observations, it is tempting to assume the BH relations to be universally valid.

Figure 7.15 shows that the data set collected with the MASG does not agree with the relation given by BH (green line). Unfortunately, the data set from the Meteor cruise does not contain measurements at very low wind speeds (below 3 m/s) or higher wind speeds (in the 10–15 m/s range), where the relation given by BH predicts large differences between observed γ values.

CM speculate that the variability of γ is related to the characteristics of wave generation by wind: Constant wind speed should lead to a more directed wave field with a clear anisotropy and larger slopes in the alongwind direction. If the wind is gusty, the wave field should be more isotropic. During the Meteor cruise, wind conditions were mostly relatively stable so that the dependence of wave field

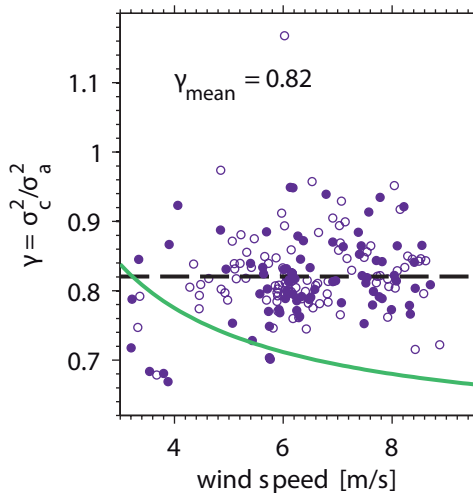


Figure 7.15

The anisotropy ratio $\gamma = \sigma_c^2 / \sigma_a^2$ over wind speed. No trend with wind speed is observable, the mean value of the whole data set (dashed line) is 0.82. The BH relation (eq. (7.6)) is shown as the green line. Clearly, it is not reproduced in the MASG data set. There is no trend with respect to gustiness either, open symbols are for less than 4% variability in the wind speed, filled symbols for more than 4%.

directivity on gustiness cannot easily be determined. Also, wind speed data is available only as one-minute mean values, so that gustiness of the wind can hardly be analyzed. Still, the data set was separated in two groups of approximately equal size: Open symbols denote measurements during which the standard deviation of wind speed was less than 4% of the mean, filled symbols measurements where the variability was greater than 4%. Both groups exhibit a similar distribution, no trend is visible.

Skewness parameters

The Gram-Charlier expansion skewness parameters c_{03} and c_{21} were found by CM and by BH to depend on wind speed. While CM assumed a linear dependence, the BH data set suggests a sigmoidal relation, because at higher wind speeds the skewness saturates. The skewness parameters that were extracted from the fits to the MASG data are shown in Fig. 7.16a,b. There is no trend visible, the data are scattered around mean values of $c_{03,mean} = 0.067$ and $c_{21,mean} = 0.013$.

The deviation from the behavior seen in the BH and CM data sets may well be due to the introduction of a shift of the origin x_0, y_0 as free parameters of the fit (see sec. 6.3.3). The two components of the shift are shown in Fig. 7.16c and d. There is also no obvious trend with wind speed, although it seems that the shift in the alongwind direction increases at higher wind speeds, consistent with the expectation that skewness of the distribution increases (panel d).

To study the dependencies of higher order moments of the probability distribution, measurements which capture the pdf for a wider range of slopes are recommended. The experiences with the MASG during the Meteor cruise showed that the light source has sufficient power to illuminate a much larger area, so that it can be used to measure a wider range of slopes.

In addition, contamination from ship motion should be excluded by measuring

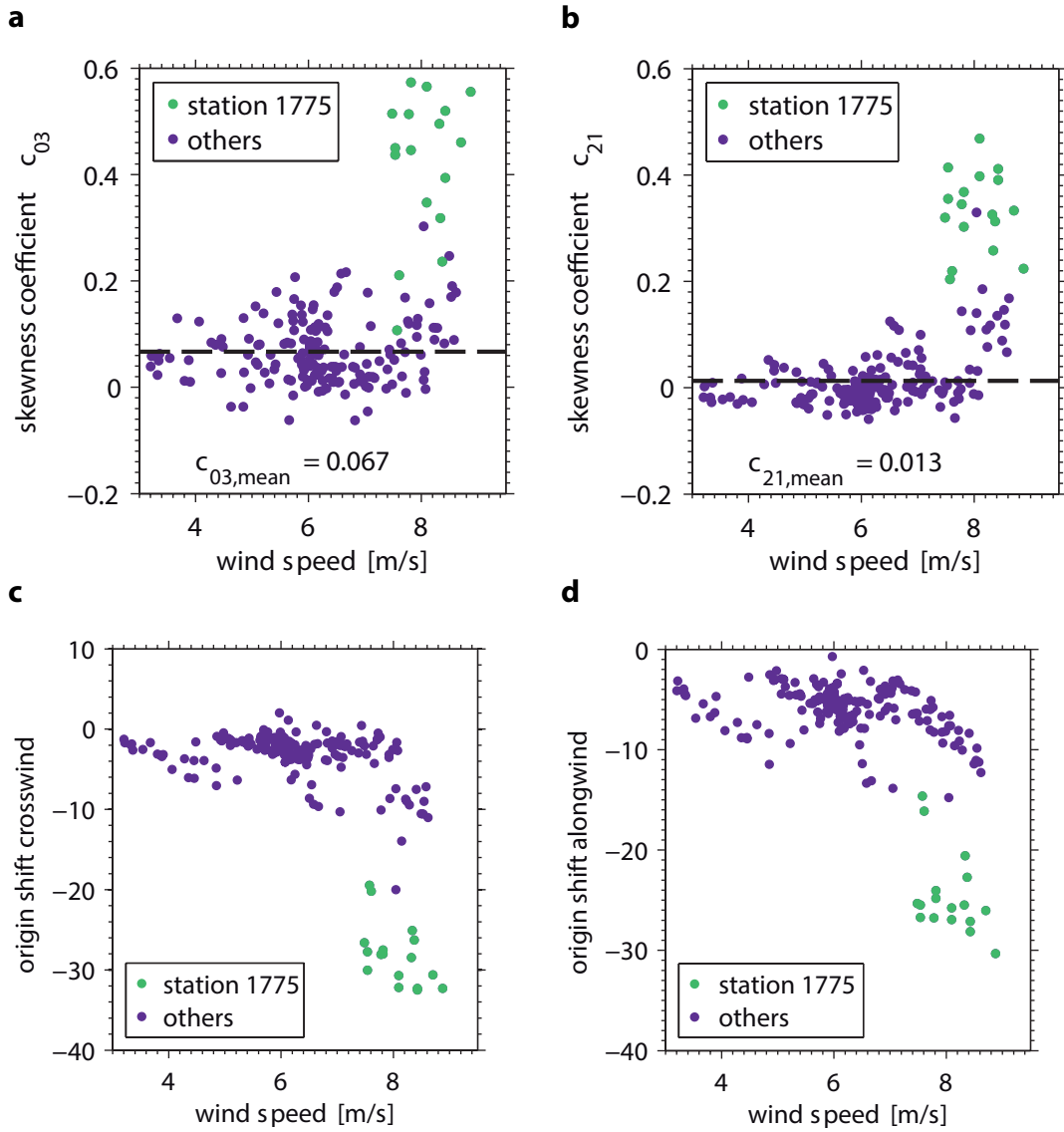


Figure 7.16.: **a, b:** The skewness parameters c_{03} and c_{21} show no dependence on wind speed. Except for the outliers from station 1775, there is no trend with wind speed visible for either of the parameters.
c, d: The shift of the origin in the fit does show a hint of a tendency towards larger shifts at higher wind speeds, at least in the alongwind component (**d**).

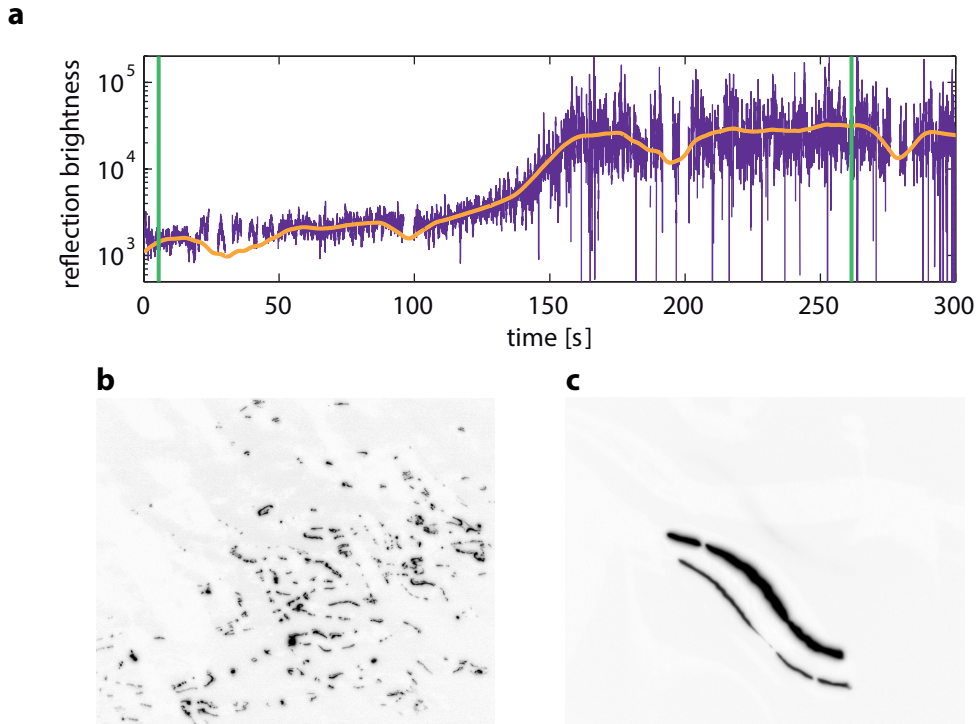
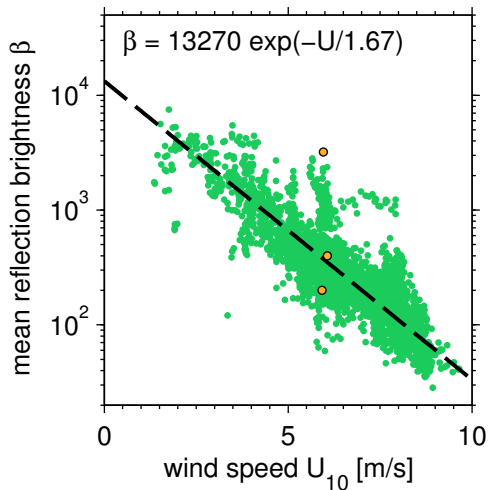


Figure 7.17.: Effect of surface slicks on RSSG images: **a** Time series of mean reflection brightness in a 6 min measurement. Raw values are shown in purple, a running mean with a time constant of 15 s is overlaid in orange. A slick is moving into the footprint after about 3 min and increases mean reflection brightness by more than an order of magnitude. Green lines indicate time at which example images were taken **b** before and **c** after the arrival of the slick. Surface roughness decreases dramatically.

from a fixed platform. There, instrument alignment could also be very precise (and stable), so that allowing for a shift in of the origin of the coordinate system is not required in the fitting routine (see sec. 6.3.3).

7.2.2 Surface curvature measurements

The brightness of individual reflections in the images can be related to the local curvature radius of the surface (see sec. 3.4.2). The local radius is determined by the smallest scale waves that are present. In other words: In the presence of capillary waves, local curvature will be very small, reflections will be dim on average. If capillary and short gravity waves are not present, local curvature radii will be much larger, and reflections will be bright. In sec. 2.1.3, the damping of waves by monomolecular slicks of surface active substances (surfactants) was described. This strength of wave damping due to the Marangoni effect is wavenumber-dependent. Short gravity and capillary waves are damped more efficiently than large wind waves or swell. Therefore, the local curvature radius should be a good indicator of the presence of surfactants.

**Figure 7.18**

The relation of the mean reflection brightness and wind speed. With increasing wind speed, the brightness decreases by multiple orders of magnitude (note the logarithmic y-axis). The large amount of scatter is mostly due to the changing presence of surface slicks. Each point is a 5-minute average of reflection brightness. The exponential fit is not meant to suggest a physical relationship, but will be useful for further analysis. The three circles mark the locations of the example images given in Fig. 7.19.

An example of this is shown in Fig. 7.17: During the 6 minute measurement, surface roughness decreases significantly. The change in surface conditions occurs over a time span of less than one minute. During the measurement, the Meteor was slowly moving forward, three minutes into the measurement, it entered a surface film and mean reflection brightness increased strongly, by more than an order of magnitude (due to decreasing local curvature radius). Two example images are shown, Fig. 7.17b is from the beginning of the measurement in clean water (at the left green line in panel a), Fig. 7.17c is after entering the slick. While in the left image many reflections are visible, the surface is almost perfectly smooth in the right image and only very few large reflections are visible, their shape is a distorted image of the RSSG line light sources.

The very strong dependence of reflection size and brightness on wind speed and surface contaminations is also visible from Fig. 7.18. Shown is the mean reflection brightness β , as determined with the watershed method described in sec. 6.4. Each point corresponds to a 30 s average value of reflection brightness. Over the range of wind speeds which were encountered during the Meteor M91 cruise, the reflection brightness drops by more than two orders of magnitude. On the other hand, at a given wind speed, there is often a variability of the order of one magnitude, caused by surface films.

As an example of the variability at one wind speed, three RSSG images are shown in Fig. 7.19. They were all acquired at $U = 6$ m/s, but at very different surface conditions (see markers in Fig. 7.18). The surface in Fig. 7.19a is clearly smoothed by a surfactant, and reflections are relatively large. Panel 7.19c is the opposite, the surface was likely clean, there are many small-scale roughness elements, the mean reflection brightness is almost three orders of magnitude lower than in 7.19a. The measurements at 6 m/s with even lower values in Fig. 7.18 were affected by the ship's bow thruster, surface roughness was not wind-created. The center image is an intermediate case. It can clearly be distinguished from 7.19a. The differences to the

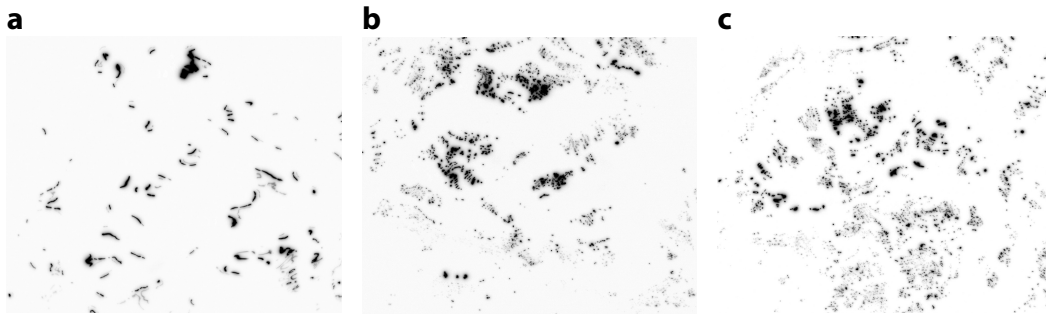


Figure 7.19.: Example images from the marked locations in Fig. 7.18. Gray values of the raw images were inverted for better visibility. Surfactant influence is clearly visible in panel **a** (top marker in Fig. 7.18), the surface appears clean in **c** (bottom marker). The difference between the intermediate (**b**) state and the clean state is not as pronounced.

“clean” image are not as pronounced.

The dashed line in Fig. 7.18 is an exponential fit to the full dataset. This is not meant to suggest a physical exponential relationship between reflection brightness and wind speed. However, this fit can help to distinguish clean water situations from slick situations. This is shown in Fig. 7.20. Six example 5 minute time series are shown, highlighting the strong variability of conditions. The dashed light blue line is the “expectation value” of reflection brightness, computed from the measured wind speed using the function determined by the exponential fit in Fig. 7.18. The purple line is the raw signal; it is the average reflection brightness for individual images. A running mean with a 15 s time constant is shown in green. Whenever the reflection brightness is clearly below the dashed “parameterization”, the water surface is likely not contaminated with surfactants, e.g. most of panel 7.20a. When reflection brightness is well above the dashed line – or in cases when significant changes occur at constant wind speed – the presence of slicks is likely (for instance the humps in panels 7.20b-d). There are limits to the informative value of the parameterization. Especially in panel 7.20e at the relatively high wind speed of 7.9 m/s it is quite possible that the water surface is clean. The lack of reference data of clean water surfaces at all wind speeds, or even of a ground truth of where surface films were present, complicates the interpretation of the measurements. The measurement in panel 7.20f is affected by surfactants. At this wind speed, the differences between clean water and surfactant covered surfaces were already shown in Fig. 7.19.

The inhomogeneous distribution of surfactants that can be seen from the variability of reflection brightness in Fig. 7.20 is also evident in Fig. 7.21. This picture was taken during the Peru experiment and clearly shows that the water surface is not homogeneously covered with surfactants. The scales on which the conditions change can be estimated from the measured time series (e.g. Fig. 7.20b-d): During the measurement, the Meteor was slowly moving forward at a speed of approximately 1.5 kn. The “humps” in the time series have a typical duration of about 100 s, which

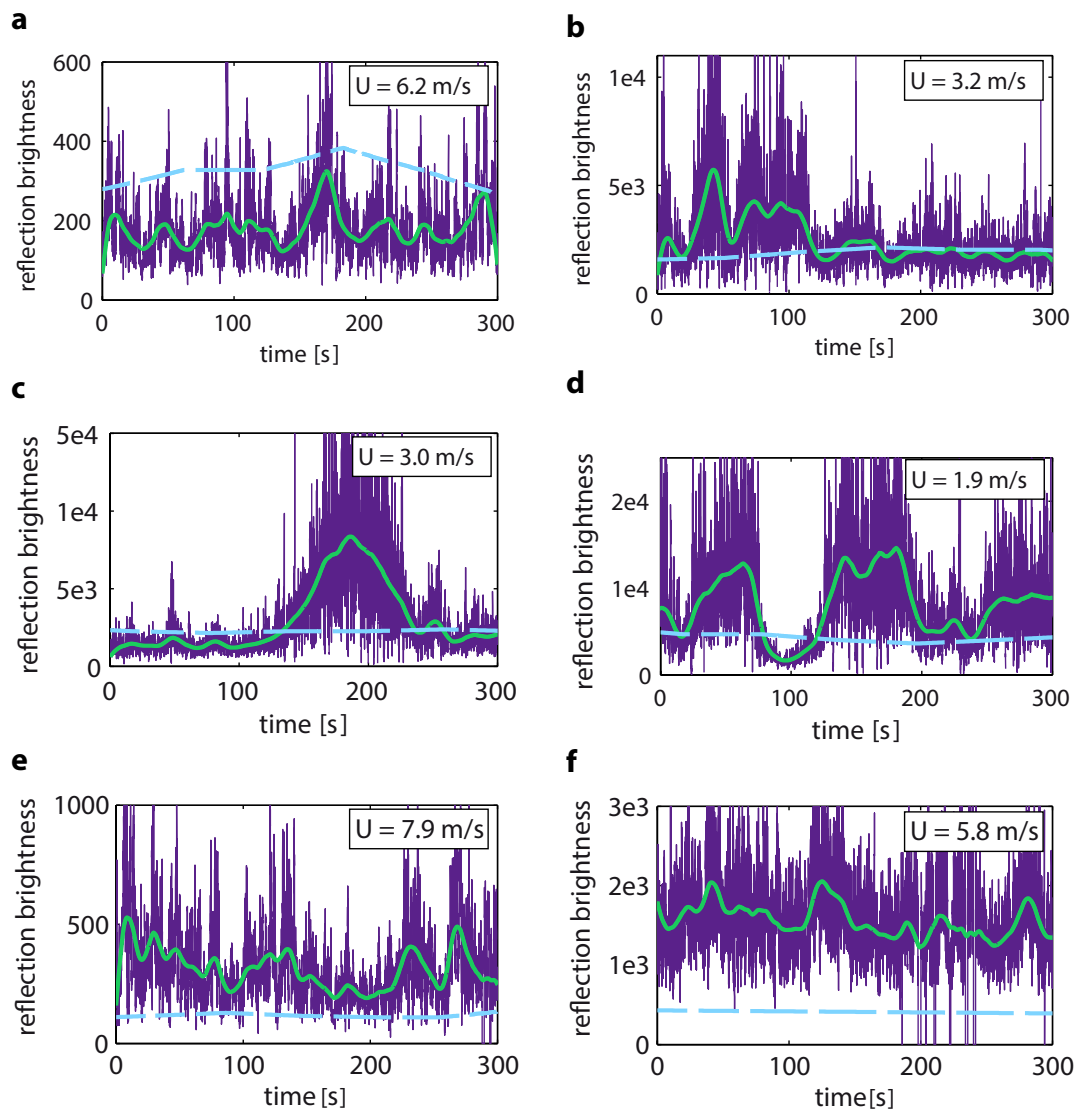


Figure 7.20.: Six example time series of reflection brightness. The dashed line is computed from measured wind speed and the parameterization of brightness with wind speed from Fig. 7.18. The purple line are the raw values (mean brightness of reflections in a single image), shown in green is a running average with a time constant of 15 s. Values well below the parameterization (**a**) are probably clean water, values well above (**f**) likely surfactant influenced. In panels **b-d**, the inhomogeneity of surface slicks is evident.



Figure 7.21.: In this image of the water surface taken during the M91 cruise on FS Meteor surface films are visible. They reduce the roughness of the surface because of their damping effect on small-scale waves.

then corresponds to a size of the slick patch of 75 m.

Overall, detailed information on surface conditions and short wind waves could be collected using the RSSG and MASG. When transfer velocities from the ACFT will be available, their dependence on mss and surfactant coverage can be explored. The data set from the Meteor cruise is large and significantly increases the data basis of simultaneous measurements of mss and transfer velocities from the field that is available from the literature. For the first time, measurements of local transfer velocities and mss have been performed at the same footprint on the water surface. In the light of the results from the curvature measurements and the observed fast changes in surfactant coverage, this is of paramount importance.

7.3 Waves and gas exchange

In the Aeolotron 2011 experiment, the effect of the soluble surfactant Triton-X 100 on waves and gas exchange was studied. Gas transfer velocities from this experiment are reported by Kräuter (2011) and Krall (2013). Here, transfer velocities for nitrous oxide (N_2O) taken from Krall (2013; section A.4.1) are used to study the effects of wave suppression by surfactants on gas exchange.

Data from four different measurement days are presented. A clean water reference case (2011/03/01), a measurement with a “low” concentration of Triton X-100 (2011/03/03) and two days with “high” concentration (2011/03/08 and 2011/03/10). The nominal surfactant concentrations were $c_{\text{low}} = 0.052 \mu\text{mol/l}$ and $c_{\text{high}} = 0.26 \mu\text{mol/l}$ (Krall 2013).

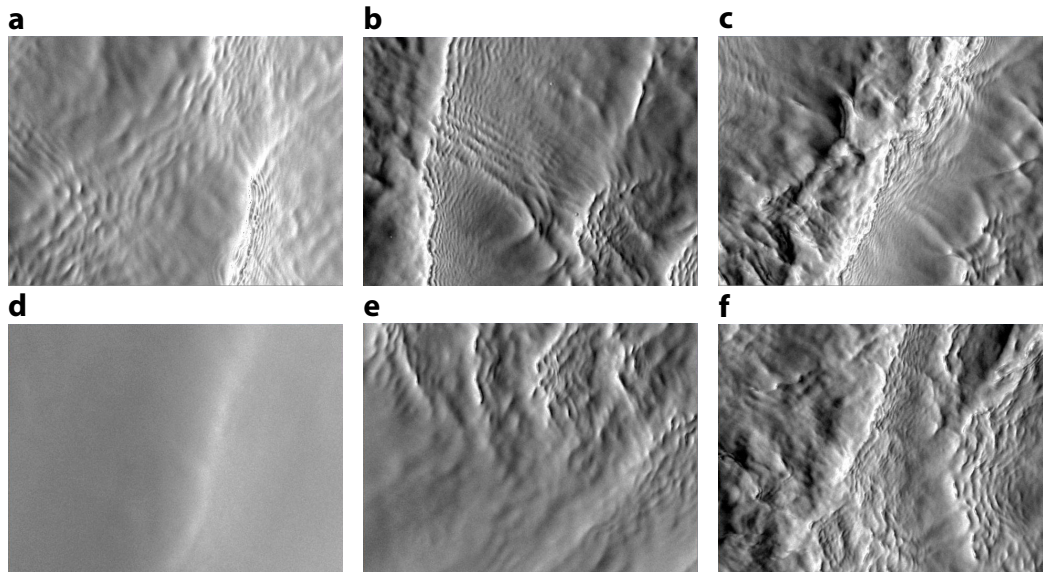


Figure 7.22.: Wave slope images measured with the Color Imaging Slope Gauge. Shown is the alongwind slope, displayed range is ± 0.7 , wind is coming from the left. The footprint size is 19×14 cm. Top row: clean water (2011/03/01). Bottom row: High surfactant concentration (2011/03/10). Wind speeds are 4.9 m/s (**a** and **d**), 6.6 m/s (**b** and **e**), and 8.3 m/s (**c** and **f**). The effect of the surfactant is clearly visible in panel **d**. In **e**, waves are damped especially in the lower part of the image (towards the inner wall of the Aeolotron).

7.3.1 Wave suppression by surfactants

The suppression of waves by the addition of the soluble surfactant is obvious from visual inspection, or more quantitatively from the study of slope power spectra.

Example images

The example images shown in Fig. 7.22 give a good impression of the effect of a surfactant. The top row shows the wave slope in the alongwind direction in clean water. The wind is blowing from the left to the right. The bottom row is from measurements with the high surfactant concentration, at the same wind speeds. The gray value scaling is identical for all images, black corresponds to $s_a = -0.7$, white to $s_a = 0.7$, where s_a is the slope in the alongwind direction.

At low wind speeds, waves are fully suppressed by the surfactant and the water surface is flat. With increasing wind speed (condition 6, $U_{\text{ref}} = 4.9$ m/s), first waves begin to develop (7.22d). The structure of the wave field is very different from the clean water case (7.22a), where many gravity-capillary waves are visible. The surfactant suppresses small-scale waves through the Marangoni effect (sec. 2.1.3), by which energy of small-scale waves is transferred into longitudinal waves that propagate in the surface film. These longitudinal waves are strongly damped by viscous forces, which leads to the overall wave damping.

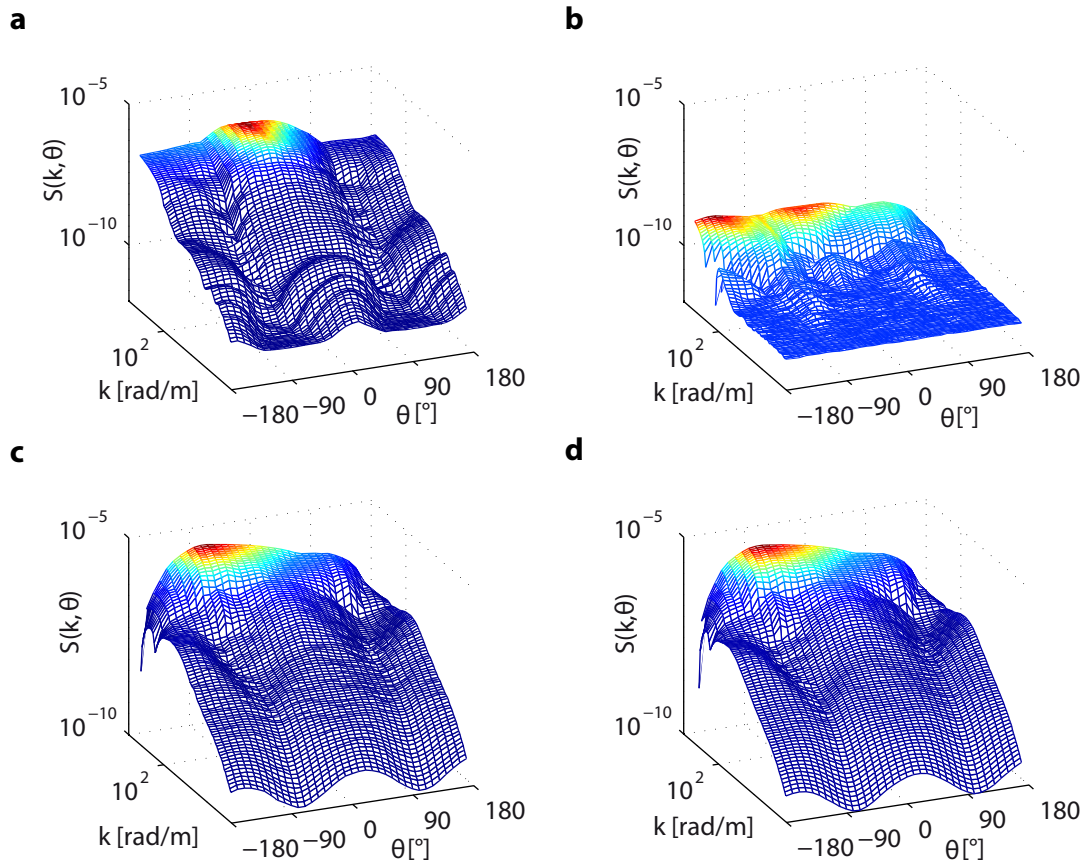


Figure 7.23.: Wave slope power spectra measured at the Aeolotron $S(k, \theta)$ in clean water (left) and with (right) the addition of Triton-X 100 (high concentration, 2011/03/08). Wind speeds are 2.7 m/s and 8.3 m/s. At lower wind speeds, the surfactant effectively suppresses the waves (**a**, **b**). At high wind speeds, the spectra look very similar (**c**, **d**).

At higher wind speeds (condition 7, $U_{\text{ref}} = 6.6$ m/s), the impact of the surfactant diminishes, capillary waves are not fully suppressed anymore (7.22e). There is a notable inhomogeneity in the wave field, the water surface is much smoother in the lower part of the image. This corresponds to the inner wall of the Aeolotron. In the further processing of the wave slope data, the assumption of homogeneous conditions over the footprint is implicitly made. At least at this stage of the wave field development, the average over the whole footprint may not be representative of the real conditions.

At the highest measured wind speed (condition 8, $U_{\text{ref}} = 8.3$ m/s), an effect of the surfactant is not noticeable anymore. Both in the clean water and in the surfactant case, the wave field is dominated by breaking larger scale waves. A breaking event is visible in Fig. 7.22c.

Directional slope spectra

The dramatic impact a surfactant can have on waves can also be seen in Fig. 7.23. Wave slope power spectra are shown for clean water (left) and water with added surfactant (right, highest concentration). At low wind speeds, the water surface is mostly flat in the surfactant case, any wave generation is prohibited (compare panel a to panel b). The total energy in the spectrum is orders of magnitude lower than for the clean water case.

With increasing wind speed, the film is torn open by the increased shear stress and waves can start to develop. At higher wind speeds, the film is mixed into the bulk by wave breaking and cannot reform due to continuing wave breaking. The wave field is almost the same as in the clean water case (compare Fig. 7.23c and d).

Omnidirectional saturation spectra

The transition from full suppression of waves by the surfactant to a wave field similar to that of the clean case can be studied in more detail in Fig. 7.24. There, the omnidirectional saturation spectrum $B(k)$ (see eq. (6.12)) is plotted over the wavenumber. The clean water reference case is shown in green, the “low” surfactant concentration case in light blue and the two “high” concentration cases in purple (2011/03/08) and light purple (2011/03/10). The dashed line is the noise level. White noise in the measured slope power spectra $S(k)$ is amplified at higher wave numbers because $B(k) = k^2 S(k)$.

At the lowest wind speed, waves are suppressed in all surfactant cases (panel 7.24a). At a certain wind speed which depends on surfactant concentration, the surface film begins to “tear open”, waves start to develop. While the development of waves starts at 2.7 m/s for the low concentration (7.24b), waves are still mostly suppressed at 4.9 m/s in one of the high concentration cases (7.24d). Apparently, the “high” concentration of Triton X-100 was not identical in the two repetitions, as the development of waves starts at very different stages of the experiment.

Another feature of the suppression of waves by surfactants is visible: Spectral energy is not raised homogeneously as the influence of the surface film reduces. Energy is first put into lower wavenumbers (below 100 rad/m), while high frequency waves are still suppressed (see the light blue and light purple line in Fig. 7.24c). This is consistent with the expectation from Marangoni theory (see sec. 2.1.3). Energy is exchanged resonantly at the wavenumber at which the “normal” transversal gravity-capillary waves have the same frequency as the longitudinal Marangoni waves. These horizontal excitations of the surface film are heavily damped because of the strong velocity gradients they induce (Alpers 1989), the energy is supplied by the gravity-capillary waves. Through non-linear interactions, also neighboring wavenumbers (and ultimately the whole spectrum) can be affected.

At higher wind speeds (panel e and f), the spectra are very similar for all four cases. This indicates that the influence of the film disappears, as it is mixed into the

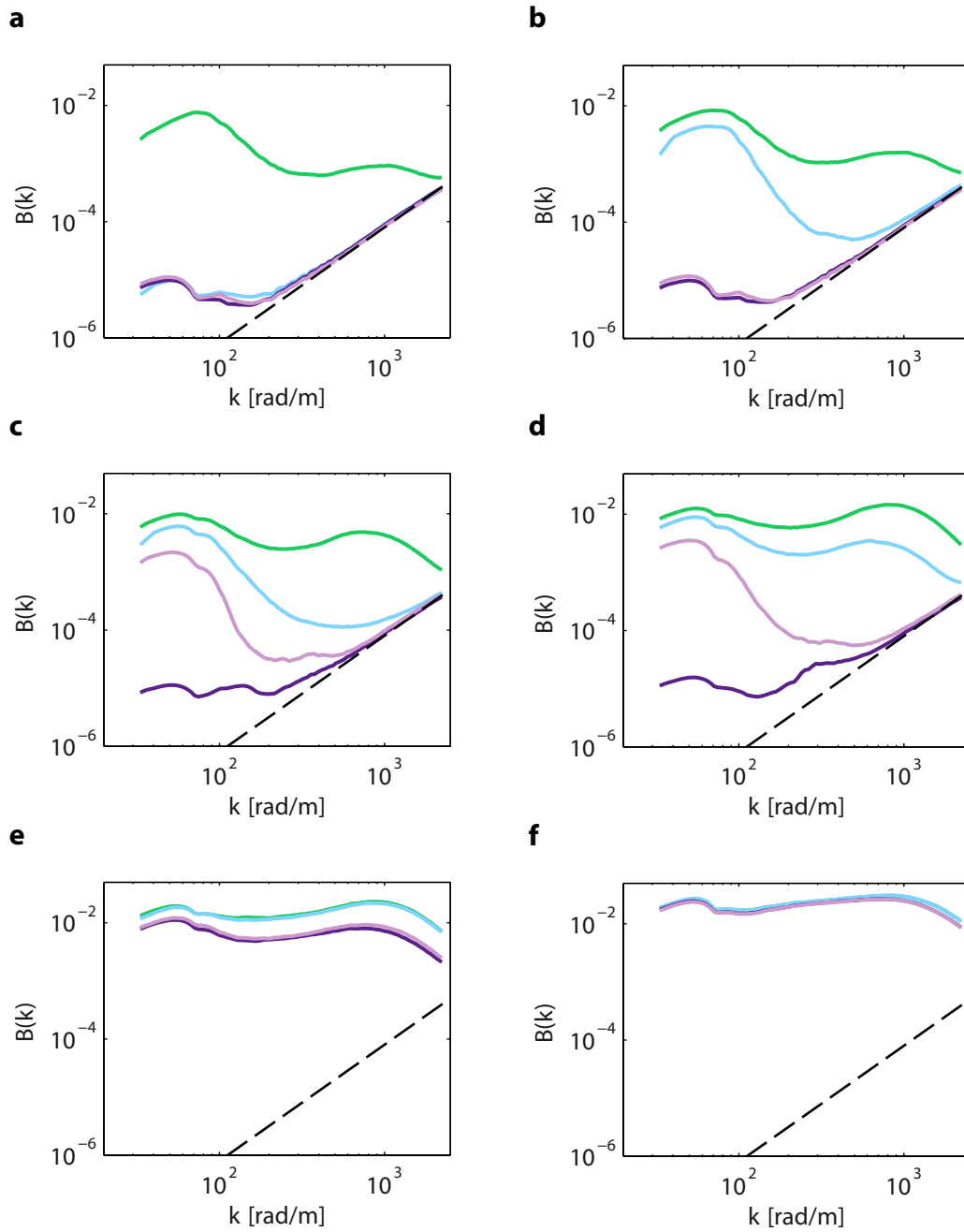


Figure 7.24.: Omnidirectional saturation spectra $B(k) = k^2 S(k)$ plotted over k . The clean water case is shown in green, the low concentration of surfactant in blue, the high concentrations in purple. Wind speeds are **a** 2.1 m/s, **b** 2.7 m/s, **c** 3.7 m/s, **d** 4.9 m/s, **e** 6.5 m/s, **f** 8.3 m/s. The dashed line is the noise level (white noise in $S(k)$). Depending on the concentration of Triton X-100, waves start to develop at different wind speeds. Lower frequency waves develop first, while high frequency waves are still suppressed. At the highest wind speed the spectral shape is nearly identical for all cases, but total spectral energy is still reduced for the cases with high surfactant concentration.

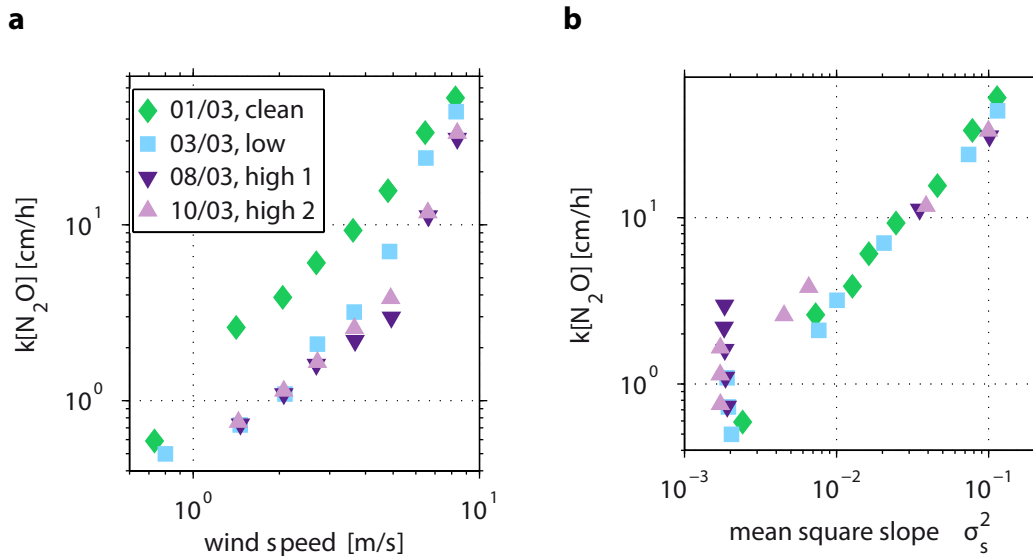


Figure 7.25.: The dependence of transfer velocities on **a** reference wind speed and **b** mean square slope σ_s^2 (cf. Krall 2013; fig. 7.11 and 7.17). Surfactants lead to a reduction of transfer velocities at the same wind speed, especially for medium wind speeds. Mean square slope can account for the surfactant effects at higher wind speeds, but fails for the lower ones.

bulk water by wave breaking and cannot reform quickly. However, there is still a slight (total) energy difference between the clean water case and the high surfactant concentration cases, even at the highest wind speed. Because the scaling was kept constant in Fig. 7.24, this is hardly visible in Fig. 7.24f.

7.3.2 Effect on gas transfer velocity

The effect of the suppressed waves on gas transfer velocities is studied with the dataset of Krall (2013). A brief analysis of the dependence of transfer velocities on mean square slope and waves is already given in her dissertation. However, the mean square slope values made available to her by Roland Rocholz from his evaluation of the wave measurements by the imaging slope gauge were only preliminary and the data set was incomplete. The reprocessed imaging slope gauge data allows for a reanalysis of the effect of surfactants on the wave field and gas transfer velocities.

Mean square slope

Figure 7.25 shows the dependence of the transfer velocity of N_2O on wind speed (left) and the mean square slope σ_s^2 (right). The color code used here is retained for the remainder of the section. Clean water is shown as green diamonds, surfactant cases as blue squares, light purple upward triangles, dark purple downward triangles, in the order of increasing concentration.

Since surfactants suppress waves and change the hydrodynamic boundary conditions at the water surface, they reduce near-surface turbulence and thus the transfer velocities k . At the same wind speed, k is reduced in the surfactant cases compared to the clean water reference. The effect is particularly large for medium wind speeds, where in clean water, turbulence induced by (microscale) wave breaking is contributing to an enhancement of the transfer velocity. The surfactant covered water surface at this stage is still flat. At higher wind speeds, when waves develop also for the surfactant cases, the discrepancy to the clean case decreases. However, even at the highest measured wind speed there is a reduction of the transfer velocity due to surfactant effects.

The correlation of transfer velocities with mean square slope (Fig. 7.25b) is good for $\sigma_s^2 > 0.01$. Clean water and surfactant cases collapse onto a single line. At low mss, the transfer velocities do not correlate at all. These are the conditions in which the water surface is basically flat. In the absence of waves, energy is transferred in the water body only by generating a shear current. The only source for near-surface turbulence then is the shear current instability. Since waves do not play a role, it is not surprising that a wave parameter cannot explain the transfer velocity behavior in this regime.

The lowest measured mss values are slightly below 2×10^{-3} . This corresponds to the noise level in the Color Imaging Slope Gauge images. Because mss is computed simply as the variance of the measured slopes, any noise on the measurement is interpreted as a contribution to mss. At higher wind speeds, wave slopes can exceed the measurement range, especially in parasitic capillary waves and when bubbles are covering parts of the surface. The data processing scheme described in sec. 6.5.2 interpolates the slope values surrounding the out-of-range surface areas to “fill” the holes. Thus, the computed mss values there are biased low. The effect is not expected to be grave due to the sparsity of these out-of-range areas.

In Fig. 7.26, another aspect of the wave dependence of gas exchange is shown: Mean square slope was computed for longer wave contributions ($k < 100$ rad/m) and short wave contributions ($k > 100$ rad/m). The correlation of k with long waves is shown in Fig. 7.26a, the correlation with short waves in Fig. 7.26b. The overall correlation is similar for both wavenumber intervals. The most prominent difference is the placement of the transfer velocities in the transition region between shear-dominated and wave-dominated: It was already noted in sec. 7.3.1 that in this transition, energy increases for the longer wave components first, before energy levels are also increased in the short wave region. This is reflected in Fig. 7.26: For $\sigma_{s,\text{long}}^2$, the transfer velocities

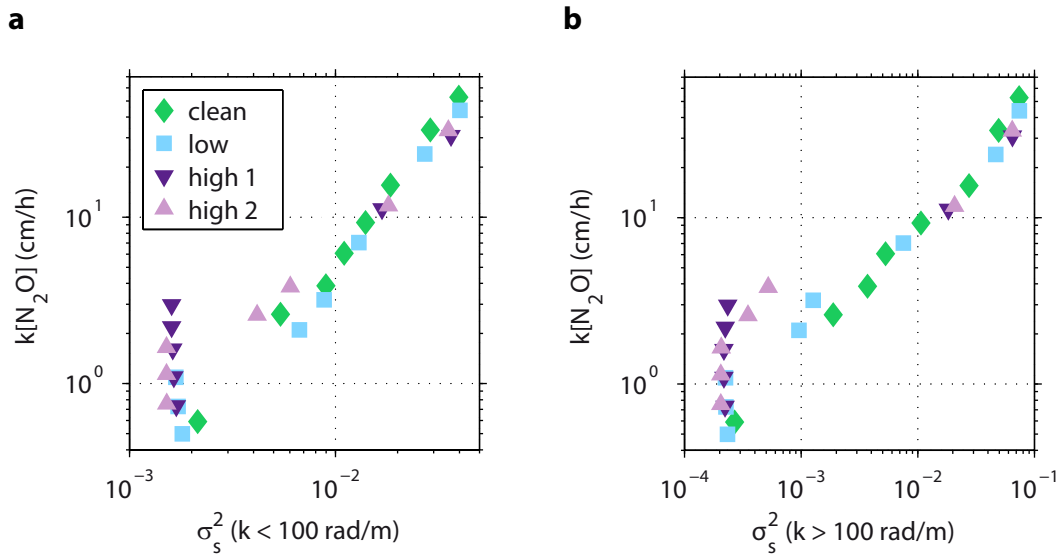


Figure 7.26.: Gas transfer velocities for N_2O plotted over mean square slope for wavenumbers **a** below and **b** above 100 rad/m. At high wind speeds, clean water and surfactant cases coincide for both. The transition towards the clean water line has a notable lag in the higher wavenumbers compared to the transition in the lower wavenumbers.

in the transition region almost coincide with the “clean water line”. When plotted against $\sigma_{s,short}^2$, there is still a large discrepancy.

The better correlation with longer waves is in contradiction to the findings of Bock et al. (1999), who found a good overall correlation of k with mean square slope, but not a good correlation of k with longer waves. Their measurements were also conducted in circular tanks, but with smaller size than the Aeolotron. Their “large” tank has a diameter of 4 m and a water body cross-section of 0.3×0.25 m (width \times height). The Aeolotron has a diameter of 8.8 m and water body cross-section of 0.6×1.0 m.

There is another discrepancy between the Bock et al. (1999) data set and the one presented here: Even at a surfactant concentration of $1.47 \mu\text{mol/l}$, they still record $\sigma_s^2 = 0.017$ at $U = 3.5$ m/s (measured at 30 cm height, corresponding to $u_* = 0.66$ cm/s). This is above the $\sigma_s^2 = 0.01$ “threshold” from which on the transfer velocities correlate well with total mean square slope in the Aeolotron data. They also note that waves were present in all their measurements, only the shorter waves are fully suppressed by the surfactant. This is in contrast to the situation in the Aeolotron experiment, where waves are fully suppressed up to $U_{ref} = 4.9$ m/s ($u_* = 0.86$ cm/s) at a much lower surfactant concentration of $c_{high} = 0.26 \mu\text{mol/l}$. The minimum mss values measured by Bock et al. (1999) suggest that they were always outside the regime with a flat water surface and full wave suppression by surfactants. Due to the different wave tank geometry it is possible that the absolute value of the friction velocity at which a transition occurs is different.

Friction velocity

Friction velocities for the conditions of the 2011 experiment were measured by Bopp (2011). At the same wind speed condition, friction velocities are consistently lower by 10-30 % in the case of high surfactant concentration⁵.

The reduction of wind stress by surface films is not surprising: The roughness of the wavy water surface is known to support a portion of the total wind stress. In the absence of waves, this additional channel for the transfer of momentum is missing. This is also visible in the measured wind speeds (see sec. A.6); wind speeds in the surfactant cases systematically exceed wind speeds for the clean water case. This is due to the way the measurement conditions are defined: Wind speed is defined by a power setting of the variable frequency drive controlling the axial fans. There is no feedback mechanism that accounts for actual wind speed. The lower wind stress in the surfactant case then leads to an increase in wind speed. The effect is small (1-2 %), but persistent, even at the highest wind speeds where an effect of the surfactant on the wave field is hardly noticeable.

Unfortunately, there are no measurements of u_* for the low surfactant case. It is expected that the friction velocity should also be reduced. However, in the absence of data, the parameterization given by Nielsen (2004) and confirmed by Bopp (2011) for the clean water case is used to compute friction velocities for the low concentration.

In Fig. 7.27, the measured transfer velocities are shown over u_* . Also shown are the two parameterizations for gas exchange used by Krall (2013). The lower bound to the transfer velocities is the Deacon model (see eq. (2.66))

$$k = \frac{1}{\beta_s} u_* Sc^{-n_s} = \frac{1}{12.2} u_* Sc^{-2/3}. \quad (7.7)$$

It is assumed to be valid so long as the water surface behaves like a rigid wall. At a free and rough surface, the hydrodynamic boundary conditions and the Schmidt number exponent change. Krall (2013) determines the following parameterization for this case, based on her full dataset⁶ of clean water transfer velocities at high wind speeds:

$$k = \frac{1}{\beta_w} u_* Sc^{-n_w} = \frac{1}{6.7} u_* Sc^{-1/2}. \quad (7.8)$$

The dimensionless constant β is a measure for turbulence intensity, its exact dependence on other physical parameters is an open question (Krall 2013).

The measured transfer velocities shown in Fig. 7.27 mostly show the expected behavior, with a transition from the Deacon model lower bound to the free surface case at higher wind speeds. It is notable that in the clean water case this transition seems to occur already at the second measured condition. In the surfactant cases, the transition is delayed. The correlation of transfer velocities with u_* is good before

⁵Due to the large errors in the estimation of u_* , the deviation is not always significant.

⁶Results from only 1 of 4 measurement days with clean water are presented here.

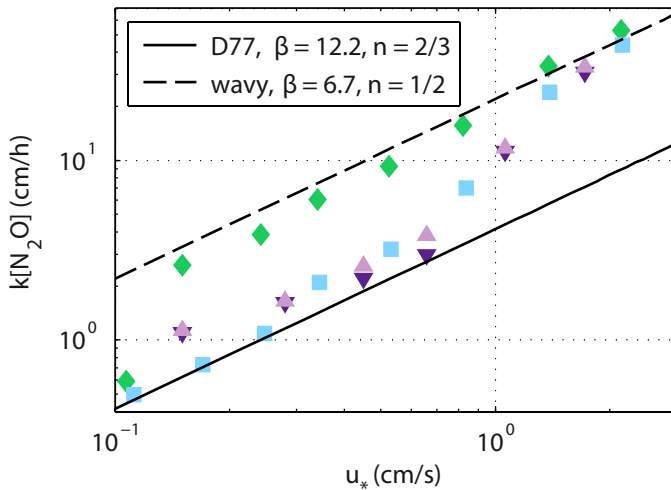


Figure 7.27
The dependence of transfer velocities k on wind stress, characterized by the (water-sided) friction velocity u_* (cf. Krall 2013; fig. 7.16). Transfer velocities are close to the Deacon (1977) parameterization as long as waves are suppressed, then ascend to the parameterization for a wavy surface.

the transition, where the water surface was flat. This is expected, as turbulence in these cases is only generated from shear-current instability. Turbulence levels should then be directly related to the momentum input and thus to the friction velocity.

7.3.3 The facet model

The facet model describes the transition of the turbulence boundary conditions from the case of a smooth water surface which acts like a rigid wall to a fully wavy water surface. In both limits, the transfer velocity is described as (see eq. (2.65))

$$k = \frac{1}{\beta} u_* Sc^{-n}. \tag{7.9}$$

The intermittency of gas exchange (Jähne et al. 2005) is accounted for by allowing certain patches of the water surface to behave like a free wavy water surface ($\beta = 6.7$, $n = 1/2$), while other patches still follow the laws for rigid walls ($\beta = 12.2$, $n = 2/3$). As was seen in Fig. 7.22e, this is not at all unnatural, especially during beginning wave development in the surfactant cases. There, wave damping was depending on radial position in the Aeolotron.

The model assumes that the fraction of the surface which is subject to “wavy” boundary conditions is depending on mean square slope alone. Two model parameters are used for the description of this transition. A midpoint parameter δ corresponds to the mss at which half of the water surface is subject to the boundary conditions of a rough surface. The steepness parameter γ determines how fast the transition between the two limiting cases occurs.

Krall (2013) shows that the facet model can be fitted to her measurements of the Schmidt number exponent. However, the model then fails to predict the transfer velocities correctly. Because the dataset used here is very similar to the data used by

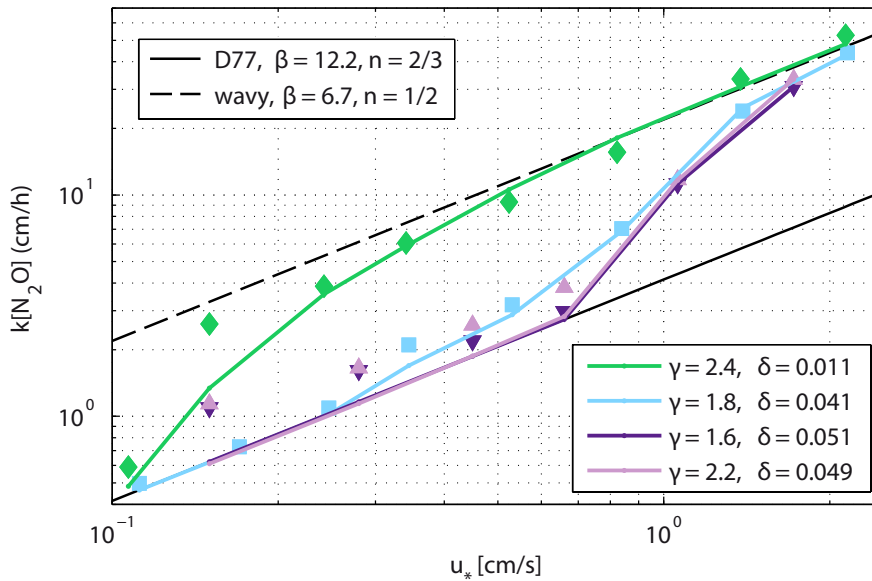


Figure 7.28.: The application of the “extended” facet model to the data set. By allowing the Schmidt number exponent transition to occur at different values of mss , the transfer velocities can be described with acceptable deviations. Color code is as in the previous figures: Clean water: green diamonds, low surfactant concentration: light blue squares, high surfactant concentration: purple upward and downward triangles.

Krall, a different outcome of the model fit cannot be expected. Therefore, a different approach is chosen. Instead of determining the model parameters δ and γ from a fit to the measured Schmidt number exponents n , the model is directly fitted to the transfer velocities. It is found that the facet model as described in sec. 2.3.3 cannot explain the behavior of the transfer velocities. Therefore, the model is extended, by allowing the model parameters to depend on surfactant concentration. The result is shown in Fig. 7.28.

The transfer velocities are shown over the friction velocity u_* . In addition to the two limiting cases for smooth (solid line) and wavy surface (dashed line), the four model curves are shown as solid lines with the usual color code. The model is generally able to capture the trends in the data, but cannot fully describe the observed values for k . In the surfactant cases, deviations occur mostly at the lowest wind speeds. This is also because the fit penalizes the absolute difference between the model value and the measurement. The small values can thus have a large relative deviation.

If the friction velocities for the low wind speed conditions can be trusted, the transfer velocities are consistently above the Deacon line (with the exception of the low concentration case, for which the friction velocity is known to be overestimated). Then, maybe it would be sensible to use a different parameterization for the transfer velocity at a smooth (surfactant covered) water surface. The transfer velocities for

the surfactant cases never reach the upper bound that was fitted to clean water data. As a consequence, the model predicts that even at the highest wind speed not the full surface is subject to “rough” boundary conditions. In the light of the observed reduced mean square slope and friction velocity of these cases in comparison with clean water, this may be a valid assumption.

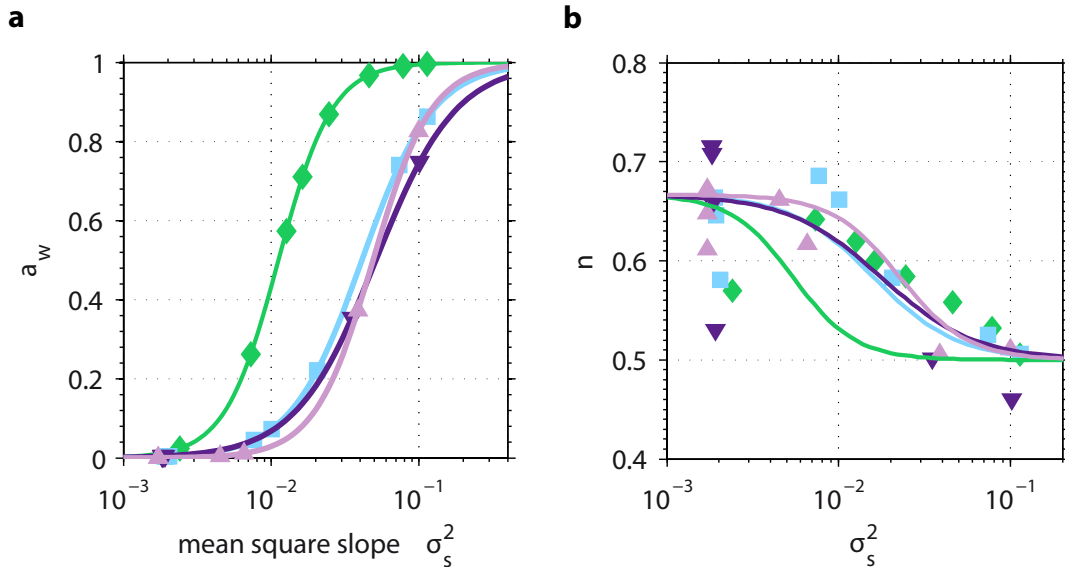


Figure 7.29: **a** The fraction of the water surface that is bound by rough water surface conditions a_w as a function of mss σ_s^2 . **b** The transition of the Schmidt number exponent from 2/3 to 1/2. The model does not agree with the measured Schmidt number exponents.

The most important consequence of the extension of the facet model is the different midpoint of the transition for the different surfactant concentrations, shown in Fig. 7.29a. In the extended model, mean square slope alone cannot describe the transition between the smooth and the wavy conditions anymore. The midpoint for clean water is at $\sigma_s^2 = 0.011$, well below the midpoints for the surfactant cases, which are at values of 0.041, 0.049, and 0.051, in the order of the suspected concentrations. Figure 7.29b shows a comparison of the facet model prediction of the Schmidt number exponent n and the measured values given by Krall (2013). The model certainly does not reproduce the measured transition of the exponent. It should be noted however, that the concept of a variable Schmidt number exponent is not part of the facet model. In deriving the relation of n and σ_s^2 , it is necessary to assume that the transfer velocity can also be described as

$$k = \frac{1}{\beta} u_* Sc^{-n}, \quad (7.10)$$

with variable β and n . This is not a prerequisite of the facet model. Also, it is questionable how accurate the measurements of the exponent n are. As an example,

the values for March 8 (purple downward pointing triangles) scatter from values larger than 0.7 down almost to 0.5 at mss values of below 2×10^{-3} . At the higher wind speed conditions, values of and below 0.5 are reached.

This seems to be in contradiction to the measured transfer velocities, which are in general agreement with the Deacon formulation as long as waves are suppressed. Even at the highest wind speed, the transfer velocities are reduced in comparison to clean water. Of course this reduction can also be explained in terms of the parameter β for which no physical model is given. This possibility is explored by Krall (2013), but no clear tendency is found. Looking at the transfer velocities for clean water in Fig. 7.28, it appears reasonable to assume that a transition occurs right at the lowest wind speeds. Also, the low midpoint parameter $\delta = 0.011$ claimed by the extended facet model for the clean case is still above the value determined by Nielsen (2004), $\delta = 0.0095$ in his experiments at the Aeolotron.

8

Discussion

8.1 Routine measurements of wave slope statistics

The usefulness of a parameterization of gas exchange is strongly correlated with the availability of data of the specific parameter. Mean square slope (mss) has been shown before to be a better parameter than wind speed to explain transfer velocities (Bock et al. 1999, Jähne et al. 1987). However, since its measurement required significant effort, gas exchange experiments with mss measurements are scarce (Frew et al. 2004). Due to this, mss parameterizations could never be established as a serious alternative to the standard gas transfer velocity/wind speed relations.

In sec. 7.2.1 it was shown that mss measurements are possible with the Medium Angle Slope Gauge only by measuring the reflection of its own light source at the water surface. Robust estimates of mss are possible from 5 minute measurements. Since the instrument uses an artificial light source and does not rely on sky- or sunlight, measurements are independent of daytime and possible also at night. It has been shown with the RSSG that in the spectral band around 950 nm natural light is strongly inhibited and daytime measurements are possible. The light source of the current MASG has an 850 nm light source due to the lack of high power wide angle LEDs with an emission peak at 940 nm at the time of construction of the MASG in summer 2012. These LEDs are now commercially available and an upgrade of the instrument is possible.

The MASG provides an elegant way to measure wave slope probability distributions (including mean square slope) under a wide range of conditions. With some minor changes in software including a direct integration of motion processing, it can measure continuously without required user interaction. The instrument simply needs to be installed sufficiently far away from the ship so that the camera footprint

is undisturbed. Since the instrument is very lightweight (less than 2 kg), mounting should not be a major concern.

During the Meteor experiment in Peru, it became also clear that the output power of the MASG light source is sufficient to illuminate an area at least 5 times larger than the current footprint of the camera. The only other requirement is to replace the camera with one that is capable of acquiring images in global shutter mode. This allows to flash the light source only during image acquisition which is crucial for thermal management in the very compact setup of the high power LEDs. With such a wide field of view, it is possible to measure slope pdf to very high slopes, which permits the robust estimation of higher order moments (skewness, peakedness) of the probability distribution which give additional insight into the properties of the wave field (Longuet-Higgins 1982). This is relevant not only to air-sea gas exchange but also to wave modeling (Kudryavtsev et al. 1999) and remote sensing (Caulliez and Guérin 2012).

An additional, potentially very simple method for the measurement of mss has emerged in the comparison of the Riegl laser altimeter with the RSSG (Fig. 7.6) during the first field experiment. It appears that the probability for slope zero can also be determined from the amplitude and quality signals of the altimeter. This was tested during the OSSPRE cruise on R/V Kilo Moana, where unfortunately the conditions were relatively stable and not a lot of variation of wind speed was encountered. From the limited data set, the laser altimeter appears to also allow measurements during the day, as the signal did not seem affected by changing solar irradiation. While unlike the MASG, the altimeter is not capable of measuring absolute values of mean square slope, an absolute calibration may be possible. A detailed laboratory investigation should follow to characterize the range and conditions under which mss can be estimated from the commercially available altimeter. These devices are popular for the measurement of wave heights in field experiments. Since they have been used in multiple air-sea interaction or wave studies (e.g. Cifuentes-Lorenzen et al. 2013, Sun et al. 2005, Veron et al. 2009, Zappa et al. 2012), it may be possible to obtain large sets of surface roughness measurements from an analysis of already acquired data.

8.2 Gas exchange and waves

One of the goals of the field experiment in Peru was to study the dependence of gas exchange on the wave field. Unfortunately, transfer velocities from active thermography are not yet available. From the wave data, it is evident that surfactants play a large role in this region, as was expected. The upwelling of nutrient rich waters from the deep ocean allows excessive biological activity. As a byproduct, surfactants are produced. Due to the large variability of surface conditions, the data set is well suited to study to which extent wave parameters can account for surfactants in explaining transfer velocities.

This was also studied in the laboratory experiment in Heidelberg, where conditions were varied in an even wider range. Transfer velocities were measured at 8 conditions, with wind speeds equivalent to $U_{10} = 1 - 15$ m/s. Also, three different concentrations of a soluble surfactant (Triton X-100) were used. The results show that mean square slope is *not* overall a good parameter (Fig. 7.25), as suggested by former studies (Frew et al. 2004, Jähne et al. 1987). At sufficient surfactant concentrations, there exists a regime in which waves are fully suppressed and turbulence can only be created from shear flow instability. This was not observed in similar laboratory studies (e.g. Bock et al. 1999).

In this regime, the transfer velocity scales reasonably well with the friction velocity. Transfer velocities are consistently higher than those predicted by the Deacon model, but this might also be due to erroneous friction velocity estimates. Recent (and preliminary) measurements by Bopp (2013) suggest that at high wind speeds and for clean water the friction velocity may be up to 20 % lower than previously assumed, while at low wind speeds (below 3 m/s) it is slightly higher. The strength of the reduction of the friction velocity for surfactant measurements will also be reexamined.

During the Meteor cruise, very smooth slick-covered surfaces were encountered (e.g. Fig. 7.17) at very low wind speeds. Still, some waves were always present and mean square slope values generally exceeded the threshold $\sigma_s^2 = 0.01$ for which mss was found to be a better parameter for gas transfer velocities than wind speed or friction velocity in the Aeolotron.

The total mean square slope seems capable of explaining the transfer velocities at a wavy water surface. It is not expected that waves at all wavenumbers contribute evenly to enhancing gas exchange. Several small-scale processes have been shown to increase gas transfer velocities or near-surface turbulence. These are the (microscale) breaking of short wind waves with wavelength of the order of 0.1 – 0.5 m (Jessup et al. 1997, Siddiqui et al. 2004); small-scale Langmuir circulation which appears coincidental with the onset of waves (Melville et al. 1998, Veron and Melville 2001); and shear induced turbulence, visible as “fish scales” in thermal imagery (Schnieders et al. 2013). These processes have all been linked to gas exchange separately, a unified parameterization explaining the relative contributions of the different processes does not yet exist. Evidence suggests, that microscale breaking is the dominant process at moderate wind speeds (Zappa et al. 2004). It has also been shown that it can be parameterized with mean square slope (Zappa et al. 2002). The question of what the exact spectral fingerprint of microscale breaking looks like is not answered yet. While microscale breaking requires short gravity waves with wavelengths of tens of centimeters, it is also linked to the generation of steep parasitic capillary waves, which may strongly influence mean square slope.

For the surfactant cases, it was clearly shown that energy is put into the longer waves ($k < 100$ rad/m) first, before the very small-scale ripples appear (Fig. 7.24). The capabilities of the Color Imaging Slope Gauge to measure longer waves are too limited to further investigate the development of the wave field in the presence of a

surfactant. With the new Imaging Slope Gauge (Kiefhaber et al. 2013), higher quality data for small-scale waves and better frequency resolution will be available. The additional integration of a wave height point measurement adds information on the longer waves.

The facet model was extended to account for the effects of surface films. The extension requires that the transition of the surface from rigid wall-like to free, wavy boundary conditions occurs at very different surface roughnesses (σ_s^2) depending on whether or not a surfactant is added to the water. The midpoint, at which half is subject to wavy boundary conditions, is at $\sigma_s^2 = 0.011$ for clean water, and at $\sigma_s^2 = 0.041, 0.049, 0.051$ for the surfactant conditions (in the order of increasing concentration). If this is correct, it suggests that for the surfactant cases at some point waves develop, but do not contribute to near-surface turbulence. This generally seems possible, especially since capillary waves are still suppressed much longer than larger waves. These capillary waves are usually a byproduct of instable or microscale breaking gravity capillary waves. It is unclear however if the lack of capillaries is due to their rapid damping by the surfactant or due to the lack of processes that generate them. After the current rebuilding of the Aeolotron is completed and the air can be dehumidified, this can be studied directly using thermal imagery. If microscale breaking in fact occurs at these conditions, it will be visible in the IR images (Jessup et al. 1997).

The transition of the average Schmidt number exponent n from $2/3$ to $1/2$ can be derived from the facet model. Direct measurements of n by Krall (2013) disagree with the prediction of the facet model. On the other hand, some doubts were raised as to whether or not the measured Schmidt number exponents are correct. These measurements are complicated, especially when diffusion constants are not known with the required precision and gases that are used have relatively close Schmidt numbers. For future experiments, a new mass spectrometer is available. This allows to extend the range of Schmidt numbers for which gases can be measured. This should lead to robust measurements of the exponent. With these new measurements, the extended facet model can be tested.

Finally, combining what has been learned from the analysis of the gas exchange data, mean square slope is a good correlate for transfer velocities, as long as waves are present on the water surface. Even though the connection between mean square slope and gas exchange is not fully understood, the current data set once again shows that surfactant influence can generally be parameterized with the total mean square slope of the waves. Especially the comparison with a parameterization with wind speed (Fig. 7.25) highlights the need for a replacement of the currently used wind speed-parameterizations. With the advances in instrument development presented in this work, a large step towards simple routine mss measurements is taken. This is a prerequisite for any parameterization that should be of practical use.

8.3 Future measurement of waves in the field

The main goal of this study was to develop a robust measurement method for short wave statistics, particularly mean square slope. The RSSG and MASG are capable of this. As a byproduct of the experience gained in the development and deployment of these instruments and from the investigation of alternatives, a number of conclusions can be drawn for the development of future instruments capable of collecting even more information on the wave field on different scales.

8.3.1 Long wave measurements

The measurement of wave heights using the Helmholtz stereopsis principle with two light sources and two cameras was shown capable of producing accurate results in the RSSG (sec. 7.1.1) on a small footprint of little more than a square meter.

The recent progress in LED technology enables the use of Helmholtz stereopsis also on larger scales. Since the distribution of specular reflections is depending on the distribution of the smallest scale waves that are present on the water surface, in looking at larger scales the relative importance of the inhomogeneity of the reflections is decreased. If the width of areas without information is much less than the wavelengths of interest, the measurement should not be severely affected by the data dropout. Therefore, such a system could be used to measure directional wave spectra of longer wind waves (in the range of the spectral peak) and swell. The measurement of directional spectra on this scale is not a simple task and an optical system capable of reliably delivering this information should be appreciated.

In such a setup, the use of (expensive) near infrared LEDs is not required. Upwelling light (reflected back from scattering particles in the water) will only add a diffuse background to the sharp reflections. This should not interfere with the disparity estimation. In a specialized system, in which the gray values do not need to be interpreted for slope or curvature statistics, reflections may be oversaturated. Therefore, the light sources can be set to a high brightness, so that also very faint reflections become visible.

The small pixel size of current CMOS cameras and the ability of reconstruction algorithms to determine the disparity with subpixel accuracy allow for a compact setup with a small stereo base. The disparity d seen by a stereo setup with parallel optical axes is given by (Jähne 2005; sec. 8.2.1)

$$d = \frac{bf}{h} \Rightarrow \Delta d \approx \frac{bf\Delta h}{h^2}, \quad (8.1)$$

with the stereo baseline b , the focal length of the lenses f and the distance to the water surface h . At a working distance of $h = 10$ m and with a stereo base of $b = 0.3$ m, a change in surface elevation of 1 cm causes a change in disparity of $\Delta d \approx 0.1$ pixel, if lenses with focal length $f = 8$ mm are used on cameras with $2.2 \mu\text{m}$ pixel pitch. In

this setup, with a standard 5 mega-pixel camera, an area of 5×7 m can be observed. An accuracy of 0.1 pixel in the determined disparity is certainly close to the limit of what can be achieved under realistic conditions. The height measurement accuracy will also be impacted by the window size, over which the disparity is averaged in block matching (sec. 6.2.1). Over typical window sizes used in this study, the height of the sea surface certainly changed more than a centimeter, which limits the required maximum accuracy of disparity estimation. From such measurements, it should be possible to determine directional wavenumber spectra even for swell. Because the wavelength of swell is much longer than the window size, the wavenumber can be obtained with techniques like the wavelet directional method (Donelan et al. 1996) or the Fourier decomposition method (Troitskaya et al. 2012). In these methods, virtual wave point probes are used to determine directional spectra of waves with wavelengths much longer than the separation of the virtual probes.

8.3.2 Curvature measurements

The mean brightness of reflections was shown to be very sensitive to changes in the wave field, e.g. by varying surfactant coverage of the surface (sec. 7.2.2). The measurement of such information on the local curvature of the water surface was not a design goal of the RSSG. While the RSSG performed surprisingly well and important information on surfactants was collected during the Meteor cruise, the setup was optimized for wave height and slope measurements and improvements are possible to gain more robust estimates of curvature statistics.

Due to the large light sources of the RSSG, individual reflections cannot be separated easily in the images. A watershed algorithm is used to separate overlapping reflections (sec. 6.4) but tends to “oversegment”: Larger reflections with inhomogeneous gray values are cut into multiple pieces.

The use of a “point-like” light source should allow for a more simple separation of reflections. Then also the number of reflections, which is linked to the mean square curvature (sec. 3.4.2), can be estimated reliably. Curvature measurements with “point” light sources are not trivial. The large size of the LED arrays in the RSSG are the consequence of the experiences made with smaller light sources in experiments at the Aeolotron (Kieffer 2010). With the LEDs available at the time (2009), it was not possible to generate a sufficiently strong signal for height measurements at higher wind speeds. Again, the progress in LED technology has been enormous and a compact light source built from a few state-of-the-art (2013) emitters should be sufficient to illuminate a spot of $1 - 2 \text{ m}^2$.

8.3.3 Drones

The slope pdf and curvature measurement techniques are ideally suited for drone-based measurements. The rapid development of small, inexpensive multi-rotor autonomous drones (e.g. “octocopters”) will likely continue as logistics companies and retailers are exploring their capabilities for delivering goods. At least in low wind speed conditions, they can easily be started off and landed on research vessels and allow to sample large areas on short time scales. With a sufficient altitude, it should be guaranteed that the wave field is not affected by the vehicle. This is not always the case for ship-borne measurements.

Motion correction is certainly one of the major problems with such small-scale drones. During daytime measurements, a solution for this problem can come from image processing: By adding a camera which observes the horizon with a suitable wide-angle lens, the motion of the drone can be determined from the motion of the horizon in the images (assuming that the height is nearly constant). Standard computer vision algorithms should be able to determine the apparent motion of the horizon in real time at a sufficient frame rate. This approach may seem complicated. On the other hand, the inertial measurement unit used for motion correction in this study is worth >10.000 EUR. For the computer vision approach, only an inexpensive camera is needed.

9

Conclusion and Outlook

9.1 Conclusion

Robust measurement of short wind waves in the field

Establishing an alternative parameterization for air-sea gas exchange that does not rely on wind speed measurements requires the availability of robust estimates of the used correlate (sec. 2.3). In this work, novel imaging techniques have been developed, capable of measuring the mean square slope of the ocean surface in a robust way. This parameter is the only realistic candidate for replacing wind speed as the standard correlate (sec. 2.3.4).

Unlike other available instruments (sec. 3.1), the Reflective Stereo Slope Gauge (RSSG, sec. 4.1.1) and its successor the Medium Angle Slope Gauge (MASG, sec. 4.1.2) are independent of natural light, capable of measuring day and night. The instruments are easy to deploy and underwater parts are not required as the measurements solely rely on the reflection of the instruments' light sources on the ocean surface. From the acquired images of specular reflections, the two-dimensional slope probability distribution, the mean square slope, as well as wave heights and a parameter related to local surface curvature of short wind waves are extracted (see sec. 3.2, sec. 3.3, and sec. 3.4).

Data processing schemes that were developed in this work allow for automated processing of these height (sec. 6.2), slope sec. 6.3, and curvature parameters (sec. 6.4). For ship-based measurements, a motion correction scheme was implemented (sec. 6.1).

The new instruments' performance was validated extensively with reference measurements both in the laboratory (sec. 5.1) and in the field (sec. 5.2, sec. 7.1). The mean square slope measurements agree well with values determined by a laser slope

gauge in the Marseille wind wave facility (sec. 7.1.2). Wave height measurements were validated with a wave wire in the laboratory and with a commercial laser altimeter in the field (sec. 7.1.1).

To replace wind speed parameterizations and establish mean square slope as a correlate, instruments capable of measuring mss robustly and with minimal user interaction are required. This study is an important step in this direction. In addition to the mss values obtained from the MASG measurements, it was shown by a comparison with the RSSG, that data from a commercially available laser altimeter, which is built for distance measurements in industrial applications, can be used to derive a surface roughness parameter which is proportional to mss (sec. 8.1). If this can be confirmed under more variable conditions, it will solve the problem of robust local mean square slope measurements. If additional information on short wind waves is sought, it can be provided in the form of slope probability distribution functions (pdf) measured by the MASG (sec. 7.2.1). Higher order moments of this distribution (skewness, peakedness) are valuable additional statistical parameters to characterize the wave field (sec. 8.1).

Measurement of wave statistics in field experiments

Wave statistics were measured during a four week field experiment in the tropical Pacific off the coast of Peru (sec. 5.2.2). Moderate wind speeds prevailed, but very different surface conditions were encountered, from clear and clean water to heavy surfactant coverage due to enhanced biological production in the coastal upwelling zones. The variability of measured mss covered the whole range spanned by the parameterizations given by Cox and Munk (1954a) for clean water and for an oil-covered water surface. The observed anisotropy of the wave field with the wind direction was much less pronounced than predicted by other studies (sec. 7.2.1).

The mean reflection brightness in RSSG images, a measure for local surface curvature, was found to be very sensitive to the damping of waves by slicks (sec. 7.2.2). This is not surprising, as the reflection brightness is governed by the smallest scale of waves on the water surface. These waves are most strongly damped by surfactants. In some situations, surfactants were very inhomogeneous, significant changes occurred on spatial scales of less than a hundred meters. Information on surfactant coverage will be particularly valuable for the processing of the local transfer velocity measurements with the Active Controlled Flux Technique (ACFT), which is part of a separate study. Based on the positive experiences made with curvature and height measurements in the RSSG data, specialized instruments for the measurement of curvature statistics and directional spectra of long wind waves and swell have been proposed (sec. 8.3).

Waves and gas exchange in the laboratory

High quality wave data from a laboratory experiment in 2011 investigating the effect of surfactants on gas exchange was processed. The data set had been acquired with a Color Imaging Slope Gauge (CISG) set up by Roland Rocholz, but was never properly processed due to problems with the optical setup. After these problems were solved (sec. 6.5), the damping effect of the surfactant could be studied with wave slope power spectra. The transition from full suppression of waves (at low wind speeds) to a wave field comparable with that for clean water (at high wind speeds) is complex. This is due to the wavenumber selective damping by the Marangoni effect and the circular geometry of the Aeolotron (sec. 7.3.1).

Mean square slope was found to be a better correlate for transfer velocities under the influence of surfactants than wind speed or the friction velocity (sec. 7.3.2). For very low wind speeds, a regime was found in which turbulence is only generated from shear current instabilities because waves were suppressed. In this regime, the friction velocity can mostly explain transfer velocities. Comparable conditions were not experienced in the field experiment (sec. 8.2).

Overall, the Aeolotron experiment suggests that whenever waves are present at the surface, mean square slope is a good correlate for transfer velocities. This adds to the evidence that is available in the literature and strengthens the case for demanding a replacement of wind speed parameterizations with a better model for gas transfer velocities including mean square slope.

9.2 Outlook

The extensive data set of wave statistics measured during the Meteor M91 cruise off the coast of Peru adds to the few available data sets of short wave statistics in the field. As soon the data acquired with the Active Controlled Flux Technique (ACFT) is processed and transfer velocities are available, existing parameterizations with mean square slope can be reviewed and extended.

For future field experiments, design improvements have been suggested to enhance the performance of the current versions of the RSSG and MASG. A longer term study of measurements of the slope pdf, covering a wider range of wind speeds and surfactant conditions can help to improve the old Cox & Munk model for the slope distribution that is still widely used. In combination with low-cost drones, the presented surface curvature measurement technique allows surveying larger areas for surfactant distribution.

The prospect of being able to measure mean square slope with commercial laser altimeters is fascinating. A detailed laboratory and possibly field comparison is desirable to fully assess the capabilities and limitations of these instruments. Should it be possible to extend the positive results obtained in this study to a wider range of conditions, routine measurements of wave statistics would be enabled at unprece-

dedented scope. This would certainly strengthen the case of replacing wind speed as the only parameter for transfer velocities.

For the next laboratory experiment, the new high speed Imaging Slope Gauge (Kiefhaber et al. 2013) is available. Together with collocated and synchronized infrared imagery and a novel two-dimensional boundary layer visualization technique (Kräuter et al. 2013), detailed studies of the processes causing near-surface turbulence are possible.

Bibliography

- Alpers, W. (1989), The damping of ocean waves by surface films: A new look at an old problem, *J. Geophys. Res.*, 94(C5), 6251–6265.
- Apel, J. R. (1994), An improved model of the ocean surface wave vector spectrum and its effects on radar backscatter, *J. Geophys. Res.*, 99, 16,269–16,292, doi:10.1029/94JC00846.
- Asher, W., and T. Litchendorf (2009), Visualizing near-surface concentration fluctuations using laser-induced fluorescence, *Exp. Fluids*, 46, 243–253.
- Asher, W., H. Liang, C. Zappa, M. Loewen, M. Mukto, T. Litchendorf, and A. Jessup (2012), Statistics of surface divergence and their relation to air-water gas transfer velocity, *J. Geophys. Res.*, 117, C05,035, doi:10.1029/2011JC007390.
- Asher, W. E., and J. F. Pankow (1986), The interaction of mechanically generated turbulence and interfacial films with a liquid phase controlled gas/liquid transport process, *Tellus B*, 38B(5), 305–318, doi:10.1111/j.1600-0889.1986.tb00256.x.
- Balschbach, G. (2000), Untersuchungen statistischer und geometrischer Eigenschaften von Windwellen und ihrer Wechselwirkung mit der wasserseitigen Grenzschicht, Dissertation, Institut für Umweltp Physik, Fakultät für Physik und Astronomie, Univ. Heidelberg.
- Banerjee, S., and S. McIntyre (2004), The air-water interface: Turbulence and scalar exchange, in *Advances in Coastal and Ocean Engineering*, edited by J. Grue, World Scientific, Hackensack, N.J.
- Banner, M. L., and O. M. Phillips (1974), On the incipient breaking of small-scale waves, *J. Fluid Mech.*, 65, 647–656.
- Barsic, P., and C. Chinn (2012), Sea surface slope recovery through passive polarimetric imaging, in *Oceans*, 2012, pp. 1–9, doi:10.1109/OCEANS.2012.6404776.
- Bass, M. (Ed.) (2010), *Handbook of Optics*, Vol. 1–5, 3 ed., McGraw Hill.
- Bauer, P. S. (2013), Development of an imaging polarimeter for wave slope measurements, Master's thesis, Institut für Umweltp Physik, Univeristät Heidelberg, Germany.

- Benetazzo, A. (2006), Measurements of short water waves using stereo matched image sequences, *Coast. Eng.*, 53, 1013–1032, doi:10.1016/j.coastaleng.2006.06.012.
- Benetazzo, A., F. Fedele, G. Gallego, P.-C. Shih, and A. Yezzi (2012), Offshore stereo measurements of gravity waves, *Coast. Eng.*, 64, 127 – 138, doi:10.1016/j.coastaleng.2012.01.007.
- Bock, E. J., and T. Hara (1995), Optical measurements of capillary-gravity wave spectra using a scanning laser slope gauge, *J. Atmos. Oceanic Technol.*, 12, 395–403.
- Bock, E. J., and J. A. Mann (1989), On ripple dynamics II. A corrected dispersion relation for surface waves in the presence of surface elasticity, *J. Colloid Interf. Sci.*, 129, 501–505.
- Bock, E. J., T. Hara, N. M. Frew, and W. R. McGillis (1999), Relationship between air-sea gas transfer and short wind waves, *J. Geophys. Res.-Oceans*, 104(C11), 25,821–25,831, j NOV 15.
- Bopp, M. (2011), Messung der schubspannungsgeschwindigkeit am heidelberger aeolotron mittels der impulsbilanzmethode, Bachelor thesis, Institut für Umweltphysik, Fakultät für Physik und Astronomie, Univ. Heidelberg.
- Bopp, M. (2013), Personal communication.
- Bréon, F. M., and N. Henriot (2006), Spaceborne observations of ocean glint reflectance and modeling of wave slope distributions, *J. Geophys. Res.-Oceans*, 111, 6005–+, doi: 10.1029/2005JC003343.
- Broecker, H. C., W. Siems, and J. Petermann (1978), The influence of wind on CO₂-exchange in an wind-wave tunnel, including effect of monolayers, *J. Mar. Res.*, 36, 595–610.
- Butt, T., and P. Russell (2004), *Surf Science: An Introduction to Waves for Surfing*, University of Hawaii Press.
- Caulliez, G. (1998), The generation of the first visible wind waves, *Phys. Fluids*, 10, 757–759.
- Caulliez, G. (2011), Personal communication.
- Caulliez, G., and C.-A. Guérin (2012), Higher-order statistical analysis of short wind wave fields, *J. Geophys. Res.-Oceans*, 117(C6), C06,002.
- Chapron, B., V. Kerbaol, D. Vandemark, and T. Elfouhaily (2000), Importance of peakedness in sea surface slope measurements and applications, *J. Geophys. Res.-Oceans*, 105, 17,195–202.
- Cifuentes-Lorenzen, A., J. B. Edson, C. J. Zappa, and L. Bariteau (2013), A multisensor comparison of ocean wave frequency spectra from a research vessel during the southern ocean gas exchange experiment, *J. Atmos. Oceanic Technol.*, doi:10.1175/JTECH-D-12-00181.1.
- Cini, R., and P. P. Lombardini (1981), Experimental evidence of a maximum in the frequency domain of the ratio of ripple attenuation in monolayered water to that in pure water, *J. Colloid Interf. Sci.*, 81(1), 125 – 131, doi:http://dx.doi.org/10.1016/0021-9797(81)90309-X.

- Coantic, M. (1986), A model of gas transfer across air–water interfaces with capillary waves, *J. Geophys. Res.*, 91, 3925–3943, doi:10.1029/JC091iCo3p03925.
- Coantic, M., and P. Bonmarin (1975), The air-sea interaction simulation facility at the Institut de Mecanique Statistique de la Turbulence, Atmospheric Technology, (7), 72–79.
- Cox, C., and W. Munk (1954a), Measurements of the roughness of the sea surface from photographs of the sun's glitter, *J. Opt. Soc. Am.*, 44(11), 838–850.
- Cox, C., and W. Munk (1954b), Statistics of the sea surface derived from sun glitter, *J. Mar. Res.*, 13(2), 198–227.
- Cox, C., and W. Munk (1956), Slopes of the sea surface deduced from photographs of sun glitter, Tech. rep., University of California.
- Cox, P. M., R. A. Betts, C. D. Jones, S. A. Spall, and I. J. Totterdell (2000), Acceleration of global warming due to carbon-cycle feedbacks in a coupled climate model, *Nature*, 408, 184–187, doi:10.1038/35041539.
- Crapper, G. D. (1957), An exact solution for progressive capillary waves of arbitrary amplitude, *J. Fluid Mech.*, 2, 532–540, doi:10.1017/S0022112057000348.
- Davies, J. T., and E. K. Rideal (1963), *Interfacial Phenomena*, 2 ed., Academic Press, New York.
- Deacon, E. L. (1977), Gas transfer to and across an air-water interface, *Tellus*, 29, 363–374, doi:10.1111/j.2153-3490.1977.tb00746.x.
- Dean, R. G. (1991), *Water Wave Mechanics for Engineers and Scientists*, World Scientific, Singapore.
- Degreif, K. (2006), Untersuchungen zum Gasaustausch - Entwicklung und Applikation eines zeitlich aufgelösten Massenbilanzverfahrens, Dissertation, Institut für Umweltphysik, Fakultät für Physik und Astronomie, Univ. Heidelberg.
- Dieter, J. (1998), Analysis of Small-Scale Ocean Wind Waves by Image Sequence Analysis of Specular Reflections, Dissertation, IWR, Fakultät für Physik und Astronomie, Univ. Heidelberg.
- Donelan, M. A., W. M. Drennan, and A. K. Magnusson (1996), Nonstationary analysis of the directional properties of propagating waves, *J. Phys. Oceanogr.*, 26, 1901–1914, doi:10.1175/1520-0485(1996)026.
- Doney, S. C., V. J. Fabry, R. A. Feely, and J. A. Kleypas (2009), Ocean acidification: the other CO₂ problem, *Annual Rev. Marine Sci.*, 1, 169–192, doi:10.1146/annurev.marine.010908.163834.
- Dore, J. E., R. Lukas, D. W. Sadler, and D. M. Karl (2003), Climate-driven changes to the atmospheric CO₂ sink in the subtropical north Pacific ocean, *Nature*, 424, 754–757.

- Drennan, W. M., H. C. Graber, D. Hauser, and C. Quentin (2003), On the wave age dependence of wind stress over pure wind seas, *J. Geophys. Res.-Oceans*, 108(C3), 8062, doi:10.1029/2000JC000715.
- Ebuchi, N., and S. Kizu (2002), Probability distribution of surface wave slope derived using sun glitter images from geostationary meteorological satellite and surface vector winds from scatterometers, *J. Oceanogr.*, 58, 477–486.
- Edson, J. B., A. A. Hinton, K. E. Prada, J. E. Hare, and C. W. Fairall (1998), Direct covariance flux estimates from moving platforms at sea, *J. Atmos. Oceanic Technol.*, 15, 547–562.
- Fahle, P. (2013), Hochauflösende Messung der raumzeitlichen Variation der Neigung winderzeugter Wasserwellen, Diplomarbeit, Institut für Umwelphysik, Universität Heidelberg, Germany.
- Fedele, F., A. Benetazzo, G. Gallego, P.-C. Shih, A. Yezzi, F. Barbariol, and F. Ardhuin (2013), Space-time measurements of oceanic sea states, *Ocean Model.*, 70(0), 103–115, doi:http://dx.doi.org/10.1016/j.ocemod.2013.01.001.
- Frew, N. M., et al. (2004), Air-sea gas transfer: Its dependence on wind stress, small-scale roughness, and surface films, *J. Geophys. Res.*, 109, C08S17, doi:10.1029/2003JC002131.
- Frew, N. M., D. M. Glover, E. J. Bock, and S. J. McCue (2007), A new approach to estimation of global air-sea gas transfer velocity fields using dual-frequency altimeter backscatter, *J. Geophys. Res.*, 112, C11,003, doi:10.1029/2006JC003819.
- Friedl, F. (2013), Investigating the transfer of oxygen at the wavy air-water interface under wind-induced turbulence, Dissertation, Institut für Umwelphysik, Fakultät für Physik und Astronomie, Univ. Heidelberg.
- Gallego, G., A. Yezzi, F. Fedele, and A. Benetazzo (2011), A variational stereo method for the three-dimensional reconstruction of ocean waves, *IEEE T. Geosci. Remote*, 49(99), 4445–4457, doi:10.1109/TGRS.2011.2150230.
- Glover, D. M., N. M. Frew, and S. J. McCue (2007), Air-sea gas transfer velocity estimates from the Jason-1 and TOPEX altimeters: Prospects for a long-term global time series, *J. Mar. Syst.*, 66, 173–181, doi:10.1016/j.jmarsys.2006.03.020.
- Green, M. A. (2008), Self-consistent optical parameters of intrinsic silicon at 300 K including temperature coefficients, *Sol. Energ. Mat. Sol. C.*, 92(11), 1305 – 1310, doi:http://dx.doi.org/10.1016/j.solmat.2008.06.009.
- Guizar-Sicairos, M., S. T. Thurman, and J. R. Fienup (2008), Efficient subpixel image registration algorithms, *Opt. Lett.*, 33(2), 156–158, doi:10.1364/OL.33.000156.
- Hara, T., E. J. Bock, N. M. Frew, and W. R. McGillis (1995), Relationship between air-sea gas transfer velocity and surface roughness, in *Air-Water Gas Transfer*, edited by B. Jähne and E. Monahan, AEON Verlag.

- Hasselmann, K. (1962), On the nonlinear energy transfer in a gravity wave-spectrum. part 1: General theory., *J. Fluid Mech.*, 12, 481–500.
- Hasselmann, K. (1963), On the nonlinear energy transfer in a gravity wave-spectrum. part 2: Conservative theorems; wave-particle analogy; irreversibility., *J. Fluid Mech.*, 15, 273.
- Helmholtz, H. (1867), *Handbuch der physiologischen Optik*, Leopold Voss, Leipzig.
- Herlina, I., and G. H. Jirka (2008), Experiments on gas transfer at the air–water interface induced by oscillating grid turbulence, *J. Fluid. Mech.*, 594, 183–208, doi:10.1017/S0022112007008968.
- Hühnerfuss, H. (2006), Basic physicochemical principles of monomolecular sea slicks and crude oil spills, in *Marine Surface Films*, edited by M. Gade, H. Hühnerfuss, and G. M. Korenowski, pp. 21–35, Springer.
- Hühnerfuss, H., W. Walter, P. Lange, and W. Alpers (1987), Attenuation of wind waves by monomolecular sea slicks and the Marangoni effect, *J. Geophys. Res.*, 92, 3961–3963.
- Ho, D. T., C. S. Law, M. J. Smith, P. Schlosser, M. Harville, and P. Hill (2006), Measurements of air-sea gas exchange at high wind speeds in the southern ocean: Implications for global parameterizations, *Geophys. Res. Lett.*, 33, 16,611–16,616, doi:10.1029/2006GL026817.
- Ho, D. T., R. Wanninkhof, P. Schlosser, D. S. Ullman, D. Hebert, and K. F. Sullivan (2011), Toward a universal relationship between wind speed and gas exchange: Gas transfer velocities measured with $3\text{He}/\text{SF}_6$ during the southern ocean gas exchange experiment, *J. Geophys. Res.-Oceans*, 116, doi:10.1029/2010JC006854.
- Hoegh-Guldberg, O., et al. (2007), Coral reefs under rapid climate change and ocean acidification, *Science*, 318(5857), 1737–1742, doi:10.1126/science.1152509.
- Holthuijsen, L. H. (2007), *Waves in Oceanic and Coastal Waters*, Cambridge Univ. Press.
- Horn, J. (2013), *Hochaufgelöste Wellenhöhenmessung am Aeolotron mit Laser-induzierter Fluoreszenz*, Master's thesis, Universität Heidelberg.
- Hsu, S., E. A. Meindl, and D. B. Gilhousen (1994), Determining the power-law wind-profile exponent under near-neutral stability conditions at sea, *J. Appl. Meteor.*, 33, 757–765, doi:10.1175/1520-0450(1994)033<0757:DTPLWP>2.0.CO;2.
- Huhn, F. (2008), *A simple instrument for the measurement of the slope and height distributions of small scale wind-driven water waves*, Diplomarbeit, Institut für Umweltphysik, Universität Heidelberg.
- IPCC (2007), *Climate Change 2007: The Physical Science Basis. Contribution of Working Group I to the Fourth Assessment Report of the Intergovernmental Panel on Climate Change*, Cambridge University Press, Cambridge, United Kingdom and New York, NY, USA.
- Jackson, J. D. (1998), *Classical Electrodynamics*, 3rd ed., Wiley.

- Janssen, P. (2004), *The Interaction of Ocean Waves and Wind*, Cambridge Univ. Press, doi:10.2277/0521465400.
- Jenkins, A. D., and S. J. Jacobs (1997), Wave damping by a thin layer of viscous fluid, *Phys. Fluids*, 9(5), 1256–1264, doi:http://dx.doi.org/10.1063/1.869240.
- Jessup, A. T., C. J. Zappa, et al. (1997), Infrared remote sensing of breaking waves, *Nature*, 385(6611), 52–55.
- Jähne, B. (2005), *Digital Image Processing*, 6 ed., Springer, Berlin, doi:10.1007/3-540-27563-0.
- Jähne, B. (2009), Air-sea gas exchange, in *Encyclopedia Ocean Sciences*, edited by J. H. Steele, K. K. Turekian, and S. A. Thorpe, pp. 3434–3444, Elsevier, doi:10.1016/B978-012374473-9.00642-1, invited.
- Jähne, B., and H. Haußecker (1998), Air-water gas exchange, *Annu. Rev. Fluid Mech.*, 30, 443–468, doi:10.1146/annurev.fluid.30.1.443.
- Jähne, B., and K. Riemer (1990), Two-dimensional wave number spectra of small-scale water surface waves, *J. Geophys. Res.*, 95(C7), 11,531–11,646, doi:10.1029/JC095iC07p11531.
- Jähne, B., K. O. Münnich, and U. Siegenthaler (1979), Measurements of gas exchange and momentum transfer in a circular wind-water tunnel, *Tellus*, 31, 321–329, doi:10.1111/j.2153-3490.1979.tb00911.x.
- Jähne, B., W. Huber, A. Dutzi, T. Wais, and J. Ilmberger (1984), Wind/wave-tunnel experiments on the schmidt number and wave field dependence of air-water gas exchange, in *Gas transfer at water surfaces*, edited by W. Brutsaert and G. H. Jirka, pp. 303–309, Reidel, Hingham, MA.
- Jähne, B., K. O. Münnich, R. Bösinger, A. Dutzi, W. Huber, and P. Libner (1987), On the parameters influencing air-water gas exchange, *J. Geophys. Res.*, 92, 1937–1950, doi:10.1029/JC092iCo2p01937.
- Jähne, B., J. Klinke, and S. Waas (1994), Imaging of short ocean wind waves: a critical theoretical review, *J. Opt. Soc. Am.*, 11, 2197–2209, doi:10.1364/JOSAA.11.002197.
- Jähne, B., R. Nielsen, C. Popp, U. Schimpf, and C. S. Garbe (2005), Air-sea gas transfer; Schmidt number dependency and intermittency, in *Presented at: International Liege Colloquium on Ocean Dynamics, Gas Transfer at Water Surfaces*.
- Jähne, B., C. Popp, U. Schimpf, and C. Garbe (2007), The influence of intermittency on air/water gas transfer measurements, in *Transport at the Air Sea Interface — Measurements, Models and Parameterizations*, edited by C. S. Garbe, R. A. Handler, and B. Jähne, Springer, doi:10.1007/978-3-540-36906-6_18.
- Joelson, M., and M. C. Néel (2008), On alpha stable distribution of wind driven water surface wave slope, *Chaos*, 18(3), 033,117; 1–11, doi:10.1063/1.2955742.

- Johnson, R. S. (1997), *A Modern Introduction to the Mathematical Theory of Water Waves*, Cambridge Univ. Press.
- Khatiwala, S., et al. (2013), Global ocean storage of anthropogenic carbon, *Biogeosciences*, 10(4), 2169–2191, doi:10.5194/bg-10-2169-2013.
- Kiefhaber, D. (2010), Development of a Reflective Stereo Slope Gauge for the measurement of ocean surface wave slope statistics, Diplomarbeit, Institut für Umweltphysik, Fakultät für Physik und Astronomie, Univ. Heidelberg.
- Kiefhaber, D., R. Rocholz, and B. Jähne (2011), Improved optical instrument for the measurement of water wave statistics in the field, in *Gas Transfer at Water Surfaces 2010*, edited by S. Komori, W. McGillis, and R. Kurose, pp. 524–534.
- Kiefhaber, D., S. Reith, R. Rocholz, and B. Jähne (2013), High-speed imaging of short wind waves by shape from refraction, submitted to *J. Eur. Opt. Soc.-Rapid*, Nov 2013.
- Kinsman, B. (1965), *Wind Waves: Their Generation and Propagation on the Ocean Surface*, Prentice-Hall, Englewood Cliffs.
- Kitaigorodskii, S. A. (1984), On the fluid dynamical theory of turbulent gas transfer across an air-sea interface in the presence of breaking wind-waves, *J. Phys. Oceanogr.*, 14, 960–972.
- Klinke, J., and B. Jähne (1995), Measurements of short ocean waves during the mbl ari west coast experiment, in *Air-water Gas Transfer*, edited by B. Jähne and E. C. Monahan, pp. 165–173, Aeon, Hanau.
- Kock, A., J. Schafstall, M. Dengler, P. Brandt, and H. W. Bange (2012), Sea-to-air and diapycnal nitrous oxide fluxes in the eastern tropical north atlantic ocean, *Biogeosciences*, 9(3), 957–964, doi:10.5194/bg-9-957-2012.
- Kohlschütter, E. (1906), Die Forschungsreise S.M.S. Planet II. Stereophotogrammetrische Aufnahmen, *Annalen der Hydrographie und Maritimen Meteorologie*, 34, 220–227.
- Kosnik, M. V., and V. A. Dulov (2011), Extraction of short wind wave spectra from stereo images of the sea surface, *Meas. Sci. Technol.*, 22(1), 015,504.
- Kou, L., D. Labrie, and P. Chylek (1993), Refractive indices of water and ice in the 0.65–2.5 μm spectral range., *Appl. Opt.*, 32, 3531–3540.
- Krall, K. E. (2013), Laboratory investigations of air-sea gas transfer under a wide range of water surface conditions, Dissertation, Institut für Umweltphysik, Fakultät für Physik und Astronomie, Univ. Heidelberg.
- Kräuter, C. (2011), Aufteilung des transferwiderstands zwischen luft und wasser beim austausch flüchtiger substanzen mittlerer löslichkeit zwischen ozean und atmosphäre, Diplomarbeit, Institut für Umweltphysik, Fakultät für Physik und Astronomie, Univ. Heidelberg.

- Kräuter, C., D. Trofimova, D. Kiefhaber, and B. Jähne (2013), High-resolution 2-d fluorescence imaging of the mass boundary layer at free water surfaces, submitted to *J. Eur. Opt. Soc.-Rapid*, Nov 2013.
- Kudryavtsev, V. N., V. K. Makin, and B. Chapron (1999), Coupled sea surface atmosphere model. 2. spectrum of short wind waves, *J. Geophys. Res.*, 104, 7625–7640, doi:10.1029/1999JC900005.
- Kundu, P. K. (2008), *Fluid Mechanics*, 4th ed., Academic Press, Elsevier, San Diego, CA.
- Laas, W. (1905), Photographische Messung der Meereswellen, *Zeitschr. d. Vereins Dtsch. Ingenieure*, 49, S.1889 ff. S.1937 ff. und S.1976 ff.
- Laas, W. (1906), Messung der Meereswellen und ihre Bedeutung für den Schiffsbau, *Jahrbuch der Schiffsbau-techn. Gesellschaft*, 7, S.391 ff.
- Laas, W. (1921), Die photographische Messung der Meereswellen, *Veröff. Inst. f. Meereskunde N. F. Reihe A*, Heft 7.
- Lamont, J. C., and J. C. Scott (1970), An eddy cell model of mass transfer into the surface of a turbulent liquid, *AIChE Journal*, 16, 513–519, doi:10.1002/aic.690160403.
- Le Quéré, C., et al. (2007), Saturation of the southern ocean CO₂ sink due to recent climate change, *Science*, 316(5832), 1735–1738, doi:10.1126/science.1136188.
- Le Quéré, C., T. Takahashi, E. T. Buitenhuis, C. Rödenbeck, and S. C. Sutherland (2010), Impact of climate change and variability on the global oceanic sink of CO₂, *Global Biogeochem. Cy.*, 24(4), GB4007, doi:10.1029/2009GB003599.
- Levich, V. G. (1962), *Physicochemical hydrodynamics*, Prentice-Hall (Englewood Cliffs, N.J.).
- Liss, P. S., and L. Merlivat (1986), Air-sea gas exchange rates: Introduction and synthesis, in *The role of air-sea exchange in geochemical cycling*, edited by P. Buat-Menard, pp. 113–129, Reidel, Boston, MA.
- Liu, Y., X.-H. Yan, W. T. Liu, and P. A. Hwang (1997), The probability density function of ocean surface slopes and its effects on radar backscatter, *J. Phys. Oceanogr.*, 27, 782–797, doi:10.1175/1520-0485(1997)027.
- Longuet-Higgins, M. S. (1957), The statistical analysis of a random, moving surface, *Phil. Trans. R. Soc. Lond. A*, 249, 321–387, a. 966.
- Longuet-Higgins, M. S. (1960), Reflection and refraction at a random moving surface. ii. number of specular points in a gaussian surface, *J. Opt. Soc. Am.*, 50(9), 845–850.
- Longuet-Higgins, M. S. (1963a), The effect of non-linearities on statistical distributions in the theory of sea waves, *J. Fluid Mech.*, 17, 459–480.
- Longuet-Higgins, M. S. (1963b), The generation of capillary waves by steep gravity waves., *J. Fluid Mech.*, 16, 138–159.

- Longuet-Higgins, M. S. (1980), On the distribution of the heights of sea waves: Some effects of nonlinearity and finite band width, *J. Geophys. Res.*, 85(C3), 1519–1523, doi:10.1029/JCo85iCo3p01519.
- Longuet-Higgins, M. S. (1982), On the skewness of sea-surface slopes, *J. Phys. Oceanogr.*, 12, 1283–1291.
- Lucassen, J. (1968a), Longitudinal capillary waves. part 1.-theory, *Trans. Faraday Soc.*, 64, 2221–2229, doi:10.1039/TF9686402221.
- Lucassen, J. (1968b), Longitudinal capillary waves. part 2.-experiments, *Trans. Faraday Soc.*, 64, 2230–2235, doi:10.1039/TF9686402230.
- Lucassen, J. (1982), Effect of surface-active material on the damping of gravity waves: A reappraisal, *J. Colloid Interf. Sci.*, 85, 52–58.
- Lucassen-Reynders, E., and J. Lucassen (1969), Properties of capillary waves, *Adv. Colloid Interfac.*, 2, 347–395.
- McKenna, S. P., and W. R. McGillis (2004), The role of free-surface turbulence and surfactants in air-water gas transfer, *Int. J. Heat Mass Tran.*, 47, 539–553, doi:10.1016/j.ijheatmasstransfer.2003.06.001.
- Melville, W. K., R. Shear, and F. Veron (1998), Laboratory measurements of the generation and evolution of langmuir circulations, *J. Fluid Mech.*, 364, 31–58.
- Meyer, F. (1994), Topographic distance and watershed lines, *Signal Process.*, 38(1), 113 – 125, doi:http://dx.doi.org/10.1016/0165-1684(94)90060-4, <ce:title>Mathematical Morphology and its Applications to Signal Processing</ce:title>.
- Miller, S., T. Hristov, J. Edson, and C. Friehe (2008), Platform motion effects on measurements of turbulence and air-sea exchange over the open ocean, *J. Atmos. Oceanic Technol.*, 25, 1683–1694, doi:10.1175/2008JTECHO5471.
- Mironov, A. S., M. V. Yurovskaya, V. A. Dulov, D. Hauser, and C. A. Guérin (2012), Statistical characterization of short wind waves from stereo images of the sea surface, *J. Geophys. Res.-Oceans*, 117(C12), C00J35, doi:10.1029/2011JC007860.
- Münsterer, T., and B. Jähne (1998), LIF measurements of concentration profiles in the aqueous mass boundary layer, *Exp. Fluids*, 25, 190–196, doi:10.1007/s003480050223.
- Munk, W. (2009), An inconvenient sea truth: spread, steepness, and skewness of surface slopes, *Annual Rev. Marine Sci.*, 1, 377–415, doi:10.1146/annurev.marine.010908.163940.
- Naegler, T., P. Ciais, K. Rodgers, and I. Levin (2006), Excess radiocarbon constraints on air-sea gas exchange and the uptake of CO₂ by the oceans, *Geophys. Res. Lett.*, 33(11), L11,802, doi:doi:10.1029/2005GL025408.

- Nielsen, R. (2004), Gasaustausch – Entwicklung und Ergebnis eines schnellen Massenbilanzverfahrens zur Messung der Austauschparameter, Dissertation, Institut für Umweltphysik, Fakultät für Physik und Astronomie, Univ. Heidelberg.
- Nightingale, P. D., G. Malin, C. S. Law, A. J. Watson, P. S. Liss, M. I. Liddicoat, J. Boutin, and R. C. Upstill-Goddard (2000), In situ evaluation of air-sea gas exchange parameterization using novel conservation and volatile tracers, *Glob. Biogeochem. Cy.*, 14, 373–387, doi:10.1029/1999GB900091.
- Oppenheim, A. V., and R. W. Schaffer (2010), *Discrete-Time Signal Processing*, 3 ed., Pearson, Upper Saddle River, NJ.
- Oppenheim, A. V., R. W. Schaffer, and J. R. Buck (1999), *Discrete Time Signal Processing*, Prentice Hall.
- Orr, J. C., et al. (2005), Anthropogenic ocean acidification over the twenty-first century and its impact on calcifying organisms, *Nature*, 437, 681–686, doi:10.1038/nature04095.
- Pezzaniti, J. L., D. Chenault, M. Roche, J. Reinhardt, J. P. Pezzaniti, and H. Schultz (2008), Four camera complete Stokes imaging polarimeter, in *Polarization: Measurement, Analysis, and Remote Sensing VIII*, SPIE Proc., vol. 6972, p. 69720J, doi:10.1117/12.784797.
- Phillips, O. M. (1958), The equilibrium range in the spectrum of wind-generated waves, *J. Fluid Mech.*, 156, 426–434.
- Phillips, O. M. (1977), *The Dynamics of the Upper Ocean*, 2 ed., Cambridge University Press.
- Phillips, O. M. (1985), Spectral and statistical properties of the equilibrium range in wind-generated gravity waves, *J. Fluid Mech.*, 4, 426–434.
- Plant, W. J. (2003), Bound waves and sea-surface slopes, in *OCEANS 2003. Proceedings*, vol. 4, pp. 1825–1828.
- Quack, B., E. Atlas, G. Petrick, V. Stroud, S. Schaffler, and D. W. R. Wallace (2004), Oceanic bromoform sources for the tropical atmosphere, *Geophys. Res. Lett.*, 31(23), n/a–n/a, doi:10.1029/2004GL020597.
- Richter, K., and B. Jähne (2011), A laboratory study of the Schmidt number dependency of air-water gas transfer, in *Gas Transfer at Water Surfaces 2010*, edited by S. Komori, W. McGillis, and R. Kurose, pp. 322–332.
- Rocholz, R. (2008), Spatiotemporal measurement of short wind-driven water waves, Dissertation, Institut für Umweltphysik, Fakultät für Physik und Astronomie, Univ. Heidelberg.
- Rocholz, R. (2012), *Wisscy waves and wind*, unpublished manuscript.
- Sabine, C. L., et al. (2004), The ocean sink for anthropogenic CO₂, *Science*, 305, 367–372.

- Schaper, J. (2011), Wave height estimation with stereo images of the Reflective Stereo Slope Gauge (rssg), Diplomarbeit, Institut für Umweltphysik, Fakultät für Physik und Astronomie, Univ. Heidelberg.
- Scharr, H. (2000), Optimal separable interpolation of color images with bayer array format, Tech. rep., DFG research unit Image Sequence Analysis to Investigate Dynamic Processes, Interdisciplinary Center for Scientific Computing, University of Heidelberg, Germany.
- Schnieders, J., C. S. Garbe, W. L. Peirson, G. B. Smith, and C. J. Zappa (2013), Analyzing the footprints of near-surface aqueous turbulence: An image processing-based approach, *J. Geophys. Res.-Oceans*, 118(3), 1272–1286, doi:10.1002/jgrc.20102.
- Schooley, A. H. (1954), A simple optical method of measuring the statistical distribution of water surface slopes, *J. Opt. Soc. Am.*, 44(37).
- Siddiqui, M., M. R. Loewen, W. E. Asher, and A. T. Jessup (2004), Coherent structures beneath wind waves and their influence on air-water gas transfer, *J. Geophys. Res.*, 109, C03,024, doi:10.1029/2002JC001559.
- Soloviev, A., M. Donelan, H. Graber, B. Haus, and P. Schlüssel (2007), An approach to estimation of near-surface turbulence and CO₂ transfer velocity from remote sensing data, *J. Mar. Syst.*, 66(1-4), 182–194.
- Stokes, G. G. (1849), On the theory of oscillatory waves, *Trans. Camb. Philos. Soc.*, 8, 441.
- Sun, J., S. P. Burns, D. Vandemark, M. A. Donelan, L. Mahrt, T. L. Crawford, T. H. C. Herbers, G. H. Crescenti, and J. R. French (2005), Measurement of directional wave spectra using aircraft laser altimeters, *J. Atmos. Oceanic Technol.*, 22, 869–886, doi:10.1175/JTECH1729.1.
- Sweeney, C., E. Gloor, A. R. Jacobson, R. M. Key, G. McKinley, J. L. Sarmiento, and R. Wanninkhof (2007), Constraining global air-sea gas exchange for CO₂ with recent bomb ¹⁴C measurements, *Global Biogeochem. Cy.*, 21, B2015, doi:10.1029/2006GB002784.
- Takahashi, T., et al. (2002), Global sea-air CO₂ flux based on climatological surface ocean pCO₂ and seasonal biological and temperature effects, *Deep-Sea Res. Pt. II*, 49, 1601–1622.
- Takahashi, T., et al. (2009), Climatological mean and decadal change in surface ocean pCO₂, and net sea-air CO₂ flux over the global oceans, *Deep Sea Res. Pt. II*, 56, 554–577, doi:doi:10.1016/j.dsr2.2008.12.009.
- Tatarskii, V. I. (2003), Multi-gaussian representation of the cox-munk distribution for slopes of wind-driven waves, *J. Atmos. Oceanic Technol.*, 20(11), 1697–1705.
- Toba, Y., N. Iida, H. Kawamura, N. Ebuchi, and I. S. Jones (1990), Wave dependence of sea-surface wind stress, *J. Phys. Oceanogr.*, 20, 705–721.
- Troitskaya, Y., D. Sergeev, A. Kandaurov, G. Baidakov, M. Vdovin, and V. Kazakov (2012), Laboratory and theoretical modeling of air-sea momentum transfer under severe wind conditions, *J. Geophys. Res.-Oceans*, 117, C00J21, doi:10.1029/2011JC007778.

- Tucker, M., and H. Charnock (1954), A capacitance-wire recorder for small waves, *Coast. Eng. Proc.*, 1(5).
- van den Tempel, M., and R. van de Riet (1965), Damping of waves by surface-active materials, *J. Chem. Phys.*, 42, 2769–2777, doi:10.1063/1.1703235.
- Veron, F., and W. K. Melville (2001), Experiments on the stability and transition of wind-driven water surfaces, *J. Fluid Mech.*, 446, 25–65, doi:10.1017/S0022112001005638.
- Veron, F., W. K. Melville, and L. Lenain (2009), Measurements of ocean surface turbulence and wave-turbulence interactions, *J. Phys. Oceanogr.*, 39(9), 2310–2323, doi:10.1175/2009JPO4019.1.
- Waas, S., and B. Jähne (1992), Combined slope-height measurements of short wind waves: first results from field and laboratory measurements, in *Optics of the Air-Sea Interface: Theory and Measurements*, SPIE Proc., vol. 1749, edited by L. Estep, pp. 295–306.
- Wanninkhof, R. (1992), Relationship between wind speed and gas exchange over the ocean, *J. Geophys. Res.*, 97, 7373–7382, doi:10.1029/92JCo0188.
- Wanninkhof, R., and W. R. McGillis (1999), A cubic relationship between gas transfer and wind speed., *Geophys. Res. Lett.*, 26, 1889–1892, doi:10.1029/1999GL900363.
- Wanninkhof, R., W. E. Asher, D. T. Ho, C. Sweeney, and W. R. McGillis (2009), Advances in quantifying air-sea gas exchange and environmental forcing, *Annu. Rev. Mar. Sci.*, 1, 213–244, doi:10.1146/annurev.marine.010908.163742.
- Welch, P. D. (1967), The use of fast fourier transform for the estimation of power spectra: A method based on time averaging over short, modified periodograms, *Audio and Electroacoustics, IEEE Transactions on*, 15(2), 70–73, doi:10.1109/TAU.1967.1161901.
- Wentz, F. J. (1976), Cox and Munk's sea surface slope variance, *J. Geophys. Res.*, 81, 1607–1608, doi:10.1029/JCo81i009p01607.
- Young, I. R. (1999), *Wind generated ocean waves*, Elsevier.
- Young, I. R., and G. P. V. Vledder (1993), A review of the central role of nonlinear interactions in wind-wave evolution, *Philos. T. Roy. Soc. A*, 342(1666), 505–524, doi:10.1098/rsta.1993.0030.
- Zappa, C., M. Banner, H. Schultz, A. Corrada-Emmanuel, L. Wolff, and J. Yalcin (2008), Retrieval of short ocean wave slope using polarimetric imaging, *Meas. Sci. Technol.*, 19, 055,503 (13pp).
- Zappa, C. J., W. E. Asher, and A. T. Jessup (2001), Microscale wave breaking and air-water gas transfer, *J. Geophys. Res.-Oceans*, 106(C5), 9385–9391.

- Zappa, C. J., W. E. Asher, A. T. Jessup, J. Klinke, and S. R. Long (2002), Effect of microscale wave breaking on air-water gas transfer, in *Gas Transfer at Water Surfaces*, Geophysical Monograph, vol. 127, edited by E. Saltzman, M. Donelan, W. Drennan, and R. Wanninkhof, pp. 23–29, American Geophysical Union.
- Zappa, C. J., W. E. Asher, A. T. Jessup, J. Klinke, and S. R. Long (2004), Microbreaking and the enhancement of air-water transfer velocity, *J. Geophys. Res.*, 109, Co8S16, doi: doi:10.1029/2003JC001897.
- Zappa, C. J., W. R. McGillis, P. A. Raymond, J. B. Edson, E. J. Hintsa, H. J. Zemmeling, J. W. H. Dacey, and D. T. Ho (2007), Environmental turbulent mixing controls on air-water gas exchange in marine and aquatic systems, *Geophys. Res. Lett.*, 34, L10,601, doi:10.1029/2006GL028790.
- Zappa, C. J., M. L. Banner, H. Schultz, J. Gemmrich, R. P. Morison, D. LeBel, and T. Dickey (2012), An overview of sea state conditions and air-sea fluxes during RaDyO, *J. Geophys. Res.-Oceans*, 117, C00H19, doi:10.1029/2011JC007336.
- Zhang, X., and C. S. Cox (1994), Measuring the two-dimensional structure of a wavy water surface optically: A surface gradient detector, *Exp. Fluids*, 17, 225–237, doi: 10.1007/BF00203041.
- Zickler, T., P. Belhumeur, and D. Kriegman (2002), Helmholtz stereopsis: Exploiting reciprocity for surface reconstruction, *Int. J. Comp. Vis.*, 49(2-3), 215–227, doi:10.1023/A: 1020149707513.
- Zickler, T., J. Ho, D. Kriegman, J. Ponce, and P. Belhumeur (2003), Binocular helmholtz stereopsis, in *Computer Vision, 2003. Proceedings.*, pp. 1411–1417 vol.2, doi:10.1109/ICCV. 2003.1238655.

A

Appendix

A.1 Height from disparity

In eq. (3.4), the dependence of object distance on disparity in the stereo images was given. This expression can be derived from straightforward geometric considerations, as will be shown here.

Two coordinate frames are required (see Fig. A.1): A “world coordinate system” and a “camera coordinate system”. The world system has its y -axis aligned with the stereo baseline of the cameras, and its z -axis in the plane defined by the two optical axes of the cameras. The camera systems¹ have their z -axis aligned with the optical axis of the camera lens, its y -axis with the y -axis of the camera sensor and its origin in the (pinhole) aperture.

The position of the left and right camera in the world system are²

$$\mathbf{c}_{\text{left}}^w = (0, -b/2, 0)^T \quad \mathbf{c}_{\text{right}}^w = (0, b/2, 0)^T. \quad (\text{A.1})$$

The camera systems are rotated against the world system, because the camera optical axes are tilted towards each other. Also, a 180° rotation about the z -axis is necessary because of the way the cameras are mounted in the RSSG. The tilt angle is τ , the transformation matrix for a change from the world system to the left camera system thus is

$$\mathbf{R}_w^l = \begin{pmatrix} -1 & 0 & 0 \\ 0 & -\cos \tau & \sin \tau \\ 0 & \sin \tau & \cos \tau \end{pmatrix}. \quad (\text{A.2})$$

¹There are really two camera systems, one for the left camera and one for the right

²The column-vector is written as a row vector here only to save space. The “ T ” denotes that this row vector really should be transposed into a row vector.

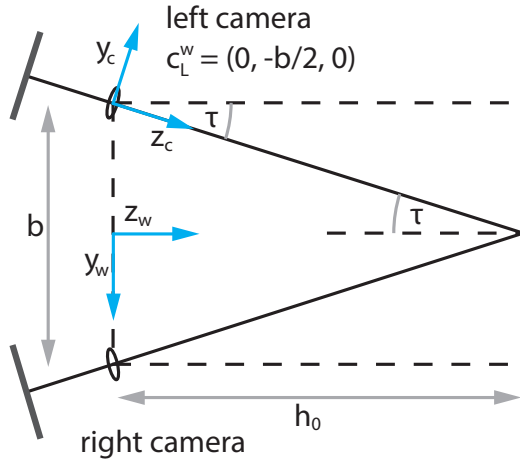


Figure A.1
The camera setup geometry and the used coordinate systems.

With eq. (A.1) and eq. (A.2) a point in space with coordinates $\mathbf{r}^w = (r_1, r_2, r_3)^T$ has coordinates

$$\mathbf{r}^l = \mathbf{R}_w^l (\mathbf{r}^w - \mathbf{c}_{\text{left}}^w), \quad (\text{A.3})$$

and similarly for the right camera

$$\mathbf{r}^r = \mathbf{R}_w^r (\mathbf{r}^w - \mathbf{c}_{\text{right}}^w), \quad (\text{A.4})$$

where the transformation matrix into the right camera system \mathbf{R}_w^r is just the transposed transformation matrix into the left camera system $\mathbf{R}_w^r = (\mathbf{R}_w^l)^T$. After transformation into a camera coordinate system, the vector \mathbf{r}^w can be normalized so that its z -component is equal to the focal length f of the lens (or the distance of the aperture to the camera sensor in the pinhole model). Then, the pixel positions (u and v) of the projection of the object with 3D coordinates (r_1, r_2, r_3) onto the camera sensor are given by the first two components of this normalized vector:

$$\hat{\mathbf{r}}^l = (u^l, v^l, f)^T = \left(-\frac{f r_1}{\sin(\tau)(r_2 + b/2) + \cos(\tau)r_3}, \frac{f(-\cos(\tau)(r_2 + b/2) + \sin(\tau)r_3)}{\sin(\tau)(r_2 + b/2) + \cos(\tau)r_3}, f \right)^T \quad (\text{A.5})$$

An equivalent expression can be written down for the right camera. The dependence of the second vector component (parallel to the stereo baseline) on the distance of the object r_3 is much stronger than that of the first component (orthogonal to the baseline). In the following, only this second component is used. The difference of the positions of the object in the two camera systems is the disparity d :

$$d = v^l - v^r. \quad (\text{A.6})$$

The resulting lengthy expression can be simplified by removing the angle τ . This angle is given by

$$\tau = \arctan\left(\frac{b}{2h_0}\right), \quad (\text{A.7})$$

with stereo baseline b and the target distance, at which the two optical axes intersect, h_0 (see Fig. A.1). The dependence on r_2 (see eq. (A.5)) can be replaced by a dependence on v^l with the help of eq. (A.5). The result is an expression for the disparity d in dependence of the distance to the object r_3 , which can easily be inverted to obtain

$$h \equiv r_3 = -\frac{b(4f^2h_0^2 - 2dbfh_0 + dv^lb^2 - (v^l)^2b^2)}{-4dfh_0^2 - (4b(v^l)^2 - 4dbv^l + 4bf^2)h_0 + dfb^2}, \quad (\text{A.8})$$

which was given as eq. (3.4) and is used for converting measured disparities into wave heights.

A.2 Marseille 2011

Table A.1 lists the measurement conditions that were set during the experiment in Marseille in March 2011. In the last four columns, the set LED current, the length of an individual image sequence, the total length of the records in this measurement, as well as the total duration of the measurement, in which the individual records are more or less evenly spread.

The measurement runs named *runXX* were used to compute mss, the runs named *longXX* were dedicated to measuring wave spectra, the runs named *mitDrahtXX* are runs for which synchronized and collocated measurements of wave wires are available.

Listed are the computed surface roughness parameter χ and reference mean square slope σ_s^2 values that were kindly provided by Dr. Caulliez of MIO, Marseille.

Given are also the length of each sequence (“seq.”), the total length of all data records at this conditions (“tot. data”) and the total duration of the measurement (“dur.”). For later experiments, a number of improvements in software (and measurement PC hardware) allowed for continuous measurements.

A.3 Marseille 2012

Table A.2 lists the measurements performed during the experiment in Marseille in September 2012. For reference with older publications, wind speed is not only given in m/s, but also the raw setting of the wind control potentiometer and the rotational speed of the fan are given. Thanks to upgrades in software, acquisition of the RSSG was continuous for the time given in *duration*, the big discrepancy between the duration of the measurement run and the actual duration of acquired data in the above experiment vanishes.

Table A.1.: Measurement runs and surface roughness results during the Marseille 2011 experiment. σ_s^2 (LSG) provided by Dr. Caulliez from MIO, Marseille.

U_{ref} [m/s]	date	run	LED [mA]	seq. [s]	tot. data [s]	dur. [min]	χ (RSSG)	σ_s^2 (LSG)
2	09/03	run1b	100	1	401	30	0.073	0.828
	10/03	run1	100	1	201	18	0.057	
	11/03	long1	100	19	56	8		
3	09/03	run2	230	1	402	32	0.571	1.392
	10/03	run2	230	1	301	27	0.554	
	11/03	long2	230	19	56	5		
4	09/03	run3	250	1	906	73	0.818	1.954
	10/03	run3	250	1	300	27	0.823	
	11/03	long3	250	19	56	14		
5	10/03	run4	260	1	800	72	1.010	2.606
	11/03	long3	260	19	56	4		
	11/03	mitDraht6-8	260	8	23	1		
6	09/03	run4	280	1	436	35	1.343	3.641
	10/03	run5	280	1	300	27	1.312	
	11/03	long5	280	19	56	7		
7	09/03	run5	280	1	505	55	1.939	4.263
	11/03	long6	280	19	56	14		
	11/03	mitDraht4-5	280	8	15	1		
8	09/03	run6	325	1	405	32	2.266	5.440
	10/03	run6	325	1	610	55	2.398	
	11/03	long7	325	19	56	7		
9	09/03	run7	350	1	314	25	2.720	6.727
	10/03	run7	350	1	400	36	2.849	
	11/03	long8	350	19	56	6		
10	09/03	run8	420	1	808	65	2.911	7.593
	11/03	long9	420	19	56	7		
11	10/03	run8b	500	1	700	65	3.234	8.948
	11/03	long9	500	19	56	7	4.032	
	11/03	mitDraht1-3	500	8	23	1		
12	09/03	run9	1000	1	617	50	4.476	10.190
	10/03	run9	1000	1	505	47	4.550	
	11/03	long11	1000	19	56	6		
13	09/03	run10	1000	1	712	62	4.737	10.740
	10/03	run10	1000	1	515	51	4.836	
	11/03	long11	1000	19	56	6		

Table A.2.: Measurements during the Marseille 2012 experiment.

wind speed m/s	fetch m	run	date	time local	Pitot mm	wind Skt	wind rpm	T_w °C	T_a °C	duration min
0.0	26.0	032	120913	18:10	0.00	0	0			10
2.5	2.2	001	120910	08:57	0.39	1.65	158	22.8	24.2	35
2.5	4.6	009	120911	08:37	0.39	1.73	164	22.8	24.2	35
2.5	9.4	013	120911	14:15	0.39	1.73	164	22.8	24.3	45
2.5	26.0	019	120912	10:35	0.38	1.73	165	22.9	24.6	35
3.0	2.2	002	120910	11:30	0.56	1.97	188	22.8	23.7	35
3.0	4.6	010	120911	10:15	0.56	2.02	193	22.9		30
3.0	9.4	014	120911	15:45	0.55	2.02	193	22.8	24.2	42
3.0	26.0	020	120912	12:00	0.54	2.02	193	22.9	24.3	30
3.0	26.0	033	120913	18:25		2.02				13
4.0	2.2	003	120910	13:12	1.00	2.6	246	22.7	23.8	65
4.0	4.6	011	120911	11:16	1.00	2.64	252	22.8	24.1	50
4.0	9.4	015	120911	16:55	1.00	2.64	252	22.8	24.2	50
4.0	26.0	021	120912	13:00	0.99	2.64	252	22.9	24.3	
4.4	26.0	035	120914		1.22					
5.0	2.0	026	120913		1.49	3.2	304	22.7	24.1	35
5.0	2.2	004	120910	14:45	1.56	3.2	304	22.8	23.9	40
5.0	4.6	012	120911	12:18	1.56	3.24	306	22.8	24.2	28
5.0	6.0	027	120913		1.49	3.2	304	22.6	23.8	20
5.0	9.4	016	120911	18:00	1.55	3.24	307	22.8	24.3	40
5.0	26.0	022	120912	14:10	1.55	3.24	307	22.9	24.2	30
5.0	26.0	031	120913	17:40		3.24			24.1	15
6.0	13.0	029	120913	16:00	2.24	3.9		22.5	23.9	15
7.0	6.0	028	120913	15:00	3.00	4.5	427	22.5	24.3	10
8.0	2.2	005	120910	15:40	4.00	5.09	481	22.7		40
8.0	4.6	007	120910	18:07	4.00	5.14	485	22.7	24.8	35
8.0	9.4	017	120911	19:05	4.01	5.14	484	22.8	24.5	35
8.0	26.0	023	120912	15:00	4.00	5.09	482	22.9	24.2	30
8.0	26.0	034	120914		4.01	5.09		22.2		10
8.0	26.0	038	120914	10:40	4.03	5.09				120
10.0	1.2	025	120913	09:00	6.20	6.27		22.8	24.4	
10.0	2.2	006	120910	16:35	6.25	6.27	595	22.7	24.7	35
10.0	4.6	008	120910	19:07	6.25	6.31	599	22.7		35
10.0	9.4	018	120912	08:40	6.25	6.31	599	22.9	24.4	30
10.0	26.0	024	120912	16:15	6.47	6.31	599	22.9	24.8	30

A.4 OSSPRE 2011

In Fig. A.2, the cruise track of the KM11-30 cruise (“OSSPRE”) on R/V Kilo Moana from Apia, Samoa to Honolulu, Hawaii in December 2011 is shown.

A.5 Meteor M91

Figure A.3 shows the stations at which wave measurements were conducted with the RSSG and MASG during the M91 cruise on FS Meteor in December 2012.

A list of the stations is provided in Tab. A.3. The last two columns give wind direction and wind speed, as measured by the Meteor’s meteorological instrumentation (measured at 35.3 m).

A.6 Aeolotron 2011

Table A.4 shows the effect of surfactants on the wind speed in the Aeolotron. The axial fans are set to a certain power, there is no feedback mechanism to adjust wind speed. Waves support additional wind stress which reduces the wind speed in the air space. If waves are suppressed, wind speeds are enhanced.

Table A.5 lists the results from the Aeolotron 2011 experiment. Reference wind speed and transfer velocities for nitrous oxide N_2O are taken from Krall (2013). Friction velocities for the clean water and low surfactant concentration case are also from Krall (2013), who computed them using the parameterization first given by Nielsen (2004) and confirmed by Bopp (2011). For the high surfactant concentration, the values measured by Bopp (2011) are used (while Krall 2013; used Nielsen’s clean water parameterization).

A.7 Reflectance measurements

One of the procedures for calibrating the angular dependence of the RSSG and MASG light sources is measuring the intensity of light reflected from a diffusely reflecting surface. For this type of calibration, the angular dependence of the reflecting material itself needs to be accounted for.

A diffusely reflecting material (a *Lambertian* reflector) exhibits a $\cos \theta$ -dependence of the intensity of light reflected back into the direction of incidence. The reflectance of a fully specular reflector (a mirror, a water surface) on the other hand is described by a Dirac delta function, light is reflected only at normal incidence (incidence angle $\theta = 0^\circ$). Real materials lie between these extrema.

For the calibration of the light sources, a reflecting material which has a negligible specular component is desired. Otherwise, in the vicinity of normal incidence, the

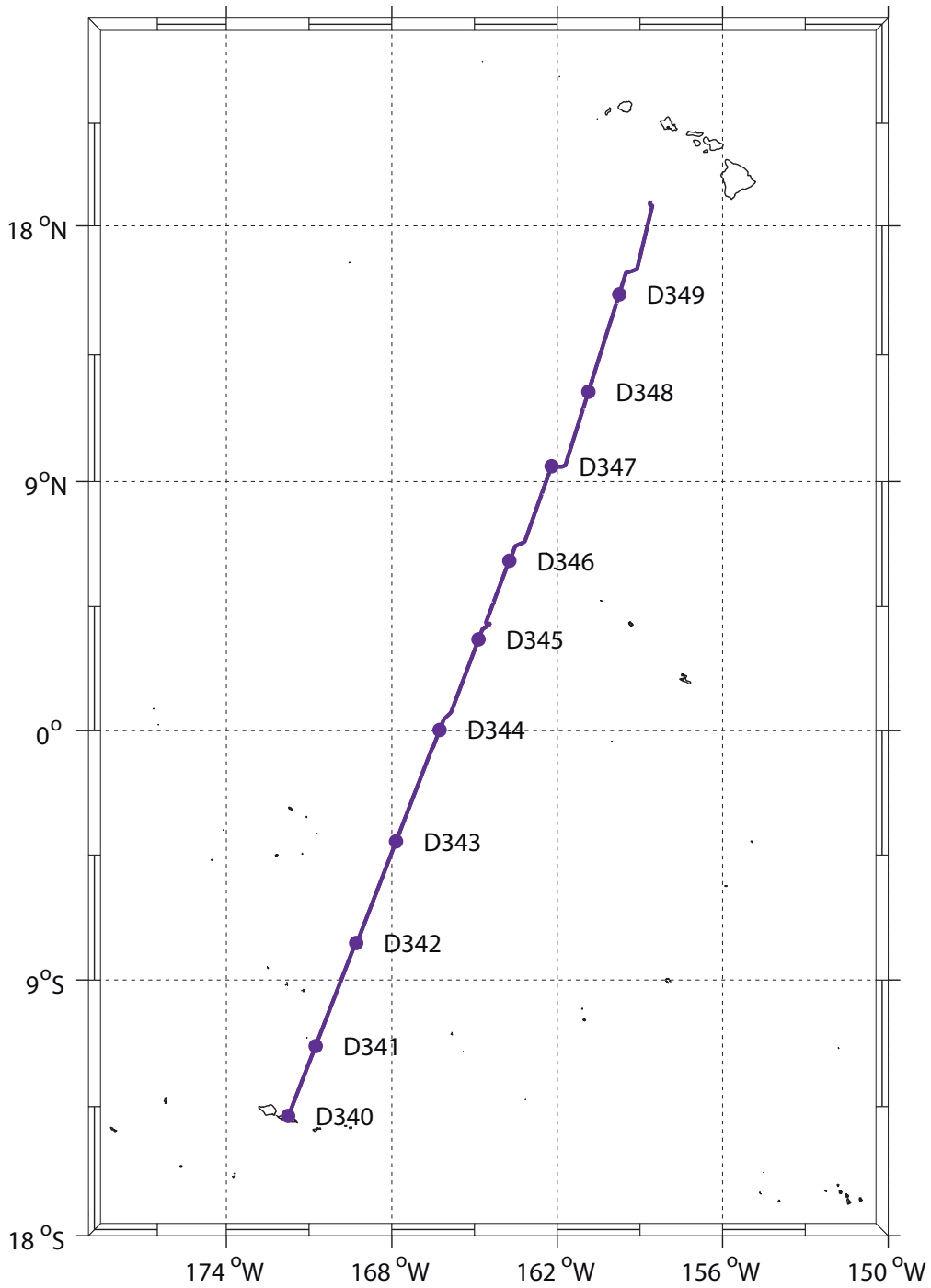


Figure A.2.: The track of KM11-30 from Apia, Samoa to Honolulu, Hawaii in December 2011.

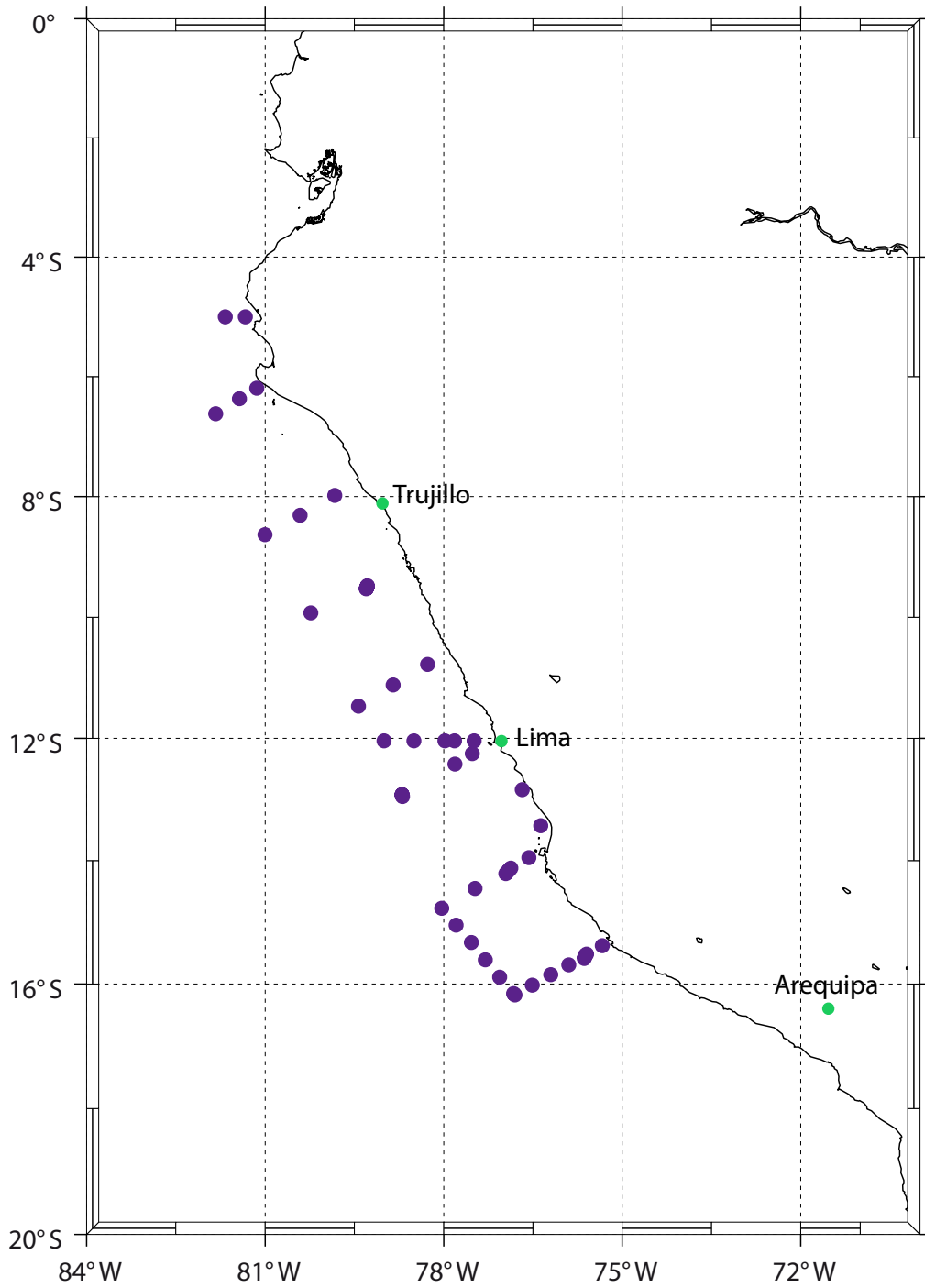


Figure A.3.: Location of the stations sampled with the RSSG and MASG.

Table A.3.: Measurements during the Meteor M91 cruise.

Date	Time	Station	Latitude	Longitude	W dir. [°]	U [m/s]
03.12.2012	23:11	1715-2	5° 0.02' S	81° 40.21' W	174	9
04.12.2012	06:41	1717-2	5° 0.03' S	81° 19.81' W	–	–
04.12.2012	16:43	1719-2	6° 11.52' S	81° 8.44' W	146	5
05.12.2012	01:05	1721-2	6° 22.02' S	81° 25.84' W	129	5
05.12.2012	12:35	1724-2	6° 37.20' S	81° 49.80' W	147	6
06.12.2012	03:43	1725-2	8° 37.87' S	81° 0.02' W	189	6
06.12.2012	15:18	1727-2	8° 18.67' S	80° 24.62' W	127	2
07.12.2012	02:24	1729-2	7° 58.82' S	79° 49.82' W	147	4
07.12.2012	23:56	1733-2	9° 28.81' S	79° 16.81' W	154	5
08.12.2012	03:58	1733-3	9° 29.52' S	79° 17.07' W	154	5
08.12.2012	08:03	1733-4	9° 30.24' S	79° 17.39' W	180	4
08.12.2012	11:58	1733-7	9° 31.27' S	79° 17.89' W	139	5
08.12.2012	16:00	1733-8	9° 31.85' S	79° 18.16' W	132	4
09.12.2012	12:58	1736-2	9° 55.82' S	80° 13.83' W	156	7
10.12.2012	02:48	1737-2	11° 28.24' S	79° 25.79' W	149	9
10.12.2012	14:13	1739-2	11° 7.25' S	78° 50.97' W	137	8
11.12.2012	01:05	1741-2	10° 46.82' S	78° 16.21' W	156	7
11.12.2012	21:54	1746-2	12° 2.42' S	77° 29.42' W	176	5
12.12.2012	03:37	1748-2	12° 2.40' S	77° 49.19' W	138	8
12.12.2012	08:44	1749-1	12° 2.41' S	77° 58.80' W	150	5
12.12.2012	16:07	1750-2	12° 2.44' S	78° 30.01' W	149	6
13.12.2012	00:34	1751-2	12° 2.41' S	79° 0.02' W	142	8
13.12.2012	12:04	1752-3	12° 55.23' S	78° 42.00' W	136	7
13.12.2012	18:38	1752-6	12° 57.03' S	78° 41.43' W	158	5
14.12.2012	00:30	1752-10	12° 55.23' S	78° 42.03' W	147	6
14.12.2012	05:31	1752-11	12° 55.26' S	78° 42.05' W	143	6
15.12.2012	00:42	1755-3	12° 25.23' S	77° 48.60' W	152	9
15.12.2012	07:06	1756-2	12° 15.03' S	77° 31.21' W	153	4
16.12.2012	13:09	1760-2	12° 50.44' S	76° 40.78' W	352	2
16.12.2012	23:38	1762-3	13° 25.81' S	76° 22.24' W	184	6
17.12.2012	04:02	1763-2	13° 57.04' S	76° 34.22' W	160	9
17.12.2012	10:16	1764-1	14° 7.27' S	76° 52.26' W	166	6
17.12.2012	16:02	1764-5	14° 8.79' S	76° 53.93' W	182	6
17.12.2012	22:30	1764-10	14° 11.11' S	76° 56.01' W	164	5
18.12.2012	04:00	1764-11	14° 12.57' S	76° 57.42' W	163	6
18.12.2012	18:58	1766-2	14° 27.07' S	77° 28.33' W	195	6
19.12.2012	08:30	1768-2	14° 46.40' S	78° 1.94' W	145	6
19.12.2012	14:46	1769-2	15° 2.93' S	77° 47.39' W	165	6
19.12.2012	22:11	1770-3	15° 19.70' S	77° 32.03' W	146	9
20.12.2012	04:16	1771-2	15° 36.58' S	77° 18.06' W	158	7
20.12.2012	10:21	1772-2	15° 53.52' S	77° 3.45' W	157	7
20.12.2012	16:19	1773-1	16° 10.71' S	76° 48.25' W	146	8
20.12.2012	23:33	1773-4	16° 9.36' S	76° 49.47' W	139	11
21.12.2012	21:15	1774-2	16° 1.14' S	76° 30.73' W	147	11
22.12.2012	04:06	1775-2	15° 50.99' S	76° 12.15' W	142	10
22.12.2012	10:58	1776-2	15° 41.46' S	75° 54.01' W	149	7
22.12.2012	18:34	1777-3	15° 31.19' S	75° 36.03' W	151	3
23.12.2012	00:31	1777-6	15° 32.46' S	75° 37.36' W	141	9
23.12.2012	06:34	1777-8	15° 33.65' S	75° 37.77' W	145	7
23.12.2012	12:34	1777-9	15° 35.19' S	75° 38.24' W	137	9
23.12.2012	20:39	1778-2	15° 22.83' S	75° 20.04' W	134	6

Table A.4.: The effect of surfactants on the wind speed in the Aeolotron: At the same frequency of the variable frequency drive, wind speeds are generally slightly higher in the surfactant cases, when wind stress is reduced at the smoother water surface.

	01.03.2011	03.03.2011	08.03.2011	10.03.2011
	[m/s]	[m/s]	[m/s]	[m/s]
condition 1	0.733	0.8	–	–
condition 2	1.414	1.46	1.463	1.438
condition 3	2.056	2.091	2.075	2.074
condition 4	2.691	2.717	2.695	2.718
condition 5	3.619	3.65	3.675	3.659
condition 6	4.795	4.851	4.927	4.898
condition 7	6.466	6.502	6.625	6.604
condition 8	8.251	8.288	8.372	8.369

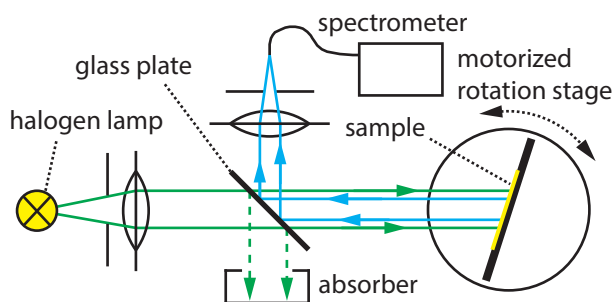


Figure A.4
Setup for the measurement of reflectances: The sample is placed on a motorized rotation stage and illuminated with a halogen lamp; the reflected light is analyzed with a spectrometer.

reflectance changes rapidly and a very precise alignment of the calibration setup is required. If the material is closer to a Lambertian reflector, the changes in reflectance are gradual and small alignment errors do not have severe consequences.

Figure A.4 shows the setup built for the characterization of reflectances: The sample is placed on a rotation stage whose orientation can be controlled precisely by a stepper motor. A halogen lamp serves as the light source, it is placed in the focal point of a lens, to guarantee near parallel illumination. The reflected light is coupled into an *OceanOptics* Maya Pro 2000 spectrometer with a wide-band grating (200 – 1100 nm). A thin glass plate is used as beam splitter to separate the reflected from the incident light.

Figure A.5a shows the result of two reference measurements to verify the setup. The measured reflectance of the mirror (green line) agrees with expectations, the finite width of the peak is due to the finite size of the illuminated and observed spot on the sample. A Lambertian calibration standard (blue dots) also agrees well with the cosine law predicted from theory (red line). The deviations are likely due to the standard and not due to the measurement setup.

Reflectances were measured for different materials (Fig. A.5b shows a selection). The first sample was a *white card*, a coated plastic sheet that is used in photography for white balance (blue curve). The white card has the highest reflectance of the shown materials, but clearly exhibits a specular component of the reflection around

Table A.5.: Results from the Aeolotron 2011 experiment. Wind speed and transfer velocities are taken from Krall (2013), friction velocities from Bopp (2011).

U_{ref} [m/s]	u_* [cm/s]	$k[\text{N}_2\text{O}]$ [cm/h]	σ_s^2	$\sigma_s^2(k < 100 \text{ rad/m})$	$\sigma_s^2(k > 100 \text{ rad/m})$
0.733	0.11	0.590	0.0024	0.0021	0.0003
1.414	0.15	2.610	0.0073	0.0054	0.0019
2.056	0.24	3.867	0.0127	0.0090	0.0037
2.691	0.34	6.070	0.0163	0.0110	0.0053
3.619	0.52	9.296	0.0246	0.0140	0.0106
4.795	0.82	15.607	0.0460	0.0185	0.0275
6.466	1.38	33.446	0.0782	0.0288	0.0493
8.251	2.14	52.658	0.1136	0.0397	0.0740
0.800	0.11	0.498	0.0020	0.0018	0.0002
1.460	0.17	0.728	0.0019	0.0017	0.0002
2.091	0.25	1.091	0.0019	0.0017	0.0002
2.717	0.35	2.100	0.0076	0.0067	0.0010
3.650	0.53	3.191	0.0101	0.0088	0.0013
4.851	0.84	7.042	0.0205	0.0130	0.0075
6.502	1.39	23.958	0.0738	0.0271	0.0467
8.288	2.15	43.913	0.1144	0.0402	0.0743
–	–	–	–	–	–
1.463	–	0.734	0.0019	0.0017	0.0002
2.075	0.15	1.093	0.0019	0.0016	0.0002
2.695	0.28	1.606	0.0018	0.0016	0.0002
3.675	0.45	2.191	0.0018	0.0016	0.0002
4.927	0.66	2.973	0.0018	0.0016	0.0002
6.625	1.06	11.218	0.0351	0.0168	0.0183
8.372	1.72	30.875	0.1013	0.0364	0.0649
–	–	–	–	–	–
1.438	–	0.756	0.0017	0.0015	0.0002
2.074	0.15	1.138	0.0017	0.0015	0.0002
2.718	0.28	1.355	0.0017	0.0015	0.0002
3.659	0.45	2.581	0.0045	0.0042	0.0003
4.898	0.66	3.828	0.0065	0.0060	0.0005
6.604	1.06	11.731	0.0387	0.0181	0.0207
8.369	1.72	33.258	0.0997	0.0353	0.0644

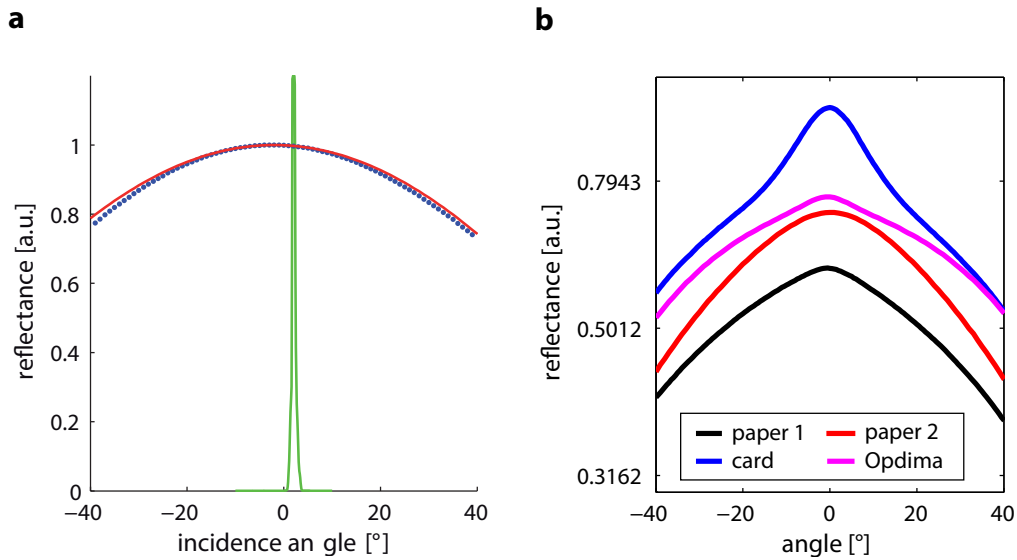


Figure A.5: **a** Reference measurements with a *Labsphere* radiance standard with Lambertian characteristic (blue dots) and a mirror (green line). The *Labsphere* standard agrees well with the theoretical cosine law (red line). **b** Reflectance measurements for different materials. Note that a logarithmic y-axis is used, absolute reflectance values are shown in arbitrary units.

0° incidence. A sample of OpDiMa, a material that is used for coating integrating spheres (magenta) has a much smaller specular component, but also a much lower absolute reflectance.

The reflectance of two kinds of paper was also measured, regular printer paper (paper 1, black) and a thicker paper used for filtering (paper 2, red). Both show no specular component, although they also differ significantly from a Lambertian reflector at larger incidence angles. Of all the measured materials, paper 2 was found to be best suited for the calibration measurements because of the combination of no specular component and relatively high absolute reflectance.

Danksagung

Mein Dank gilt allen, die zum Gelingen dieser Arbeit beigetragen haben. Zuallererst danke ich Herrn Prof. Dr. Bernd Jähne für die Betreuung und die Ermöglichung der Arbeit auf diesem spannenden Gebiet, seine Unterstützung während der gesamten Durchführung und seine allgemeine Wertschätzung von Eigeninitiative. Insbesondere weiß ich es sehr zu schätzen, dass er es mir (vor allem auch finanziell) ermöglichte, meine Arbeit auf mehreren internationalen Konferenzen zu präsentieren, selbst wenn dafür auf Mittel des Aversums zurückgegriffen werden musste. Auch für seine Unterstützung meiner Bemühungen um einen Auslands-Forschungsaufenthalt bin ich sehr dankbar. Der Kontakt zu internationalen Wissenschaftlern hat mir in der Durchführung dieser Arbeit sehr geholfen und wird sicher auch für die Zukunft von unermesslichem Wert sein.

Herrn Prof. Dr. Ulrich Platt möchte ich für seine freundliche Bereitschaft zur Zweitbegutachtung der Arbeit über die Weihnachtszeit danken. Herrn Prof. Dr. Matthias Bartelmann und Herrn Priv. Doz. Dr. Ulrich Schmidt danke ich für die Bereitschaft, Teil meines Prüfungskomitees zu sein.

I want to thank Dr. Christopher Zappa for his willingness to host me during my nine month Fulbright research visit to Lamont-Doherty Earth Observatory. My time in New York was a valuable experience for me both personally and professionally. Many aspects of this work have only been possible through the close collaboration with Chris and his group. My participation in the OSSPRE 2011 cruise on R/V Kilo Moana would not have been possible without his support. In this context, I also want to thank Dr. Andrew Jessup and Dr. William Asher from the Applied Physics Lab at University of Washington, Seattle, for the opportunity to participate in this cruise.

Vielen Dank auch an Dr. Hermann Bange (und Dr. Annette Kock) für die Möglichkeit der Teilnahme am Meteor M91 Experiment und die exzellente Planung von Gerätetransport, Reisen und allem was dazugehört.

Merci à Dr. Guillemette Caulliez de l'Institut Méditerranéen d'Océanologie pour l'assistance pendant les experiments à Marseille et tous les discussions et suggestions de l'interprétation des images du RSSG. Merci aussi pour les resultats du Laser Slope Gauge pour comparaison et la validation du RSSG.

Ein großer Dank geht an alle Mitglieder der *Windis*-Arbeitsgruppe am IUP. Einerseits für die gute Zusammenarbeit und angenehme Arbeitsatmosphären während meiner gesamten Zeit dort, andererseits insbesondere für die Unterstützung gegen Ende. Christine Kräuter danke ich für ihr Korrekturlesen des größten Teils dieser Arbeit und die vielen nützlichen Diskussionen über Gasaustausch, Wellen, und Pfeile in Abbildungen. Dr. Felix Friedl und Nils Krah danke ich für die immer offene Tür und das Interesse an Diskussionen über beliebige komplexe und oft unlösbare Probleme. Dr. Roland Rocholz gilt ein besonderer Dank für die gute und enge Zusammenarbeit insbesondere zu Beginn meiner Zeit am IUP und in der Konstruktion der RSSG. Bei Dr. Günther Balschbach bedanke ich mich für seine wertvollen

Erfahrungen aller Art, von Holzkonstruktionen über LED-Elektronik bis hin zu Imaging Slope Gauge Datenauswertung. Wolfgang Mischler danke ich für die Erstellung von Kamera-Treibermodulen, die die Handhabung der Instrumente erheblich erleichterten, sowie für die zahlreichen Diskussionen über Elektronik, Optik und Kamerakalibrierung. Ein großer Dank geht auch an Max Bopp für seine großen Bemühungen, das Rätsel der Schubspannungsgeschwindigkeit am Aeolotron zu lösen. Kerstin Krall danke ich für die Gasaustauschdaten des Aeolotron-Experiments und die hilfreichen Erläuterungen dazu. Für das Korrekturlesen von Teilen dieser Arbeit danke ich außerdem Darya Trofimova, Svenja Reith, und Paul Bauer. Leila Nagel, Sophia Brumer (LDEO, New York), Julia Schaper und allen Teilnehmern der M91 und OSSPRE 2011 Fahrten danke ich für die gute Arbeitsatmosphäre während der Durchführung der Labor- und Feldexperimente.

Der Werkstatt des IUP, insbesondere Ralph Pfeifer und Heribert Sommer, gebührt großer Dank für die Konstruktion der RSSG und des Aufbaus für den Bug der Meteor.

Meinen Freunden und meiner Familie danke ich für ihr Verständnis und die mentale Unterstützung insbesondere in den letzten Monaten, in denen ich vollständig abgetaucht war. Ich freue mich darauf, dass sich das bald wieder ändert und ich mehr Zeit mit euch verbringen kann.